Characterization of Na-Loaded Type II Si and Ge Clathrates: A Systematic Structure–Property Evaluation of Thermoelectric Materials

by

Andrew Ritchie

Submitted in partial fulfilment of the requirements
for the degree of Doctor of Philosophy

at

Dalhousie University
Halifax, Nova Scotia
December 2011

DALHOUSIE UNIVERSITY

DEPARTMENT OF CHEMISTRY

The undersigned hereby certify that they have read and recommend to the Faculty of Graduate Studies for acceptance a thesis entitled “Characterization of Na-Loaded Type II Si and Ge Clathrates: A Systematic Structure–Property Evaluation of Thermoelectric Materials” by Andrew Ritchie in partial fulfilment of the requirements for the degree of Doctor of Philosophy.

Dated: December 8, 2011

External Examiner: _______________

Research Supervisor: _______________

Examining Committee: _______________

____

____

Departmental Representative: _______________

DALHOUSIE UNIVERSITY

DATE: December 8, 2011

AUTHOR: Andrew Ritchie

TITLE: Characterization of Na-Loaded Type II Si and Ge Clathrates: A Systematic Structure–Property Evaluation of Thermoelectric Materials

DEPARTMENT OR SCHOOL: Department of Chemistry

DEGREE: PhD CONVOCATION: May YEAR: 2012

____
Signature of Author

For The Fou,
Who never learned to read...

Table of Contents

List of Tables

List of Figures

Abstract

The present study aims to increase understanding of the physical processes that govern thermoelectric efficiency in Na-containing group 14 type II clathrates. This has been achieved through structural characterization and physical property measurements.

Local and electronic structures of Si clathrates with the formula Na_xSi_{136}, where $x = 0$, 1.3, 5.5, 7.2, 8.8, 14.1, 20 and 21.5 were studied using x-ray absorption spectroscopy. Thermoelectric properties, namely Seebeck coefficient, electrical conductivity and thermal conductivity were measured from 2.5 K to 400 K. Low Na content samples, $x < 8$, showed reduced thermal conductivity compared to the empty clathrate, $x = 0$. For $x > 8$, increased Na content led to increased charge transfer, increased thermal conductivity and decreased magnitude of Seebeck voltages.

The heat capacities of the Na_xSi_{136} materials were measured from 2.5 K to 300 K. Analysis of the heat capacity data showed that the vibrational modes associated with Na in the Si_{28} cages are of sufficiently low energies to interact with heat transporting acoustic phonons, leading to reduced thermal conductivity as x is increased up to ~ 8. Increasing Na content beyond $x = 8$ introduces Na into the Si_{20} cages. This stiffens the lattice, increasing (or maintaining) phononic contributions to thermal conductivity, and increasing electronic contributions. Electronic thermal conductivity is responsible for upwards of 50 % of heat conduction when $x = 21.5$.

Na containing type II Ge clathrates were produced using an ionic liquid reaction medium. Seebeck coefficients observed in Na_9Ge_{136} materials, were negative but larger in magnitude than those of the Na_xSi_{136} materials and thermal conductivities of Na_9Ge_{136} were lower than those of the Na_xSi_{136} materials.

While both Si and Ge type II clathrates showed modest figures of merit, with maximum ZT values of 2.5×10^{-6} and 2.8×10^{-5} observed in $Na_{20}Si_{136}$ and Na_9Ge_{136}, of the two framework elements, type II Ge clathrates have been shown to have more favourable thermoelectric properties.

List of Abbreviations and Symbols Used

ΔV – potential difference

ΔT – temperature difference

S – Seebeck coefficient

E_F – Fermi energy

I – current

$\dot{Q}$ – rate of heat flux

Π - Peltier coefficient

T – temperature

$\dot{q}$ – heat

κ – thermal conductivity

A – cross-sectional area

n – as a subscript designates the n-type semiconductor branch of a p-n junction

p – as a subscript designates the p-type semiconductor branch of a p-n junction

$\mathrm{d}T/\mathrm{d}x$ – temperature gradient

ρ – electrical resistivity

c – as subscript designates the cold side

h – as subscript designates the hot side

l – length

x – position in gradient or Na fraction in type II clathrate structure, as determined from context

K – thermal conductance

R – electrical resistance

$I_{\dot{q}_{max}}$ – current that produces maximum cooling

$\dot{q}_{c_{max}}$ – maximum cooling power

Z – figure of merit

σ – electrical conductivity

ZT – unitless figure of merit

η – efficiency

W – work

q□$_h$ – net heat exchange

η_C – Carnot limit for efficiency

T_{M} – average temperature

PGEC – Phonon Glass/ Electron Crystal

j_{U} – flux of thermal energy

C – heat capacity per unit volume

v – mean speed of energy carrier or speed of sound, as determined from context

λ – mean free path or wavelength of radiation, as determined from context

κ_e – electronic contribution to thermal conductivity

$\kappa_{lattice}$ – lattice contribution to thermal conductivity

N – number of atoms or normal, as determined from context

ω - frequency

k – wavevector or Boltzmann constant, as determined from context

a – lattice constant or empirical constant used for thermal conductivity shoe calibration, as determined from context

U – *umklappen* (to turn back)

$\overset{\varpi}{G}$ – momentum transfer to the lattice

C_v – heat capacity at constant volume

C_E – Einstein heat capacity

θ_E – Einstein characteristic temperature

h – Planck’s constant

υ_E – Einstein frequency

ν_D – Debye frequency

C_D – Debye heat capacity

θ_D – Debye characteristic temperature

n – number of charge carriers

e_{o} – charge of charge carriers

μ – mobility of charge carriers

m_{e} – mass of particle

λ_e – mean free path of particle

L – Lorenz number

NMR – Nuclear Magnetic Resonance

PPMS – Physical Properties Measurement System

TTO – Thermal Transport Option

d – diameter or spacing between lattice planes, as determined from context

ε – emissivity

dT/T – temperature stability with respect to the temperature at which measurement is taken

K_{total} – total heat conductance

P – heater power

K_{sample} – heat conductance of sample

P_{rad} – power loss due to radiation

K_{shoes} – heat conductance of shoes

b – empirical constant used for thermal conductivity shoe calibration

c – empirical constant used for thermal conductivity shoe calibration

S_A – total sample surface area

ΔT_∞ – approximated steady state temperature difference

τ_1 – long empirical time constant

t – time

τ_2 – short empirical time constant

ΔV_∞ – approximated steady state voltage difference

τ_2' – time constant

d – linear drift parameter

e – offset voltage parameter

AC – alternating current

DC – direct current

h – height

w – width

$R_{\Delta T}$ – approximated steady state temperature difference residual

$R_{\Delta \mathrm{V}}$ – approximated steady state voltage difference residual

R_ρ – resistivity residual

V_{pp} – peak-to-peak amplitude of voltage versus time signal

$\sigma(S)$ – uncertainty in Seebeck coefficient

$\sigma(\kappa)$ – uncertainty in thermal conductivit

$\sigma(\rho)$ – uncertainty in electrical resistivity

$\sigma(ZT)$ – uncertainty in unitless thermoelectric figure of merit

t_o – time of discontinuation of heater current

T_{pl} – temperature of platform

C_{pl} – heat capacity of platform

K_W – thermal conductance between the platform and the heat-sink via the connecting wires

$T_\circ$ – temperature of the thermal bath (the puck frame)

$P(t)$ – power applied to heater

C_p – heat capacity at constant pressure

m – mass

XRD – x-ray diffraction

PXRD – powder x-ray diffraction

n - integer

θ – angle between incident rays and scattering planes

XAS – X-ray Absorption Spectroscopy

UV-Vis – ultraviolet-visible

HOMO – Highest Occupied Molecular Orbital

LUMO – Lowest Occupied Molecular Orbital

$\mu(E)$ – x-ray absorption coefficient

FLY – Fluorescence yield

TEY – Total electron yield

XANES – x-ray absorption near edge structure

EXAFS – x-ray absorption fine structure

SGM – spherical grating monochromator

LDOS – local (orbital) density of states

$\chi(k)$ – normalized k-space absorption coefficient

S_o^2 – amplitude reduction factor

SEM – Scanning Electron Microscopy

EDS – Energy-Dispersive X-ray Spectroscopy

WDS – Wavelength Dispersive X-ray Spectroscopy

$F(k)$ – backscattering amplitude

N_j – number neighbouring atoms of the j-th type

R_j – interatomic distance

σ^2 – Debye-Waller factor

$\delta(k)$ – total phase shift experienced by the photoelectron

R(avg) – average bond distance

CN – coordination number

R(avg) XRD – bond distance of a particular scattering path as determined from XRD data

ΔR – difference in bond distance as determined by EXAFS and PXRD

E_o – empirical parameter related to the fitting used to compensate the small atom approximation

SPS – Spark Plasma Sinter

ϕ – fractional porosity

ρ_{eff} – measured density

ρ_{bulk} – theoretical density from PXRD

γ – electronic contribution to heat capacity, the Sommerfeld constant

pT^3 – phononic contribution to heat capacity

$D(E_F)$ – electronic density of states at the Fermi level

C_p^{latt} – lattice contribution to heat capacity

θ_D^{eff} – effective (lattice-average) Debye temperature

Δx – difference in Na content

α – coefficient of thermal expansion

β_T – coefficient of isothermal compressibility

C_{ENas} – Einstein heat capacity for Na in the Si_{20} cages

C_{ENal} – Einstein heat capacity term for Na in the Si_{28} cages

C_{ESi1} – Einstein heat capacity terms for Si framework

C_{ESi2} – Einstein heat capacity term for Si framework

C_{DSi} – Debye heat capacity term for Si framework

θ_{DSi} – Debye temperature associated with C_{DSi}

θ_{ESi1} – Einstein temperature associated with C_{ESi1}

θ_{ESi2} – Einstein temperature associated with C_{ESi2}

θ_{ENas} – Einstein temperature associated with C_{ENas}

θ_{ENal} – Einstein temperature associated *with* C_{ENal}

V – volume of unit cell

β – thermal conductivity correction factor

$\kappa_{\mathrm{experiment}}$ – experimental thermal conductivity

$\kappa_{\mathrm{calculated}}$ – calculated thermal conductivity

$C_{p,vol}$ – heat capacity at constant pressure per cubic meter

κ_{ph} – calculated phononic contribution to thermal conductivity

L_{eff} – effective Lorenz number

Acknowledgements

I would like to thank my supervisor, Prof. Mary Anne White for her patience, guidance and support throughout my research and writing efforts. Members of the Mary Anne White lab group, past and present, have also been very helpful in discussion and made my time here a pleasure. Special thanks Mike Johnson for technical assistance with the PPMS, to him and Cathy Whitman for help in editing this document and to John Niven for heat capacity fitting and modeling work.

I gratefully acknowledge Prof. Jeff Dahn for the use of lab equipment and his students for their help and instruction on that equipment. I would especially like to acknowledge the welding and x-ray work done by Dr. Fu Zhu and assistance from Dr. Andrew van Bommel with x-ray equipment. Ge synthesis work was made possible by Andy George in the high temperature physics lab, and for his efforts, I am grateful. Thanks to Dan MacDonald for SEM and microprobe analysis.

I would like to thank Dr. Matt Beekman for producing and characterizing the Na_xSi_{136} samples, the main materials of interest in this thesis as well as for heat capacity data. I would like to thank Prof. Terry Tritt for producing the Si_{136} sample and for heat capacity data on that sample and Prof. George Nolas for heat capacity data.

Thanks to Dr. Robert Blyth and Dr. Tom Reigers (SGM beamline of the Canadian Light Source) for synchrotron technical support. Thanks to Prof. Peng Zhang for assistance in XAS interpretation and Mark MacDonald for EXAFS refinement work.

I thank my family and friends for their enduring support, encouragement and understanding. Finally, a huge thanks to the one Ms. Natalie Hunt for keeping me this side of crazy these last few months (that was a close one).

Chapter 1: Introduction

1.1 General Introduction

Over the past several decades it has become commonly accepted that humans are having a significant negative impact on environments. Our high consumption of fossil fuels and haphazard release of harmful substances into water systems and the atmosphere have had a global effect that even our wholly self-centred species can no longer avoid observing. Along with the realization that we are having a significant negative influence on our surroundings has come a (self-preservationalist) sense of responsibility to stop or slow as best we can the (self-) destruction we have initiated. A large part of our reform initiative is to reduce consumption of fossil fuels and the quantity of harmful substances released into our surroundings. Since we do not want to have to trade use of energy, our main commodity, in exchange for a healthier environment and our continued existence, increased efficiency and environmentally safe alternatives are the only available choices.

The main mechanism for acquiring energy from fossil fuels is combustion. This mode of energy production can be quite inefficient. Over half of the energy released from the combustion of gasoline is wasted, lost as heat.[1] Thermoelectric materials present a possible means to reduce fuel consumption by harvesting waste heat and converting it to useful energy.

As well as being able to produce electricity from a heat source, thermoelectric elements can be used for purposes of temperature control. While these materials are capable of both localized heating and cooling, it is the ability to cool that is of greater technological significance. Because thermoelectric elements are solid state devices, they avoid the release of harmful gasses into the atmosphere as frequently occurs when employing gas-phase refrigeration methods.

In addition to environmental benefits, thermoelectric materials present practical advantages for purposes of power generation and temperature control. Radioisotope thermoelectric generators, for example, have been used in areas where it is not practical to have a person present for maintenance and operation. An extreme example is the use of such generators to power space missions,[1] where alternatives to internal combustion must be used to generate electricity for instruments. In addition, solid-state cooling devices have no moving parts, and are therefore much less susceptible to mechanical failure than are refrigeration devices that rely upon compression. In fact, thermoelectric devices have demonstrated reliability over periods of time measuring in the tens of years.[1, 2]

Despite the many advantages thermoelectric devices offer, there have been only relatively moderate advances in these materials since the late 1950's when a microscopic understanding of thermoelectric phenomena and the materials currently in use were developed.[3] The developments leading to these materials were the culmination of 20 years of interest which followed 80 years of inactivity. Initial research into thermoelectrics began in 1821 with the observation of the Seebeck effect, then later by the observation of the Peltier effect, both named for their discoverers. Due to growing environmental concerns, increased need for power generation in remote and unpopulated locations and low efficiencies of existing thermoelectric technologies, there has been recent renewed interest in thermoelectric materials.

1.2 Seebeck Effect

When two dissimilar materials are joined, and the junction is placed at a temperature different from that of the free ends, a voltage is produced across the junction. This is known as the Seebeck effect and the magnitude of the potential difference, ΔV, across the junction is proportional to the temperature difference, ΔT, between the free ends and the junction through a constant. The proportionality constant that describes this effect is known as the Seebeck coefficient, S. The Seebeck coefficient is specific to the material and temperature, such that:[3]

$$\Delta V = S\Delta T. \tag{1.1}$$

Initially, when two dissimilar materials are placed in contact the voltage produced is a contact potential that arises due to the equalization of the Fermi energies of the dissimilar materials. In the case of doped semiconductors, the energy gaps shift to equalize their Fermi energies and electrons flow from the valence band of the *n*-type semiconductor to the conduction band of the *p*-type semiconductor. Figure 1.1 illustrates this contact potential process.

The Seebeck effect is observed when such a system is placed in a thermal gradient because thermal energy promotes charge carriers into the conduction band of the material. The charge carriers then diffuse to a region of lower thermal energy, resulting in a build up of charge and an overall potential difference across the junction.

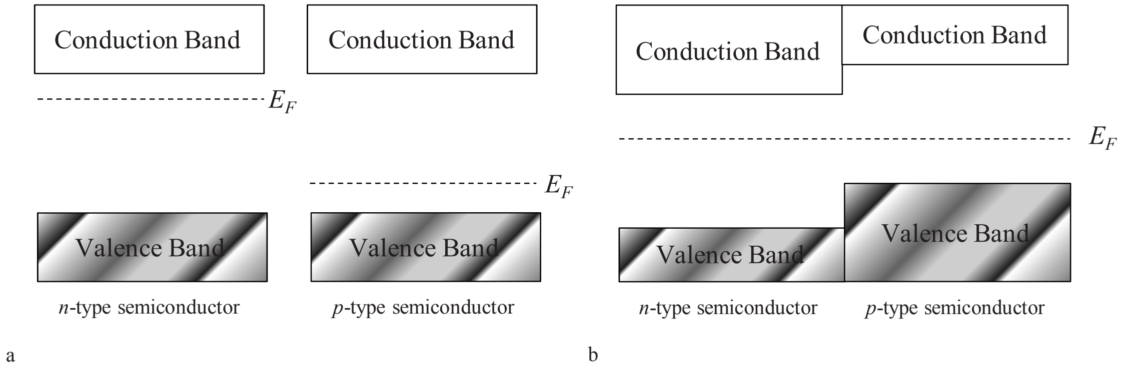

Figure 1.1 – Energy diagram for a junction between an *n* –type semiconductor and a *p* –type semiconductor (a) before contact and (b) after contact. Styled after Ref. 4.

Metals are observed to have low Seebeck coefficients, typically below 10 μV K^{-1}, whereas typical values for semiconductors are greater than about 100 μV K^{-1} and usually range in magnitude between 150 and 250 μV K^{-1} for semiconductors used in thermoelectrics.[5] Equation (1.1) shows that higher Seebeck coefficients produce higher voltages, consequently semiconductors are the thermoelectric materials of choice.

The sign as well as the magnitude of the Seebeck coefficient measured for a given material varies depending on the concentration and identity of the majority charge carrier of a material (holes or electrons). The Seebeck coefficient is negative for *n*-type semiconductors, having electrons as the majority charge carries, and positive for *p*-type semiconductors, having positively charged holes as majority charge carriers.

1.3 Peltier Effect

The Peltier effect can be thought of as the reverse Seebeck effect, whereby a current, *I*, is passed across the junction between two dissimilar materials and heat results at the junction. The amount of heat produced at the junction is greater than that which can be accounted for by resistance (Joule) heating alone. The rate of heat flux at the junction $\dot{Q}$, is related to the amount of current passed across it through the Peltier coefficient, Π,[3]

$$\dot{Q} = \Pi I. \tag{1.2}$$

When the direction of the current is reversed, instead of an increase in temperature at the junction, a decrease in temperature is observed. The cooling effect is related to the current through the Peltier coefficient as described in Equation (1.2). As with the Seebeck effect, semiconductors exhibit stronger Peltier effects than metals. Figure 1.2 shows that the Peltier effect and the Seebeck effect are closely related to one another.

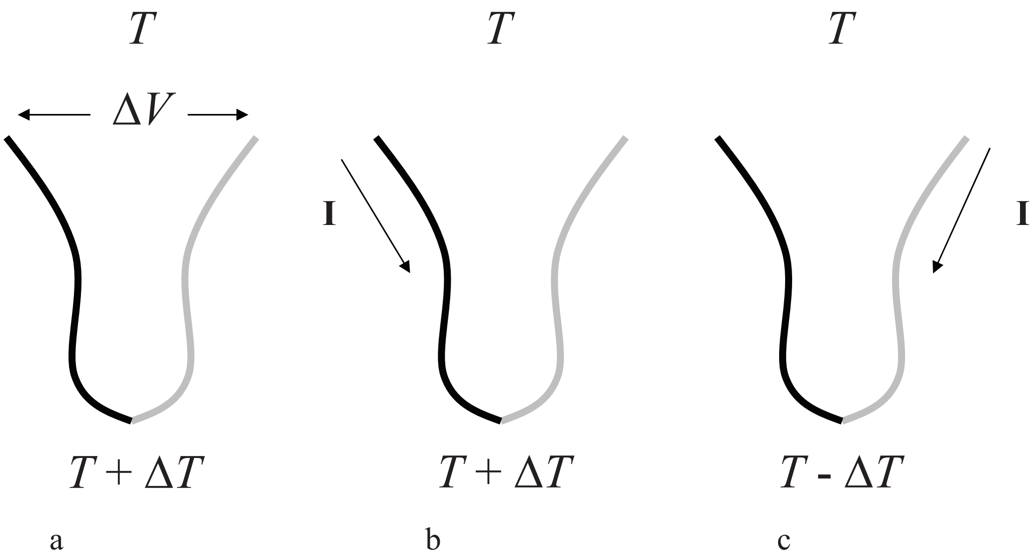

Figure 1.2 – Schematic representation of (a) Seebeck effect, (b) Peltier heating and (c) Peltier cooling. The different colours indicate the dissimilarity of the two components.

In quantifying the relationship between S and Π, one finds that the Peltier coefficient is correlated to the Seebeck coefficient through temperature, T, alone,[3]

$$\Pi = ST. \tag{1.3}$$

1.4 Practical Applications

For charge carriers to travel in the same direction, parallel to the temperature gradient, the dissimilar materials should have oppositely charged majority charge carriers, i.e., one *p*-type semiconductor and one *n*-type semiconductor. From Figure 1.3 it can be seen that in this configuration both electrons and holes travel in the same direction along the temperature gradient axis, resulting in either power generation or solid state cooling.

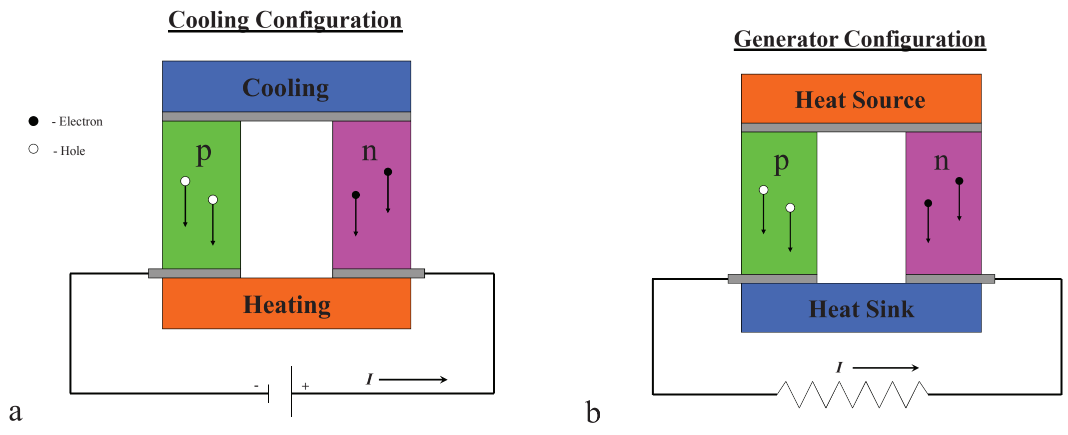

Figure 1.3 – Schematic representation of thermoelectric elements used for (a) cooling applications and (b) power generation. Styled after Ref. 5.

To make a thermoelectric element, many *p*-*n* junctions are connected electrically in series to give a larger net effect. Thermoelectric elements are used commercially in both energetically demanding applications such as power sources for deep-space probes as well as small consumer applications such as personal coolers and air circulation fans.

1.5 Thermoelectric Figure of Merit

In order to achieve a simple term to describe the thermoelectric efficiency of a material, several simplifying assumptions must be made. These assumptions have relatively small overall effect on the final term, but reduce the number of parameters needed to produce a useful quantitative descriptor for thermoelectric materials. Firstly, contacts between the two branches (*p* and *n*) of the thermocouple are assumed to have zero resistance. Secondly, it is assumed that heat is transferred from the source to the sink by conduction alone, *i.e.*, ignoring convection and radiation. Thirdly, there is assumed to be no thermal resistance between the ends of the branches and the heat source or sink, and finally, the Seebeck coefficient is assumed to be independent of the temperature gradient and the Thomson effect, therefore, is absent.

Equation (1.2) described the relationship between current and heat produced via the Peltier effect. If the Peltier coefficient is replaced by the Seebeck coefficient through Equation (1.3), the heat, *q*□, transported from the source to the sink for each branch (*p* or *n*) of the thermocouple is[6]

$$\dot{q}_p = S_p I T - \kappa_p A_p \frac{dT}{dx} \tag{1.4.a}$$

and

$$\dot{q}_n = -S_n IT - \kappa_n A_n \frac{dT}{dx} \qquad (1.4.b)$$

where κ is thermal conductivity, A is the cross-sectional area of the branch, $\mathrm{d}T/\mathrm{d}x$ is the temperature gradient and the subscripts p and n refer to the semiconductor branch being described. The second term, $\kappa A \mathrm{d}T/\mathrm{d}x$, accounts for the heat conduction that opposes Peltier heat flow. Conduction opposes the heat flow for both *n*- and *p*-branches since the Seebeck coefficient is positive for the *p*-branch and negative for the *n*-branch.

Joule heating also opposes the thermal gradient and is described as $I^2\rho/A$ where ρ is the electrical resistivity of the material. Joule heating results in a non-uniform temperature gradient along the branches, where[6]

$$-\kappa_p A_p \frac{d^2T}{dx^2} = \frac{I^2\rho_p}{A_p} \qquad (1.5.a)$$

and

$$-\kappa_n A_n \frac{d^2T}{dx^2} = \frac{I^2\rho_n}{A_n}. \qquad (1.5.b)$$

If $T = T_\mathrm{c}$, the cold side temperature, at $x = 0$ (the heat source), and $T = T_\mathrm{h}$, the hot side temperature, at $x = l_\mathrm{p}$ or l_n (the heat sink), Equations (1.5 a and b) give[6]

$$\kappa_p A_p \frac{dT}{dx} = -\frac{I^2\rho_p(x-\frac{l_p}{2})}{A_p} + \frac{\kappa_p A_p (T_h - T_c)}{l_p} \qquad (1.6.a)$$

and

$$\kappa_n A_n \frac{dT}{dx} = -\frac{I^2\rho_n(x-\frac{l_n}{2})}{A_n} + \frac{\kappa_n A_n (T_h - T_c)}{l_n}. \qquad (1.6.b)$$

Combining Equations (1.4 a and b) with (1.6 a and b) yields the expressions[6]

$$\dot{q}_p(x=0) = S_p I T_c - \frac{\kappa_p A_p (T_h - T_c)}{l_p} - \frac{I^2 \rho_p l_p}{2A_p} \tag{1.7.a}$$

and

$$\dot{q}_n(x=0) = -S_n I T_c - \frac{\kappa_n A_n (T_h - T_c)}{l_n} - \frac{I^2 \rho_n l_n}{2A_n} \tag{1.7.b}$$

to describe the rate of heat flow for each branch at the heat source ($x = 0$). Let the total thermal conductance K, of the two branches in parallel be,[6]

$$K = \frac{\kappa_p A_p}{l_p} + \frac{\kappa_n A_n}{l_n} \tag{1.8}$$

and the total electrical resistance, R, of the two branches be

$$R = \frac{l_p \rho_p}{A_p} + \frac{l_n \rho_n}{A_n}. \tag{1.9}$$

Adding the heat flow term from Equations (1.7 a and b) for each branch gives the total heat flow, $q\square_{\mathrm{c}}$, at the source ($x = 0$),

$$\dot{q}_c(x=0) = \left(S_p - S_n\right) I T_c - K(T_{\mathrm{h}} - T_c) - \frac{I^2 R}{2}. \tag{1.10}$$

The Peltier contribution to the total heat flow at the heat source (the first term in Equation (1.10)) varies linearly with current, whereas the Joule heating contribution, $I^2R/2$, is proportional to I^2. This means that there is a value for the current that produces maximum cooling/heat flow. Focusing on Peltier heat flow, by setting d q□$_c$/dI = 0, the current that produces maximum cooling, $I_{\dot{q}_{max}}$ is found to be[6]

$$I_{\dot{q}_{max}} = \frac{(S_p - S_n)T_c}{R}. \tag{1.11}$$

Substituting Equation (1.11) into Equation (1.10) provides a maximum cooling power,[6]

$$\dot{q}_{c_{max}} = \frac{(S_p - S_n)^2 T_c^2}{2R} - K(T_h - T_c). \tag{1.12}$$

The maximum temperature difference achievable for a thermocouple, $(T_h - T_c)_{max}$, is found to be[6]

$$(T_h - T_c)_{max} = \frac{(S_p - S_n)^2 T_c^2}{2RK} \tag{1.13}$$

when $\dot{q}_{c_{max}} = 0$.

The figure of merit, Z, of the thermocouple is thus defined as

$$Z = \frac{(S_p - S_n)^2}{KR}, \tag{1.14}$$

so a maximum Z value is attained by minimizing KR. KR is dependent on the geometry of the sample and minimized when[6]

$$\frac{l_n A_p}{l_p A_n} = \left(\frac{\rho_p \kappa_n}{\rho_n \kappa_p}\right)^{1/2}. \tag{1.15}$$

When this condition is met, the expression for the figure of merit becomes

$$Z = \frac{(S_p - S_n)^2}{\left[(\rho_p \kappa_p)^{1/2} + (\rho_n \kappa_n)^{1/2}\right]^2} \tag{1.16}$$

for a pair of materials. Because it is awkward to try to optimize so many variable conditions for a pair of materials, the thermoelectric figure of merit for a single material is defined as

$$Z_p = \frac{{S_p}^2}{\rho_p \kappa_p} \tag{1.17.a}$$

and

$$Z_n = \frac{{S_n}^2}{\rho_n \kappa_n} \tag{1.17.b}$$

for the *p*-type and *n*-type branches, respectively. A *Z* value is specific to a given material at a given temperature. Since the figure of merit is calculated from a combination of temperature-dependent properties, namely S, σ, and κ, its value at any given temperature must be calculated from values of those properties for that temperature.

Multiplying both sides of Equation (1.17 a and b) by temperature gives the unitless thermoelectric figure of merit, *ZT*. The unitless figure is a more approximate value than those used to describe a thermocouple or pair of materials; it is only really accurate in a few special cases, such as when the *n*-type and *p*-type branches are identical to one another except for the sign of their Seebeck coefficients, or when the $\rho\kappa$ term of one branch is so small as to be negligible, as is the case if a superconductor is used. Despite this, the unitless thermoelectric figure of merit, *ZT*, is convenient due to its simplicity and its prevalence in the literature renders it very useful when dealing with a single material. The *ZT* for a given material is determined by its Seebeck coefficient, electrical conductivity and thermal conductivity for a specific temperature through the relationship

$$ZT = \frac{S^2 \sigma T}{\kappa}. \tag{1.18}$$

From Equation (1.18) it can be seen that higher Seebeck coefficients, higher electrical conductivity and lower thermal conductivities produce higher *ZT* values.

1.6 Efficiency

When building a thermocouple, one is attempting to maximize the *Z* value in Equation (1.16) describing the figure of merit of a thermocouple. However, the best performing thermocouple does not necessarily result from combining the *n*-type and *p*-type materials with the highest magnitude figure of merit. The efficiency, η, of a generator is given by

$$\eta = \frac{W}{\dot{q}_h} \tag{1.19}$$

where *W* is work, and $q\square_h$ is the net heat exchange. The Carnot engine describes a theoretical upper limit of efficiency, η_C, for a generator, where no heat is dissipated, in terms of temperatures and is defined as

$$\eta_C = \frac{\Delta T}{T_h}. \tag{1.20}$$

The Carnot efficiency is equal to $\Delta T/T_h$, the temperature drop divided by the temperature of the hot side, T_h. Ioffe has shown that for a thermoelectric device, efficiency can be described through the Carnot limit in terms of *ZT* by[7]

$$\eta = \frac{T_h - T_c}{T_h}\left\{\frac{(1+ZT_M)^{1/2}-1}{(1+ZT_M)^{1/2}+\left(\frac{T_c}{T_h}\right)}\right\} \tag{1.21}$$

with T_M equal to the average of T_h and T_c. Through Equation (1.21), it can be seen that as *ZT* approaches infinity, the efficiency of the thermocouple approaches the Carnot limit.

1.7 Thermoelectric Materials

It has been shown above that the thermoelectric figure of merit, *ZT*, is a unitless quantifier that describes a material's thermoelectric performance. Higher *ZT* values correspond to better performing materials. Bismuth telluride, Bi_2Te_3, is the current industry standard in thermoelectric materials. It has high atomic masses of its constituent atoms and a small Debye temperature, contributing to low thermal conductivity, good electrical properties and is easily doped to produce both *n* and *p* type variants.[3] Bi_2Te_3 has a *ZT* value of ~ 0.9 at room-temperature[8] which corresponds to an efficiency of approximately 10 % of the Carnot limit.[9] Current household refrigeration technology, compression, has an efficiency of approximately 30 % of the Carnot limit.[9] It has been estimated that to bring thermoelectrics on par with traditional refrigeration technologies, *ZT* values approaching 4 must be achieved.[10]

In recent years, thermoelectric materials with *ZT* values in excess of unity have been produced.[11,12,13] Thermoelectric performance of bulk materials can be quite sensitive to processing. Bulk samples of $Cu_{0.2}Ag_{2.8}SbSeTe_2$ that were quenched in an attempt to reduce microcracking of the material were found to give *ZT* values ~ 1.5 at 700 K while slow-cooled samples achieved values upwards of 1.75 despite the presence of microcracks. The compound $In_4Se_{3-x}Cl_{0.03}$ has a *ZT* of 1.53 at 700 K[14] and $(GeTe)_{10}(Ag_ySb_{2-y}Te_{3-y})_{90}$ compounds where $y = 0.6$, 0.7 and 0.8 have shown *ZT* values greater than 1.6 at temperatures approaching 800 K.[15] From these examples it can be seen that the improved performance of bulk materials have been achieved at higher temperatures.

Lower temperature, *e.g.* room-temperature, materials have shown improvements in *ZT* not so much through the discoveries of new high performance compositions but through nano-processing. Many of the best performing room-temperature thermoelectric materials are based on proven materials such as Bi_2Te_3. Ball-milled, hot-pressed samples of Bi_2Te_3 have shown room-temperature *ZT* values of 1.2 and an improvement from ~ 0.9 in the bulk case to 1.4 in consolidated nano-crystals at 100 °C.[16] While high-performance low-temperature thermoelectrics tend to be nano-processed materials there are nano materials that perform well at higher-temperatures as well. For example,

$Ag_{0.4}Pb_{22.5}SbTe_{20}$ has demonstrated a *ZT* of 1.5 at 700 K.[17] In addition to figure of merit improvements, nano-scale thermoelectric materials also show much faster response times. Thin-film superlattices have been shown to cool as much as 2.3×10^4 times faster than their bulk material counterparts.[18]

Most of these performance enhancements have been the result of minimizing thermal conductivity, however, electrical conductivity and Seebeck coefficient are important properties as well.[19] By finding materials with low intrinsic thermal conductivity and combining those with size effects, minimum practical thermal conductivities can be achieved.[20] These low thermal conductivity materials can then be doped to optimize the electrical properties and achieve higher *ZT* values.

Based on the need for materials with high electrical conductivity and low thermal conductivity, Slack introduced the concept of a phonon glass/ electron crystal (PGEC).[6] This is an idealized material that combines electrical transport characteristic of a single-crystal semiconductor with glass-like thermal transport,[6] based on phonon disrupting rattlers.[21] The PGEC approach has proven a practical route to maximizing the efficiency of thermoelectrics by tailoring the most influential contributing properties.[22,23] Research towards producing such materials is a promising approach being employed in an effort to produce materials with higher *ZT* values.

1.8 Physical Properties

1.8.1 Thermal Conductivity, κ

Equation (1.18) shows that lowering the thermal conductivity of potential thermoelectric materials is a promising route towards improved thermoelectric performance. Minimal thermal conductivity is essential for power generation since it is the presence of a temperature gradient across the device that produces the current through the Seebeck effect. Similarly, in cooling applications it is the temperature gradient that must be maintained, as cooling power is lost when heat is transported from the hot side of the element back to the location where cooling is desired.

Thermal conductivity is a measure of the rate at which heat is transported across a sample. For a solid, the thermal conductivity coefficient, κ, is defined with respect to the steady-state temperature gradient, dT/dx, along the sample by[24]

$$j_U = -\kappa \frac{dT}{dx} \tag{1.22}$$

where j_U is the flux of thermal energy. Debye used the kinetic theory of gases to derive an expression for κ:[25]

$$\kappa = \frac{Cv\lambda}{3}, \tag{1.23}$$

where C is the heat capacity of the material per unit volume, v is the mean speed of the energy carriers and λ is their mean free path. For insulating solids, phonons carry heat.

In semiconductors, heat is carried by both the lattice (phonons) and by electrons. The total thermal conductivity is the sum of these conductivities

$$\kappa_{total} = \kappa_e + \kappa_{lattice}. \tag{1.24}$$

where κ_e is the electronic contribution and $\kappa_{lattice}$ is the lattice contribution to thermal conductivity. Although the electronic contribution to thermal conductivity can be significant, for most thermoelectric materials it is much smaller than the lattice contribution. The focus of this discussion will, therefore, be on lattice thermal conductivity.

Heat is carried throughout an insulating solid by phonons, quantized waves of lattice vibrations. These vibrations can be approximated as harmonic oscillators, as if the atoms were connected to one another by springs. There are two main categories of phonons, or “modes,” defined by their types of oscillation: acoustic modes and optic modes. For the generalized unit cell, containing N atoms, there are 3, low-frequency, acoustic modes and $3N$-3 optic modes. The number and frequency of phonons available to a solid are dependent on lattice properties, defined by interatomic interactions: phononic properties are determined by a material’s structure and composition. Dispersion curves are used to graphically describe the number and frequency of phonons that can be activated within a given solid. Figure 1.4 presents a simplified version of a phonon dispersion curve.

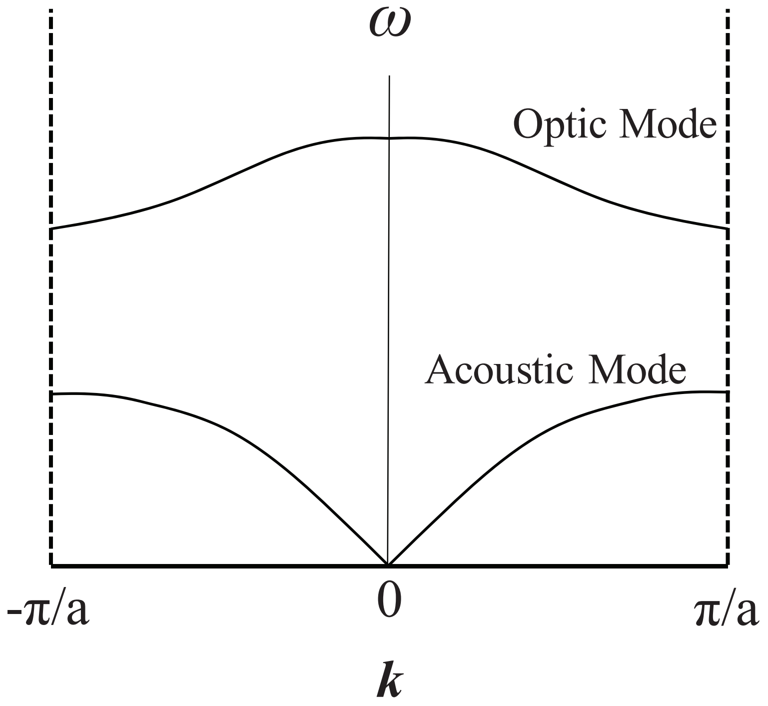

Figure 1.4 – Dispersion curve of a primitive cell containing two atoms of different masses including optical and acoustical branches. Phonon frequency ω is plotted against its wavevector, k, across the first Brillouin zone. a is the lattice constant. Each mode is triply degenerate. Styled after Ref. 26.

The speed, v, of a phonon is determined by the rate of change in frequency with respect to its wavevector, k, which describes its magnitude and direction of travel. This speed is equal to the slope of the curve, $v = \mathrm{d}\omega/\mathrm{d}k$, corresponding to the vector of interest. From Figure 1.4 above it is clear that optic modes are low speed, while acoustic modes travel at significant speed at the zone centre. Although optic modes can contribute significantly to a solid's heat capacity, due to their relative low velocity they do not usually contribute greatly to thermal conductivity. Thus, acoustic modes are largely responsible for heat conduction.

While acoustic phonons do travel through a solid, they are not unimpeded. If they were, a sample heated at one end would transport heat directly to the other and no significant thermal gradient would be produced across it. Phonons are able to undergo several kinds of interaction. Many of these interactions reduce phonon mean free path which in turn hampers thermal conductivity (as per Equation (1.23)).

At minimum, in a perfect crystal, phonon mean free path is limited by the dimensions of the solid. This is true for both single-crystals in air, and for polycrystals. In such systems, reducing the distance between phase boundaries can reduce λ, thereby reducing κ. Size effects, via nano-processing, have been successfully used to reduce thermal conductivity.[27,28,29,30] Highly disordered materials such as glasses and non-periodic solids optimize size effects, although often to the detriment of other thermoelectric properties.[31,32,33,34]

Point defects give rise to localized interatomic potentials different to those of a pure crystal lattice. When a phonon encounters a point defect, it is scattered from the disruption of periodicity. Since phonon scattering shows an ω^4 dependence, point defect scattering has less impact on the heat carrying acoustic phonons than on high frequency optic phonons.[35] Point defects that do not occupy regular lattice sites, such as interstitials residing in the voids of cage structures, also can scatter phonons, giving “phonon glass” materials that possess periodic lattices.[21]

Because they are not truly harmonic, in addition to interacting with the lattice, phonons are able to interact with one another. Such interactions are known as “three-phonon processes” and are described in terms of phonon wavevectors. There are two possible types of three-phonon processes. Normal, or *N*, processes occur when two phonons interact to give a single phonon traveling in the sum direction of the original two phonons. *N* processes conserve overall phonon momentum and direction and as such, do not affect thermal conductivity. The other category of three-phonon processes is *U*

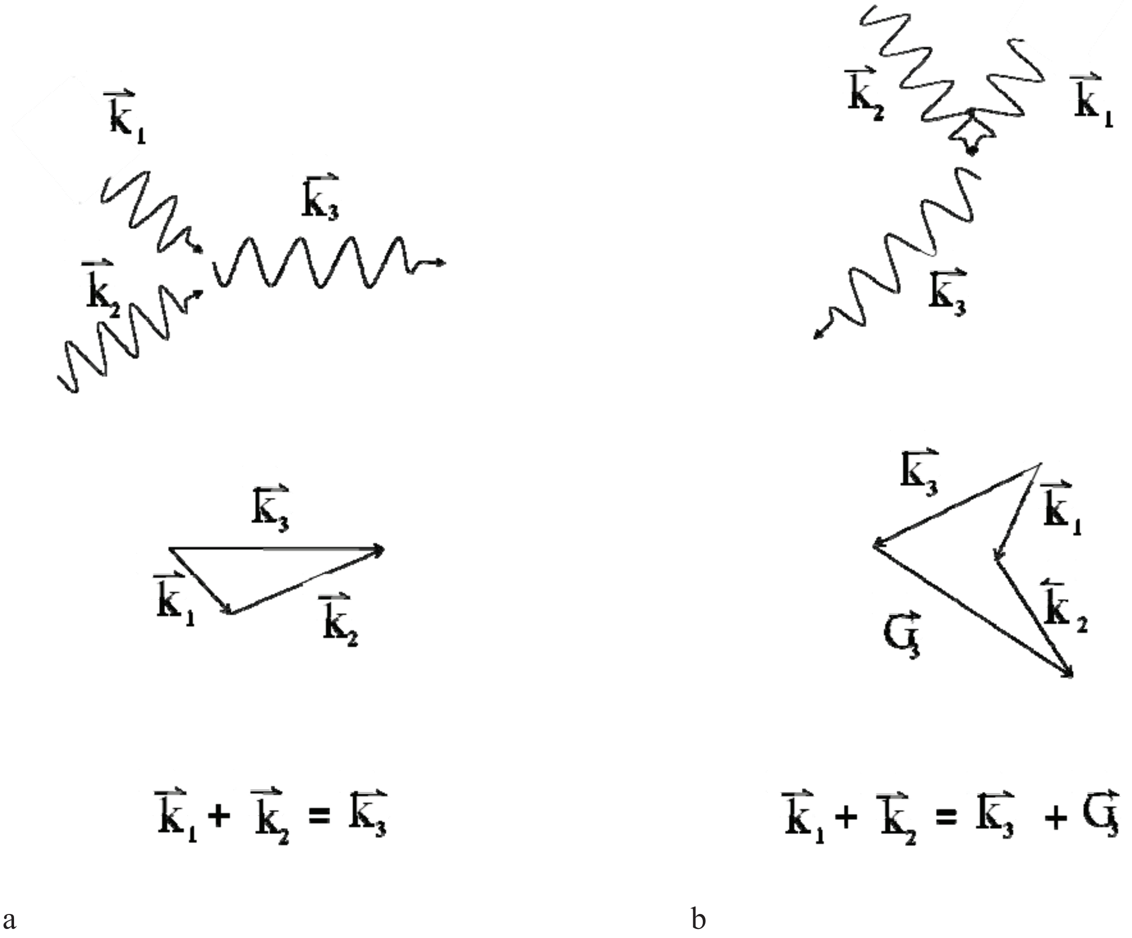

Figure 1.5 – Schematic representation of three-phonon interactions, (a) a momentum conserving *N* process, with no effect on thermal conductivity, and (b) a *U* process which counters heat flow via momentum transferred to the lattice, $\vec{G}$. Styled after Ref. 24.

processes, taken from the German *umklappen* (to turn back). These occur when two phonons interact to produce a third phonon that can be described as the sum of the original phonons with a reciprocal lattice vector. This is more clearly understood through Figure 1.5 which describes both *N* and *U* processes. Unlike *N* processes, as a result of momentum transfer to the lattice, *U* processes reduce thermal conductivity.

In order to increase the number of *U* processes, one can incorporate heavy elements into materials: heavier elements produce lower-frequency phonons.[9] This frequency reduction increases the probability of interactions between optic modes and low-frequency, heat carrying, acoustic modes, increasing the probability of *U* processes.

Large unit cells also have the effect of increasing *U* processes,[36] since the number of optic phonons increases with the number of atoms in a unit cell by almost a factor of three. These modes are at a variety of frequencies and as the unit cell increases in size the probability of low-frequency optic modes also increases.[9] As in the case of heavier elements, increasing the unit cell increases the probability of *U* processes and decreases thermal conductivity.

With these processes in mind, one would expect that semiconducting polycrystals of large unit cells comprised of heavy elements and containing many point defects would be ideal thermoelectric materials. For κ there is credence to this description, however, there is more to consider.

1.8.2 Heat Capacity, C_v

Thermal conductivity is an important property for the evaluation of materials for thermoelectric applications. It has direct energy conversion implications and through sample size and form can be manipulated, somewhat. Heat capacity has significant impact on thermal conductivity and is a more fundamental property that is largely resistant to size and form effects. Looking back to Equation (1.23) the significance of heat capacity is apparent. Equation (1.23) includes the velocity of sound and phonon mean free path as well, but these variables can be quite affected by sample form. As such, heat capacity can be used to produce a more fundamental and general description of the thermal properties of a material.

Heat capacity describes the ability of a substance to store heat. Since heat is an energetic manifestation of the random vibrations within a substance, it follows that an understanding of the heat capacity of a system reflects the available vibrational states, or lattice dynamics, of that system. At low temperatures fewer vibrations are excited and at higher temperatures more vibrations are excited. As temperature is increased the number of active phonons increases and Figure 1.6 depicts the resulting general shape of a heat capacity curve as a function of temperature. Heat capacity goes to zero as temperature does and approaches a maximum value at higher temperatures.

While high temperature heat capacity had been successfully described, empirically, for quite a long time, for example, through the Dulong-Petit law, it was the advent of quantum mechanics that really propelled theory into an accurate description of

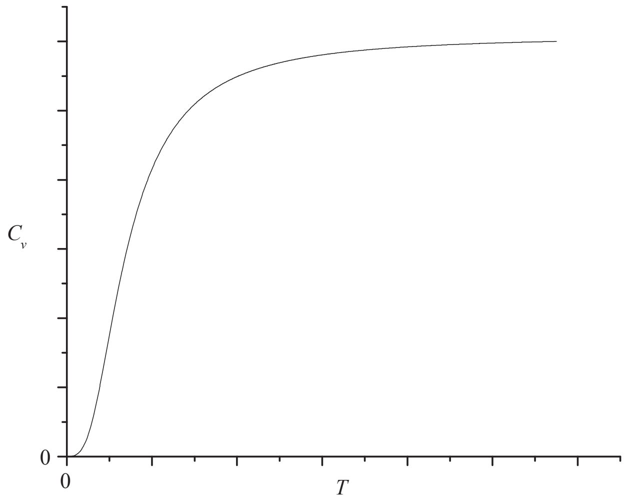

Figure 1.6 – Generalized heat capacity curve illustrating the temperature dependence of heat capacity.

the underlying processes. In 1907 Einstein suggested that the atoms of a solid be described as a set of quantized harmonic oscillators.[25, 37] The Einstein heat capacity, C_E, assumes that these vibrations are thermally excited as described by[37]

$$C_E(T) = 3Nk\left(\frac{\theta_E}{T}\right)^2 \frac{e^{\theta_E/T}}{\left(e^{\frac{\theta_E}{T}}-1\right)^2} \tag{1.25}$$

where N is the number of atoms, k is the Boltzmann constant and θ_E is the Einstein characteristic temperature, defined as

$$\theta_E = \frac{h\upsilon_E}{k}, \tag{1.26}$$

h being Planck's constant and υ_E, the (Einstein) frequency of the oscillator. This model successfully described the high-temperature limit of heat capacity and approached zero as the absolute temperature did, but at low temperatures the theory noticeably underestimated the true (experimental) heat capacity for monotonic solids.

A revised vision of quantized thermal vibrations, in which atomic vibrations were still responsible for heat was proposed by Debye. Instead of assuming that all the atoms in a solid vibrate at a single characteristic frequency, Debye's model assumed a distribution of frequencies up to some maximum frequency, v_D. The Debye heat capacity, C_D, model gives[38]

$$C_D(T) = 9Nk\left(\frac{T}{\theta_D}\right)^3 \int_0^{\frac{\theta_D}{T}} \frac{x^4 e^x}{(e^x-1)^2}\,dx, \tag{1.27}$$

where θ_D is the characteristic Debye temperature. This is defined mathematically by analogy to the Einstein characteristic temperature ($\theta_D = h\nu_D/k$, ν_D being the upper frequency limit) but represents an upper limit to a frequency distribution rather than a single characteristic frequency. This upper limit reflects the rigidity of the interatomic interaction of a material. Just as the vibrational frequencies of springs increase with spring constants, θ_D increases with the strength of interatomic interactions. This means that a stiffer material has a larger Debye characteristic temperature and its heat capacity for $T > 0$ K rises more slowly with increasing temperature than a less stiff material. Conversely, materials with smaller θ_D have higher heat capacities at a given temperature.

The Debye and Einstein theories produce similar agreement to experiment at high temperatures, but the Debye model improves on the Einstein model at low temperatures. Both theories, however, have proven to be quite useful in describing the relationship between crystal structure and thermal response. Referring to Figure 1.4, the Einstein model describes the little dispersed optic modes in its approximations of discrete vibrational frequencies, while the Debye model describes the highly dispersed acoustic modes. As will become apparent throughout the thesis, these models are quite useful in describing the dynamics of the clathrate systems studied for this project.

1.8.3 Electrical Conductivity, σ

While Equation (1.18), describing ZT, mathematically indicates that high electrical conductivity delivers better performance, the effect also can be understood conceptually. High electrical conductivity improves the performance of thermoelectric materials for both power generation (Seebeck effect) and for active cooling (Peltier effect). Both processes convert energy through charge carrier transport. From the perspective of Seebeck applications, reduced electrical conductivity hinders the charge build-up that occurs as a result of the diffusion of thermally mobilized electrons and, thus, reduces the voltage across the junction. Similarly, Peltier cooling is the result of heat being transported across the length of a material via charge carriers. Lower electrical conductivity reduces the amount of charge being transported across the device, reducing the heat transported across the device and, ultimately, reducing the thermal gradient across the device. In addition, Joule heating is inversely proportional to the electrical conductivity of the material. While such a thermal effect is less pronounced in the low-current Seebeck scenario, it directly counters the thermal gradient that Peltier devices are designed to produce.

The electrical conductivity of a material reflects the ability of charged particles to move within it. A material's electrical conductivity, σ, is dependent on the number of charge carriers, n, their charge, e_o, and their mobility, μ, as,[39]

$$\sigma = n e_o \mu. \tag{1.28}$$

Since charge carriers are either electrons or holes, their charges are constant for all materials (although they may be either positive or negative). The numbers and mobilities of charge carriers are, therefore, the variables instrumental in determining electrical conductivity. While the number of charge carriers is generally dependent only upon the composition of a material, the mobility is also dependent on the form. Charge carrier mobility is determined by the charge of particle, the mass of the particle, m_e, and its mean free path, λ_e, through the following equation:[39]

$$\mu = \frac{e_o \lambda_e}{m_e}. \tag{1.29}$$

Similar to phonons, the mean free path of charge carriers is dependent on temperature, density of lattice imperfections and phase boundaries. Like thermal conductivity, a reduction in electrical conductivity also can be associated with the loss of periodicity. Heavy elements, and disorder, tend to reduce both electrical conductivity and thermal conductivity.

The electrical conductivity and Seebeck coefficients for a material are both optimized through the power factor, $S^2\sigma T$, as a function of charge carrier concentration. While σ increases with increasing charge carrier concentration S decreases with charge carrier concentration. In addition, too high a charge carrier concentration increases κ due to electronic contributions. Charge carrier concentrations on the order of 10^{19} carriers/cm^3 are typical values for optimized thermoelectric materials.[40] Optimization is done by doping a material with impurity elements to increase the number of charge carriers (either electrons or holes) to give an optimum carrier concentration. By breaking periodicity, dopants increase disorder and decrease thermal conductivity.

Because electrons have a *significant* contribution to heat conduction in metals, from Equation (1.18) describing ZT, it is apparent that metals do not make good thermoelectric materials, while semiconductors do. (Furthermore, the magnitude of S is higher for semiconductors; see below.) Equation (1.18) shows that these two physical properties, σ and κ, which are tethered to one another in metals via the Wiedmann-Franz law[41]

$$\frac{\kappa}{\sigma} = LT \tag{1.30}$$

where L is the Lorenz number, equal to $2.44 \times 10^{-8}\ \mathrm{W\Omega K^{-2}}$, must be optimized in opposite directions. That is to say, that the thermal conductivity of a material must be minimized while the electrical conductivity must be maximized in order to obtain maximum ZT values.

For materials where both charge and heat are carried by the same particle, *i.e.* the electron in metals, this optimization is impossible, and only very modest thermoelectric efficiencies are possible. In semiconductors and insulators, thermal energy is mainly transported by phonons, not electrons. As a result, for non-metallic materials thermal and electrical transport properties can be isolated from one another. By introducing impurities that occupy non-regular lattice sites (interstitial impurities) σ can be increased via electron transfer and κ can be decreased by introducing disorder. Because interstitial defects do not occupy regular lattice sites, they can add an element of disorder to the system without interrupting electrical conductivity. Although this is true for insulators as well as semiconductors, the poor electrical conductivity of insulators excludes them from thermoelectric applications. Therefore semiconductors are the only suitable candidates for thermoelectric materials.

1.8.4 Seebeck Coefficient, *S*

From Equation (1.1) and Equation (1.2), it is apparent that a high magnitude *S* improves the performance of thermocouples. Since *S* is an electronic property, it scales with charge carrier concentration: more charge carriers means lower thermal voltages. This is shown in Figure 1.7. In addition, accompanying greater charge carrier concentrations is greater charge carrier mobility. This, especially in combination with increased κ_e works against thermoelectric efficiency. Realistically this means that the properties that most directly rely on charge carrier concentration, *S* and σ, must be optimized after achieving a minimal κ. Optimization of electronic properties is best done by doping a material to achieve the optimum charge carrier density mention above, ~ 10^{19} carriers/ cm^3.

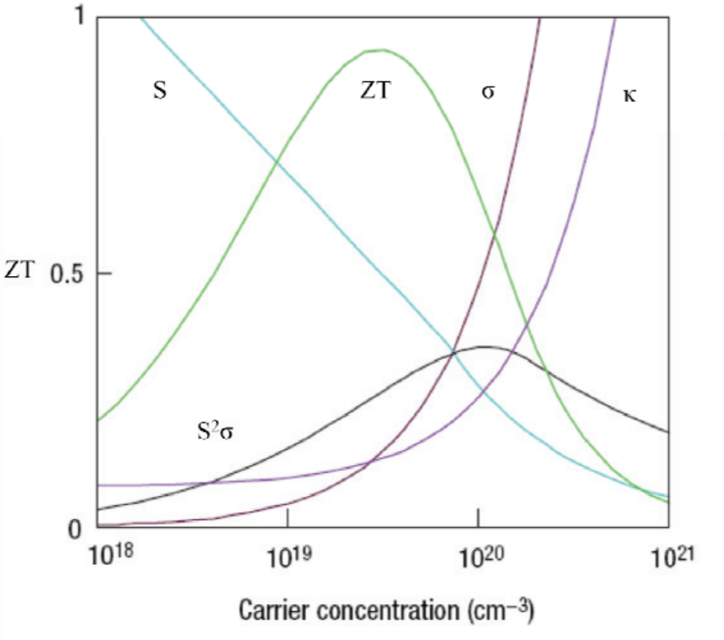

Figure 1.7 – Optimization of *ZT* as a function of charge carrier concentration. The unmarked y-axes are 0 to 500 μV K^{-1}, 5 000 Ω^{-1} m^{-1} and 10 W m^{-1} K^{-1} for *S*, σ and κ respectively. Reproduced from Ref. 12 with permission.

Figure 1.7 illustrates how the constituent properties of the thermoelectric figure of merit depend on charge carrier concentration. From Figure 1.7 it can be seen that the constituent properties optimize differently with charge carrier concentration and this generally leads to a maximum *ZT* value at charge carrier concentrations on the order of 10^{19} cm^{-3}.

1.9 Clathrates

Known since the mid 1960s,[42] intermetallic clathrates have received considerable attention in the literature in recent years.[43] Renewed interest has been related to observed novel superconductivity,[44,45] possible applications as photovoltaics and optoelectronics[46] and their potential role in the development of more efficient thermoelectric materials.[47] With rigid, crystalline structures and the ability to incorporate dynamic disorder, clathrates are promising phonon glass electron crystal candidates.

Analogous to the clathrate hydrate structure,[42] semiconductor clathrates are comprised of a continuous network of face-sharing polyhedra encapsulating various guest species.[48,49,50] Whereas the framework of a clathrate hydrate can act as a storage medium for such compounds as methane[51] and CO_2,[52] in semiconductor clathrates the framework provides a continuous conductive pathway for electricity (electron crystal), while the encaged guest atoms, often referred to as “rattlers,” provide dynamic disorder that hinders phonon propagation and thus reduces thermal conductivity (phonon glass). It has been found that when the clathrates’ caged frameworks are made of metals or semi-metals, they demonstrate semiconductor character.[5] Semiconducting clathrates have been most commonly composed of the group 14 elements Si, Ge and Sn.

“Rattlers” are species that reside within the voids of the cages of clathrates. These species occupy some equilibrium position within the cages, and are disturbed from that position through thermal excitation and interactions with phonons, resulting in vibration or “rattling” of the resident atom or molecule. The reduction of thermal conductivity resulting from the incorporation of rattlers has been attributed to their localized low-frequency optical modes.[21] These low lying optic modes can couple with acoustic modes to give three-phonon scattering, reducing phonon mean free path and thus reducing thermal conductivity.

The interactions of these localized optical modes with the acoustic lattice vibrational modes provide an efficient process for three-phonon scattering. At high temperatures all vibrational modes are fully excited, therefore giving a short mean free path for phonon scattering. Figure 1.8 illustrates type I and type II (see below for description) clathrate structures with their constituent cages fully occupied by rattler atoms. Several factors can affect the magnitude of the reduction of thermal conductivity due to the inclusion of rattlers, such as distribution, the size of the rattler atom and their masses. Although Figure 1.8 shows 100 % cage occupancy in both structures, examples of partially filled type II clathrate are known.[53,54,55,56] Cage filling rattler atoms have been found to reduce the room-temperature thermal conductivity by as much as 50 % with as little as 5 % cage occupancy in the porous $CoSb_3$ skutterudite system.[57]

Rattlers can simultaneously reduce thermal conductivity and act as dopants to optimize electrical properties. It has been found that smaller, heavier atoms are more

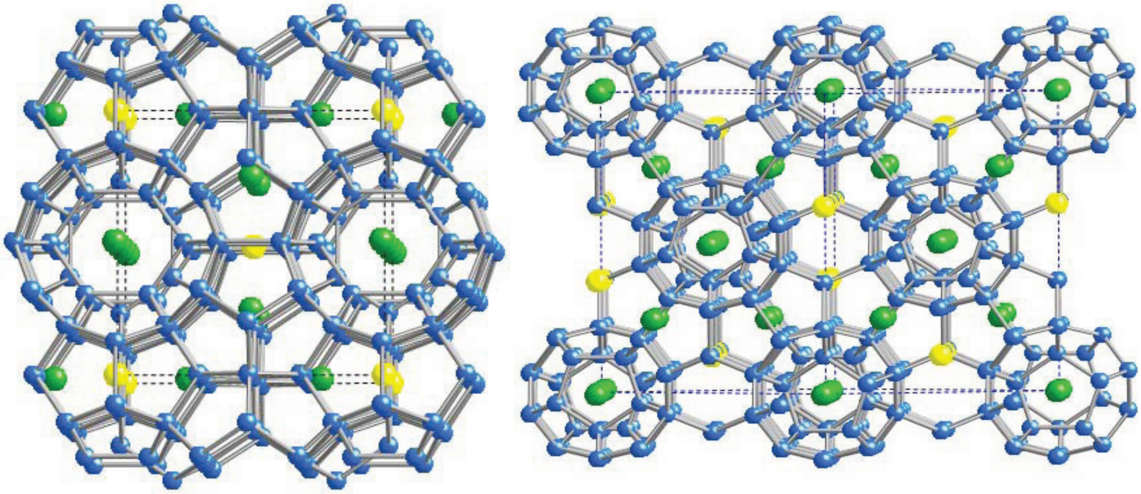

Figure 1.8 – (a) Type-I and (b) type-II clathrates with cages occupied by "rattler" atoms. The two different sites of each clathrate structure are occupied by two different "rattlers." Those inside the tetrakaidecahedra of the type-I clathrate and those inside the hexakaidecahedra of the type-II clathrate are shown in green, while rattlers within the pentagonal dodecahedra are shown in yellow. Styled after Ref. 11.

useful as rattlers. For example, the thermal conductivities of the germanium clathrates $Eu_8Ga_{16}Ge_{30}$ and $Sr_8Ga_{16}Ge_{30}$ both show minima between 20 K and 30 K.[58] $Eu_8Ga_{16}Ge_{30}$ has cages occupied by the heavier, slightly smaller, Eu rattlers and has a minimum value of ~ 0.2 W m^{-1} K^{-1} while $Sr_8Ga_{16}Ge_{30}$ with the lighter, slightly larger, Sr rattlers has a minimum thermal conductivity of ~ 0.7 W m^{-1} K^{-1} .[58] The heavier atoms have lower frequency optic modes that can interact more efficiently with heat carrying acoustic phonons. While heavier rattlers lower the frequency of localized modes, smaller rattlers introduce greater static and/or dynamic disorder to the system since they are allowed greater freedom of motion within the cages than is possible for larger atoms. The greater freedom of rattler motion allows absorption of more acoustic phonons, reduces the phonon mean free path, and thus lowers the thermal conductivity.[3] Rattlers can therefore most significantly reduce thermal conductivity when small and heavy.

As with the clathrate hydrates, intermetallic clathrates come in a variety of "types,"[22,59,60,61,62,63] two of which are shown in Figure 1.8. By far the most common are types I and II which are also known structures for clathrate hydrates.[42] Type I is comprised of six tetrakaidecahedra (24-atom cages) for every two dodecahedra (20-atom cages),[64] while the type II clathrate is made up of eight hexakaidecahedra (28-atom cages) with 16 dodecahedra.[65] Figure 1.9 illustrates the face-sharing polyhedral, which are made up of five and six membered rings that comprise these two structures.

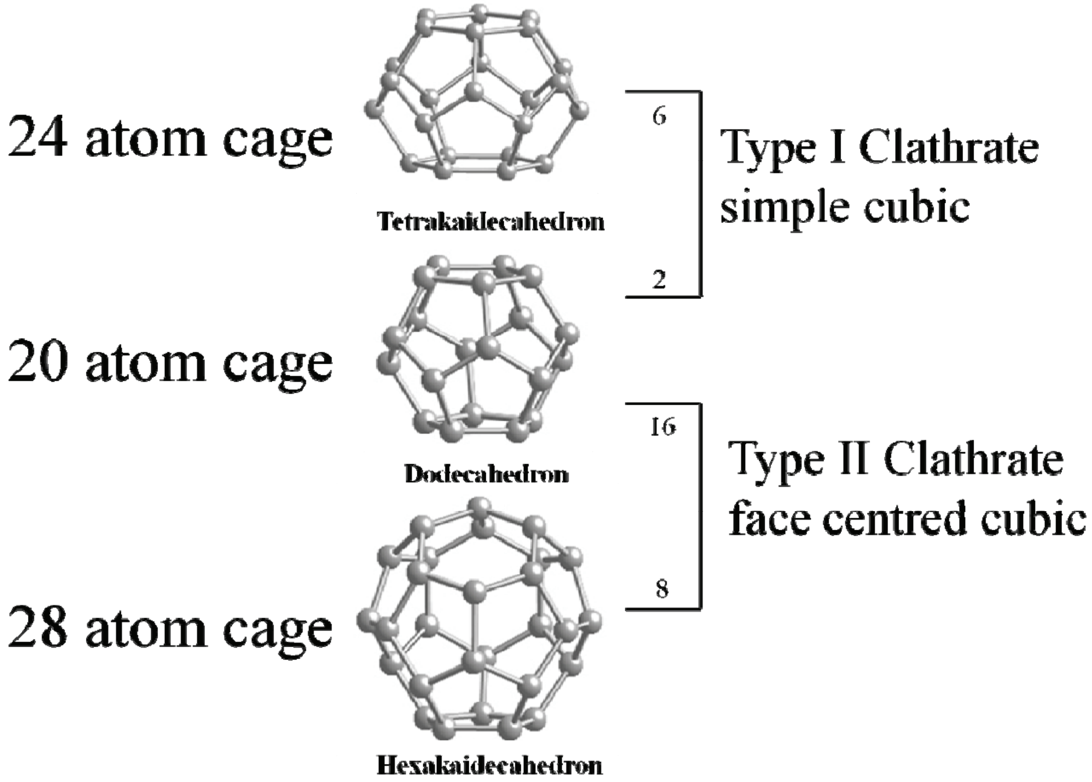

Figure 1.9 – Different combinations of polyhedra in face-sharing arrangements give rise to the different clathrate structures. The two most commons clathrate forms are shown here. Styled after Ref. 66.

Type I clathrates are typically stoichiometric crystalline solids that can accommodate a wide variety of guest atoms. Studies on such materials as Na_8Si_{46} have shown that these filled clathrate structures can exhibit glass-like thermal conductivity[67,68] due to enhanced low-temperature anharmonicity associated with motions of the guests in the cages.[69] It is possible to alter both the host and the guest composition,[70] and varying the elements incorporated as guests has lead to the conclusion that small, heavy rattler atoms produce the most dramatic decreases in lattice thermal conductivity.[58]

In addition to varying guest identity, the guest loadings are tuneable in some type II clathrates. Altering the guest concentration of type II clathrates can be accomplished by removing some of the guest atoms from fully or nearly fully occupied type II structure.[71,72] This ability to remove guest atoms has led to the production of nearly empty clathrate samples (negligible guest concentrations) and the further discovery that the extensive clathrate framework itself contributes significantly to lowering the thermal conductivity of these materials when compared to more compact structures.[73,51] Examples of such findings are also present in organic clathrate examples.[74] While removal of Na atoms from clathrate frameworks is known to be possible, the details and mechanisms of which Na atoms are removed from the two different cages remain intriguing open questions. This thesis addresses some of these questions through investigation of the Na filled Si type II clathrate series Na_xSi_{136}, where x represents the tuneable Na content.

The structures of many clathrate systems have been studied by x-ray diffraction.[70,75] These studies have provided consistent, detailed information about the structure for the stoichiometric type I clathrates. In type II structures, those of interest to this thesis, the composition, *i.e.*, guest content, is tuneable, adding complexity to the interpretation of experimental data. Due to this complexity, there have been conflicting findings with regard to the occupancies of the two different polyhedral cages that compose the type II clathrate structure of the general formula Na_xSi_{136}. Powder x-ray diffraction studies have suggested that the smaller Si_{20} polyhedra are the first to lose their Na guests and the larger Si_{28} cages are evacuated only after all of the small-cage Na atoms have been removed.[66,76,77] This has been further supported by theoretical studies that attribute the preferential loss from the Si_{20} cages to a decreased stability stemming from stronger Na-Si repulsion in the smaller Si_{20} cages.[78] One interpretation of NMR data suggested that under some conditions there may be a preferential loss from the Si_{20} cages,[79] while another suggested loss occurs preferentially from Si_{28} cages.[80]

Understanding the details of cage occupation is significant since such details can shed light on the origins of physical properties. For example, a deeper understanding of the crystal and electronic structures of these systems could explain why the tuneable Na_xSi_{136} system transitions from metallic to insulating behaviour, for x 9.[77] Some authors have suggested that the displacement of the Na atoms from the centre of the larger Si_{28} cage leads to a Peierls-like distortion related to the preferential occupation of the Si_{28} cages.[81] However, the precise location of Na within the larger Si_{28} cages has been the subject of some controversy with both experiments and calculations indicating a range of displacements from the centre of those cages.[66,76,78,81 ,82] The present study aims to further understanding of thermoelectric efficiency by examining how Na content affects the structure and physical properties of a Na_xSi_{136} series of samples.

While thermal properties of clathrate compounds are quite interesting, promising electrical conductivities have been demonstrated in these materials as well. For example, $Rb_8Na_{16}Si_{136}$ and $Sr_8Ga_{11}Si_{35}$ have shown high room-temperature electrical conductivities of 1.25 x 10^6 Ω^{-1}cm^{-1} and 5.00 x 10^5 Ω^{-1}cm^{-1}, respectively.[65,83] However, no single clathrate material has been shown to be a stand-out thermoelectric performer, mostly due to a lack of demonstrably high *S* values. So while this class of materials might not hold the most promise as PGEC materials themselves, their variability makes them an excellent model system to further theory towards such a material. Semiconductor clathrates offer an opportunity to better understand the complex structure-property relationships that dictate the suitability of a material for thermoelectric applications.

1.10 Clathrands

Clathrates have large unit cells, which can contain in excess of 100 atoms even without considering guest rattlers.[84,67] Their large unit cells reduce thermal transport in these materials when compared to other simpler crystal systems of comparable compositions. For example, a type-II clathrate of elemental silicon, Si_{136}, has been produced.[71,73] This material has been observed to have a room-temperature thermal conductivity only about 3 % of that of diamond-structured silicon.[73] The thermal conductivity of Si_{136} is almost as low as that of amorphous (vitreous) silica as illustrated in Figure 1.10.

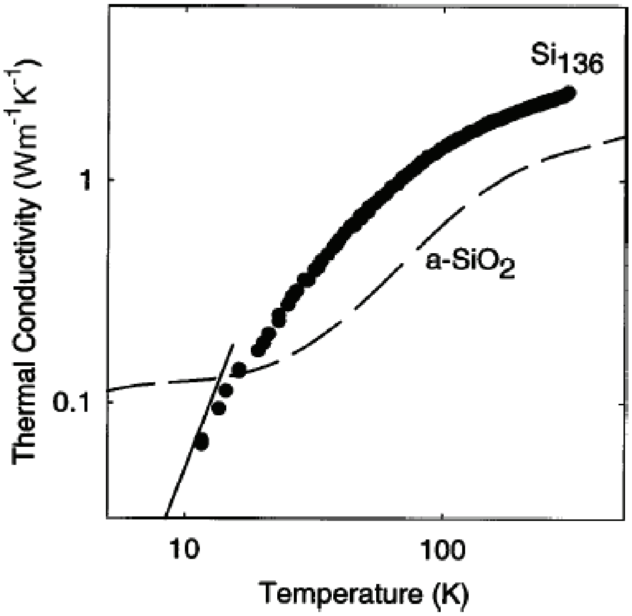

Figure 1.10 – Low thermal conductivity of the elemental clathrate Si$_{136}$ is comparable to that of an amorphous solid, vitreous silica. Reproduced from Ref. 73 with permission.

The unoccupied germanium clathrate Ge$_{136}$ has also been synthesized.[85] It has been observed to exhibit semiconductor behaviour, and a relatively high room-temperature electrical resistivity, 0.17 Ωm. It is expected that the Ge clathrate would exhibit low thermal conductivity as, previous to its synthesis, it had been shown theoretically that the elemental germanium clathrate Ge$_{46}$ could be expected to show a reduction of thermal conductivity by an order of magnitude when compared to its diamond-structured counterpart.[86]

It has been suggested that the reduced thermal conductivity observed in clathrands (empty clathrate frameworks) arises from interactions between low-frequency optic modes and the heat-carrying acoustic modes in Si$_{136}$ due to increased anharmonicity.[86,36] These interactions are possible in clathrand structure because the number of optic modes increases with the number of atoms in the unit cell, *N*, as 3*N*-3. This means that with 136 atoms per unit cell in the clathrand structure there are 405 optic modes available compared with only 21 for the diamond-structure silicon (eight atoms per unit cell). Many of the optic modes of Si_{136} are low in frequency, and therefore able to interact with the heat-carrying acoustic modes. Such interactions can lead to Umklapp processes that limit phonon mean free path and, therefore, reduce heat transport. It is apparent from Figure 1.11 that heat-impeding processes resulting from interactions between optic modes and acoustic modes are significantly more likely for the silicon structure with the larger unit cell.

The ability to separate the framework from the caged rattler atoms, totally and incrementally, offers an opportunity to gain insight into how each affects thermoelectric performance and how each can be optimized to maximize that performance.

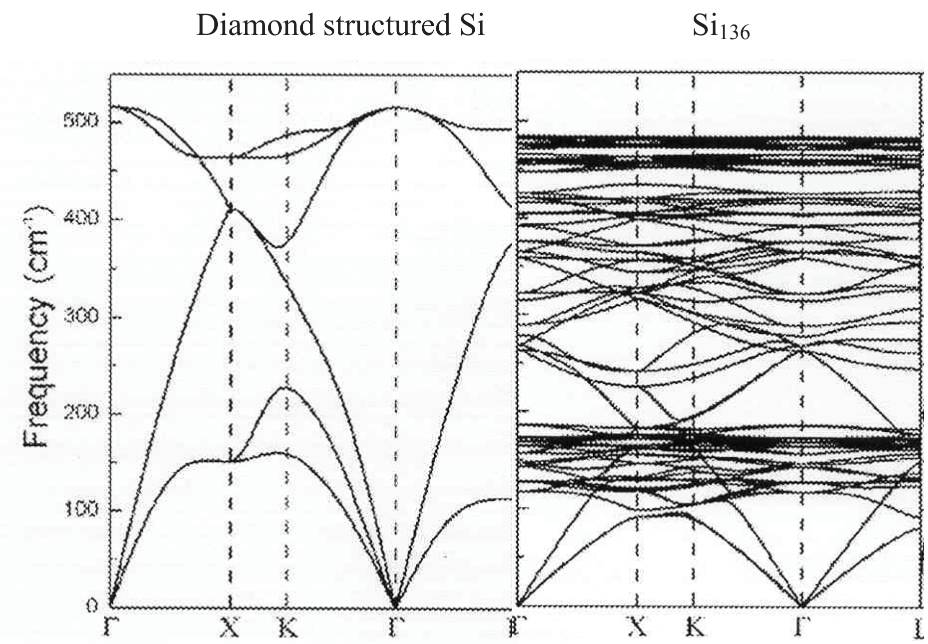
Diamond structured Si

Si_{136}

Figure 1.11 – Dispersion plots for both diamond structured silicon and Si_{136}. A high density of interactions between optic and acoustic modes can be seen in the frequency range between 100 and 200 cm^{-1} for Si_{136} whereas no interactions between the two are seen in the plot for diamond structured silicon. Reproduced from Ref. 36 with permission.

1.11 Goals

This research aims to further the understanding of how structure affects the physical properties that govern thermoelectric performance. The goal is to relate structural features with measured physical properties through modeling and theory. By understanding how varying the concentration of rattlers in a porous framework affects its structure, physical properties and dynamics, it is possible to optimize such systems for particular applications. Thus, future materials production could more rationally design materials in the quest for higher performance thermoelectric materials.

Chapter 2: Techniques

Several techniques have been used throughout this study, both to characterize the structures of materials and to characterize their physical properties. The following should give the reader a theoretical understanding of the techniques used, an appreciation for some of the specific challenges and requirements of the systems studied herein, and will illustrate how these experiments have led to a deeper understanding of structure-property relationships.

2.1 Transport Properties

The main interest of this thesis is to understand the ability of a variety of semiconducting materials to convert energy from random thermal energy to electrical potential, and vice versa. This goal is achieved by experimentally studying several separate properties that all contribute to the material's ability to do this. Those contributing properties are thermal conductivity, electrical conductivity/ resistivity and the Seebeck coefficient. In addition, the heat capacities of many samples also were measured. Significant effort was spent on heat capacity measurements since such data can give a great deal of insight into the lattice dynamics that govern those thermoelectrically relevant properties and provide a strong theoretical link between the material's structure and properties.

A single instrument was used to measure all four pertinent physical properties, the Physical Properties Measurement System (PPMS, Quantum Design, San Diego, CA). This is a commercially available, programmable instrument that is able to measure a diverse variety of physical properties. The model at Dalhousie University is equipped with an Evercool^{TM} system for liquefaction and recondensation of helium. This gives the instrument continuous access to temperatures ranging from 2 K to 400 K for all measurements and as low as 0.4 K for select experiments. Combined with magnetic field capabilities from 0 to 9 T, this is a very versatile measurement apparatus. Using the thermal transport option, TTO, the three properties contributing to the thermoelectric figure of merit can be measured in a single experiment, practically simultaneously. The PPMS also can be used to measure the heat capacity of an appropriately prepared sample, and give data reflecting a range of physical properties which can then be interpreted in the context of a material's structural data.

2.1.1 Measurement Preparations

Samples needed to be in forms suitable for measurements in the thermal transport option (TTO) PPMS. For κ, S and R measurements, powdered samples were cold-pressed into cylindrical pellets using a high pressure apparatus that was developed in house. This sample form also was found to be appropriate for heat capacity measurements.

2.1.1.1 Pellet Preparations

Powder samples were consolidated for TTO measurement by subjecting them to pressures of 0.75 GPa to 1.65 GPa. This was achieved with press/die assemblies built to the specifications shown schematically in Figures 2.1 and 2.2. This cold-pressing

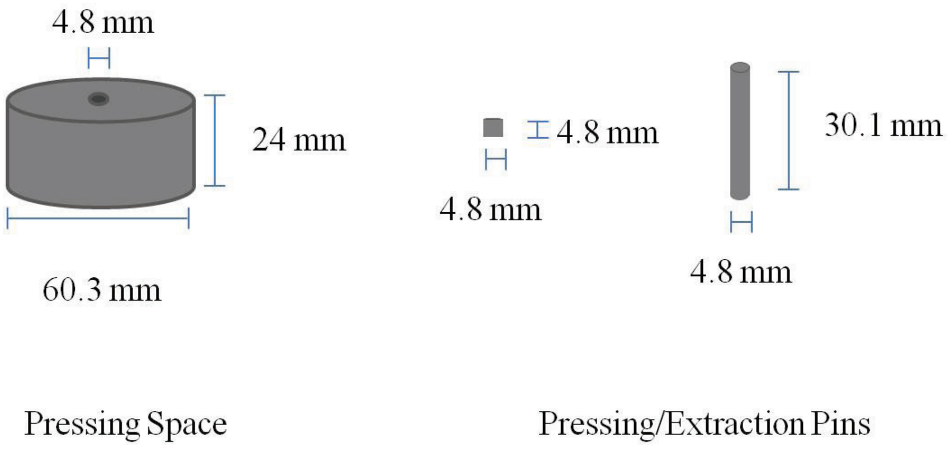

Figure 2.1 – A schematic representation of the pellet apparatus first used to press semiconductor powders into pellets. Components were made of steel.

resulted in pellets that were of appropriate dimensions to mount on the TTO puck. Initially the apparatus shown in Figure 2.1 was used.

However, occurrences of jammed and broken pressing pins led to the development of a more robust system, shown in Figure 2.2.

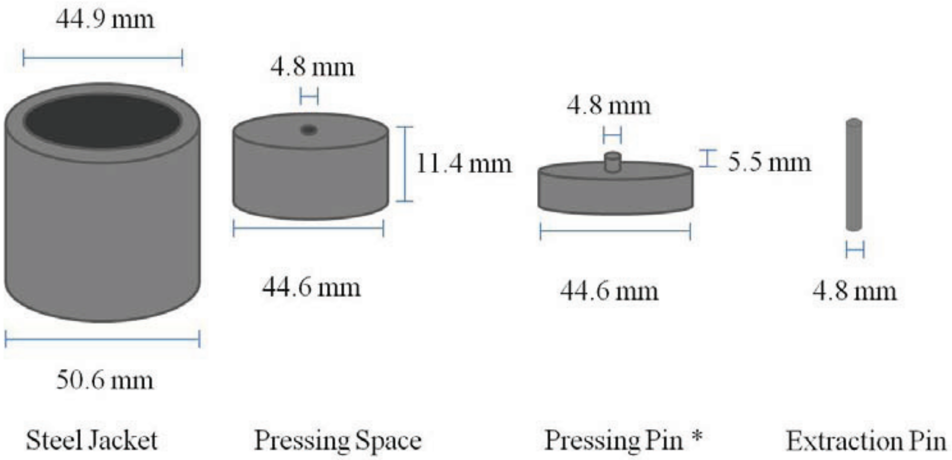

Figure 2.2 – A schematic representation of the improved pellet apparatus used to press sodium containing clathrate powders into pellets. *Two pressing pins are required although only one is shown here. Components were made of steel.

The major improvements of the newer design over the previous were the inclusion of a steel jacket and large flat bases attached to the pressing pins. The steel jacket surrounding the pressing space was added as a safety measure and both it and the large pressing pin bases acted to ensure straight downward force, reducing the chances of damage to the pressing pins. This significantly reduced the number of broken pressing pins and jams.

Powder samples of ~23 mg of the Na_xSi_{136} clathrate samples series were subjected to pressure of ~ 1.7 GPa for 5 minutes at room-temperature. This resulted in pellets of ~ 0.7 mm thickness. Once a mechanically robust pellet was made, the pellet thickness and diameter were measured to 0.02 mm precision. Pellet masses were also recorded.

2.1.1.2 Mounting Samples

Pressed pellets, measuring between ~ 0.5 mm and ~ 1 mm in thickness and 4.8 mm in diameter, were connected to two gold-plated copper sample leads using TRA-DUCT 2902, an electrically and thermally conducting silver epoxy produced by Tra-Con. Gold and copper contacts were used because of their high thermal and electrical conductivities. Figure 2.3 shows a sample mounted between two leads for transport measurements. In the cases of samples with small thicknesses (less than 1 mm), the close proximity of the leads required that each contact be independently secured to the sample using epoxy and allowed to cure. This greatly reduced the incidences of electrical or thermal shorts through the epoxy.

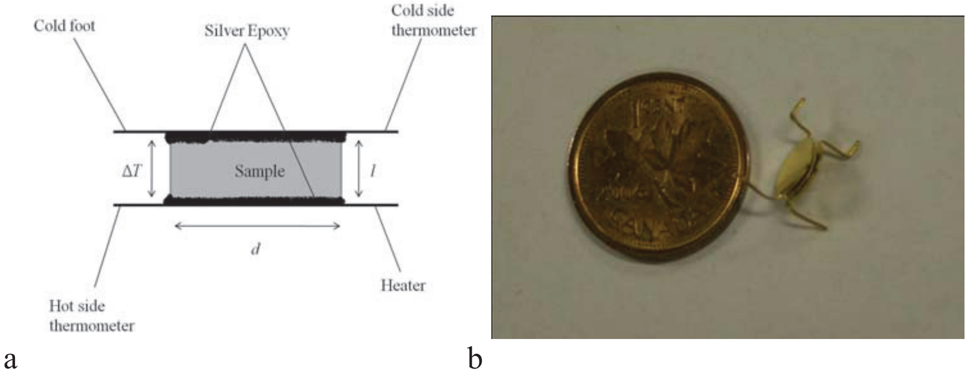

Figure 2.3 – (a) A schematic representation of a sample mounted between two gold-plated copper leads, where ΔT is the temperature difference across the sample, l is the distance across which the thermal and electrical transport are measured and d is the diameter of the cylindrical sample. (b) A photograph of a pellet connected at either end to two gold-plated copper leads. The penny is for scale.

After securing a sample between the leads, it was connected to the thermal transport puck by three contact "shoes" and a cold foot. Figure 2.4 shows a sample mounted on the TTO puck.

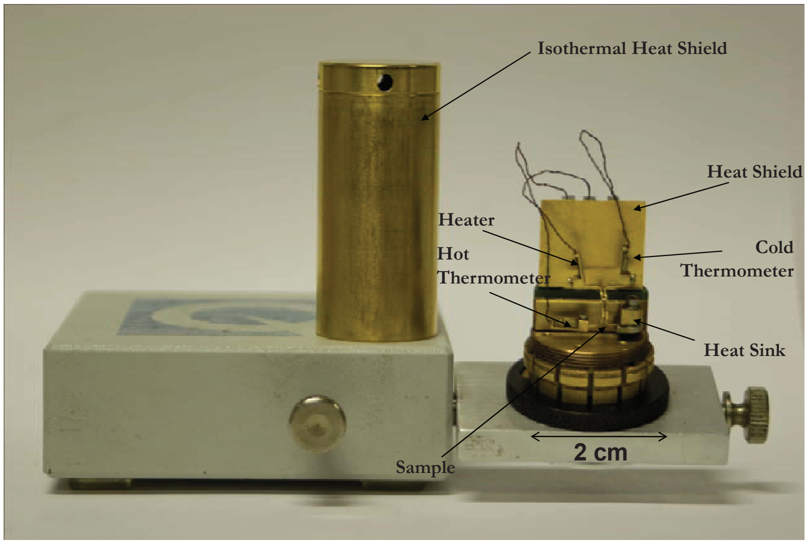

Figure 2.4 – Thermal transport option (TTO) puck with a clathrate sample mounted in preparation for measurement. The radiation shield, seen on the left, was placed over the puck to minimize radiative heat losses.

Heat was applied via the resistive heater chip (2 kΩ heater, 0 to 50 mW power) located on one of the sample shoes. The shoe with the heater also contained a current lead. Heat dissipation was accomplished by coupling the sample, via one of the lead connectors, to the hefty metal base of the TTO puck with Apiezon® N grease. A radiation shield encased the system and another radiation shield separated the sample from the electronics located on the puck. These shields were used to reduce radiative heat loss. Each of the other two shoes contained a Cernox™ 1050 model thermometer from Lake Shore Cryotronics and a voltage lead. All electrical connections to the heater and thermometers were made with 5.08 cm-long, 7.62×10^{-3} cm-diameter manganin alloy in order to minimize heat conduction from the sample to the puck. Manganin also was used because it has a small Seebeck coefficient (no greater than ~ 1 μV/K at any temperature).[88] This contribution was estimated and subtracted from the measured Seebeck coefficient by the instrument software. The current lead was made of the low-resistance copper alloy, PD-135.

After mounting the sample, the thermal transport puck was inserted into the PPMS and the chamber was evacuated to, $P < 10^{-4}$ Torr. Measurements under vacuum conditions significantly reduce convective loss. In addition, by making use of radiation shields and estimating emissive losses, it was possible to significantly minimize and account for all undesired thermal processes.

While Figures 2.3 and 2.4 show sample preparation for a two-probe experimental configuration, using the TTO puck, it is also possible to take measurements with a four-probe setup. A four-probe setup avoids errors associated with contact resistance by using separate sets of leads for excitation (to pass current or heat across a sample) and measurement (potential or temperature response). The samples described herein were available in such small quantities that it would not have been possible to prepare samples of adequate dimensions for four-probe measurements. This does not introduce significant errors as samples for this thesis were not highly conductive and thus neither thermal nor electrical contact resistance needed to be addressed.

2.1.2 Thermal Conductivity, κ

Thermal conductivity was determined by applying a known amount of heat via heat-pulses of constant power supplied by a resistance heater to a sample, while monitoring temperature responses of both the hot and cold sides of the sample. This gave the total thermal conductance.

To calculate the sample conductivity from the measured total conductance, the instrument software takes into account surface area, cross-section and thickness as well as the sample's emissivity, ε, i.e. the sample's ability to emit energy via radiation relative to a true black body.[87] The more a sample resembles a true black body, the closer ε is to 1. Since all of the samples examined here were dull black, non-metallic materials, the emissivity was estimated to be 1. Emissivity is used to account for radiative heat losses and is discussed in greater detail later in this chapter. There are two methods available to the PPMS user for implementing this general experimental procedure, both employing the sample mounting scheme shown in Figure 2.4.

2.1.2.1 Single-Measurement Mode for κ

Samples, mounted on the TTO puck and under vacuum, had the constant-power heat pulses applied to one side via the resistance heater. An increase in temperature on the side of the heater, the hot side, was followed by an increase in temperature on the far side of the sample, the cold side. Heater current was passed until a stable user-defined steady state temperature difference, ΔT, across the sample was observed. Steady-state temperature difference is defined as $\Delta T = (T_{h2} - T_{c2}) - (T_{h1} - T_{c1})$; Figure 2.5 illustrates its determination. Both ΔT and the stability condition were set by the user at the beginning of a measurement. Temperature stability and ΔT were defined as 0.1 % dT/T and 2 % of the temperature at which the measurement was being taken, respectively. This means that the system applied constant heater power to achieve a temperature difference of 2 % of the system temperature across the sample with the temperature of the hot side varying by less than 0.1 % of the system temperature over a one minute period. Once a measurement was started, the system waited for temperature stability before applying heater power. Heater power was then applied until the user-defined ΔT magnitude and stability criteria were met, at which point the hot-side and cold-side temperatures were recorded.

Since the instrument used a precisely calibrated resistance heater, the time and temperature data obtained during a measurement could be used to determine the thermal conductivity of the sample. First, the total heat conductance, K_{total}, including both

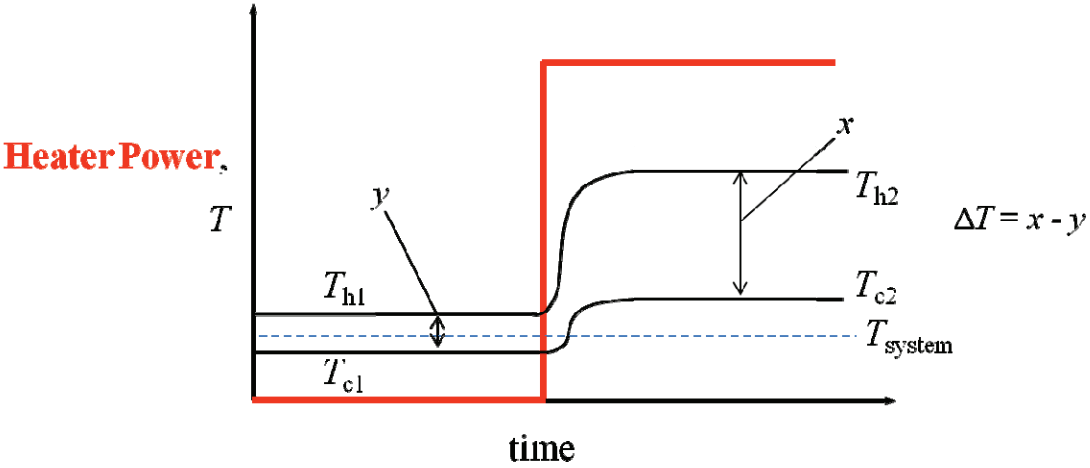

Figure 2.5 – An idealized representation of the heat-pulse (red) and temperature response (black) used to determine Δ*T* using the single-measurement mode of the TTO.

that of the sample and the shoes, was determined from monitored data by[88]

$$-, \qquad (2.1)$$

where *P* is the heater power. The conductance of the sample, K_{sample}, was obtained from the total conductance through[89]

$$\frac{\quad}{\quad} \qquad (2.2)$$

where *I* is the heater current, *R* is the heater resistance, P_{rad} is power loss due to radiation and ΔT is the temperature difference across the sample. The second term accounts for the conductance of the shoes, K_{shoes}, through the temperature and three empirical constants *a*, *b*, and *c*, defined by the PPMS software during shoe calibration. P_{rad} takes the emissivity of the sample into account; it is most significant at temperatures above 200 K. Since the total radiation from a hot body (T_h) to its colder surroundings (T_c) per unit of surface area of a black body is proportional to the fourth power of its absolute temperature, P_{rad} is described as[89]

$$P_{rad} = k \times \left(\frac{S_A}{2}\right) \times \varepsilon \times (T_h^4 - T_c^4), \tag{2.3}$$

where k is the Stefan-Boltzmann constant, S_A is the total sample surface area and ε is the emissivity. Because the two ends of the samples are at different temperatures when measurements are taken, it has been assumed that half of the sample surface radiates at the hot temperature, thus, S_A is divided by two in Equation (2.3). Due to this approximation, the approximated emissivity and the fourth power proportionality of radiation, losses are significant and difficult to estimate at temperatures ~ 300 K and greater. Errors in the measurement of thermal conductance on the order of ± 1 mW/K are expected at higher temperatures.

From the sample thermal conductance and geometry, thermal conductivity of the sample, κ, can be obtained by[88]

$$\kappa = \frac{K_{sample} l}{A}, \tag{2.4}$$

where l is the length of the sample and A is the sample cross-sectional area.

Single-measurement mode allows an experimenter a great deal of control over the input parameters and eliminates the need for the approximating extrapolations discussed in the following section. By varying the heater current and stability conditions one can minimize experimental uncertainty. However, single-measurement experiments are quite time consuming and therefore were performed mainly to obtain practical parameters for continuous-measurement mode experiments. It was found that setting a steady-state temperature difference of 2 % and stability of 0.1 % $\mathrm{d}T/T$ produced the most consistent results.

2.1.2.2 Continuous-Measurement Mode for κ

Continuous mode was employed for most transport measurements since it offered the benefit of a massive increase in data density and reduced experiment time. Continuous mode steadily and slowly changed the temperature and took κ measurements based on timed heat-pulses which were optimized to result in temperature profiles across the sample that could readily be extrapolated to approximate steady-state temperature differences. Heat-pulse optimization was done throughout experiments as different temperatures required different amounts of heat to elicit the defined temperature rise across the sample. Because temperature was varied steadily throughout experiments, the optimization was incremental and followed a temperature related trend (heater power was reduced with decreasing T). Continuous-measurement mode made assumptions about the sample and was more approximate than the single-measurement mode, but was still able to give accurate results.

Unlike in single-measurement mode, where ΔT was determined by applying heat and waiting for the sample to reach a steady-state, in continuous-measurement mode, software was used to extrapolate an approximate steady state temperature difference, ΔT_∞, from changes in T that occurred in response to precisely applied heat-pulses. As in single-measurement mode, ΔT_∞ represents a measured temperature difference between hot and cold thermometers, however, continuous mode only applied a short heater pulse. ΔT_∞ was then extrapolated from a temperature profile plot of that short heater pulse. Effectively, the steady-state condition is modeled based on the thermal response of the sample to a shorter heat-pulse than would be necessary to actually achieve that steady-state. This means that the system temperature can be continually changed and time is saved by not having to wait for stability of the sample chamber or a steady-state heat flow situation. Figure 2.6 illustrates this principle. In order to most accurately model ΔT_∞ from a short heat-pulse the PPMS software used adaptive algorithms to optimize measurement parameters such as heater current, heat-pulse period. The starting values for these parameters were obtained from single-measurement mode experiments to facilitate calculations. By starting with values close to those algorhythmically optimized, more accurate and consistent results could be obtained with less computational effort. Once the ΔT_∞ versus time data, as illustrated in Figure 2.6, had been obtained, a nonlinear least-squares fit of the data to the empirical formula,[89]

$$\Delta T_{model} = \Delta T_\infty \times \left\{1 - \frac{\left[\tau_1 \times exp\left(-\frac{t}{\tau_1}\right) - \tau_2 \times exp\left(-\frac{t}{\tau_2}\right)\right]}{\tau_1 - \tau_2}\right\} \tag{2.5}$$

was carried out. In Equation (2.5), ΔT_∞ is the estimated asymptotic temperature drop across the sample assuming the heater is left on indefinitely, τ_1 is a long empirical time

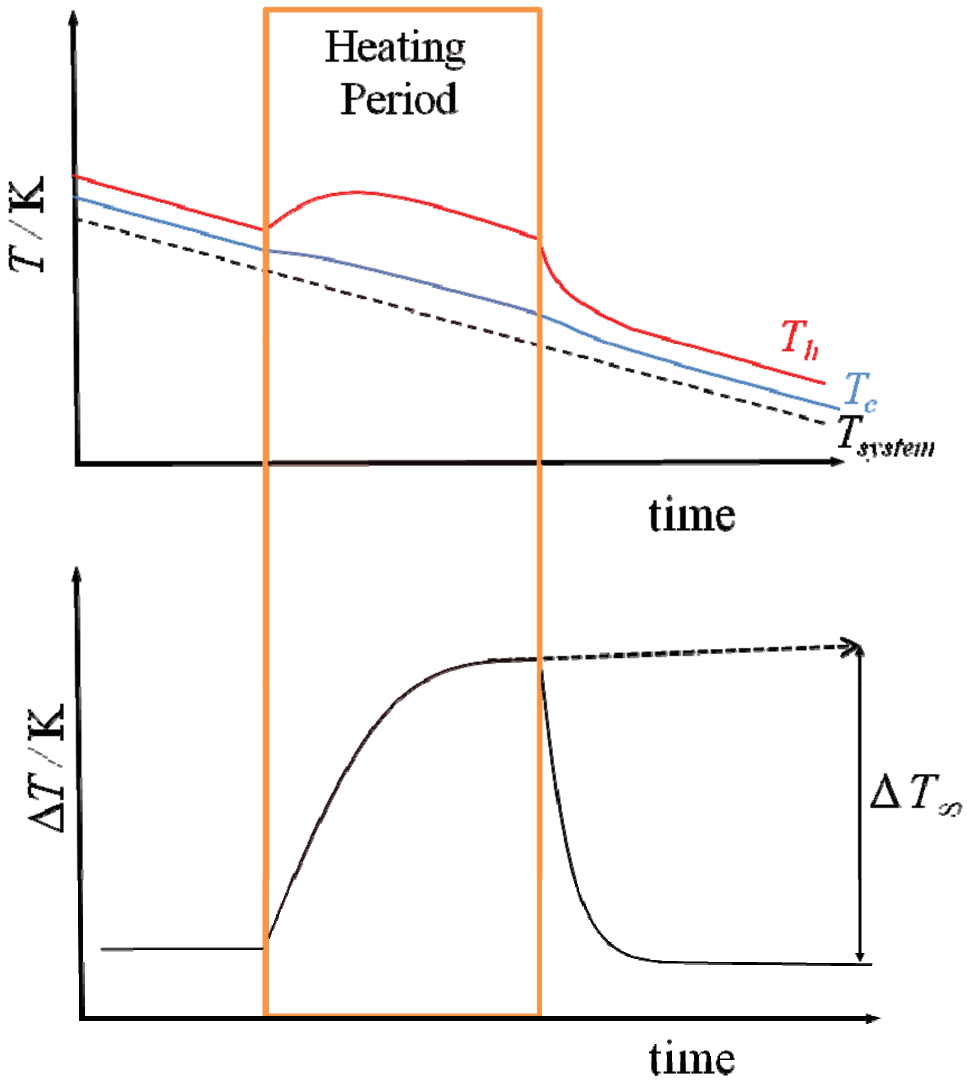

Figure 2.6 – Representation of the temperature response of the heater side (T_h) and heat sink side (T_c) of the sample during a thermal conductivity measurement. Power is supplied to the heater only for the time period within the red box. ΔT is the difference between T_h and T_c.[88]

constant which describes the ΔT curve nearing the maximum, t is time, and τ_2 is a short empirical time constant which describes the initial rise in ΔT at the beginning of the heat pulse. The short time constant originates from the heating of the sample contacts and shoes whereas the long time constant originates from the relatively low thermally conducting sample. The fitting routine employed by the software performs an exhaustive search over the space of these three parameters, optimizing them iteratively until the parameter values that yield a minimum in the residual of the curve fit are identified satisfactorily.[89]

Typical accuracies for thermal conductance quoted by Quantum Design are the greater of ± 5 % or an absolute K value for each of several temperature ranges: ± 2 μW/K for $T < 15$ K, ± 20 μW/K for 15 K $< T <$ 200 K, ± 0.5 mW/K for 200 K $< T <$ 300 K, and ± 1 mW/K for $T > 300$ K.[90] 5 % was the larger value for all measured conductances of every sample presented in this thesis across all temperature ranges. Recent thermal conductivity measurements performed on several samples of Pyrex™ glass of varying dimension have produced room-temperature results within 5 % of literature values.[91] Deviations between measurements were small, showing a standard deviation of 4 %. These values are in good agreement with those from Quantum Design.[90]

Experiments using both continuous measurement and single measurement modes were performed and continuous-measurement mode experiments were checked against single-measurement mode experiments to ensure that these approximations did not significantly impact the overall accuracy of data. Differences of less than 5 %, the uncertainty of the instrument,[90,91] were observed when both methods were optimized and so continuous-measurement mode was used for most experiments due to its more attractive data density and time aspects.

2.1.2.3 Thermal Contact Evaluation and Experimental Optimization

Initial experiments used a temperature rastering rate of 1 K/min. This produced low data density and had the effect of amplifying deviations within an experiment. Low data density made anomalous, outlying points appear as curve features, such as local maxima/ minima, rather than random aberrations. Following a demonstrated lack of reproducibility, the rate was reduced to 0.5 K/min. While this meant longer data acquisition times, it resulted in higher density data that demonstrated fewer outlying or deviating data points. All κ data presented in this thesis were acquired at the slower temperature raster rate, 0.5 K/min.

While reducing the rastering rate improved curve quality, repeat experiments often revealed pellet instability. Based on the evaluation of several curve features upon repeat experiments, data were discounted as unreliable based on one or more of four possible criteria: irregular curve shape, non-continuous curves, dramatic changes in measured κ values over short temperature ranges, and magnitude within the context of the sample series. Data for $Na_{5.5}Si_{136}$, presented in Figure 2.7, serve to illustrate each of these shortcomings, although that composition was not the only one to demonstrate these behaviours. Of the six data sets presented for $Na_{5.5}Si_{136}$, only that labelled 20100919 (labels are sample run dates given as YEARMODY) can be considered reliable.

From Figure 2.7 it can be seen that the 20100919 data are continuous; there are non-zero data points from 300 K to 2.5 K with no significantly outlying points. This is in contrast to the 20100915 data set which only meet such criteria from 150 K and above. Data for temperatures less than 150 K were output, however, they have been omitted due to very high scatter or null values. Such a drop to immeasurable thermal conductivity was indicative of a total loss of thermal contact; either the sample contact came free of the sample or the sample itself was mechanically unstable and fractured during measurement. In such cases a sample lead or sample lead attached to only a portion of a sample suspended by the lead wires was observed upon removal from the instrument.

The 20100921 experiment shows a continuous curve demonstrating a T^3 temperature dependence at low temperature and rises to approach a maximum at high temperature. If not for the context created by the data from other experiments, the 20100921data could very well have been accepted as accurate. However, the values

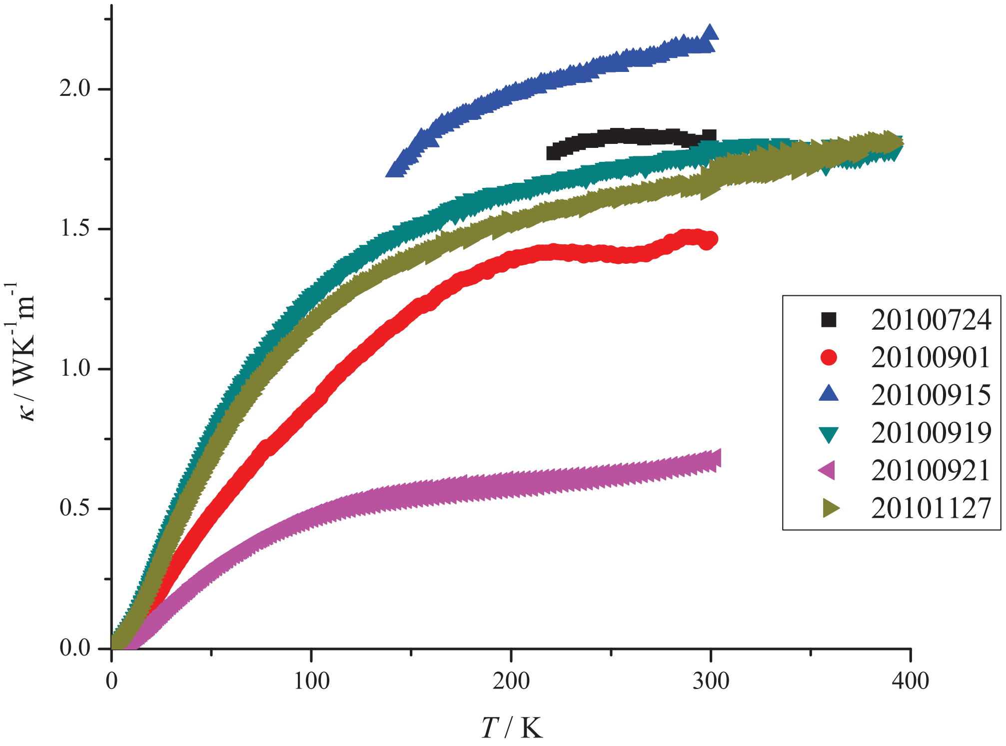

Figure 2.7 – Density-corrected κ data for $Na_{5.5}Si_{136}$. The sample was a cold-pressed powder. Legends indicate the date of each experiment (YEARMODY).

obtained from the 20100921 experiment are lower than those of similar compositions by a factor of ~ 3. As there are no extreme structural differences between this composition and those of similar x values, this difference suggested the sample and mounting to be structurally stable but with incomplete thermal contact. This occurred in situations where the samples and mounting were mechanically stable, but heat flow was restricted. Often upon removal of the leads from samples producing low magnitude κ data, incomplete epoxy coverage was observed.

The values presented by 20100919 are in a range comparable to those observed for other compositions (see later). Since changes in Na content have been shown to have relatively minor structural repercussions, this similarity is a strong indicator of data veracity. That is to say, one would not expect extreme changes in κ magnitudes, or curve shapes based on minor changes in Na content. A similar situation is suggested by the shape of the 20100901 curve, which displays continuous data but an irregular curve shape. The 20100901 data set showed apparent reproducibility between the scan from high temperature to low (down scan) and the scan for low temperature to high (up scan). Cases where there was a reproducible abnormal shape to the thermal conductivity curve were found to be due to a stable but irregular and incomplete thermal contact. Upon removal of samples displaying this kind of irregular curve behaviour, even gentle handling often resulted in total fractures normal to the path of thermal transport, or in the separation of leads from sample surfaces. This mechanical instability was not seen from samples that produced data of regular curve shapes, such as 20101127 and 20100919.

To further increase confidence in the experimental data, following TTO measurement for several samples (x = 8.8, 7.2, 6.5, 5.5 and 1.3) the conductive epoxy was removed, re-applied, re-mounted using new contacts and TTO data were re-measured. This technique was found to reproduce data from the original experiments well when good thermal contact had been achieved. This was done as a check to test the reproducibility of TTO data and as a means to evaluate sample contacts. If data from the first experiment were obtained using incomplete contacts one would expect the repeat experiment to yield data of greater magnitude. When good contact was reproduced between multiple runs on a single sample the shape of the resulting datasets were very similar although the magnitude of the re-mounted sample data tended to be somewhat lower than the original data. The 20101127 data set for $Na_{5.5}Si_{136}$ (Figure 2.7) was from re-mounting and re-measuring 20100919. The repeat experiment shows values of ~ 90 % to 95 % of the original with a similar curve shape. Re-runs showing good contact following measurement showed thermal conductivity values of more than 80 % of the original at 300 K. The decrease in thermal conductivity was reflective of a loss of material during epoxy removal. This lowering of κ values can be understood in terms of dimensional uncertainty. Epoxy was removed via grinding, a process that necessarily removes some sample along with the epoxy. Although the sample thickness was re-measured for the repeat experiments, the sample diameter was not since, following grinding, the sample was only an approximation of a cylinder. Since κ scales inversely with cross-sectional area, as seen in Equation (2.4), an overestimated cross-sectional area results in an apparent conductivity that is lower than the actual conductivity. Thus, qualitative agreement between two mountings of the same sample was used to evaluate the state of thermal contact, while initial datasets (high κ) were taken as definitive indicators of true thermal conductivity.

Experimental difficulties with the hot-press consolidated samples, $Na_{20}Si_{136}$, were somewhat different from those of the powdered samples. They stemmed from the small and somewhat irregular sample dimensions rather than poor cohesive properties of the material. There were no problems with the samples breaking during experiments but, due to the small cross sectional areas, adhesion to the sample leads still proved somewhat problematic. Such contact issues were readily diagnosed through data curve considerations.

2.1.3 Seebeck Coefficient, S

Analogous to, and in combination with, ΔT_∞, the approximated steady-state voltage difference, ΔV_∞, was determined in the PPMS and then used to determine the Seebeck coefficient of samples through[88]

$$S = \frac{\Delta V_\infty}{\Delta T_\infty}, \tag{2.6}$$

once the temperature conditions mentioned above for κ measurements were met. In single-measurement mode this simply meant measuring the potential across the sample once the steady-state criterion, ΔT_∞, had been achieved.

This simple measurement is somewhat complicated, theoretically, in continuous mode. A similar fitting routine to that used for ΔT_{model} was employed to determine ΔV_{model}. However, in this instance the calculation was less demanding since ΔV determination occurred after the ΔT fitting had provided τ_1 and τ_2. This meant that a *linear* least-squares fit routine could be used to fit the data to[89]

$$\mathit{\Delta} V_{model} = \mathit{\Delta} V_{\infty} \times \left\{ 1 - \frac{\left[\tau_1 \times exp\left(-\frac{t}{\tau_1}\right) \pm \tau_2' \times exp\left(-\frac{t}{\tau_2'}\right) \right]}{\tau_1 - \tau_2'} \right\} + dt + e, \tag{2.7}$$

where ΔV_{∞} is the asymptotic Seebeck voltage drop, analogous to ΔT_{∞}, τ_2' is a time constant and d and e are parameters used to describe linear drift and offset voltages respectively. To obtain an accurate model, τ_2' was varied from zero to τ_1 so that for each value of τ_2' a linear regression in ΔV_{∞}, d and e was performed. A full search was done for both positive and negative values. This accommodated for the fact that both positive and negative Seebeck coefficients were physical possibilities. The linear drift term, d, was included to account for any varying thermal voltages in the wiring as well as the slow microvolt-level drift in the preamp electronics. This modeling procedure was adapted by Quantum Design from methods described by Maldonado.[92]

2.1.4 κ and S Measurement Compatibility

Generally, pellets with thicknesses greater than one mm are recommended for TTO measurements using the PPMS.[88] Initially, some experiments in which thermal conductivity measurements and sample fragility indicated contact issues still showed high quality (*i.e.* sensible and reproducible) S data. Conversely, the opposite was also true: good thermal conductivity data were produced by pellets that proved unreliable (*i.e.* non-sensible and irreproducible) for S measurements. Rarely were good data obtained for both S and κ in a single experiment. By examining the details of the pellets used for measurements displaying anti-correlations in S and κ data quality, it became apparent that thicker samples (thicker than 0.7 mm) tended to be better for S measurements. Since thick pellets were often quite fragile, it can be said that the constituent crystallites were not in good contact and that the more consistently robust thinner pellets were better for κ measurements. As such, early experiments, performed on thicker samples, tended to produce better S data while later experiments, performed on thinner pellets, produced better κ data.

2.1.5 Electrical Conductivity, σ

2.1.5.1 TTO AC Measurements

Electrical conductivity was measured using a two-probe AC method wherein an alternating current, I, of known magnitude was passed across the length, l, of a sample mounted on the TTO puck and the resulting potential difference, V, was measured. Voltage and current are related to a material's conductivity and geometry through[88]

$$\sigma = \frac{Il}{VA} \tag{2.8}$$

where A is sample cross-sectional area. As discussed earlier, the two-probe method introduces some error through contact resistance between the sample and its leads. While a four-probe method avoids this possible source of error, a larger sample than was available is required for such measurements. Given the limited amounts of samples available, the relatively low contributions of the contact resistance and the small observed electrical conductivities, the two-probe method was used for the results reported herein.

2.1.5.2 DC Electrical Conductivity

For samples that were not amenable to AC electrical conductivity measurements, the (more stable) DC technique was tried. For DC electrical conductivity measurements a constant, known, direct current was passed across a sample and the resulting voltage drop was observed. This can be accomplished using a two-probe technique, as was used for AC measurements discussed above. However, contact potentials arising between the sample and contact materials can affect the accuracy of such measurements.[4]

A four-probe technique was used to avoid the problem of contact potential and increase the accuracy of measurements. This technique uses four points of contact arranged in a linear geometry. A voltage is applied across the two peripheral points, while the two inner points of contact are used to measure the current. Figure 2.8 demonstrates how this geometry was applied to samples for this study.

Given the small sample dimensions and high precision of the PPMS voltmeter, uncertainties in sample dimensions and contact separation were the dominant sources of measurement uncertainties. Sample dimensions were measured using a calliper with an

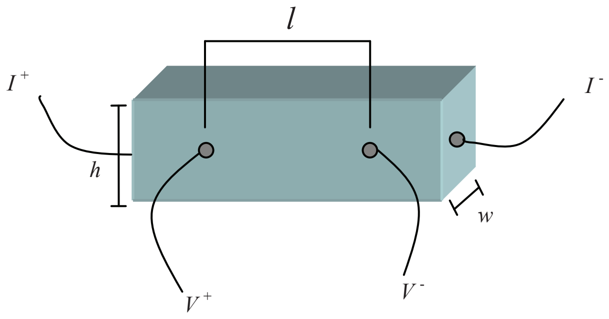

Figure 2.8 – A schematic representation of the four-probe electrical conductivity technique. *h* is height, *w* is width.

accuracy of ± 0.02 mm. Contacts were made using fine copper wires secured to the semiconductor samples using TRA-DUCT 2902, the same electrically and thermally conducting silver epoxy used for mounting TTO samples.

2.1.6 TTO Sample Prep Conclusions

Data for all three physical properties that comprise *ZT* can, in principle, be obtained in a single experiment and that would most accurately describe a sample. Although processing does not affect the ability of the TTO option to measure *S* it does, somewhat, affect the ability to measure κ and greatly affects σ measurements. It is, therefore, best to process samples, if at all possible, in such a way as to facilitate simultaneous measurements of *S*, σ and κ. This means using consolidation processes that produce high density cylindrical pellets ~ 4.8 mm in diameter that are robust enough to allow for contact separations greater than 1 mm, and to do so from powders that are as free of surface oxidation as possible.

2.1.7 Uncertainty

The PPMS software calculated the standard deviation of all reported quantities: thermal conductivity, electrical resistivity, Seebeck coefficient and *ZT*. This was done using the same residuals, $R_{\Delta T}$, used for modeling ΔT and ΔV. These are defined as[88]

$$R_{\Delta T} = \sqrt{\frac{\sum_i \left(\Delta T_i - \Delta T_{i,model}\right)^2}{N}}, \tag{2.9}$$

where N is the number of data points making up the curve. For κ and S, $N = 64$ and twice that for ρ since voltage measurements were taken before *and* after the heat-pulse. These residuals were used to calculate the standard deviation of thermal conductivity measurements by[88]

$$\sigma(\kappa) = \kappa \times \sqrt{\left(\frac{R_{\Delta T}}{\Delta T_{\infty}}\right)^2 + \left(\frac{2IR\delta I}{P}\right)^2 + \left(\frac{0.2 \times P_{loss}}{P}\right)^2 + \left(\frac{0.1 \times T_{\infty} \times K_{shoes}}{P}\right)^2} \quad , \qquad (2.10)$$

where the first term was used to account for the residual of the curve fit, the second to propagate uncertainty in the heater current due to the digital to analogue converter. The third term estimated radiative losses where a combined uncertainty of 20 % in sample surface area and emissivity was assumed, and the final term to accounted for an assumed 10 % uncertainty in the thermal conductance leak from the shoe assemblies, K_{shoes}.

Porosity must be considered when comparing thermal conductivities of different samples. Since porosity is calculated from geometric and gravimetric measurements, uncertainty in mass and sample dimensions must also be considered. The callipers used to measure sample geometries had a precision of ± 0.02 mm. This value was used to consider lead separation uncertainty and, in conjunction with the 0.00005 g mass determination uncertainty, quantified porosity uncertainty into estimations of uncertainty in thermal conductivity. Repeat thermal conductivity measurements on samples of Pyrex™ glass of varying dimensions have shown standard deviations of less than 4 % and deviation from published literature values[93] of less than 5 % at room-temperature.[91]

This is roughly twice the uncertainty reported from random error as calculated from the above expression, Equation (2.10).

Similarly, the uncertainty in Seebeck coefficient determination was calculated by[88]

$$\sigma(S) = S \times \sqrt{\left(\frac{R_{\Delta V}}{\Delta V}\right)^2 + \left(\frac{R_{\Delta T}}{\Delta T_\infty}\right)^2}. \tag{2.11}$$

Since resistivity measurements were made both before and after each thermal measurement and the average of the two was reported in the data file, the residuals, R_ρ, were obtained by[88]

$$R_\rho = \sqrt{\frac{\sum_i \left(V_i - \Delta V_{i,model}\right)^2}{N}}, \tag{2.12}$$

and the standard deviation was[88]

$$\sigma(\rho) = \rho \times \frac{R_\rho}{V_{PP}}, \tag{2.13}$$

where V_{pp} was the peak-to-peak amplitude of voltage versus time signal. Again, geometric factors (± 0.02 mm for contact separation) must be considered when determining the uncertainty of electrical conductivity. These can then be propagated with ΔT uncertainty to describe the anticipated uncertainty of S measurements.

Finally, the uncertainty in *ZT* was obtained by propagating the uncertainty from each of the measurements:[88]

$$\sigma(ZT) = ZT \times \sqrt{\left(\frac{2\sigma(S)}{S}\right)^2 + \left(\frac{\sigma(\kappa)}{\kappa}\right)^2 + \left(\frac{\sigma(\rho)}{\rho}\right)^2 + \left(\frac{\sigma(T)}{T}\right)^2}, \qquad (2.14)$$

where the last term is the standard deviation in temperature over the duration of the measurement. By including dimensional uncertainty into the constituent properties, the propagated error better describes uncertainty in *ZT* than is calculated by PPMS software. The software, in all values, reports a minimum uncertainty, assuming that all systematic sources of such as error, such as dimensional uncertainty, are avoided.

2.2 Heat Capacity

Heat capacity was determined using the PPMS through relaxation calorimetry, a technique wherein a known amount of heat is applied to a sample and the temperature response is monitored over time. Measurements were performed under vacuum, $P < 10^{-4}$ Torr, on an alumina platform that was suspended within the sample chamber of the instrument by Pt wires that served as voltage leads to the thermometer and current leads to the heating element. In this way the sample was thermally isolated to a sufficient degree that heat from both the platform and the sample was transported by the connecting wires alone. This ensured that heat dissipation occurred solely along a known path, allowing for accurate heat capacity determination. As with thermal conductivity, the measured amount of heat was delivered to the sample via a timed heat-pulse of constant

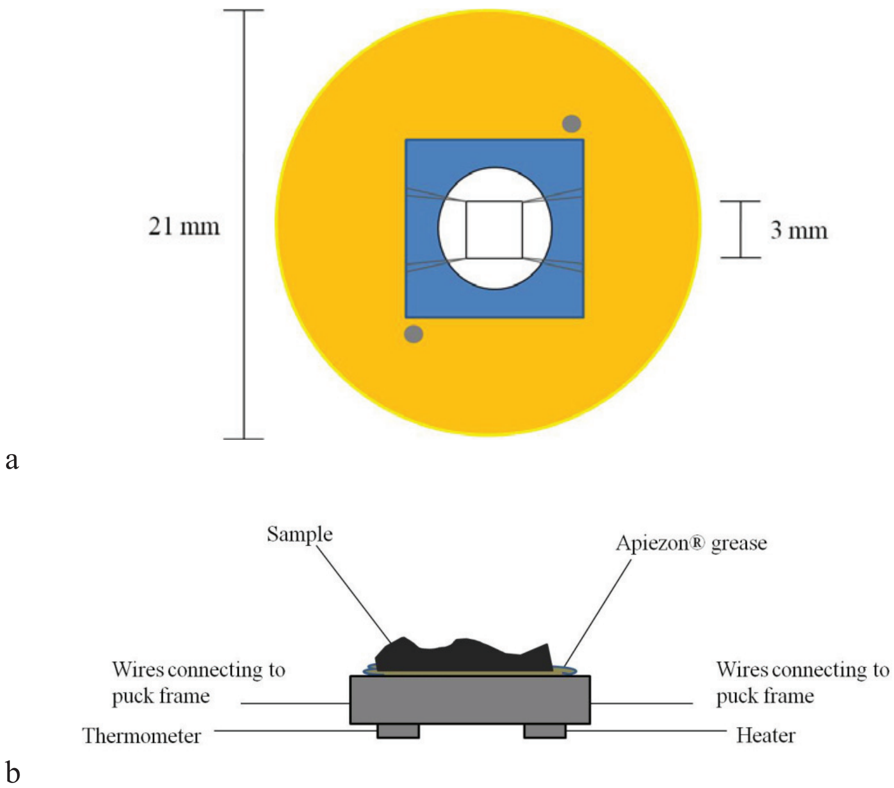

Figure 2.9 – A schematic representation of the sample and puck configuration used for C_p measurements. (a) shows a top down view of the puck and (b) shows a profile of the platform with a sample mounted on it. Modeled after Ref. 94.

power delivered by a thin film RuO resistance heater. The heater was located on the underside of the sample platform. A Cernox^{TM} sensor from Lake Shore Cryotronics, also mounted under the platform, was used to monitor temperature response. Figure 2.9 illustrates the heat capacity puck and sample configuration.

The heating period was defined in terms of temperature rise, either as a percentage of the absolute temperature at which the measurement was being taken at or as an absolute value in K. A temperature rise of 2 % of the system temperature was used. When this condition had been met, the heater was turned off and the temperature of the sample and platform was monitored for an amount of time equal to the heating period. Figure 2.10 illustrates this process.

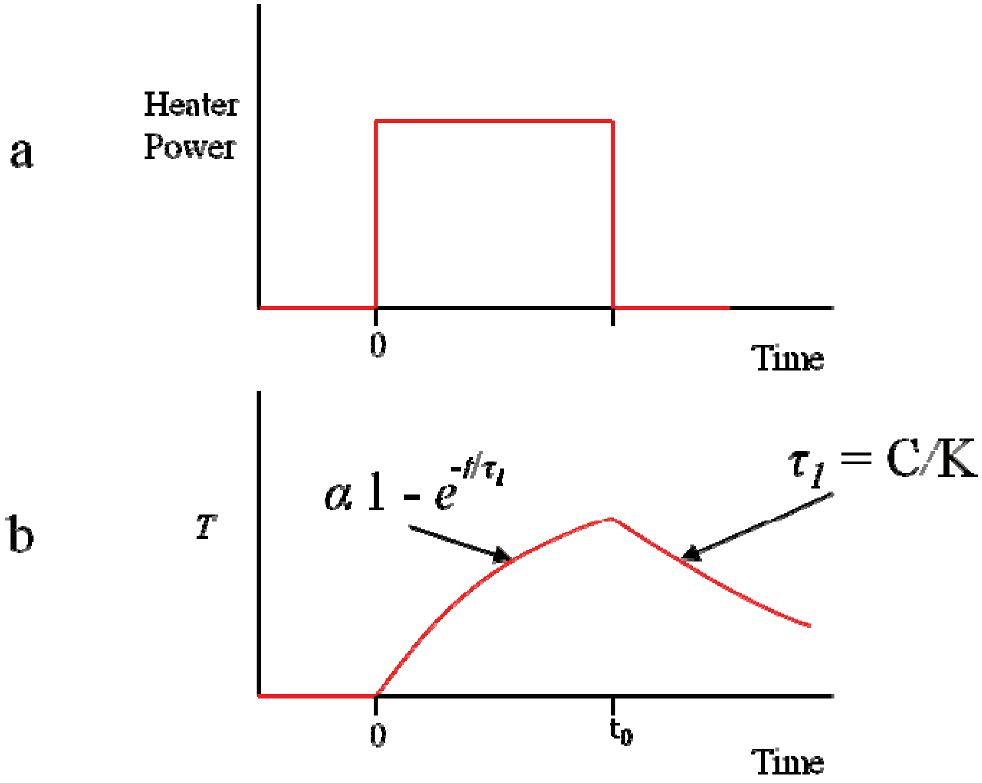

Figure 2.10 – Plots of (a) heater power versus time and (b) temperature versus time for the determination of heat capacity by the PPMS. Both plots use the same time scale and t_o corresponds to the time of discontinuation of heater current. Styled after Ref. 88.

Once the heater power had been discontinued, the temperature of the platform (and anything in thermal contact with it), T_{pl}, decayed over time as

, (2.15)

where T_o is the temperature at the time the heater was switched off. The time constant was, $\tau_1 = C_{pl} / K_W$ where C_{pl} is the heat capacity of the platform, including anything in thermal contact with it. K_W is the thermal conductance between the platform and the heat-sink via the connecting wires.[95] K_W was determined from a calibration run conducted on a clean platform: there was neither sample nor grease on it.

The platform temperature was monitored using the thermometer mounted on the platform underside and it is known that [88]

$$C_{pl}\frac{dT}{dt} = -K_w\left(T_{pl} - T_\circ\right) + P(t), \tag{2.16}$$

where $T_\circ$ is the temperature of the thermal bath (the puck frame), equal to the initial temperature, and $P(t)$ is the power applied by the heater. Therefore, by applying a known amount of heat and monitoring temperature response, the heat capacity of the platform and all materials in thermal contact with it can be determined from the recorded time versus temperature data. $P(t)$ is equal to the applied heater power when current is passed across the heater (zero otherwise).

The above holds only when the sample is in good thermal contact with the platform. Thermal contact is described in terms of a thermal coupling constant given as a percentage, as determined from the two-tau model™.[88] A value of 100 % indicates perfect thermal contact, while 0 % indicates no thermal contact. A value greater than 90 % indicated acceptable thermal contact. In cases in which there is poor thermal contact between the sample and the platform a second constant, τ_2, is introduced to better model the heat flow. This technique models the heat flow between the sample and the platform as well as between the platform and the puck. For this work, only results that had coupling constants greater than 96 % were considered to be valid. Since the two-tau method was not used for this thesis its details are not discussed further.

Thermal contact between the sample and the platform was achieved using an Apiezon® grease, the specific variety of which was chosen based on the temperature range of the experiment to be conducted. H grease was used for temperatures above 300 K as it remained relatively viscous at elevated temperatures and did not flow off the platform while N grease did tend to flow off the platform at temperatures in excess of 315 K. N grease was used at temperatures below 300 K since the H grease has an associated phase change that causes it to lose contact with the platform at temperatures between 100 K and 150 K. Since grease was used to make the thermal contact between a sample and the platform, it was necessary to run an addendum heat capacity measurement of the grease alone before an experiment was conducted including a sample. Since heat capacity is an additive property, once both runs had been completed, the addendum could be subtracted from the sample data to give the heat capacity of the sample.

For the most accurate results, a sample heat capacity should contribute no less than 30 % of the combined heat capacity of the grease and sample;[96] under these conditions, for thermal insulators, data within 1 % of those provided for standard materials can be achieved in the temperature range 5 K < T > 300 K.[96] Therefore, data for separate runs that are found to be within 2 % of one another have been considered to be consistent with one another for the purposes of heat capacity studies in this research.

2.2.1 C_p Data Evaluation

Sample size and mass had significant effect on the overall quality of heat capacity data. Size effects were related to the contact areas by which heat was transferred from the heat capacity puck; maximizing this maximized heat transfer to the sample. This effect is distinct from mass, which controlled the contributions of the sample to the total heat capacity. Heat capacity measurements benefited from large sample surface area, but only to the point that samples did not exceed the area of the sample platform. Low temperatures demonstrated better results for less massive samples. At high temperatures, more massive samples tended to produce more reliable data with less massive samples tending towards errantly high and scattered values. In general, a larger sample corresponded to a more massive sample, and only in rare cases was this not true. Such instances were usually due to thin, plate like, samples. Figure 2.11 presents heat capacity data for several measurements on $Na_{8.8}Si_{136}$.

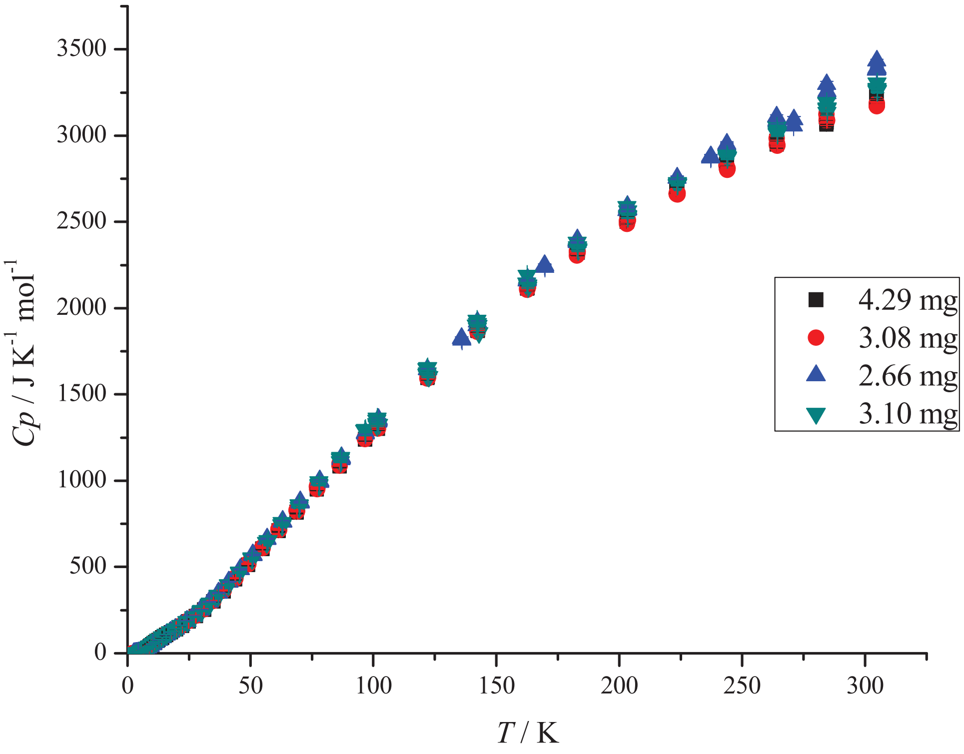

Figure 2.11 – Experimental heat capacity data obtained for $Na_{8.8}Si_{136}$, using samples of different masses.

From Figure 2.11 it can be seen that data scatter increased at the high temperature limit of these experiments, although scatter was reduced with larger samples. It shows data for several $x = 8.8$ samples of different masses. The least massive sample, $m = 2.66$ mg shows the greatest heat capacity data scatter at the highest temperatures. The other samples show some scatter around those of the most massive sample. In Figure 2.11 the 3.08 mg sample, which displays the lowest apparent molar heat capacity, was mounted with a porous fracture surface in thermal contact with the sample platform. This resulted in poor heat transfer between the platform and the sample as evidenced by low coupling constants; all were at or below 90 %. All other experiments performed on this composition produced data in good agreement with one another below ~250 K. This serves as a good indicator of the importance of sample surface morphology. For relaxation calorimetry, a smooth, flat surface improves thermal contact which in turn improves data quality. In addition, it has been observed that a thin uniform layer of thermally conducting grease achieved the best contact between the sample and platform. Early experiments were run with a "blob" of grease placed at the centre of the platform, this was then spread when the sample was pressed into it. Contact was often good, but coupling constants increase by several percent on average (~3 % increase) using the uniform, thin layer methods. Furthermore, the heat capacity of Apiezon® grease is known to depend on morphology (thin layer or globular mass).[97]

In general, the most reliable heat capacity data came for samples that had multiple experiments performed on different pieces with masses differing by a factor of two, the smaller sample having a mass greater than 2 mg. It was not possible to obtain multiple samples of optimum dimensions and masses for all compositions as heat capacity measurement processing procedures involved the fracturing of pressed pellets so that C_p

measurements could be carried out on the pieces. Fracturing of this sort was not exact and a certain degree of variation was seen in the resulting samples. However, reproducible heat capacity data for all compositions were achieved.

2.3 Structural Studies

Structural details of the samples being studied are essential to understanding the physical property data collected. Indeed it is the relationship between form and function that occupies much of chemistry; until now function has been the focus of discussion.

2.3.1 Powder X-Ray Diffraction, PXRD

Because the compounds investigated for this study were solids, the primary tool utilized for structural characterization was x-ray diffraction. X-ray diffraction was used both to determine sample structure and as a means of verifying synthesis products. Interaction between x-rays and the electrons of a material cause x-rays to diffract.[98] When the paths of two diffracted x-rays differ by an integral value of their wavelength, they are in phase and constructive interference is observed. Formally, the condition for such constructive interference is described by Bragg's law,[99]

$$n\lambda = 2dsin\theta, \tag{2.17}$$

where n is an integer, λ is the wavelength of radiation, d is the spacing between lattice planes and θ is the angle between incident rays and scattering planes. By analyzing the angles at which the Bragg condition is satisfied, one can determine interplanar distances.[100] Once all reasonable angles of diffraction have been scanned with a diffractometer, the peak positions and intensities are determined by fitting the data to a peak shape function. Peak positions are used to determine the unit cell parameters, lattice constants and angles, as well as its symmetry. Finally, since peak intensity is indicative of the number of equivalent scattering planes, peak intensity, in combination with composition, cell parameter and symmetry information, can be used to determine atomic coordinates (atomic positions).[101] Structural determinations are facilitated by computational refinement programs.

Three diffractometers were used for the work in this thesis. A Siemens D5000 and the JD2000, an instrument constructed in house, were used for verification of synthetic products. Ge clathrate structures were verified by comparison to published PXRD patterns. Calculated patterns were used to further support published structural data and to illustrate peak intensity dependencies on Na content in the absence of a sample series with varying Na contents. Calculated patterns based on published structural parameters were produced using the CrystalMaker™ and CrystalDiffract™ software packages.

Structural determinations of the Na_xSi_{136} series of materials were performed by Matt Beekman at the University of South Florida using a Bruker D8 diffractometer in Bragg-Brentano geometry.[102] Na_xSi_{136} sample crystal structures were determined by Rietveld analysis of powder x-ray diffraction data, with the aid of the GSAS[103] and EXPGUI[104] software. The relative intensities of the most intense Na_xSi_{136} diffraction peaks were found to be sensitive to the Na content in the two distinct cages. In this way, the cage occupancies and therefore sample compositions were determined.

2.3.2 X-Ray Absorption Spectroscopy, XAS

While x-ray diffraction provides insight into the crystalline order of materials, the technique is limited by its reliance on long-range translational order and a single wavelength of radiation. By using tuneable x-rays to examine samples, many experiments are available wherein one can obtain detailed information about a sample's local and electronic structures. The increase in diversity of x-ray experiments that comes with tuneability stems from the possibility of interactions with inner shell electrons whereas the monochromatic x-rays used for diffraction experiments are relatively low in energy and are only able to interact with outer-shell electrons. Core electrons are more sensitive to local structure and probing them is less reliant on long-range order.

By making use of tuneable x-rays, x-ray absorption spectroscopy, XAS, can be used effectively as a tool for structure determination.[105] This technique also can be used to obtain information, at the atomic and molecular scale, regarding the local structure around selected constituent elements of a material. Because it requires no long-range order, XAS can be used effectively to study a great variety of materials, from those with significant long-range order, *e.g.* crystals, to those with little or none, *e.g.* amorphous solids, liquids, molecular gases.[106]

XAS is an *electronic* spectroscopy that arises from transitions between bound initial states and bound and continuum final states. In this regard it is quite similar to the more common and accessible UV-Vis spectroscopy but it is not a technique that most facilities can have on site. Like bench-top spectroscopies, XAS is used to probe electronic transitions between molecular orbitals of samples. By examining transitions of inner-shell electrons, x-ray absorption spectra can be used to gain detailed information about the structure, structural disorder and thermal motions of the atoms neighbouring absorbing atoms.

Tuneable x-rays are a product of particle accelerators. At such facilities, charged particles moving near the speed of light are guided in a circular path in an evacuated space using magnetic fields. When charged particles are accelerated they emit electromagnetic radiation as a result of changes in their momentum. This means that as the charged particles are accelerated around the circular path of a particle accelerator they emit light tangential to that path. By accelerating the charged particles at speeds approaching that of light, the emitted radiation has a high average energy, great total power and is directional. The result is very bright, very tuneable light sources that span huge portions of the electromagnetic spectrum, including the x-ray region.

In order to make use of this light, it is given a path away from the evacuated tube in which the charged particles are accelerated and a sample is put in the path of the light. XAS measures the x-ray absorption coefficient, $\mu(E)$, a value that describes how strongly x-rays are absorbed as a function of their energy. Generally, this absorption is small and as energy increases, so does the ability of the photons to penetrate. As such, $\mu(E)$ tends to decrease predictably with increasing energy. This holds true as the energy of the impinging light increases until some energy, characteristic for the element being studied in a particular experiment, is achieved. At this characteristic energy, a sharp increase in absorption is observed. This increase in absorption corresponds to an electronic transition for the element of interest. The elements of interest for this study were Si and Na and the electronic transition studied was the K-edge, which denotes the transition of an innermost *s*-orbital.

Absorption occurs when a photon interacts with an electron, transferring all its energy to the electron and being annihilated in the process. At the energy range of hundreds eV to several keV this means interactions with core electrons. Upon absorption of a photon, the electron is excited into a vacant higher energy level. This leaves a hole at the core of the absorbing atom. The newly formed photoelectron then scatters from the atoms surrounding the absorbing atom and interference occurs between the outgoing and scattered parts of the photoelectron wavefunction. These quantum interference effects give rise to energy dependent variations in the x-ray absorption. Following the ejection of the photoelectron, the outer shell electrons relax to occupy the vacancies. This gives rise to the emission of radiation of energy lower than that of the incident x-ray or the non-radiative release of energy by the ejection of an electron in an "Auger process."[106]

Both the radiative and non-radiative process can be used for detection. Fluorescence yield, FLY, detection measures the incident flux and the fluorescence x-rays that are emitted following an absorption event.[106] The diffraction of incident x-rays is a significant source of noise in such spectra. Total electron yield, TEY, detects the Auger electrons produced when core-holes are refilled.[106] TEY is a relatively surface sensitive detection technique due to the short path length of Auger electrons (~100 nm), whereas FLY can be used to probe the bulk structure of a sample. Either signal can be used to construct spectra depending whether surface or bulk information is required. Figure 2.12 demonstrates a typical x-ray absorption spectrum.

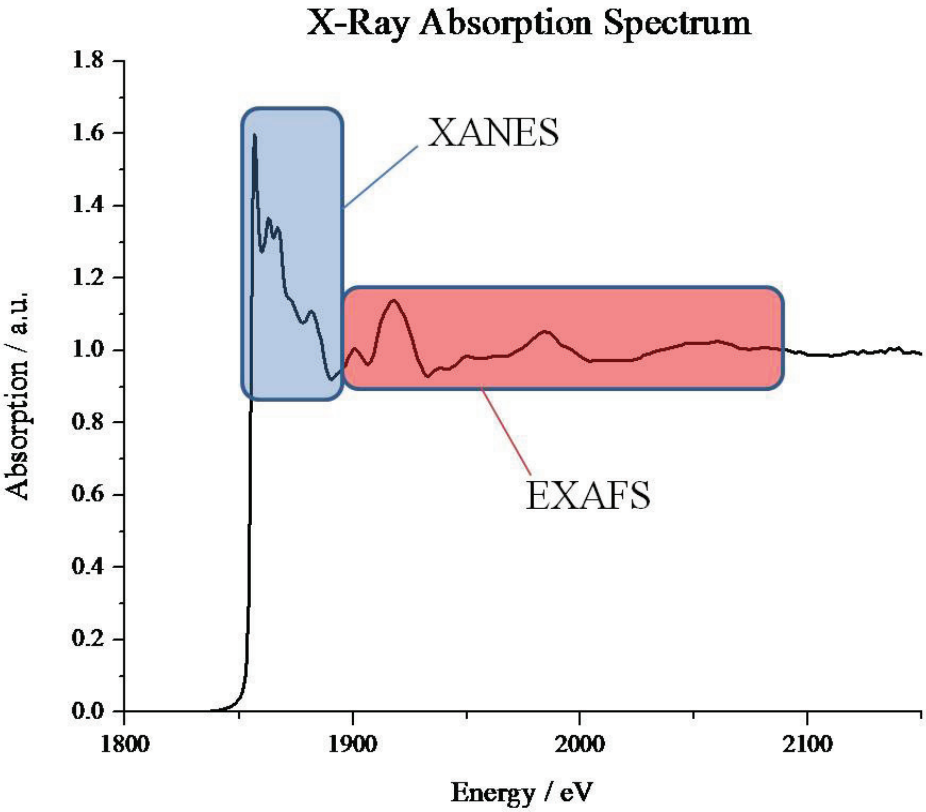

Figure 2.12 – A representative x-ray absorption spectrum illustrating the XANES and EXAFS regions of the Si K-edge. Modeled after Ref. 107.

X-ray spectra tend to be examined in two distinct regions: a low-energy region relative to the absorption edge, which is the x-ray absorption near edge structure, called XANES, and a high-energy region relative to the absorption edge, which is the x-ray absorption fine structure, called EXAFS. Figure 2.12 illustrates where the different regions are located in a typical spectrum.

2.3.2.1 XANES

The region of sharp increase, known as the absorption edge, and ~ 50 eV above that are considered the "near edge" region of x-ray absorption spectra. This region has been defined as being from the absorption edge up to the energy at which the wavelength of the excited electron is approximately equal to the distance between the absorbing atom and its nearest neighbours.[108] Because interactions between ejected photoelectrons and the potentials of the surrounding atoms are strong in this region, a single scattering event cannot be assumed. Multiply scattered photoelectrons contribute significantly to the near edge signal of spectra. XANES can give detailed information regarding the spatial arrangement of atoms neighbouring the absorbing one, including orientations relative to one another, bond angles and charge distribution.

2.3.2.2 EXAFS

As the energy of the impinging photons is increased there is a greater excess of energy imparted to the generated photoelectrons. High energy photoelectrons only undergo single interactions with neighbouring atoms before they are lost to the vacuum or reabsorbed into the material. The region of the spectrograph associated with these photoelectrons is the extended fine structure region. EXAFS starts at the energy where the XANES region ends and extends as far as there is usable signal. EXAFS can be used to obtain information about the arrangement of atoms in the immediate vicinity of the absorbing atom.

Si and Na K-edge absorption spectra were gathered at room-temperature at the high-resolution spherical grating monochromator (SGM) beamline at the Canadian Light Source in Saskatoon. Powder samples were mounted on a stainless steel disk using carbon tape. Both total electron and fluorescent yields were measured and recorded. Resolution in the range of these K-edges was approximately 0.2 eV on this beam line.

2.3.2.3 Interpretation

Because of the complex interactions that give rise to the XAS spectra, interpretation of the data is not straightforward: it requires the use of computer models and simulation. This is especially true with such complicated structures as clathrates. Interpretation started with a structural model of the system being studied. In this way x-ray diffraction and XAS were quite complementary techniques, with the former facilitating the analysis of the latter. The structural model was then used to simulate absorption spectra that were then compared to the measured spectra. The model was then adjusted to a better approximation of the system's true form, used for a more refined simulation and, again, compared to experiment. This process was repeated until simulation and experiment were in close agreement. This was possible because the energetic processes that result in such spectrographs are well understood.

The FEFF8 software package[109] was used to simulate spectra and to carry out local (orbital) density of states (LDOS) calculations based on models built using the Crystalmaker™ software. A variety of potentially important parameters that were known to change with Na content such as lattice constant, cage occupation and Na position were varied in order to determine their impact on simulated spectra. Resulting spectra were then compared to experiment and models were revised to optimize agreement between experiment and simulation. Varying Na content was found to have no observable effect on the outcome of simulations even in combination with other significant factors, namely position within the Si_{28} cages. As such, simulations were based on models that included only relevant, absorbing, Na atoms. The position of the Na within the Si_{28} cages was found to have the most significant impact on simulated spectra and thus was the focus of model optimization.

Data refinement followed a standard non-linear least squares method in R-space using the WinXAS software package. Fourier transformation of the normalized k-space absorption coefficient $\chi(k)$ was conducted for k of 2.4 to 7 $Å^{-1}$ while data refinement was performed in R-space in the region from 2 to 4.2 Å. This was done for both $\chi(k)*k$ and $\chi(k)*k^2$, yielding similar results in each case. In all cases the amplitude reduction factor, S_o^2, was fixed at a value of 0.6 based on the sample with the highest Na concentration (x = 21.5) as per previous methods.[110] Theoretical Na-Si coordination numbers were based on sodium occupancy in the Si_{20} and Si_{28} cages obtained from Rietveld refinement of powder x-ray diffraction patterns and fixed during refinement. All other fitting parameters (R(avg), σ^2, E_o) were extracted from the experimental data.

2.3.3 Scanning Electron Microscopy, SEM

A large potential applied across a large gap in vacuum will accelerate electrons towards a grounded target. Because free electrons have significantly shorter wavelengths than visible photons, they are capable of much greater magnifications than conventional light microscopy. Since microscopic techniques are limited in magnification by the wavelength of imaging particles and the wavelength of free electrons are inversely proportional to the accelerating potential, magnification increases with voltage. Upon interacting with the sample some interactions electrons are scattered back, nearly 180° to their impinging trajectory and some result in the liberation of electrons from the sample. The topography of a sample can be imaged by spatially resolving these electrons.[111] The spatial resolution of backscattered and liberated electrons is the foundation of scanning electron microscopy.

Backscattered electrons are those electrons that have been accelerated toward the sample, interacted elastically with a nucleus in the sample and sent back slightly deflected from their impinging path. Inelastic interactions of accelerated electrons with electrons of atoms making up the sample are responsible for liberated, or secondary, electrons. In addition to imaging information regarding the form of the sample, one can make use of the properties of accelerated electrons to glean other insight into the nature of samples. A Hitachi S-4700 FEG scanning electron microscope was used for imaging purposes in this research.

2.3.4 Microprobe Analysis

Energy-dispersive x-ray spectroscopy, EDS, and wavelength dispersive x-ray spectroscopy, WDS, are spectroscopic techniques that arise from interactions between accelerated electrons and matter. These techniques give compositional information about a sample and can be used to determine local compositions of a wide variety of samples.

Just as interactions between x-rays and inner shell electrons can result in vacancies within atoms, so can interactions with high-energy electrons. As was discussed for XAS, there is an atomic relaxation that occurs following such vacation. Again, this relaxation results in the emission of x-rays and Auger electrons. The energies of the resulting x-ray emissions are equal to the differences in energies of the two shells involved in the relaxation process. As such, each element has its own series of characteristic relaxation x-rays.[111] The x-rays given off can therefore be used to identify the composition of the area of sample being struck by the electron beam.

In addition to electron-hole relaxation derived x-rays, Coulombic interactions between beam electrons and the constituent atoms of a sample result in the production of continuum x-rays due to the acceleration of the beam electrons. This x-ray continuum provides some information about the average atomic number of the sample constituent atoms, however, its main contribution to a spectrum is background noise. Characteristic x-ray peaks must have amplitudes greater than this background in order to be detected and the detection limit for an element is therefore determined by the continuum radiation produced by a sample upon interaction with the electron beam.

When the accelerating voltage is increased, the volume of sample with which the electron beam interacts also is increased. This means that a greater portion of the sample interacts with the incident electron beam, and more x-rays are produced. As the depth of interaction increases, the number of characteristic x-rays produced decreases since the impinging electrons lose energy as they travel into the sample and in order to produce characteristic x-rays the incoming electron must have more energy than an element's critical ionization energy. Continuum x-rays do not require a minimum electron energy, however, and so are produced throughout the interaction volume. Therefore, a higher accelerating voltage is expected to provide a spectrum more indicative of the overall composition of a sample with a noisier background due to continuum x-rays. A lower accelerating voltage on the other hand is expected to produce fewer x-rays, and give a less noisy spectrum indicative of local, surface composition. The goal, therefore, is to use an accelerating voltage that is sufficient to excite characteristic x-rays without producing too much background noise.

The microprobe instrument used was a JEOL 8200 electron microprobe, equipped with five wavelength dispersive spectrometers, a Noran (128 eV resolution) energy-dispersive spectrometer and a cathodoluminescence photomultiplier. This instrument provides qualitative and quantitative chemical analyses for samples composed of elements ranging from boron to uranium. A Sun Ultra 10 computer controls the electron microprobe for the acquisition of data, images, and elemental maps.[112] Compositional data with spatial resolution as fine as several micrometers can be achieved with this technique. The technique is non-destructive, rapid, and provides spatial/topographical context for the analysis.

2.4 Si Clathrate Synthesis

Samples of Na_xSi_{136} were prepared by Matt Beekman at the University of South Florida by the method of thermal decomposition of Na_4Si_4, similar to that described by Cros et al.[53] First, the precursor Na_4Si_4 was synthesized by heating a stoichiometric mixture of high purity Si powder and high purity Na to 650 ºC for 36 hours in a sealed stainless steel container, under an ultra high purity nitrogen atmosphere. The Na_4Si_4 precursor was then decomposed using a modified "flash degassing" procedure originally developed by Gryko.[113] This involved the rapid heating of the precursor under dynamic vacuum (10^{-6} Torr) to 635 K at a rate of several hundred K/ min and removing the material before decomposition (~725 K under vacuum) to produce a nearly full sample ($23 < x < 24$). The Na content (determined by Rietveld refinement) was diminished by prolonged heating under vacuum at temperatures between 635 K and 700 K. Higher temperatures and longer heating times produced samples with lower Na content. This method produces dark grey Na_xSi_{136} powders with x values as low as 1.[102]

Further removal of Na was achieved by washing low Na content samples with concentrated HCl and degassing at 705 K under a vacuum of 10^{-5} Torr over a period of several days. This process was performed several times to minimize Na content. Finally, the sample fraction with Na content < 600 ppm was isolated by centrifugation in a dibromomethane-methanol solution.[114] The dark grey powder was hot-pressed into a pellet with a density of ~ 70 % of the theoretical density (from PXRD). The Si_{136} sample was prepared by Jan Gryko at the Jacksonville State University.

The composition of the samples was determined by Matt Beekman at the University of South Florida by Rietveld analysis of powder x-ray diffraction data, with the aid of the GSAS[103] and EXPGUI[104] software. The relative intensities of the most intense Na_xSi_{136} diffraction peaks are very sensitive to the Na content in the two distinct cages. In this way, the cage occupancies and therefore composition were determined. Rietveld analysis indicated that for $x < 8$, Na shows strong preferential occupation of the larger Si_{28} cage, and for $x > 8$ the Si_{20} cages become substantially occupied. This is in agreement with previous powder x-ray diffraction studies.[42,66,76,77] Figure 2.13 illustrates how the unit cell changes with Na content.

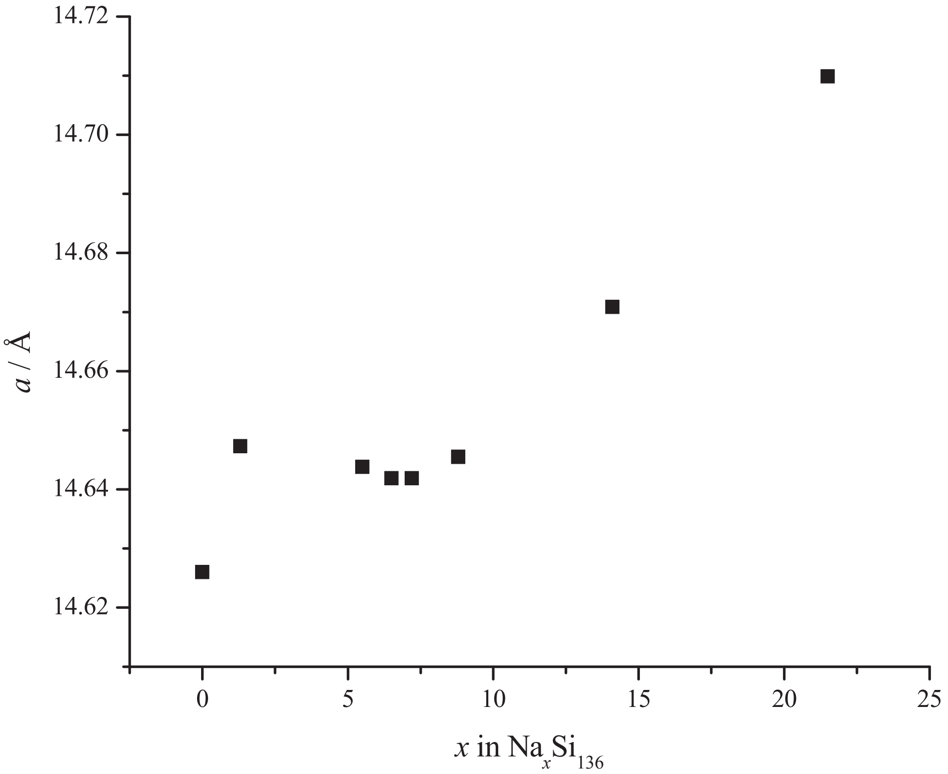

Figure 2.13 – Lattice parameter of the Na_xSi_{136} series of samples plotted as a function of Na content.[115] $x = 0$ from Ref. 114.

Chapter 3: Na Filled Type II Si Clathrates

Changes in the lattice structure and dynamics of the Na_xSi_{136} series of samples were probed using the techniques described in Chapter Two. Results of these studies were then used to interpret the samples' measured transport properties. This chapter describes how varying Na content affects the physical properties that contribute to *ZT* and discusses the dynamical origins of these effects.

3.1 X-Ray Absorption Spectroscopy, XAS

X-ray absorption spectroscopy in conjunction with theoretical modeling was used to probe both the local structure and electronic properties of the Na_xSi_{136} series of Na-containing type II Si clathrates. This study has been published in detail.[54] Both Si and Na K-edge absorption spectra were gathered at room-temperature at the high resolution spherical grating monochromator (SGM) beamline at the Canadian Light Source in Saskatoon. As an example of the experimental methodology, Figure 3.1 presents the total electron yield across the whole XAS range for both the Na K-edge and Si K-edge scans of the $Na_{21.5}Si_{136}$ sample.

The following provides a detailed connection between the clathrate materials studied and the data presented in Figure 3.1.

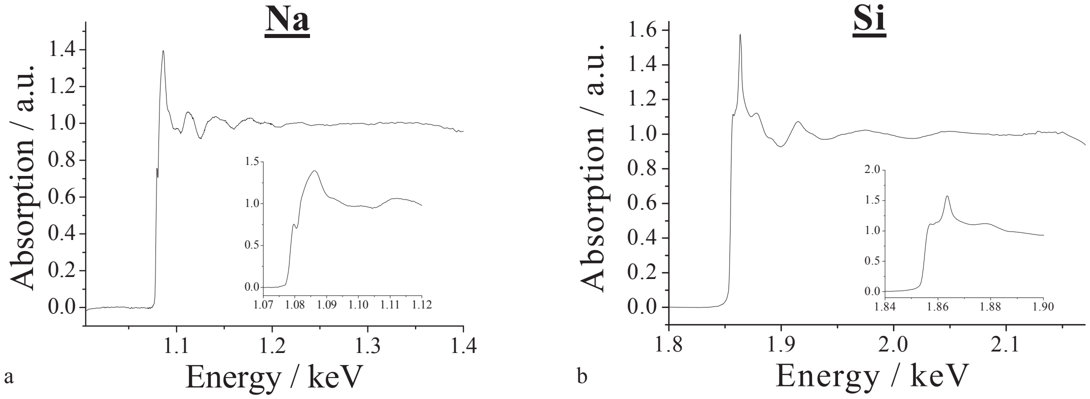

Figure 3.1 – X-ray absorption spectroscopic raw data for $Na_{21.5}Si_{136}$ at (a) the Na K-edge and (b) the Si K-edge. Near-edge regions are presented in more detail as inserts. Reproduced from Ref. 54 with permission.

3.1.1 Na K-edge EXAFS and Simulation

The Na K-edge EXAFS spectra were found to be very sensitive to Na-Si interactions and the information within this spectral region was used in a semi-quantitative fashion to discern the relative proportions of Na in the larger Si_{28} cages, compared with Na in the smaller Si_{20} cages.

Figure 3.2 (a) shows the weighted-average combinations of calculated Na K-edge EXAFS spectra. Simulations used for this averaging included the Si framework (treated as fully occupied on all sites, in accordance with Rietveld analysis results for all specimens studied here)[116] and only the interactions of Na atoms with their local environment (neighbouring Si) were included. That is, Na atoms were treated as independently absorbing in the EXAFS simulations since Na-Na interactions were found to have no observable impact on the EXAFS spectra produced. This finding was not unexpected given the long Na-Na distances: the shortest Na-Na distance was 4.8 Å (derived from PXRD data).[115] As such, the simulated spectra in Figure 3.2 (a) illustrate the shift in EXAFS from one extreme, completely Na in Si_{28} character, to the other, completely Na in Si_{20} character, and do not account for any differences due to changing overall framework occupancy. At the extremes of the relative occupancy range, where one Na environment is significantly in the majority, the correlation between the peaks and the Na environment can be seen clearly. By comparing the simulated EXAFS spectra in which Na is either fully occupying the Si_{20} cages or the Si_{28} cages (top and bottom datasets of Figure 3.2 (a), respectively), it is evident that for Na in Si_{28} cages the EXAFS oscillation intensity is much lower and the oscillation frequency is higher than that for Na in Si_{20} cages. This correlates well with the experimental findings (Figure 3.2 (b)) for low Na loading ($Na_{5.5}Si_{136}$) and high Na loading ($Na_{21.5}Si_{136}$), which are dominated by Na in Si_{28} cages and in Si_{20} cages, respectively, as discussed further below. The intermediate simulations in Figure 3.2 (a) were based on appropriate weightings of the simulations based on full occupation of the Si_{20} cages and full occupation of the Si_{28} cages, such that, for example, "Na 80 % occ. in Si_{20}, 20 % occ. in Si_{28}" refers to simulation of composition of $Na_{14.4}Si_{136}$, in which there are 12.8 (out of a possible 16) Na atoms in the Si_{20} cages, and 1.6 (out of a possible 8) Na atoms in the Si_{28} cages.

According to theory,[117] EXAFS intensity $\chi(k)$ can be expressed as

$$\chi(k)=\sum_j \frac{N_j S_0^2 F_j(k)}{kR_j^2}\cdot e^{(-2k^2\sigma^2)}\cdot e^{(\frac{-2R_j}{\lambda})}\cdot \sin[2kR_j+\delta_j(k)]\,, \tag{3.1}$$

where $F(k)$ is the backscattering amplitude from each of the N_j neighbouring atoms of the j-th type at an interatomic distance R_j, with a Debye-Waller factor of σ_j to account for thermal vibrations (assumed to be harmonic) and static disorder (assuming Gaussian pair distribution). The quantity $\delta(k)$ is the total phase shift experienced by the photoelectron, S_0^2 is the amplitude reduction factor and λ is the photoelectron mean free path. The average interatomic distance between the Na and neighbouring Si atoms is shorter for the Si_{20} cages than for the Si_{28} cages. From the form of Equation (3.1), especially the $\chi(k) \sim R_j^{-2} \exp(-R_j)$ term, it can be seen that Na in the Si_{20} cage generates a significantly greater EXAFS intensity, $\chi(k)$. Equation (3.1) shows that the EXAFS oscillation frequency is mainly determined by the term $\sin [2kR_j + \delta_j(k)]$, and therefore a longer Na-Si interatomic distance corresponds to a higher oscillation frequency in k-space. Therefore, comparison of the band at *ca*. 4.7 $Å^{-1}$, which is prominent for Na in Si_{28} cages, diminishes rapidly as the occupancy of Na in the smaller Si_{20} cages increases (Figure 3.2 (a)). By comparing this, the most prominent observable feature for Na in the Si_{28} cages, indicated by the vertical lines in Figure 3.2 (a) and 3.2 (b), with simulation, we find that the fine-structure features for Na in Si_{20} cages become dominant when more than ~ 30 % of the total Na content is in the Si_{20} cages. Therefore, the intensity of the 4.7 $Å^{-1}$ oscillation band can be used to estimate the concentration of Na in Si_{28} when visible (*i.e.*, when > 70 % of the total Na content is in the Si_{28} cages). When the band at 4.7 $Å^{-1}$ disappears, the Na occupancy in Si_{28} is < 70 % of the total Na content. From the experimental data in Figure 3.2 (b), it can be seen that this threshold occurs in Na_xSi_{136} for $x \sim 8.8$, *i.e.*, Na_xSi_{136} for $x >$ 8.8 is dominantly Na in Si_{20} cages, and for $x < 8.8$ is dominantly Na in the larger Si_{28} cages.

Figure 3.2 (b) shows that the experimental EXAFS oscillating pattern of the highest Na-loading sample, $Na_{21.5}Si_{136}$, is essentially identical to the simulated spectrum for Na in the Si_{20} cages only. This observation is consistent with nearly full Na loading,

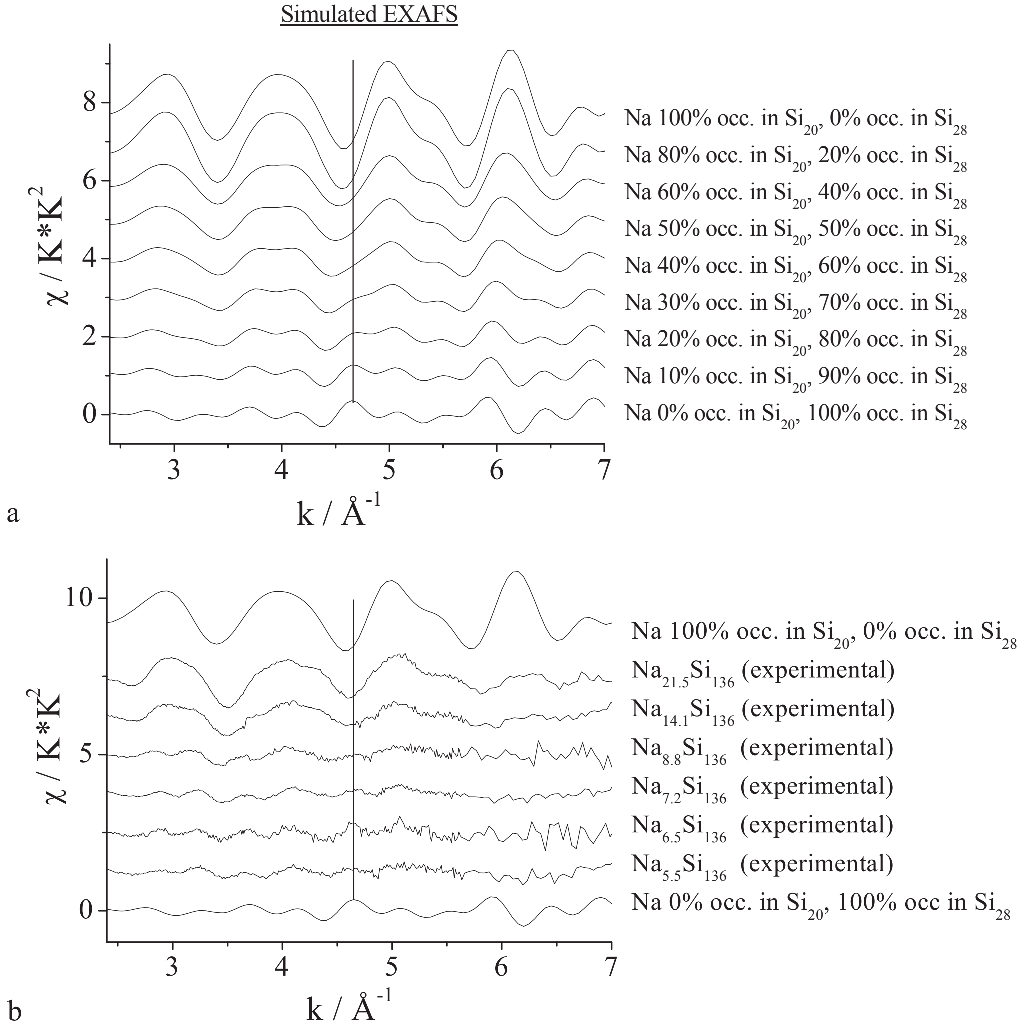

Figure 3.2 – (a) Simulated and (b) both experimental and simulated Na K-edge EXAFS spectra of several representative samples of Na_xSi_{136}. For the simulation, the Si framework is considered to be the same in all cases, the displacement of Na off the centre of the Si_{28} cages is 0.5 Å for all simulations (see section 3.2.1 for discussion) and the % occupancy of the Na in the Si_{20} cages and Na in the Si_{28} cages varies as indicated. The vertical line marks the position of the dominant oscillation for Na in the Si_{28} cages. Reproduced from Ref. 54 with permission.

since the Si_{136} framework has twice as many Si_{20} cages as Si_{28} cages, and the EXAFS features for Na in Si_{20} are more intense than for Na in Si_{28}, as discussed above. Although experimental EXAFS spectra for low-Na-content samples ($Na_{6.5}Si_{136}$ and $Na_{7.2}Si_{136}$) in the high-*k* region ($k > 6$ Å^{-1}) are rather noisy, the six oscillations in the low-*k* region are distinct, and very similar to those of the spectrum simulated for Na in Si_{28} cages. The oscillation bands at ~ 4.7 $Å^{-1}$ (characteristic for Na in Si_{28}) for the two lowest Na-content samples are of considerable intensity, indicating that the Na in Si_{28} cages dominates in these two samples. A close comparison with the simulated EXAFS in Figure 3.2 (a) leads to an estimation of 80-90 % occupancy of Na in Si_{28} cages in $Na_{5.5}Si_{136}$ and $Na_{6.5}Si_{136}$ and 70-80 % of Na in the Si_{28} cages in $Na_{7.2}Si_{136}$ and $Na_{8.8}Si_{136}$. Thus, over the loading range from $x = 8.8$ to $x = 5.5$ for Na_xSi_{136}, the Na occupancy in Si_{28} cages estimated from EXAFS drops from ~ 80 % to ~ 60 %, while the occupancy of Na in the Si_{20} cages drops from ~ 15 % to ~ 5 %. Therefore, the Na K-edge EXAFS results show that at low loadings, most of the Na is in the Si_{28} cages, and loss of Na during preparation

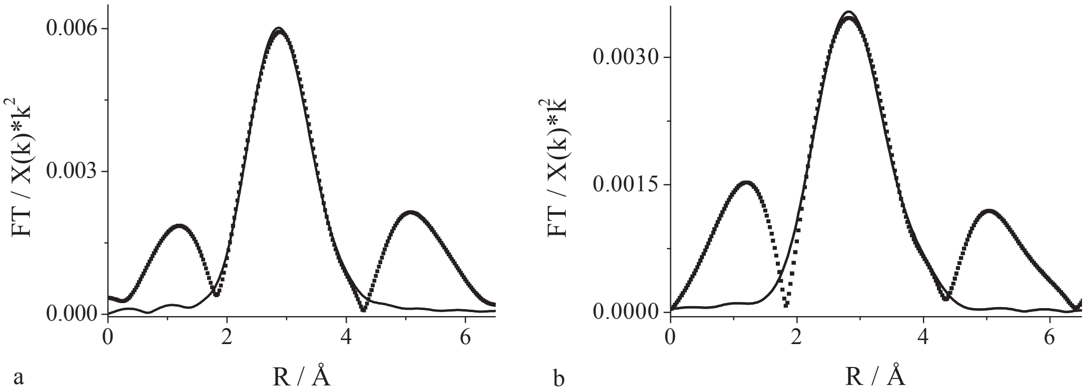

Figure 3.3 – EXAFS refinement. Experimental data (dots) and the fit (line), in R-space from 2 to 4.2 Å are presented for: (a) $Na_{21.5}Si_{136}$ and (b) $Na_{14.1}Si_{136}$. Reproduced from Ref. 54 with permission.

occurs preferentially from the smaller Si_{20} cages. This result is in agreement with Rietveld analyses of powder x-ray diffraction data for other studies of Na_xSi_{136}.[76,66,77]

From Figure 3.3, it can be seen that data refinement produced a good fit for the EXAFS region of the $Na_{21.5}Si_{136}$ and $Na_{14.1}Si_{136}$ spectra. Table 3.1 presents the quantitative data obtained from this procedure. Average bond distances, R(avg), obtained from EXAFS refinement are in good agreement with those obtained from x-ray diffraction studies.[116] Na in the Si_{20} cages appears to have consistent Debye-Waller factors (σ^2) across the two refinable spectra, while those of the Na in the Si_{28} cages increase with decreasing Na content. This trend is qualitatively continued to the $x = 8.8$ sample. However, the XAS data become noisier with decreasing Na content and quantitative conclusions have not been possible for $x < 14.1$. These values, while large compared to those typical of crystalline materials, are in line with the dynamical disorder associated with the guests in clathrate structures. The smaller Debye-Waller factor for $x = 21.5$ compared with $x = 14.1$ (Table 3.1) indicates less dynamical disorder of the Na

Table 3.1 – Quantitative results obtained from EXAFS refinement of $Na_{14.1}Si_{136}$ and $Na_{21.5}Si_{136}$. The coordination numbers (CN) were obtained from x-ray diffraction studies[115] and fixed for the refinement, while the remaining variables were determined through the fitting procedure. "Path" indicates the absorbing atom and nearest neighbour, R(avg) is the bond distance of a particular scattering path as observed with EXAFS, R(avg) XRD is the bond distance of a particular scattering path as determined from XRD data, ΔR is the difference in bond distance as determined by the two techniques, σ^2 is the Debye-Waller factor and E_o is an empirical parameter that was constrained within ± 5 eV during refinement. Reproduced from Ref. 54 with permission.

x	Path	CN	R(avg) / Å	R(avg) XRD / Å	ΔR / %	σ^2 /Å^2	E_o / eV
21.5	Na-Si_{20}	12.7	3.278(2)	3.307	0.9	0.0230(2)	-0.12(4)
	Na-Si_{28}	10.3	4.08(1)	3.979	2.5	0.0377(8)	0.4(1)
14.1	Na-Si_{20}	8.7	3.227(3)	3.318	2.7	0.0271(2)	-2.5(2)
	Na-Si_{28}	15.9	4.06(1)	3.969	2.3	0.0565(9)	0.34(7)

atoms in the Si_{28} cages with increased loading. This refinement thus supports the hypothesis that dynamic disorder and displacement from the centre of the Si_{28} cages decrease with increasing Na content.

3.1.2 Experimental Na K-edge XANES Spectra and FEFF Simulations

3.1.2.1 Off-Center Displacement of Na in the Si_{28} Cages

The Na atom is a tight fit in the smaller Si_{20} cage, but the larger Si_{28} cage has sufficient room for the Na atom to move off-center[81] as well as dynamically rattle.[118] The effect of the displacement of the Na atom from the center of the Si_{28} cage has been explored by simulation of the Na K-edge XANES (X-ray Absorption Near-Edge Structure) spectra. These results are shown in Figure 3.4. The most direct comparison with experiment is for the lowest loading ($Na_{1.3}Si_{136}$) because virtually all Na atoms are in the larger Si_{28} cages. The comparison in Figure 3.4 shows that simulated spectra for displacements of the Na atoms in the Si_{28} cages ranging from 0.4 Å to 0.6 Å most closely resemble those obtained from experiment. A previous study concluded that NMR results are consistent with *either* the Na atoms in a static position at the center of the Si_{28} cage, *or* dynamically disordered but symmetric about the centre of the Si_{28} cage (but not

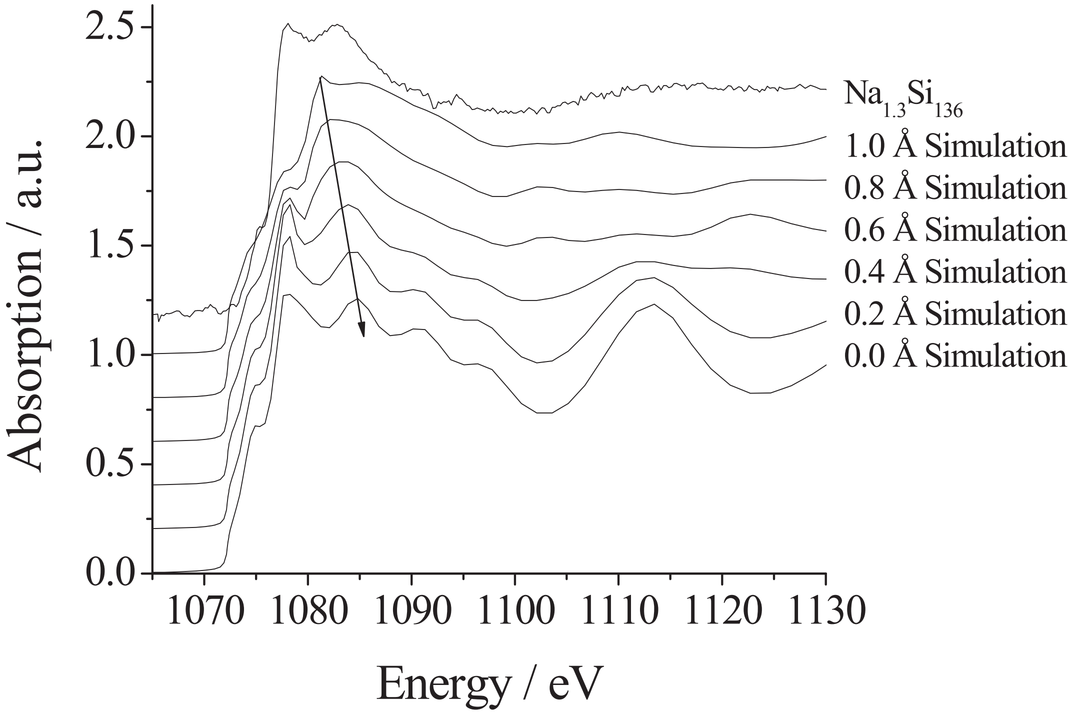

Figure 3.4 – By comparing simulated Na XANES spectra to the experimental $Na_{1.3}Si_{136}$ spectrum, the magnitude of the displacement of the Na atom from the center of the Si_{28} cage was estimated. In the simulations, the Na atom displacement from the center of the cage along the cube diagonal was varied from 0 Å to 1 Å, as indicated. The arrow shows the systematic shift in one peak with displacement. Comparison of the resulting simulated XANES spectra to the experimental spectrum for $Na_{1.3}Si_{136}$, a sample containing only Na in the large Si_{28} cages, indicates that best agreement at that loading is obtained when the displacement is ~ 0.5 Å. Reproduced from Ref. 54 with permission.

statically disordered off-center).[80] The XANES results presented here and also powder XRD refinements[119] both indicate displacements of the Na in the Si_{28} cages of 0.5 Å, uncertain to within ± 0.1 Å. Therefore, taking this together with NMR results,[80] it can be concluded that Na is dynamically disordered in the Si_{28} cages. Unfortunately, from the peak shapes and peak positions in the XANES simulations it is not possible to confirm small changes in displacement with loading, as can be seen from powder XRD refinement (~ 0.4 Å at higher Na content to ~ 0.6 Å at lower Na content).[116,119] Therefore, the median off-center displacement, 0.5 Å, was used for Na in Si_{28} cages in all the present simulations. This displacement also was used for the Na in Si_{28} cages in the

EXAFS spectra discussed above. Earlier EXAFS studies of the same system showed similar but slightly larger displacement of the Na from the center of the Si_{28} cages (0.9 ± 0.2 Å)[81,120] although LDA calculations indicate a displacement of 0.5 Å.[82] Although regular fitting of the data in the EXAFS region gives more accurate results regarding average bond distance for an absorbing atom, it does not indicate the atom's position relative to the origin of the unit cell nor its relative position within a structure such as the Si cages. Therefore, a non-routine fitting method was required to determine Na displacement from the EXAFS region, increasing the associated error (the uncertainty for regular fitting is ~ 0.02 Å compared to ~ 0.2 Å for the non-routine fitting discussed above). While the XANES method used herein relies on calculations for Na displacement determination, and is therefore also indirect, given the high-quality powder XRD data and close agreement between the two determinations the current method appears to be quite reliable. In addition, by determining the displacement using a sample in which the majority, if not all, of the Na resides in the relevant, Si_{28}, cages the determination was further simplified and representative of the physical situation being examined.

Note that XANES simulations run using models in which all cages were occupied by Na atoms were negligibly different from simulations in which only the scattering Na atom was included. In other words, the simulated spectra showed little change with Na loading, and depended only on the location of the absorbing atom (whether it was in a Si_{20} or in a Si_{28} cage). This result indicates that XANES spectral features are more dependent on the multitude of Si nearest neighbours than the relatively sparse Na neighbours, as one might expect.

3.1.2.2 Cage Occupancy from Comparison with Experimental XANES Data

Figure 3.5 shows the experimental and simulated Na K-edge XANES spectra for the full range of Na contents. In the experimental data (Figure 3.5 (a)), the lowest Na-content samples, $x \rightarrow 0$ and $x = 1.3$, show a doublet (indicated by two arrows) immediately following the absorption edge. Simulations of Na in the Si_{28} cages, Figure 3.5(b), showed the same features at the same energies as observed experimentally for the low-Na content samples, whereas simulations of Na in the Si_{20} cages produced a peak intermediate to the two components of the doublet. Therefore, the observation of a doublet with no intermediate peak was considered indicative that Na was present only in the Si_{28} cages. Inspection of the experimental spectra in Figure 3.5 (a) reveals that the doublet (characteristic for Na in the Si_{28} cages) diminishes rapidly as x increases, and is accompanied by the appearance of a peak at an intermediate energy, 1.085 keV from the experimental XANES spectra. Comparison with the simulations (Figure 3.5 (b)) shows that this intermediate peak is characteristic of Na in the Si_{20} cages. These observations suggest that the XANES spectral contribution of Na in the Si_{20} cages of Na_xSi_{136} increases as x increases from 1.3 to 5.5 and above. However, it is known that the x-ray near-edge absorption cross-section is sensitive to interatomic bond distance such that a shorter bond

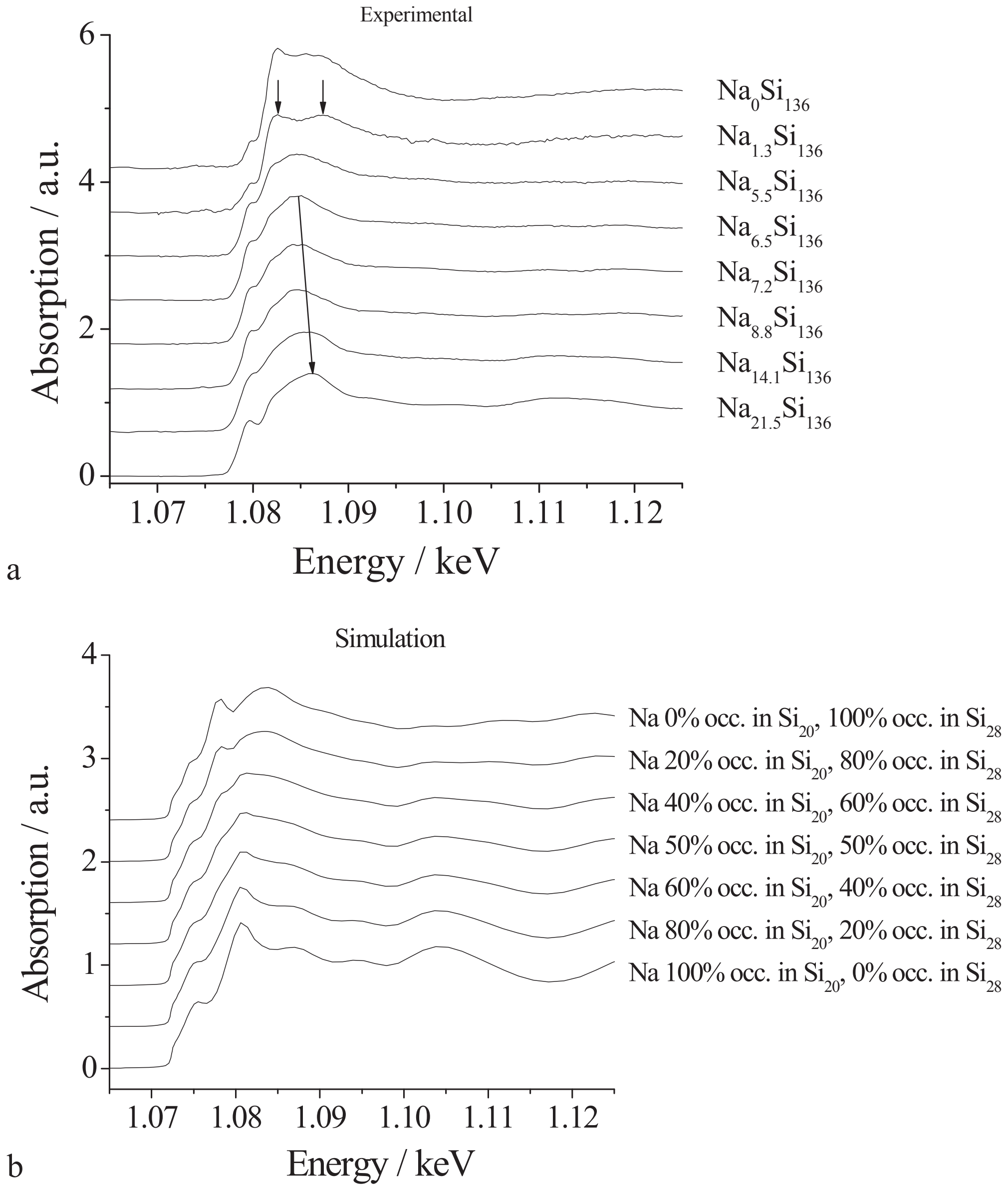

Figure 3.5 – Effect of distribution of Na in Na_xSi_{136} in the Si_{28} and Si_{20} cages. (a) Experimental XANES results and (b) simulated XANES spectra with the occupancy of Na in the larger Si_{28} and smaller Si_{20} cages varying as indicated. In (a), the upper pair of arrows indicates features associated with Na in Si_{28}. The lower arrow shows how the most intense feature shifts with increased Na loading. Reproduced from Ref. 54 with permission.

distance corresponds to a greater cross-section.[121] Unlike EXAFS, simulations of XANES spectra generate normalized spectra (*i.e.*, the absorption cross-section is not considered). Consequently, the Si_{28}/ Si_{20} cage occupancy cannot be quantitatively evaluated by comparing the results in Figures 3.5 (a) and (b). Nevertheless, based on the results of cage occupancy obtained from the EXAFS data discussed above, it is likely that a small increase in the concentration of Na in the Si_{20} cages can result in a significant change of the XANES spectra. In other words, these findings indicate that the Na K-edge XANES spectrum is more sensitive to the change of local structure of the samples than EXAFS is, and that the presence of a doublet peak in the XANES spectrum indicates that Na in the larger Si_{28} cages is responsible for a significant majority of the x-ray absorption signal.

Figure 3.5 (a) indicates that for $x > 6.5$, a shift of the most intense XANES peak to higher energy with increasing Na content is observed experimentally. This broad peak contains character from both Na in Si_{28} and Na in Si_{20}. Simulations presented in Figure 3.4 suggest that the peak position in the near-edge region migrates towards higher energies as the Na guest moves towards the center of the Si_{28} cage. When Na in the Si_{28} cage is modeled as off-center at the 32*e* crystallographic site, Rietveld refinements indicate that the magnitude of the off-center displacement decreases with increasing Na content.[115] The observed peak migration to higher energies has, therefore, been tentatively attributed to the changing Na position within the Si_{28} cages resulting from changing Na content, as per the observations from Rietveld analysis.[115]

3.1.2.3 Calculation of LDOS

Local (orbital) density of states (LDOS) calculations[109] for Na, presented in Figure 3.6, show that the absorption edge is dominated by *p*-orbital contributions as expected. These calculations also indicate that Na in the Si_{20} cage has a charge of + 0.7 e^- and Na in the Si_{28} cage has a slightly higher charge, + 0.72 e^- at high loading and ~ + 0.8 e^- at lower loadings. Such small changes in charge transfer, especially when averaged over Na in both the Si_{20} and Si_{28} cages, were too subtle under the conditions of this study to be detectable by a K-edge shift. While these values cannot be supported quantitatively by these experimental synchrotron studies, they are in agreement with the red shift observed relative to a Si wafer standard. This is further supported by earlier Compton scattering studies for the closely related type I system which have indicated a charge of

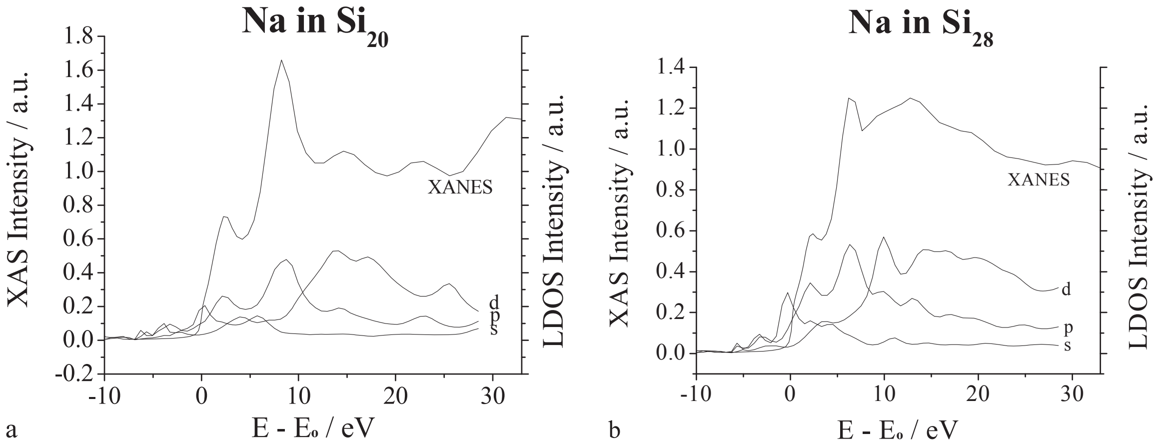

Figure 3.6 – Calculated local orbital density of states (LDOS) and simulated XANES for Na in Na_xSi_{136}, in (a) Si_{20} cages, and (b) in Si_{28} cages. The major peaks for Na in Si_{20} are due to the excitation of a core electron to the *p*-orbital, and the doublet for Na in Si_{28} appears to be due to excitation into the unoccupied *p*- and *d*-orbitals. Reproduced from Ref. 54 with permission.

+ 0.69 e^- for Na in the Si_{20} cages and + 0.78 e^- for Na in the Si_{24} cages.[122] Given the observed Si red shift, the similar nature of the two structures, and that DFT studies of both the type I and type II systems have indicated increased charge transfer with cage size,[78] it is reasonable that both structures follow similar trends.

As discussed above, it is likely that Na is displaced from the center of the Si_{28} cage. Simulations indicated that the Na position within this cage has a significant effect on the predicted charge on that Na atom (Table 3.2). The charge ranged from a minimum of 0.646 e^- at a displacement of 1 Å to a maximum of 0.865 e^- at a displacement of 0.2 Å. XRD results show that displacement off-center may decrease with increasing Na content in Na_xSi_{136},[119] and the present calculations indicate that charge transfer would correspondingly increase with increasing x.

The Na in the smaller Si_{20} cage appears to reside in the center of the cage, and its calculated charge transfer is 0.681 e^-. Therefore, when the Na is closer on average to Si atoms, either due to being in the small Si_{20} cage or due to large displacement from the center of the large Si_{28} cage, the charge transfer is less than when the average Na-Si distance is longer.

Table 3.2 – Calculated charge transfer for Na atoms in the Si_{28} cage of Na_xSi_{136}, as a function of displacement of Na from the center of the cage. Reproduced from Ref. 54 with permission.

Displacement off center / Å	Calculated charge transfer / e^-
0	0.862
0.2	0.865
0.4	0.847
0.6	0.808
0.8	0.735
1.0	0.646

3.1.3 Si K-edge EXAFS Results

Figure 3.7 shows the normalized experimental Si K-edge XANES spectra (both fluorescent yield [FLY] and total electron yield [TEY]) and EXAFS spectra (as TEY). In the XANES spectra presented in Figure 3.7 (a), an intense peak attributable to silicon oxide is observed in the TEY spectra and its intensity is significantly reduced in the FLY spectra. It has been established that TEY is more sensitive to the surface whereas FLY is more sensitive to the bulk.[123] Therefore, the XANES results indicate that the Si atoms on the surface of the samples were partially oxidized.

The edges of the Si spectra are red-shifted relative to a crystalline Si wafer, indicating that the energy of the Si conduction band minimum is lowered relative to the 1s core level and thus, a negative charge is borne by the Si framework. This is in keeping with previous studies[79] and with the present finding of positive charge on the Na. However, the resolution of the present data was not sufficient to determine if charge transfer changed with varying Na content.

In the Si K-edge EXAFS spectra shown in Figure 7 (b), there is little difference with changing Na concentration throughout the entire spectral range. This consistency throughout the range of compositions is not surprising since Si dominates the composition of all samples and therefore most of the nearest neighbours to any absorbing atom were Si. Since the silicon concentration was essentially constant, the result was that no significant change in the nearest-neighbour interactions was observed with increasing Na content. This was supported by simulation of each unique Si position as well as in the combined weighted-average simulated spectra.

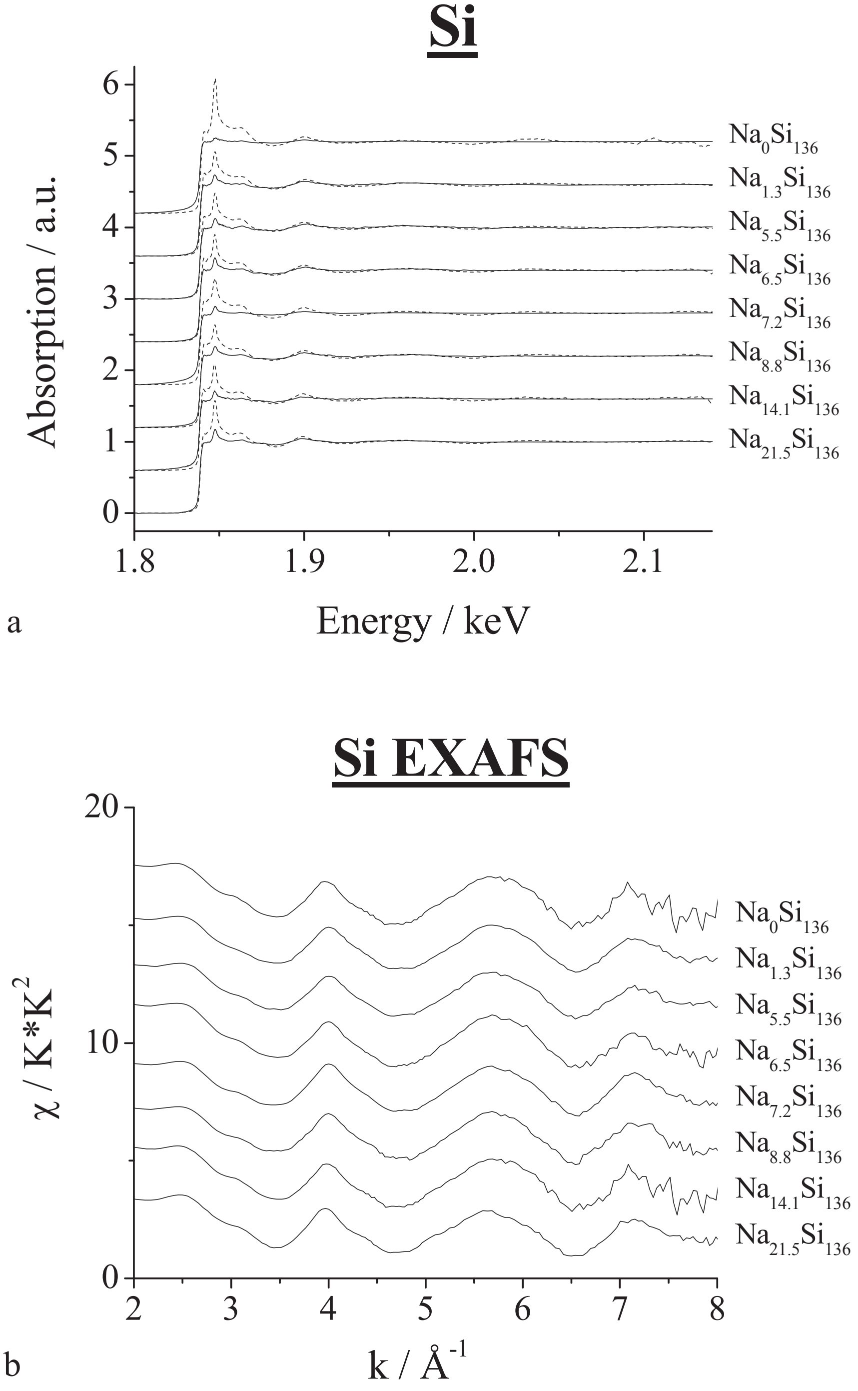

Figure 3.7 – Full Si K-edge experimental spectra for Na_xSi_{136}. (a) The XANES spectra for Na_xSi_{136}, where the dashed lines are the total electron yield (TEY) signal which is sensitive to the surface, and the solid lines are fluorescent yield (FLY), which is sensitive to the bulk. The main observable difference is the varying intensity of the oxide peak at 1.849 keV. $Na_{x\to0}Si_{136}$, prepared in 2003, and higher Na-content samples display more intense oxide peaks, as expected. (b) Si EXAFS observed for different concentration of Na in Na_xSi_{136}. Reproduced from Ref. 54 with permission.

3.1.4 Conclusions

The near-edge region of the Na K-edge x-ray absorption spectra for this series of type II sodium containing clathrates has been proven to be very sensitive to the local structure surrounding absorbing Na atoms. Relative cage occupation and off-center displacement were found to have profound effects on this region of spectra. However, due to the differences in cross-sections of the two Na environments, it has only been possible to use this information to indicate when the Si_{20} cages are nearly fully unoccupied. The EXAFS region on the other hand, by comparison to simulation, can be used to estimate the relative cage occupations when Na in the Si_{20} cages accounts for less than 30 % of the overall Na content. The XAS data indicate that Na is preferentially lost from the Si_{20} cages, consistent with Rietveld analysis. Detailed EXAFS analysis for spectra from the highest Na content samples shows an increase in both displacement off-centre of the Si_{28} cages and increased dynamic disorder within these cages with decreasing Na content. Calculated charge transfers were in qualitative agreement with observed edge shifts as well as previous studies.[122,78] The systematic investigation of such a wide range of guest occupancies makes the present results serve as a useful reference for future studies of intermetallic clathrates.

3.2 Transport Properties

The three properties used to evaluate thermoelectric performance, κ, S and σ, were measured for all compositions of the Na_xSi_{136} series of samples across the entire available temperature range. The following sections present results from those experiments, demonstrating how Na content affects each physical property. Throughout the experiments it became apparent that processing had a significant impact on measured values of physical properties and even their ability to be measured. Those aspects of sample preparation will be discussed.

3.2.1 Seebeck Coefficient, *S*

3.2.1.1 Results

Figure 3.8 presents Seebeck coefficient data for all Na filled Na_xSi_{136} clathrates except $x = 1.3$ and 0, for which reliable Seebeck coefficient data could not be obtained. The suggested[88] thickness restrictions of $l > 1$ mm provided a good guideline for obtaining high quality S data. All attempted Seebeck coefficient experiments for Na_xSi_{136} with $x = 1.3$ were performed on thin pellets (~ 0.7 mm) and it was not possible to produce a thicker pellet for this sample for Seebeck measurements (due to insufficient sample quantities). The $x = 0$ sample was too small to measure Seebeck coefficients.

The results presented in Figure 3.8 for Na_xSi_{136} with $x \geq 5.5$ all show negative Seebeck values. This shows that the majority charge carriers in these samples were electrons. Given the general tendency of Na to donate electron density and given the electron transfer results from XAS experiments (section 3.2.3) this finding was not unexpected. For all Na loadings, S nearly linearly approached zero as temperature approached 0 K. At low temperatures scatter became significant for many compositions. For samples with Na contents above those of the Mott transition,[124] where samples

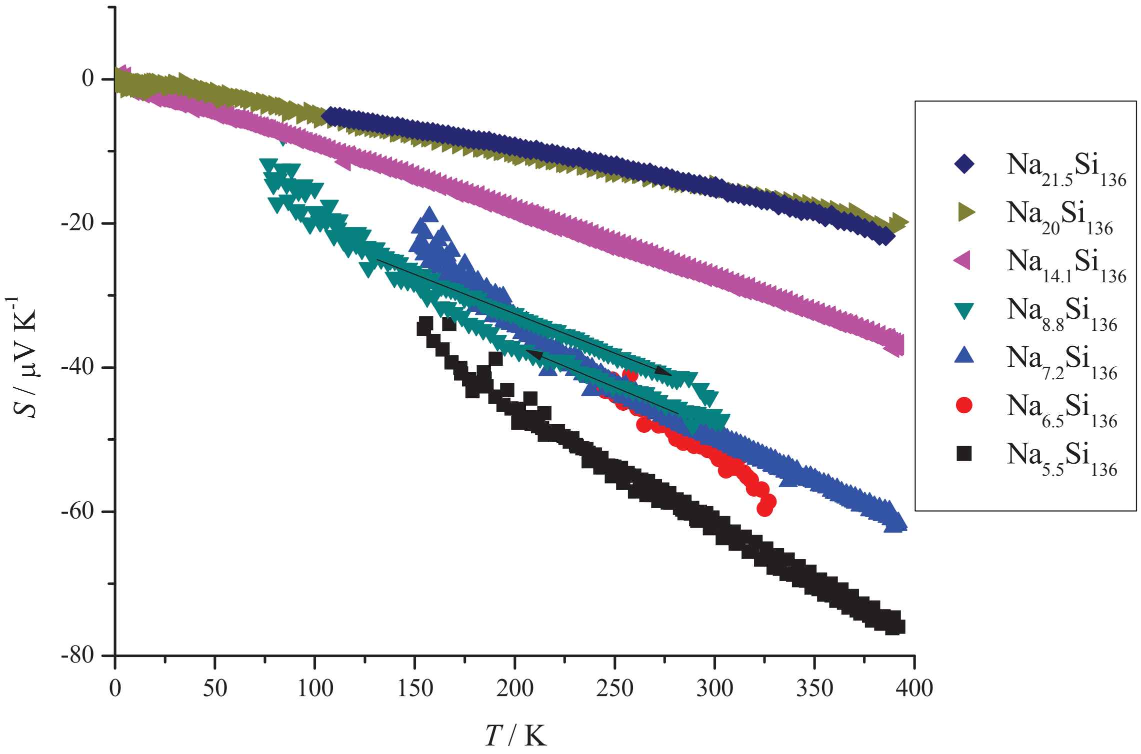

Figure 3.8 – Seebeck coefficient data for the Na_xSi_{136} series of samples. Arrows on the $x = 8.8$ data indicate heating or cooling (all samples were first cooled then heated), demonstrating apparent hysteresis ($x = 8.8$). All samples were cold-pressed powders ~ 0.7 mm thick, except for $Na_{20}Si_{136}$ which was hot-pressed. $Na_{1.3}Si_{136}$ did not exhibit measurable Seebeck voltages over the 2 K – 390 K temperature range. The $x = 0$ sample was too small for Seebeck measurements.

transition from semiconducting to metallic electrical conductivity (estimated to occur at an x value between 7 and 11)[125] the S curves are quite linear and consistent at all measureable temperatures. The same cannot be said for lower Na loadings (*i.e.* $x < 14.1$).

There is some apparent hysteresis in the $x = 8.8$ data. This is likely due to slight changes in sample contact (either internal or contact to the gold-plated copper leads).

From Figure 3.8 it is also apparent that the magnitudes of *S* values decrease with increasing Na content. This suggests that as Na is removed from the structure the thermal voltages tend from metallic to semiconductor character.

3.2.1.2 Literature Comparison

Figure 3.9 presents literature data obtained at $T = 300$ K in comparison with the present data. One factor to consider is that several different processing techniques have been used to produce the various samples. However, comparing the data for the present hot-press consolidated sample ($x = 20$) with those of the present cold-pressed sample with the most similar composition, $x = 21.5$, it is apparent that the samples of similar composition but different processing produced comparable Seebeck data.

The samples from Cros,[53] were first consolidated through cold-pressing of powders, followed by an annealing at 700 K. The extrapolated room-temperature Seebeck voltage for their $x = 11$ sample is in good agreement with the trend presented by the other data presented in Figure 3.9. However, the $x = 7$ and $x = 3$ samples from that same study[53] produced Seebeck voltages significantly outside of the trend presented here (Figure 3.9). Both of these compositions are of relatively low Na content, where *S* data can be difficult to obtain.

Aside from low *x* values, the general trends seen in Figure 3.9 are especially significant given that data were obtained from several independent laboratories using a variety of consolidation techniques. The fully occupied, $x = 24$, sample was a single-crystal,[118] $x = 22$ was spark plasma sintered,[125] $x = 20$ was hot-pressed, $x = 3$, 7 and 11

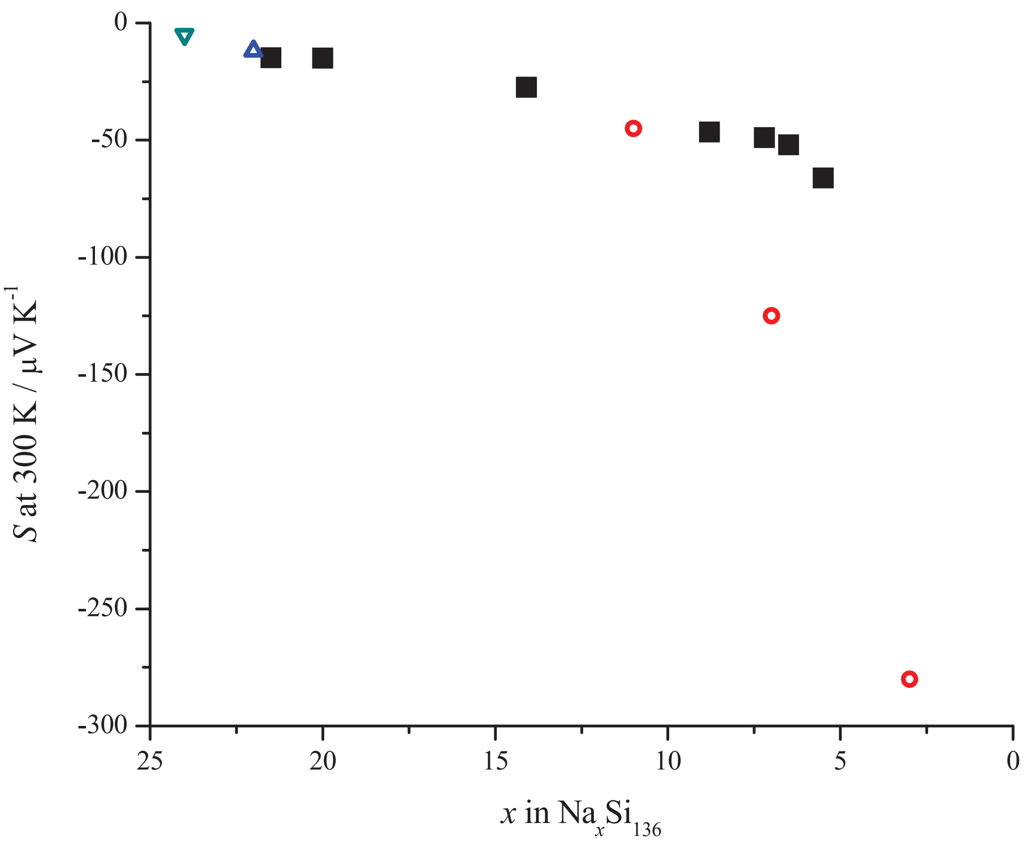

Figure 3.9 – S values at $T = 300$ K versus Na content for Na$_x$Si$_{136}$. The values for $x = 11$, 7 and 3 (○) were extrapolated from high temperature data ($T > 350$ K) published by Cros (1970),[53] the $x = 22$ data point (△) was taken from Beekman (2009)[125] from a spark plasma sintering (SPS) consolidated sample, and $x = 24$ data point (▽) from Beekman, (2010)[118] was from a single-crystal sample. All other data points (■) are from experiments performed for this thesis.

were cold-pressed and sintered,[53] and the rest were cold-pressed without sintering. Given the variety of consolidation techniques, the consistent and relatively linear trend of decreasing S values with increasing Na content (for $x = 5.5$ to 24) strongly suggests that consolidation processing has little effect on the Seebeck performance of Na filled Si clathrates.

It is apparent from these data that the Seebeck coefficient of these materials is insensitive to consolidation methods and that, in terms of energy conversion, the magnitude of the Seebeck coefficient is highest (most favourable) at high temperatures, approaching decomposition temperatures. This lack of sensitivity to consolidation technique is in contrast to the thermal conductivity case and *starkly* in contrast to electrical conductivity, discussed below.

3.2.1.3 Discussion

As discussed in section 2.1.4, early experiments conforming to PPMS sample preparation recommendations ($l > 1$ mm) produced reliable S data but unreliable κ data. This suggested that the delicate networks of inter-crystallite interactions were adequate to allow diffuse electron mobility but not phonon mobility and, thus, that S measurement is more sensitive to contact separation (sample thickness) than to internal contact.

The data in Figure 3.9 show consistent trends, independent of consolidation processing. In addition, they agree closely with Figure 1.7: the magnitude of S decreases with increasing charge carrier concentration. Therefore, the XAS experiments, which show greater charge carrier concentrations with increasing Na content, are in good agreement with the measured Seebeck voltages.

While measurements performed for this thesis did not produce data for samples with $x < 5.5$, a previous study produced S data for x values as low as 3.[53] That study, however, only reports data between 425 K and 600 K. With a thicker sample, processed to improve mechanical stability (hot-pressed, spark plasma sintering), and higher temperature measurements, it might be possible to obtain S data for an $x = 1.3$ sample. However, given that higher temperatures are required to elicit measureable Seebeck voltages as Na content decreases, it is uncertain if samples would be able to withstand the temperatures necessary for such an experiment (decomposition for these materials occurs at ~ 900 K).[102]

From the data presented in Figures 3.8 and 3.9 it can be concluded that the Seebeck coefficients of these materials are negative, indicating electrons as the majority charge carriers and that Seebeck coefficient magnitudes increase with decreasing Na content and also decrease with decreasing temperature. The change in S with x appears to be more significant at lower Na loadings, below $x = 6.5$. Confirmation of an increasing rate of change with x at lower loadings would require the examination of more low-Na content samples.

3.2.2 Electrical Conductivity, σ

3.2.2.1 Results

As with the Seebeck coefficient data, electrical conductivity measurements were attempted as a function of temperature for all available compositions. Electrical data presented their own measurement challenges. Neither the lowest Na content samples, Si_{136} and $Na_{1.3}Si_{136}$, nor the hot-pressed, $Na_{20}Si_{136}$, sample yielded electrical conductivity data using the TTO option. The Si_{136} sample was too small to attach electrical leads, and both the $x = 1.3$ and $x = 20$ samples were too resistive to produce electrical conductivity values. The results presented in Figure 3.10 show that reliable σ measurements were much more elusive than the other two ZT contributing properties, κ or S.

All of the curves presented in Figure 3.10 show increasing electrical conductivity with increasing temperature. This is typical semiconductor behaviour and was expected.

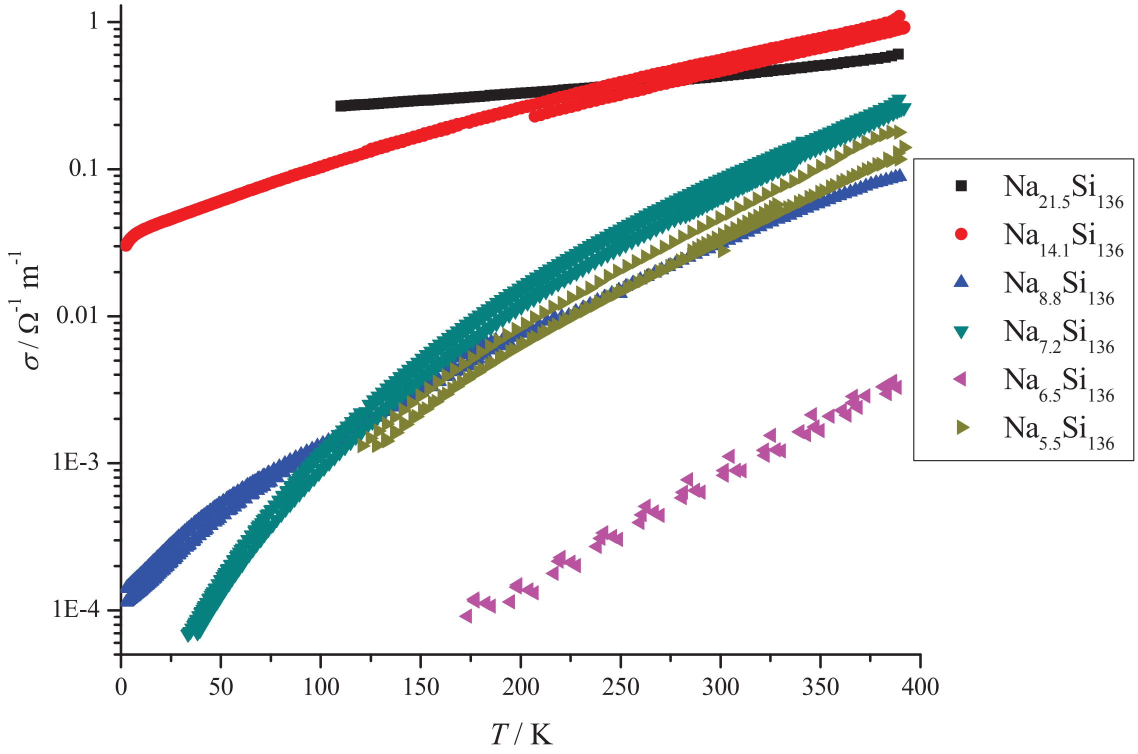

Figure 3.10 – Electrical conductivity data for Na_xSi_{136}. All data presented here were obtained from cold-pressed powder samples. These data are representative of the most reliable measurements obtained. However, due to sample oxidation, intrinsic values are expected to be greater than these which *do not present quantitative trends*.

The lower Na content samples show stronger temperature dependences and there is a general (but not always consistent) trend of increasing electrical conductivity with increasing Na content.

The hot-press consolidated sample, $Na_{20}Si_{136}$, is omitted from Figure 3.10 because it proved to be quite impossible to obtain σ data for, using the TTO. This was surprising because both of the high Na content cold-pressed samples, $Na_{14.1}Si_{136}$ and $Na_{21.5}Si_{136}$, did produce data and because the hot-pressing of this sample was expected to have resulted in improved electron mobility. It was expected that with better inter-crystallite contacts, the hot-pressed sample would demonstrate greater electrical conductivity than a cold-pressed sample of comparable composition. This did turn out to be true, however, due to difficulties in achieving high quality electrical contacts on the small cross-section hot-pressed sample, DC electrical conductivity measurements were required in order to obtain reliable data. DC measurements also were carried out for $x = 21.5$, 14.1, 8.8, 7.2 and 6.5 with results agreeing with those of Figure 3.10. Figure 3.11 presents the data from DC experiments on $Na_{20}Si_{136}$.

The data presented in Figure 3.11, DC conductivity data, show smooth curves down to low temperatures, 60 K or lower. Furthermore, the data reveal the best conditions for measurements, i.e., those with highest electrical conductivities (data set 3). Data set 1 was from the as-received sample, with an epoxy cure time of > 3 days. Data set 2 was from the same sample after an HF rinse to remove surface oxide, with an epoxy cure time of ~ 24 hours. Data set 3 was from the same sample as 2 using the same contacts after two day exposure to air, effectively allowing a longer cure time of the epoxy in contact with the oxide free sample surface. Data set 4 was from the same sample as 3 with new contacts and an epoxy cure time of ~ 24 hours. It is clear from Figure 3.11 that both surface oxidation and epoxy cure time play roles in good electrical conductivity measurements. Ideally, the sample should have minimal surface oxidation and well-cured epoxy contacts.

Despite differences in magnitude, all data sets presented in Figure 3.11 show positive temperature dependences, indicative of semiconductor rather than a metallic conduction. These data also demonstrate higher conductivities compared to data obtained

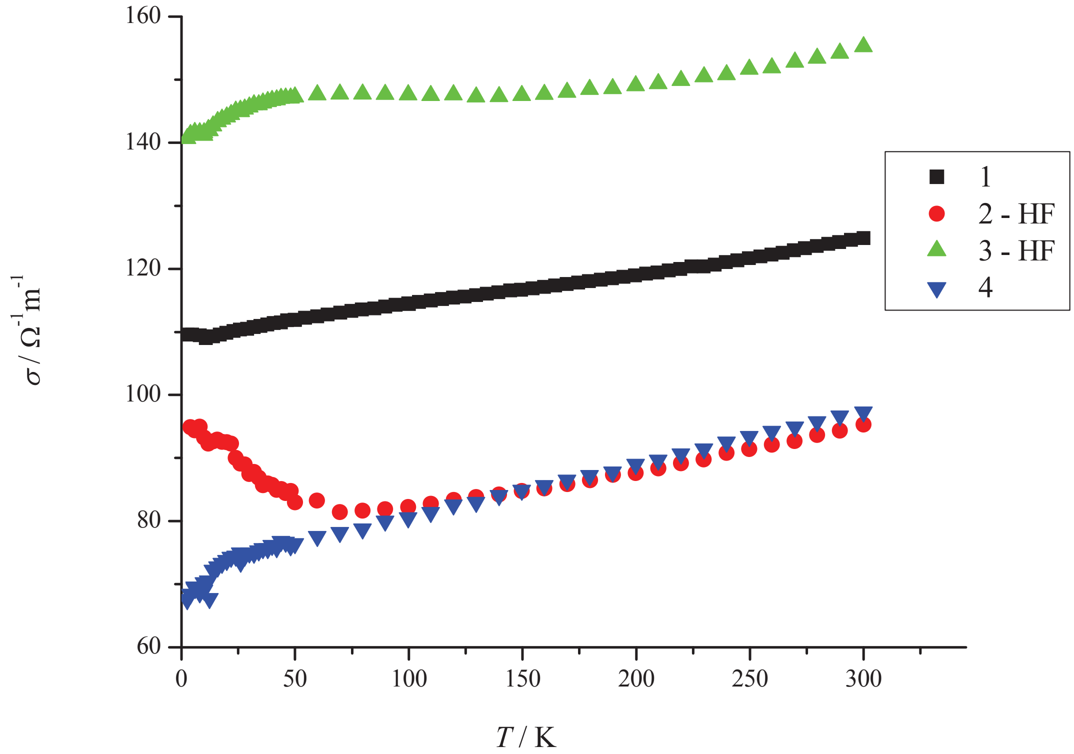

Figure 3.11 – DC conductivity data obtained for hot-pressed $Na_{20}Si_{136}$ from DC transport measurements. 1 was performed on the sample as received; 2, following an HF rinse to remove surface oxide; 3 is 2 after two days in air; 4 is after new contacts were made on sample 3. Data sets 1 and 3 had long epoxy cure times and data sets 2 and 4 had minimal epoxy cure times.

from cold-pressed samples, and are within the semiconductor range of electrical conductivities.[24] In addition, the different experiments produced consistent data and their temperature dependences are less dramatic. This is in contrast to the cold-pressed samples which showed scattered data and steeper slopes when plotted with varying temperature.

3.2.2.2 Literature Comparison

Figure 3.12 presents the present electrical conductivity data at $T = 300$ K for all measureable compositions and includes several data points from the literature.

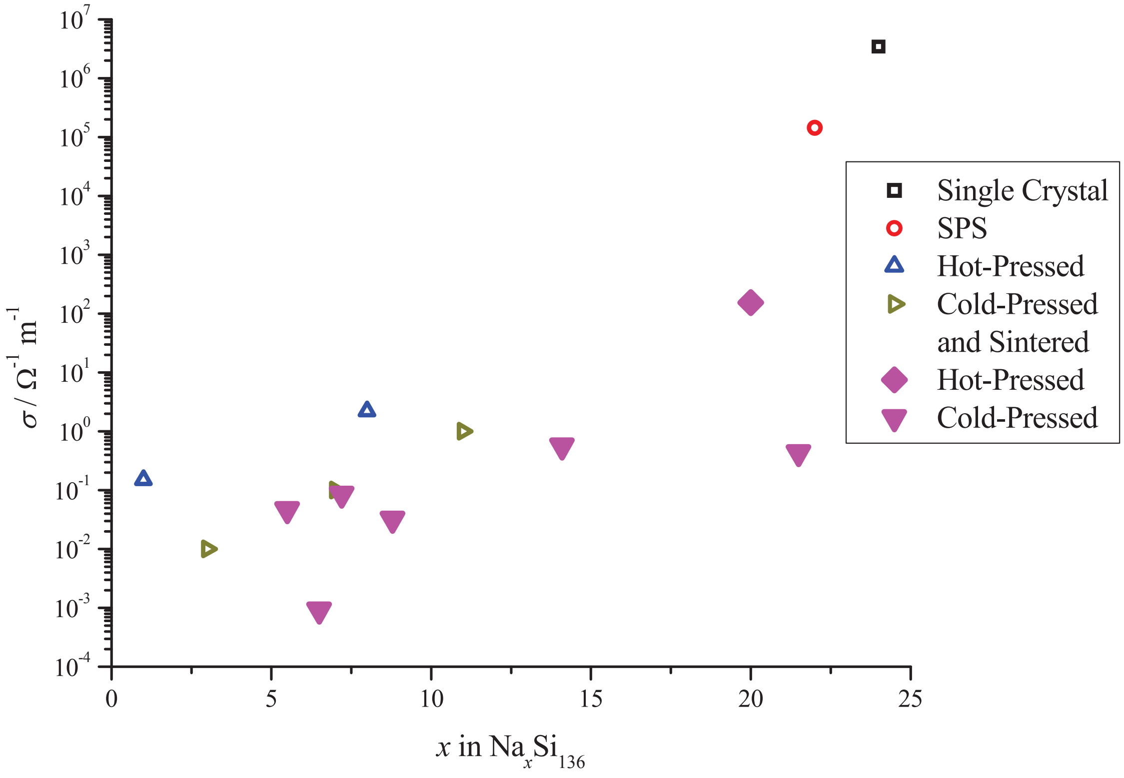

Figure 3.12 – Electrical conductivity at $T = 300$ K of the Na_xSi_{136} series of sample studied for this thesis, (◆) and (▼) represent present data, presented with literature values. The legend indicates processing methods used to prepare each sample. The (□) point is from Beekman (2010)[118] and (○) from Beekman (2009).[125] (△) data are from Beekman (2006)[126] and (▷) are from Cros (1970).[53]

From the data presented in Figure 3.12 it can be seen that the present data are close to the literature trends. It is also apparent that cold-pressed samples tended towards values lower than those of high temperature consolidation processes such as spark plasma sintering (SPS) and hot-pressing. Electrical conductivity studies would benefit significantly from the production of single-crystal samples of varying Na content. Or, more reasonably, SPS consolidation should improve experimental success.

3.2.2.3 Discussion

By comparing the data in Figure 3.11 with data from Figure 3.10, one can see the different effects of hot-press and cold-press consolidation on electrical conductivity. DC results obtained from the hot-pressed sample were several orders of magnitude higher than those of the cold-pressed samples and all well within an order of magnitude of one another. Since hot-pressing achieves better inter-granular contact (overcoming the presence of granular oxide layers), this suggests that measurement difficulties were more due to oxidation of the powder rather than the development of oxide layers on the surface of the consolidated samples. In addition, due to inadequate consolidation following initial pressing, the $x = 6.5$ sample was ground with mortar and pestle and re-pressed. This likely exposed more material for further oxidation and is likely the cause for the lower magnitude data in Figure 3.10 for $x = 6.5$. The $x = 21.5$ and $x = 5.5$ samples also required re-pressing following unsuccessful consolidation attempts, however, only mild mixing (as opposed to the heavy grinding of $x = 6.5$) was required to re-powder those samples. All other sample compositions formed pellets when first cold-pressed.

The available processing techniques have not allowed for definitive determinations of the electrical conductivities of the Na_xSi_{136} samples studied here and as such it has not been possible to fully explore this property. Consolidation processes that improve intergranular electrical transport are necessary in order to clarify this contribution. However, electrical conductivity generally increases with increasing Na content (Figure 3.12). Since Na donates electron density to the Si framework, and increasing Na content increases the concentration of conduction electrons, the observed increase in σ with increasing Na content is not surprising.

3.2.3 Thermal Conductivity, *κ*

3.2.3.1 Results

Thermal conductivity data were obtained for all compositions in the Na_xSi_{136} series of clathrate samples. These data are presented in Figure 3.13.

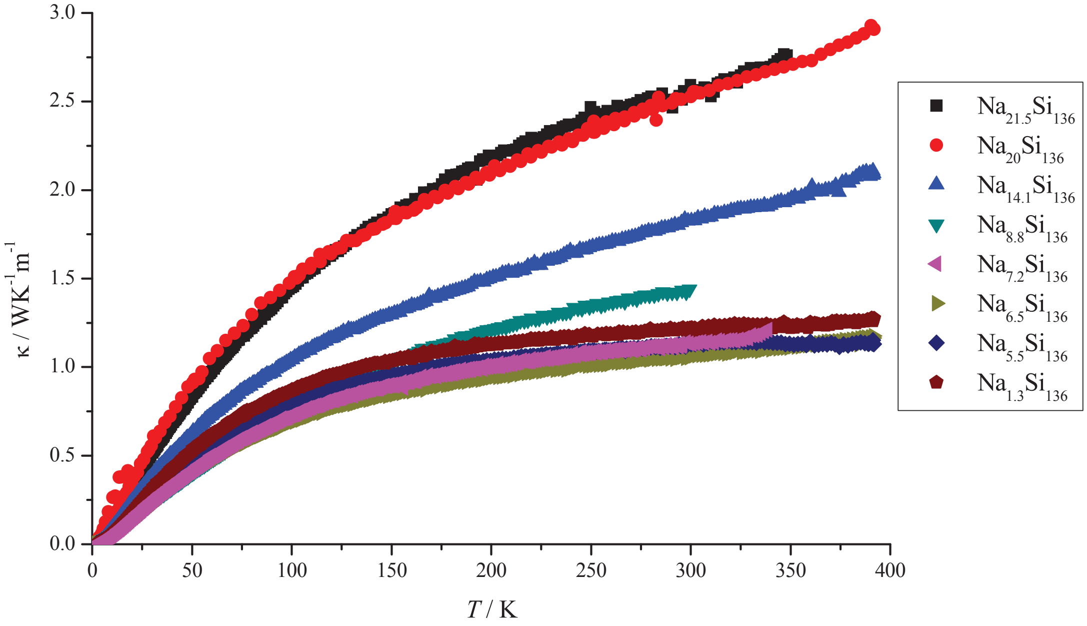

Figure 3.13 – Thermal conductivity data for all compositions of the Na_xSi_{136} series of samples. The slight increases in slope of some data sets at $T > 300$K ($x = 7.2$, 14.1 and 20) are attributed to radiative losses. All samples were cold-pressed powders, except for $Na_{20}Si_{136}$ which was hot-pressed.

By comparison of measured sample densities (from pellet geometries and masses) to PXRD data, the fractional porosity, ϕ, for each sample was calculated (Table 3.3) from

$$\phi = [\frac{(\rho_{bulk} - \rho_{eff})}{\rho_{bulk}}], \tag{3.2}$$

where ρ_{eff} is the measured density, and ρ_{bulk} is the density from PXRD. Figure 3.13, presents a comparison plot of the data as measured and provides a good basis for preliminary comparisons. However, more meaningful conclusions can be drawn once density considerations have been accounted for. Klemens[127] has shown that the ratio of

Table 3.3 – Bulk density, ρ_{bulk}, effective density, ρ_{eff}, and fractional porosity ϕ, for each Na_xSi_{136} sample.

x	Thickness / cm ± 0.002 cm	Cross-section / cm	ρ_{bulk} / g cm^{-1}	ρ_{eff} / g cm^{-1}	ϕ
1.3	0.07	0.181 ± 0.002	2.04 ± 0.003	1.48 ± 0.09	0.28 ± 0.04
5.5	0.0696	0.181 ± 0.002	2.09 ± 0.003	1.52 ± 0.09	0.27 ± 0.04
6.5	0.071	0.181 ± 0.002	2.10 ± 0.003	1.50 ± 0.09	0.29 ± 0.04
7.2	0.06	0.181 ± 0.002	2.10 ± 0.003	1.69 ± 0.1	0.19 ± 0.05
8.8	0.068	0.181 ± 0.002	2.12 ± 0.003	1.63 ± 0.1	0.23 ± 0.05
14.1	0.0753781	0.181 ± 0.002	2.18 ± 0.003	1.49 ± 0.08	0.32 ± 0.04
20	0.184	.0255 ± 0.003	2.24 ± 0.003	1.58 ± 0.08	0.29 ± 0.05
21.5	0.076	0.181 ± 0.002	2.25 ± 0.003	1.57 ± 0.09	0.30 ± 0.04

the thermal conductivity of a porous sample, κ_{porous}, to that of the fully dense sample, κ_{dense}, is related to fractional porosity, □, through

$$\frac{\kappa_{porous}}{\kappa_{dense}} = 1 - \frac{4}{3}\phi. \tag{3.3}$$

Figure 3.14 presents the density-corrected thermal conductivity data for all compositions studied here as well as literature data for the empty clathrate, Si_{136}.[73]

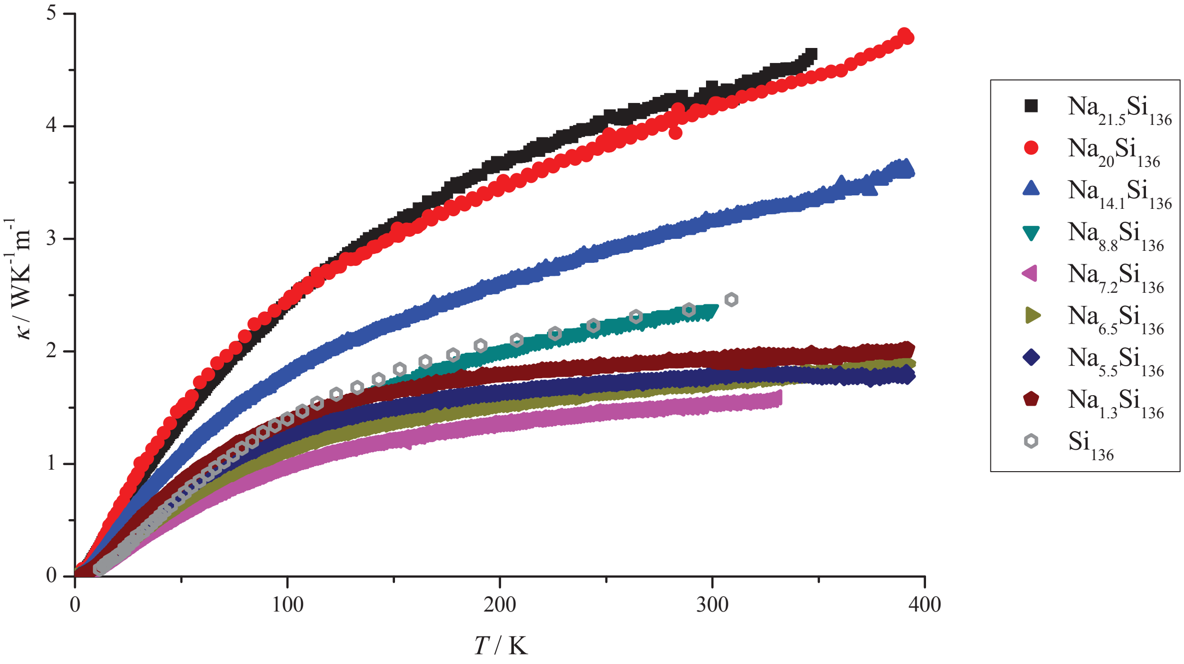

Figure 3.14 – Porosity corrected thermal conductivity data for all compositions of the Na_xSi_{136} series of samples. Porosity corrected Si_{136} data are from Ref. 73.

3.2.3.2 Literature Comparison

The observed increase in thermal conductivity with temperature presented in Figures 3.13 and 3.14 is in agreement with reported data for other Na filled Si clathrates: polycrystalline type II samples of Na_xSi_{136} where $x = 0$,[73] $x = 1$ and $x = 8$,[126] a spark plasma sintered sample where $x = 22$,[125] a single-crystal sample where $x = 24$,[118] and the polycrystalline filled type I system, Na_8Si_{46}.[68]

The magnitude of the present results agree with some earlier studies, but not all. Na_8Si_{136} data,[126] prepared by hot-pressing, indicate a room-temperature thermal conductivity of ~ 1 W m^{-1} K^{-1}.[126] This is in good agreement with the present data for samples of similar Na content, $x = 7.2$ and $x = 8.8$. However, data[126] for hot-pressed Na_1Si_{136} indicate a room-temperature thermal conductivity of approximately 3 W m^{-1} K^{-1}, considerably higher than the results for the present $x = 1.3$ sample (Figure 3.14). When corrected for porosity, the thermal conductivity of the SPS consolidated $Na_{22}Si_{136}$ sample approaches a maximum value of 7.11 W m^{-1} K^{-1} at $T = 300$ K. [125] This is significantly higher than the present data for the $x = 21.5$ sample.

Single-crystal samples of both the fully occupied type I clathrate, Na_8Si_{46}, and the fully occupied type II clathrate, $Na_{24}Si_{136}$, show thermal conductivities with crystal-like temperature dependence and room-temperature values of ~ 25 W m^{-1} K^{-1}. [128,118] A polycrystalline sample of the filled type I clathrate has shown glass-like temperature dependence and a room-temperature thermal conductivity of 6 W m^{-1} K^{-1}.[68] Given the magnitudes of room-temperature thermal conductivities of the present Na_xSi_{136} samples, it is expected that a polycrystalline $Na_{24}Si_{136}$ sample will show a room-temperature thermal conductivity ~ 6 W m^{-1} K^{-1}. This suggests that sample form (single-crystal versus polycrystalline) has a more significant affect on thermal conductivity than Na content.

Despite the few discrepancies mentioned here between data obtained from samples measured for this thesis and literature data, the two are generally in good agreement with one another. While it may be possible to evaluate evolving trends with varying Na content through data of varying sources, those obtained in this study have the benefit of being prepared using the same procedures and equipment as well as all being measured using the same apparatus and experimental parameters. Because of these experimental consistencies, direct comparisons can be made between different samples of varying Na content and observed trends can be presented with greater confidence.

3.2.3.3 Preliminary κ Discussion

From Figures 3.13 and 3.14 it can be seen that thermal conductivity increases with increasing temperature throughout the entire temperature range for all Na contents studied. Despite the crystalline nature of the samples, this behaviour is more similar to glassy materials (whereas crystalline samples tend to rise to maxima as vibrational modes are activated then decrease in thermal conductivity due to phonon-phonon interactions at higher temperatures), as has been found for other clathrates.[67,68]

By comparing the as-measured data in Figure 3.13 to the density-corrected data in Figure 3.14, one can see that the relative thermal conductivities of the samples are similar in both plots. This was expected, as all powdered samples were processed by similar methods. From Table 3.3 it can be seen that the hot-pressed $Na_{20}Si_{136}$ sample had a density on the order of 71% of its theoretical density. This is squarely in the middle of the densities determined for the cold-pressed samples and thus any significant deviation of the sample's physical properties in comparison to cold-pressed samples cannot simply be attributed to density. Although relative thermal conductivities are maintained in both plots, porosity considerations have resulted in increases in thermal conductivity values when compared to the original data. To illustrate how thermal conductivity evolves with changing sodium content, Figure 3.15 presents the 300 K data as a function of sodium content for the Na_xSi_{136} series.

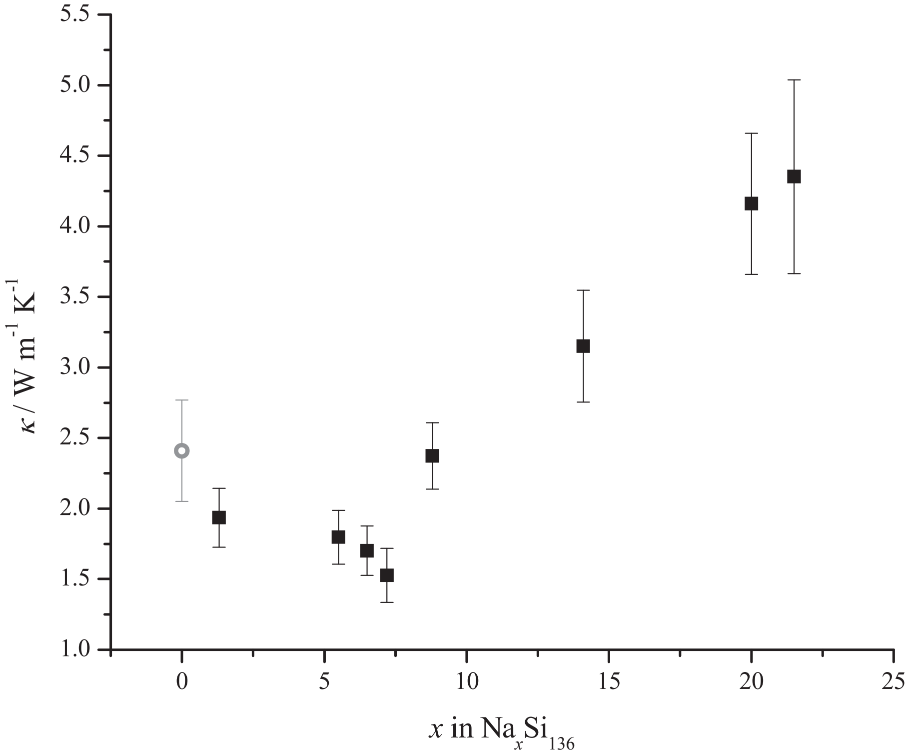

Figure 3.15 – Thermal conductivity values for Na_xSi_{136} samples at T = 300 K plotted against Na content. Error bars (10 % to 16 %) indicate error in porosity propagated through the typical 5 % uncertainty associated with measurements on glassy materials using a PPMS.[91] The Si_{136} point (◎) indicates 15 % uncertainty since this point was extracted from a published plot.[73]

Figure 3.15 demonstrates slightly decreasing thermal conductivity with increasing Na content from $x = 0$ to $x = 7.2$. This trend seems to support the proposed rattler route to thermal conductivity reduction.[21] However, a closer look at lattice dynamics is required to confirm this. At higher Na concentrations, $x \geq 8.8$, an inversion of this trend was observed: thermal conductivity increased with increasing Na content. Given the increased charge carrier density that accompanies the increase in Na content the origin of this increase is a significant question. Heat capacity data have been obtained and analysed in order to determine the electronic and phononic contributions to the observed increase in thermal conductivity, as explained further below.

From Figure 3.15, a minimum thermal conductivity at 300 K occurs in the vicinity of $x \sim 7$. At low x, the Na is predominantly in the large (Si_{28}) cages.[77] As x increases above approximately 8, the small (Si_{20}) cages are also occupied by Na.[77] The role of Na dynamics in controlling thermal conductivity will be explored more thoroughly in upcoming sections, after the heat capacity results are discussed.

3.3 Heat Capacity, C_p

3.3.1 Results

Reproducible heat capacity data for all members of the Na_xSi_{136} series of Na filled Si_{136} clathrate samples have been obtained. Figure 3.16 presents data for all compositions studied. In the interest of maximizing accuracy and verifying reproducibility, a minimum of two samples of different masses for each composition were investigated, except for the elemental clathrand, Si_{136}, since only a single sample was available. While it has been shown that heat capacity uncertainty as low as 2 % is achievable,[96] the data collected have allowed for accurate heat capacities for most compositions at 300 K and all compositions below 50 K. Variations between experiments on the same composition were as low as 1.05 % and as high as 4.36 % at 300 K. Resolving the heat capacity differences between different samples was challenging in the compositional range $x \sim 7$ since Na contents were very similar in this region. $Na_{6.5}Si_{136}$ has 99.6 % of the molar mass of $Na_{7.2}Si_{136}$ ($x = 6.5$ and 7.2 have molar masses of 3969 g/mol and 3985 g/mol respectively and differ only in their Na content).

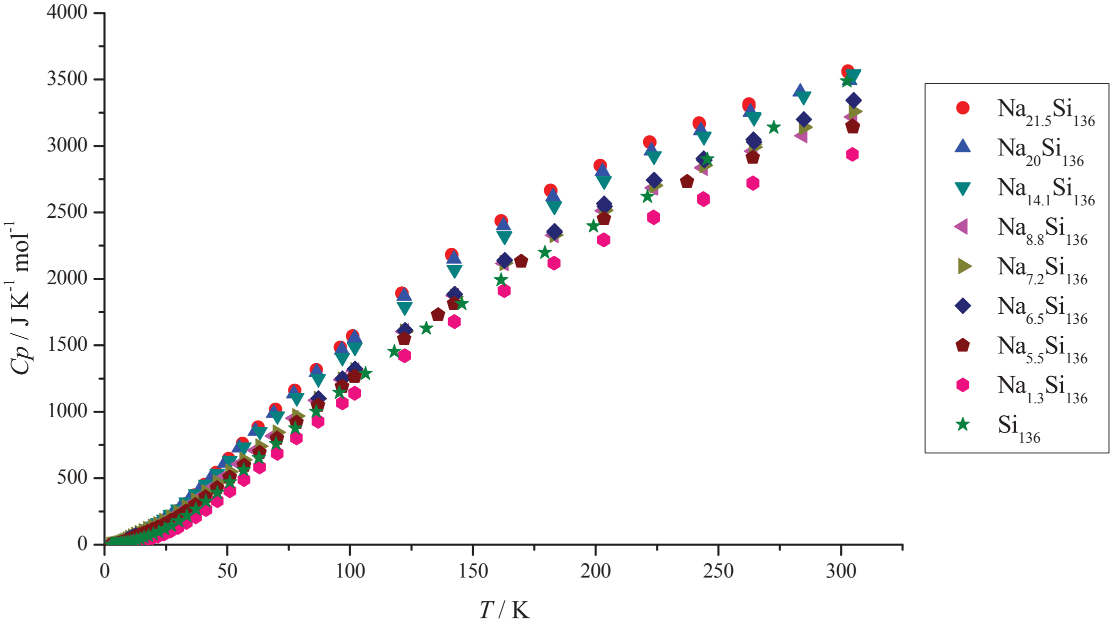

Figure 3.16 – Heat capacity data for the Na_xSi_{136} series of samples over the entire temperature range studied.

3.3.2 Literature Comparison

Earlier attempts to measure the heat capacity of Si_{136} suffered from inconsistency: different measurements on the same sample did not produce the same results.[73,129] The difficulty was likely a result of the small sample size (~ 3 mg). Data presented in this thesis are the result of several repeat measurements that showed good agreement with one another (within 2 %). The present results are within the range presented by previous measurements[73,129,130] and, due to the high degree of reproducibility, have been agreed upon by Tritt and Nolas (see Figure 3.17) as being the most definitive data to date. In achieving this level of consistency it was found that it was necessary to meticulously protect the sample from thermal grease contamination between measurements. Figure 3.17 shows the reproducible data obtained for this study in comparison to the inconsistent results that preceded them. The experimental principles developed for the small Si_{136} sample were used to successfully achieve reproducible results for the other compositions of the Na_xSi_{136} sample series.

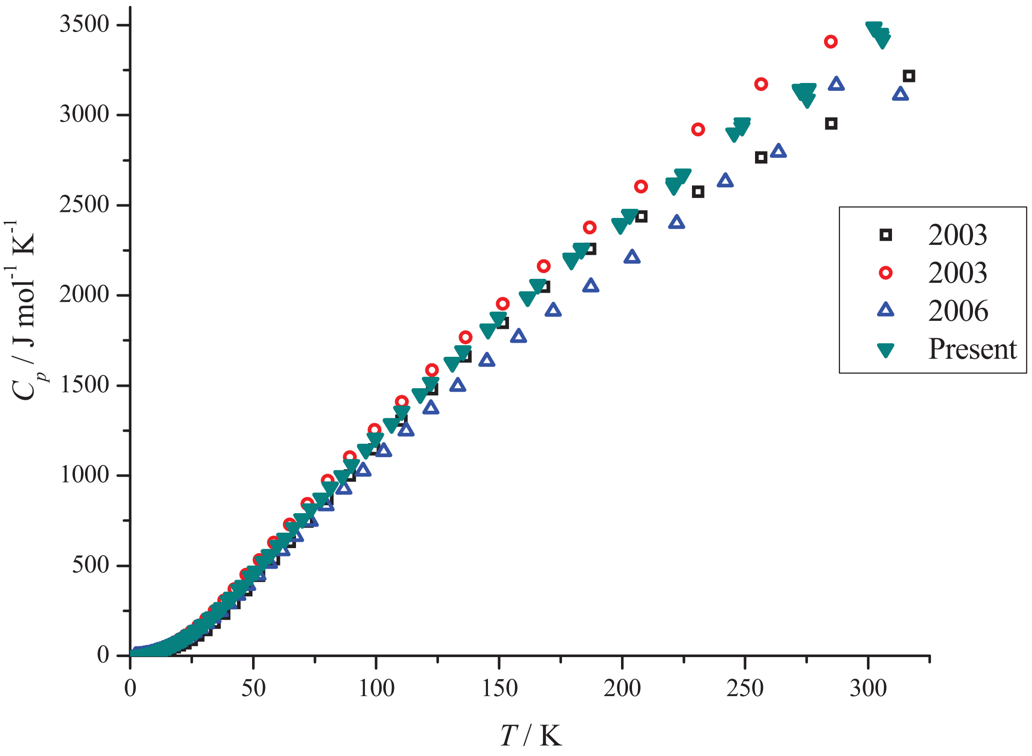

Figure 3.17 – Several heat capacity data seta obtained for the same Si$_{136}$ sample as measured by three different research groups. The legend indicates when measurements were taken, 2003 data (□[129] and ○[73]) were obtained by Nolas, 2006 data (△) by Tritt[130] and present data (▼) are those measured for the present study.

In addition to Si$_{136}$, heat capacity data for Na$_{24}$Si$_{136}$ have been published.[118] Those data are shown in Figure 3.18 along with the rest of the Na$_x$Si$_{136}$ series of samples, for comparison.

From Figure 3.18 it can be seen that the heat capacity of Na$_{24}$Si$_{136}$ shows a similar temperature dependence to the other Na$_x$Si$_{136}$ samples but is lower at high temperature than those of the $x = 21.5$, 20, 14.1, 6.5 and Si$_{136}$ samples. These differences and their structural and thermal transport implications are discussed in detail, presently.

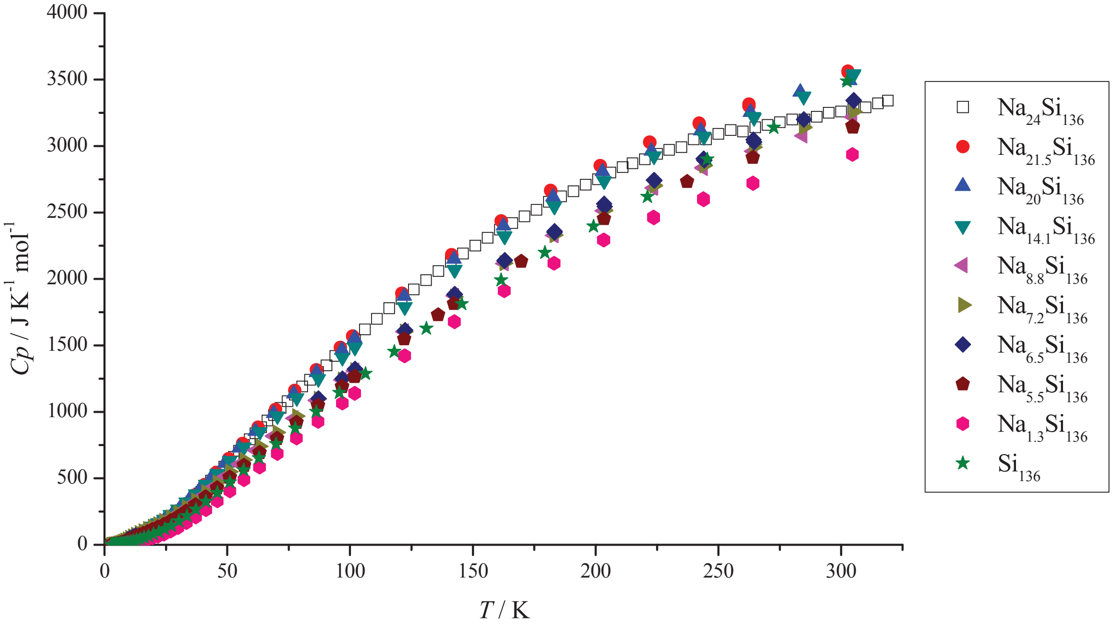

Figure 3.18 – Heat capacity data for the entire Na_xSi_{136} series of samples as well as $Na_{24}Si_{136}$ data (□) from Ref. 118 and Ref. 131.

3.3.3 Discussion

All compositions of Na_xSi_{136} investigated showed smooth, phase transition free, heat capacity curves. Figure 3.19 illustrates how heat capacities of the Na_xSi_{136} samples change with changing Na content at various temperatures.

From Figure 3.19 it can be seen that except for the full, $x = 24$, and empty, $x = 0$, Na_xSi_{136} samples there is a slight but apparent increase in heat overall capacity with increasing Na content. The outlying samples, $x = 0$ and 24, more strongly diverge from

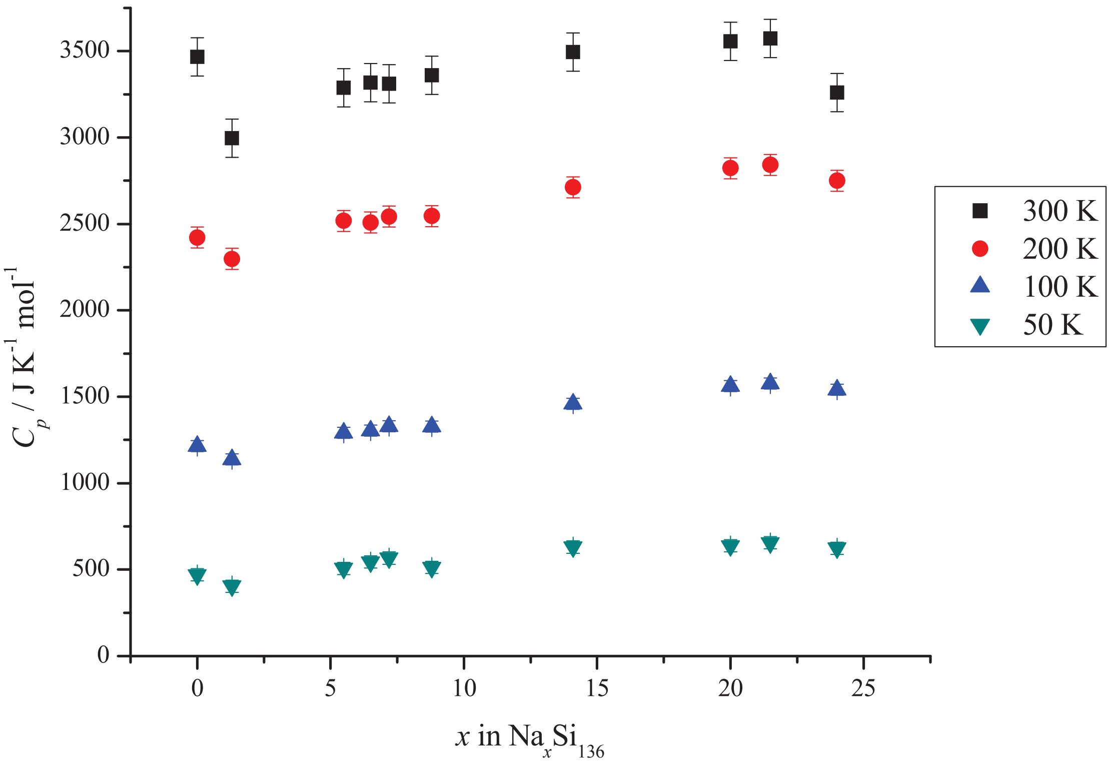

Figure 3.19 – Heat capacity data for Na_xSi_{136} samples as a function of Na content at several temperatures. Data for $Na_{24}Si_{136}$ were taken from Ref. 131.

this trend at higher temperatures. Figure 3.20 presents the data of the compositional extremes to better illustrate how they differ from one another.

From Figure 3.20 it can be seen that the heat capacity of $Na_{24}Si_{136}$ has stronger temperature dependence than Si_{136} below ~ 150 K. It is also apparent from Figure 3.20 that the heat capacity of Si_{136} exceeds that of $Na_{24}Si_{136}$ for T > 275 K. Trends in heat capacity with changing Na content will be further discussed in terms of lattice dynamics later in this chapter.

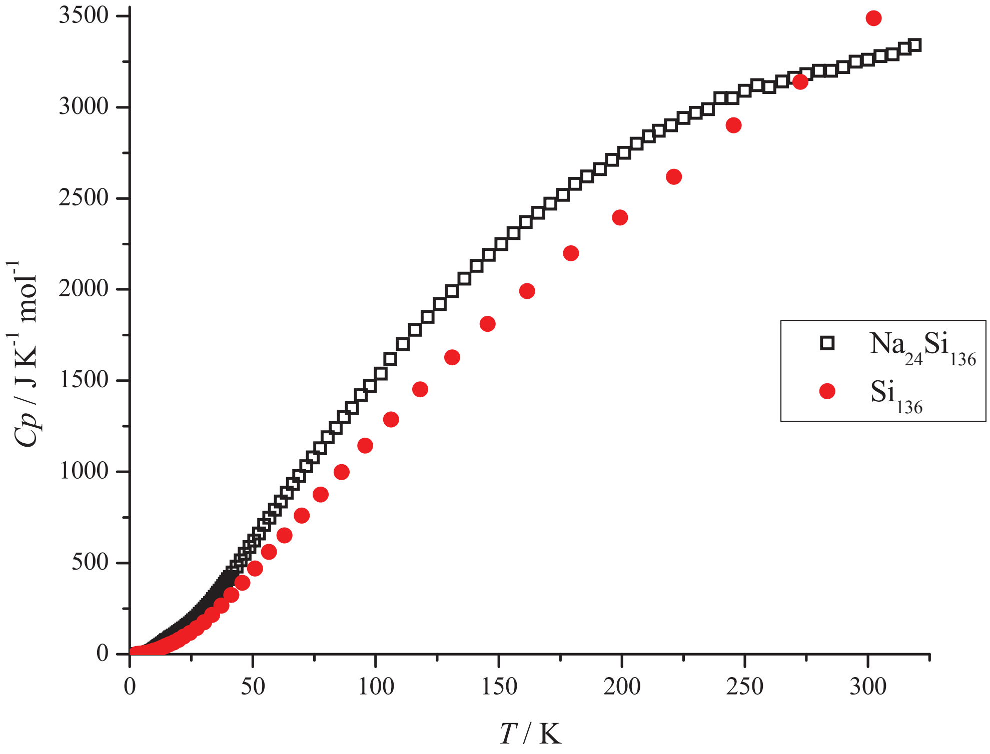

Figure 3.20 – Heat capacity data over the entire temperature range studied for the compositional extremities, $x = 0$ and $x = 24$,[131] of the Na_xSi_{136} series of samples.

3.3.3.1 Electronic Contribution

By examining very low temperature, $T < 4$ K, heat capacity data it is possible to delineate the electronic and phononic contributions to heat capacity via[24]

$$C_p = \gamma T + pT^3, \tag{3.4}$$

where C_p is the measured molar heat capacity, γ is the electronic contribution to heat capacity, also known as the Sommerfeld constant and pT^3 is the phononic contribution.

Equation (3.4) means that by plotting C_p/T versus T^2, low temperature heat capacity data can be fit linearly to

$$\frac{C_p}{T} = \gamma + pT^2, \tag{3.5}$$

with the slope, p, giving the phononic contribution and the y-intercept the electronic contribution, γ. Figure 3.21 shows a graphic of this low temperature treatment of heat capacity data for the Na_xSi_{136} series.

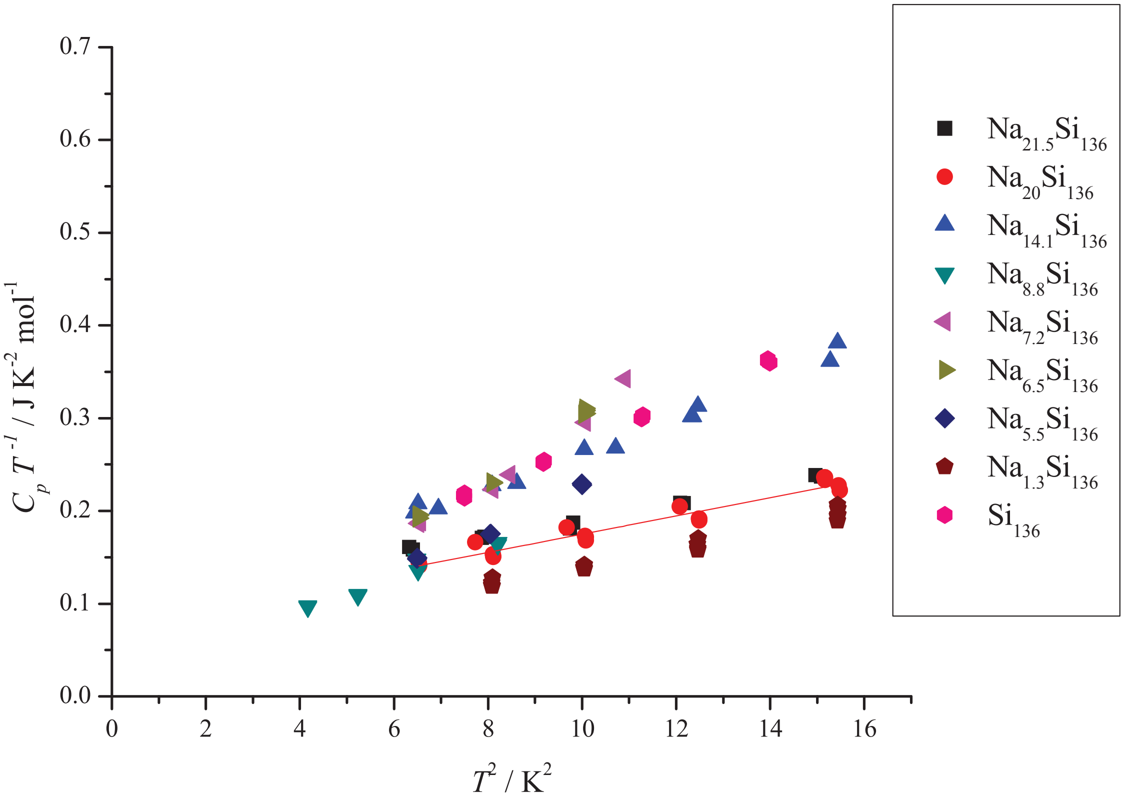

Figure 3.21 – Low temperature heat capacity data used to determine the electronic contributions to the heat capacities of Na_xSi_{136} samples. Heat capacities have been divided by temperature and plotted against T^2.

By fitting the data in Figure 3.21 to lines, the electronic contributions for the various Na contents have been determined. Those contributions, as determined from Figure 3.21, are presented in Table 3.4. From Table 3.4 it can be seen that electronic contributions, γ, are non-zero at high Na loadings ($x = 14.1, 20, 21.5$). The highest Na content sample, $x = 21.5$, shows an electronic contribution of ~ 2/3 that published for the full clathrate, $x = 24$, for which $\gamma = 0.163(4)$ J K^{-2} mol^{-1}.[118] Larger electronic contributions to heat capacity can be understood in terms of increased charge transfer from Na to the Si framework, as determined from XAS studies.[54] The greater number of electrons transferred to the lattice at elevated Na contents means greater electronic contribution to heat capacity. The $x = 8.8$ sample shows some electronic heat capacity as well, although the value, 0.022 J K^{-2} mol^{-1}, is low compared to the higher Na content samples and the error associated with it is greater than 30 %. The fits for the intermediate

Table 3.4 – Values of calculated electronic contribution to heat capacity with varying Na content in type II Si clathrates as determined from low temperature ($T < 4$ K) data shown in Figure 3.21. Note that γ values for the $x = 7.2$, 6.5 and 5.5 samples are negative, small and have significant uncertainty.

x	Slope / J K^{-4} mol^{-1}	γ / J K^{-2} mol^{-1}
21.5	0.0091 ± 0.0003	0.100 ± .004
20	0.0098 ±0.0005	0.077 ± .006
14.1	0.019 ± 0.0007	0.072 ± .008
8.8	0.018 ± .001	0.022 ± .008
7.2	0.034 ± .003	-0.042 ± .02
6.5	0.032 ± .001	-0.022 ± .01
5.5	0.023 ± .001	-0.004 ± .01
1.3	0.010 ± 0.0005	0.037 ± .006
0	0.023 ± 0.0002	0.045 ± .002

Na content samples, $x = 7.2$, 6.5 and 5.5 show small and negative (unphysical) values with significant uncertainty for γ. This indicates a small systematic difference between these samples and higher Na content samples and has been taken as an indication that the heat capacity is solely due to the lattice. Electronic contributions are insignificant for $x =$ 7.2, 6.5 and 5.5.

The lowest Na content samples, $x = 1.3$ and 0, also show non-zero y-intercepts in Figure 3.21. However, these cannot imply electronic contributions to the heat capacity for these samples since $x = 1$ and $x = 0$ samples have shown electrical conductivities of 0.15 Ω^{-1} m^{-1} (hot-pressed)[126] and 4×10^{-4} Ω^{-1} m^{-1} (cold-pressed),[114] respectively. This means that the $x = 1.3$ sample is a poorly conducting semiconductor and the $x = 0$ sample is an insulator.[24] Based on these electrical conductivity values, neither sample should exhibit significant electronic heat capacities. It is possible that the non-zero apparent γ values for the $x = 1.3$ and $x = 0$ samples are a result of the low temperature heat capacity anomalies. By plotting heat capacity over T^3 versus T^2 one can detect low frequency modes, as at low temperature ($T < \theta_D/50$), lattice-only contribution gives $C_p = pT^3 + fT^5$.[132] Figure 3.22 shows how each of the Na_xSi_{136} samples deviates from the expected low temperature behaviour.

From Figure 3.22 it can be seen that the two lowest Na content samples, $x = 1.3$ and 0, both show increasing $C_p\, T^{-3}$ with decreasing temperature at low temperature. This is different from the $x = 5.5$, 6.5, 7.2 and 8.8 samples which show positive slope in this temperature range. The data presented in Figure 3.22 indicate that further low temperature heat capacity measurements would be required to gain a full understanding of the low energy modes, especially for the $x = 1.3$ and $x =0$ samples.

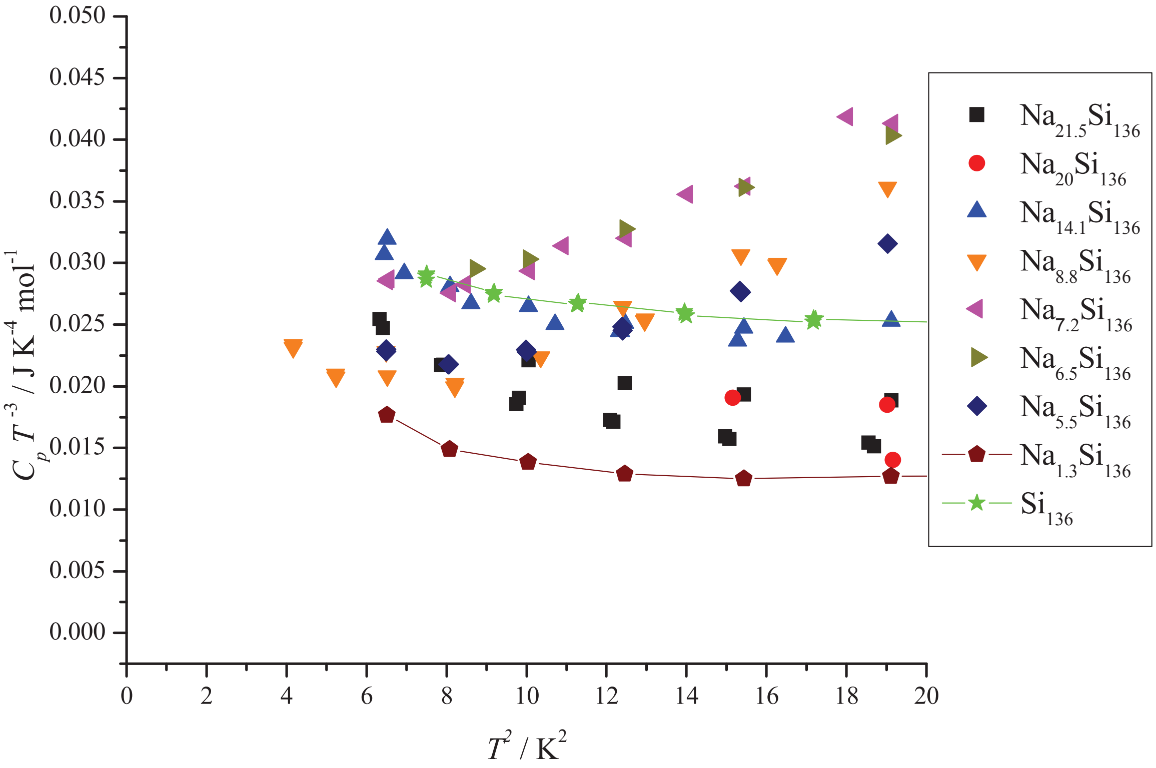

Figure 3.22 – Low temperature heat capacity, over T^3 versus T^2. This data representation shows anomalous lattice contributions to the heat capacity for $x = 0$ and $x = 1.3$ (solid lines as guide to eye), compared to the rest of the Na_xSi_{136} series, which generally show the more usual positive slope.

Assuming no electron-phonon coupling, the electronic contribution to the heat capacity also allows an estimate of the electronic density of states at the Fermi level, $D(E_F)$ from[133]

$$\gamma = \frac{\pi^2 k_B^2}{3} D(E_F). \tag{3.6}$$

This gives a density of states of 2.55 x 10^{25} eV^{-1} mol^{-1}, or 42 eV^{-1} per formula unit, for $Na_{21.5}Si_{136}$. Using the same procedure, one obtains a value of 68 eV^{-1} per formula unit from the published data for $Na_{24}Si_{136}$, the fully occupied single-crystal sample. This indicates a significant difference in electronic density of states at the Fermi energy for two samples with similarly high Na contents. Table 3.5 presents values for the density of states at the Fermi energy for all samples with $x \geq 8.8$. Table 3.5 shows the increased sensitivity to Na content of the electronic density of states at the Fermi energy of Na_xSi_{136} samples at higher Na loadings. At higher loadings small changes in Na content have more substantial effects than do large changes in Na content at lower Na loadings.

Table 3.5 – Density of states at the Fermi energy as determined from electronic heat capacity contributions. $x = 24$ values were calculated using the γ data presented in Ref. 118.

x	$D(E_F)$ / eV^{-1} mol^{-1}	$D(E_F)$ / eV^{-1} (formula unit)$^{-1}$
24	4.09×10^{25}	67.9
21.5	2.55×10^{25}	42.4
20	1.97×10^{25}	32.7
14.1	1.84×10^{25}	30.5
8.8	5.62×10^{24}	9.33

3.3.3.2 Lattice Contributions

3.3.3.2.1 Low Temperature Heat Capacity

Typically, lattice heat capacity, C_p^{latt}, can be described as[132]

$$C_p^{latt} = pT^3 + fT^5 \tag{3.7}$$

at very low temperatures ($T < \theta_D/50$). This means that if one plots heat capacity over T^3 versus T^2 at very low temperatures, a straight line should result. Deviations from linearity are indicative of additional low energy contributions to heat capacity. Figure 3.23 presents low temperature heat capacity data treated in this manner for the Na_xSi_{136} series of samples.

Figure 3.23 clearly shows peaks at $T^2 \sim 50$ K. These peaks indicate low energy vibrational mode contributions to the measured heat capacities of the Na filled Si clathrate samples, typical for frequencies of guests rattling in cages.[140] There is a distinct decrease in peak magnitude with increasing Na content. This indicates a reduction in the rattler mode contribution to the lattice heat capacity with increased Na loading. The decrease in peak magnitude follows the trend of decreasing displacement of Na off-centre of the Si_{28} cages with increasing Na content (from PXRD studies)[115] and suggests a decrease in the amplitude of rattler vibrations due to Na in the Si_{28} cages with increasing Na content.

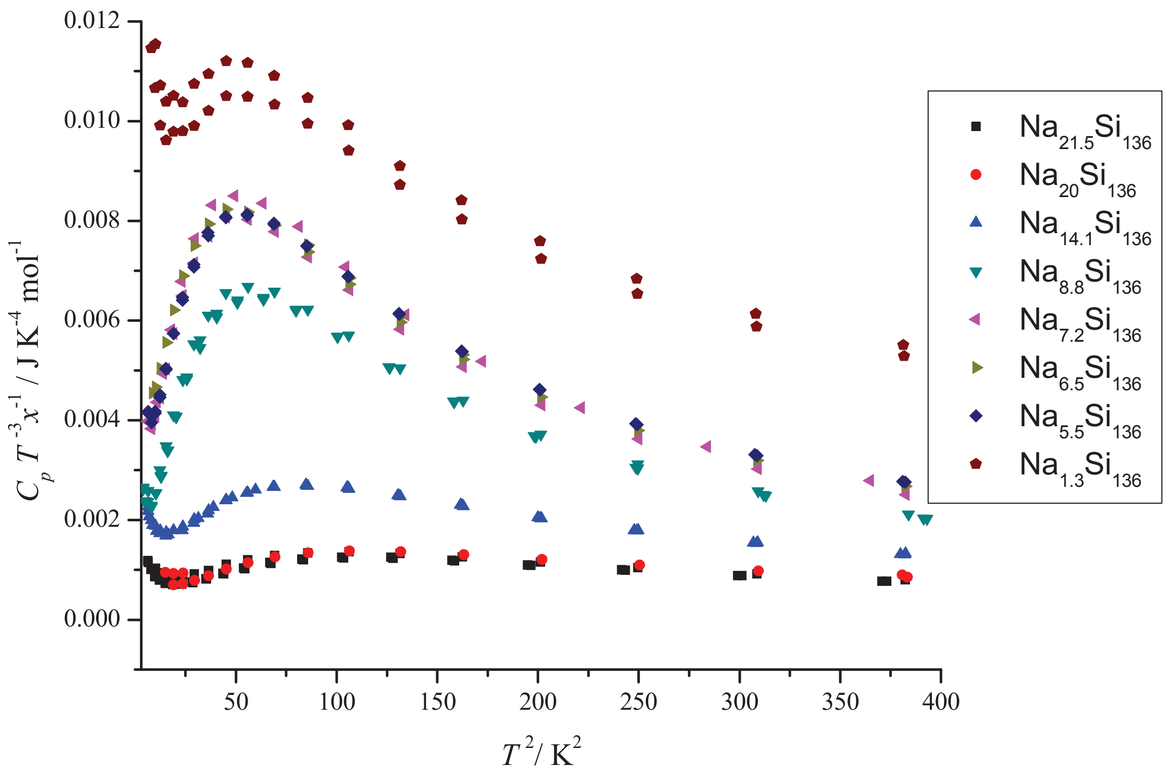

Figure 3.23 – Low temperature $C_p\,T^{-3}\,x^{-1}$ data demonstrating the presence of low energy vibrational modes associated with Na guest atoms. These data present rattler atom contributions to sample heat capacities on a per Na content bases.

While peak magnitude is indicative of rattling amplitude, peak position reflects an average rattler mode frequency. Higher temperature peak positions indicate higher energy modes. Figure 3.24 illustrates how the low temperature peak position in Figure 3.23 evolves with changing Na content.

From Figure 3.24 it can be seen that the low temperature peak shifts to lower temperatures upon going from $x = 1.3$ to $x = 5.5$, remains approximately constant at intermediate loadings ($x = 5.5, 6.5, 7.2$) and then shifts towards higher temperatures with

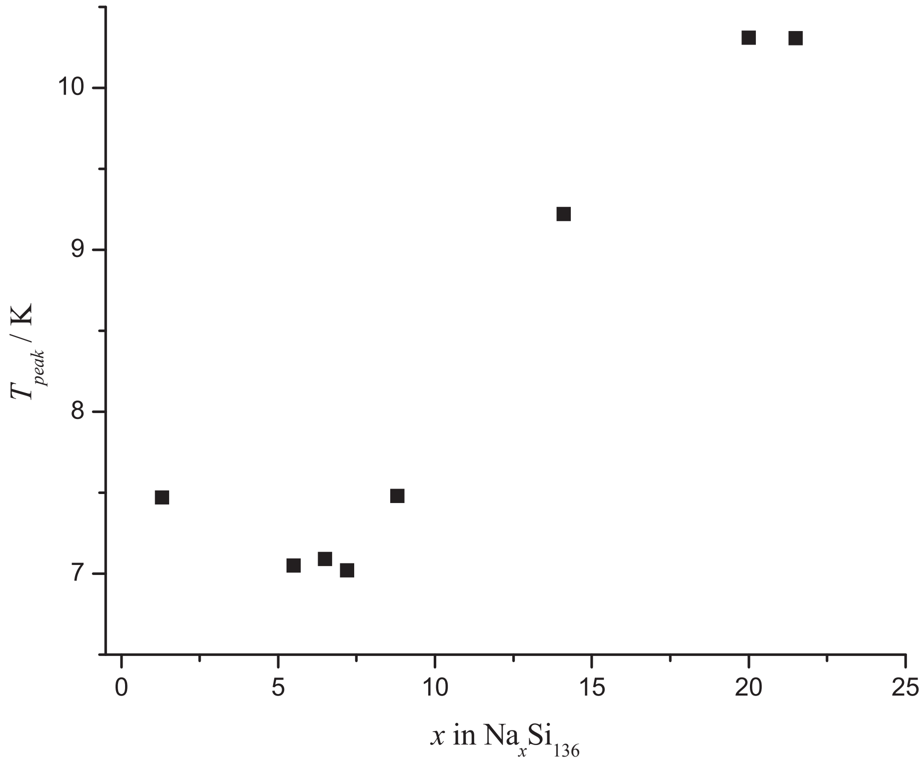

Figure 3.24 – Plot of the position of the peak of the low temperature heat capacity feature, as presented in Figure 3.23, associated with Na in Si_{28} cages for the Na_xSi_{136} series of samples.

increasing Na content beyond $x = 7.2$. This can be understood in terms of the strength of the attractive interaction between Na in Si_{28} cages and the Si framework. Initial inclusion of Na ($x = 1.3$) resulted in a strong interaction between Na in Si_{28} cages and the Si framework. Much of the available electron density from the Si framework was able to interact with the small amount of Na, resulting in few, but strong, attractive Na-Si interactions. As more Na is added ($x = 5.5$ to 7.2) the same electron density available from the Si framework is spread out over a greater number of attractive interactions. The interactions were, therefore, weaker. Finally, as Na is added to Si_{20} cages ($x \geq 8.8$), there is increased attraction between Na in Si_{28} and the framework as a result of the increased electron density provided by Na in the Si_{20} cages.

3.3.3.2.2 Debye Heat Capacity

As discussed earlier, a complete description of heat capacity requires the consideration of both lattice and electronic contributions (Equation (3.4)). By combining that description of heat capacity with the Debye model for heat capacity, Equation (1.27), one can account for the total, measured heat capacity at very low temperatures by

$$C_v = \frac{12}{5}\pi^4 N k_B \left(\frac{T}{\theta_D^{eff}}\right)^3 + \gamma T \ , \tag{3.8}$$

where θ_D^{eff} is the effective (lattice-average) Debye temperature and N is the number of atoms being considered. This means that the slope of the low temperature $C_p T^{-1}$ versus T^2 data, p, can be described as

$$p = \frac{12}{5}\pi^4 N k_B \left(\frac{1}{\theta_D^{eff}}\right)^3, \tag{3.9}$$

and used to yield an effective Debye temperature. The effective Debye temperature, θ_D^{eff}, which assumes the lattice to act only as in Debye's model, can be used to approximate the "stiffness" of the lattice. Table 3.6 presents the calculated effective

Table 3.6 – Effective Debye temperatures for each Na_xSi_{136} sample, as calculated from low temperature heat capacity data.

x	θ_D^{eff} / K
21.5	323
20	314
14.1	249
8.8	250
7.2	202
6.5	205
5.5	229
1.3	299
0	226

Debye temperatures for the Na filled Si clathrate series of materials. To better illustrate how θ_D^{eff} changes with Na content these data have been plotted as a function of Na content in Figure 3.25.

Figure 3.25 shows that with initial addition of Na there is a lattice stiffening (increase in θ_D^{eff}), followed by a relaxation. This correlates with PXRD data which show an initial expansion, then levelling off of the unit cell with increasing Na content (Figure 2.13). At some value near $x = 7$, a minimum effective Debye temperature marks the beginning of a trend of increasing θ_D^{eff} with increasing x. This increase in effective Debye temperature is also in agreement with increasing lattice parameters (Figure 2.13). Increasing θ_D^{eff} begins in the compositional range ($\sim x = 8$) where additional Na is added to the Si_{20} cages[66,76,77] rather than the Si_{28} cages and shows that the filling of the Si_{20} cages of the type II clathrate structure results in a lattice stiffening.

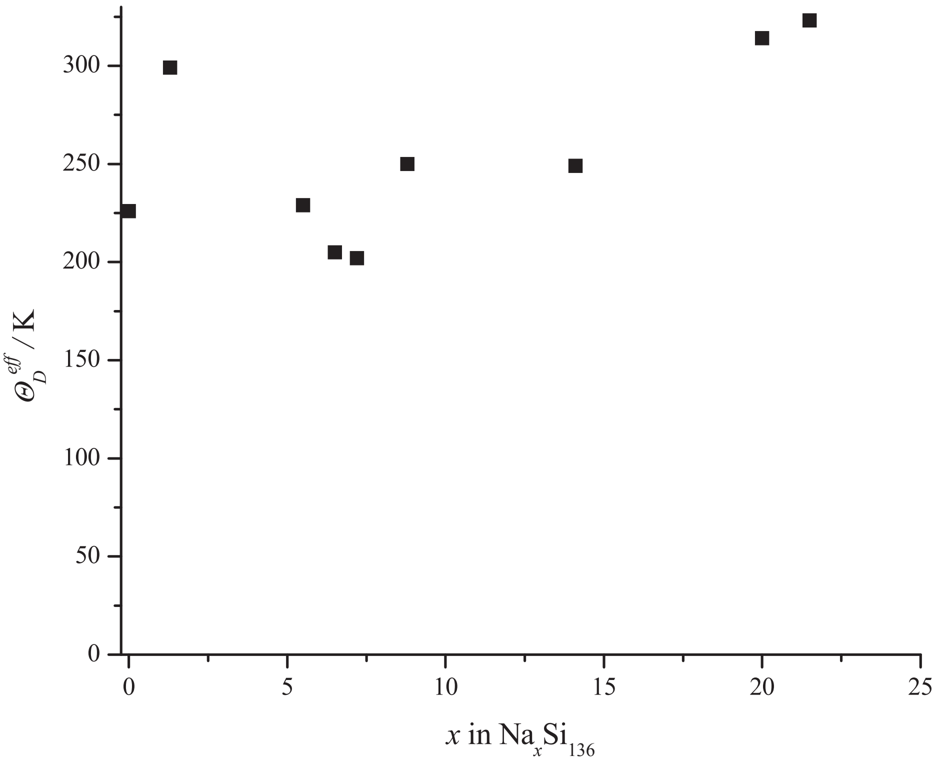

Figure 3.25 – Effective Debye temperatures as calculated from low temperature heat capacity data for Na_xSi_{136} samples.

3.3.3.2.3 Additive Model

Given that heat capacity is typically an additive property, one would expect to see increased molar heat capacity with increasing Na content (it should take more energy to increase the temperature of a mole of a material with a greater number of atoms per mole). Because of this additivity, the heat capacities of complex materials can be approximated by combining the heat capacities of their constituent atoms or molecules in appropriate ratios. This simple heat capacity model has been shown to be accurate for a variety of materials such as sodalite,[134] and thermoelectric materials such as Na_8Si_{46},

$Sr_8Zn_8Ge_{38}$, $Sr_8Ga_{16}Ge_{136}$ and $Ba_8Ga_{16}Si_{30}$.[135] In addition, the model is useful in that it provides a good basis for comparison of materials of interest: structural and dynamical comparison to constituent materials can help direct and strengthen interpretations of experimental results. Literature values of heat capacity for Na[138] and Si[136] were multiplied by Na_xSi_{136} stoichiometries and added together to model the heat capacities of Na_xSi_{136} samples. Figures 3.26 to 2.35 show experimental heat capacity data alongside heat capacities as predicted by the additivity model.

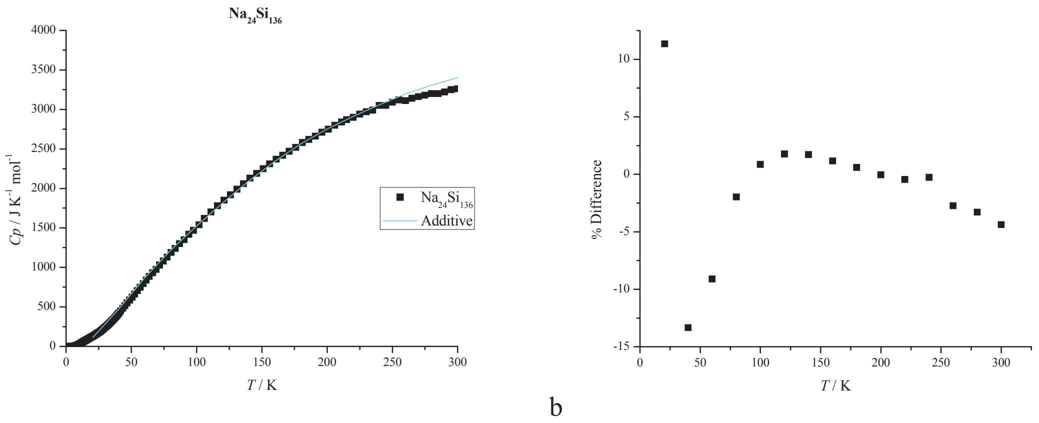

<u>Figure 3.26</u> – (a) Experimental heat capacity data[131] for $Na_{24}Si_{136}$ plotted alongside its additive model (C_p ($Na_{24}Si_{136}$) = 24 [C_p (Na)] + 136 [C_p (Si)]) representation. (b) demonstrates agreement between experiment and the additivity model as % difference, relative to experimental heat capacity values.

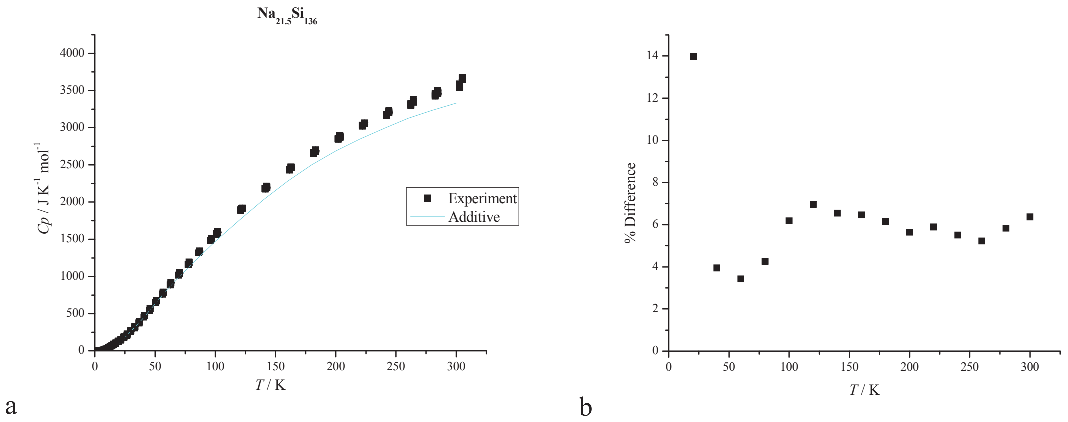

<u>Figure 3.27</u> – (a) Experimental heat capacity data for $Na_{21.5}Si_{136}$ plotted alongside its additive model (C_p ($Na_{21.5}Si_{136}$) = 21.5 [C_p (Na)] + 136 [C_p (Si)]) representation. (b) demonstrates agreement between experiment and the additivity model as % difference, relative to experimental heat capacity values.

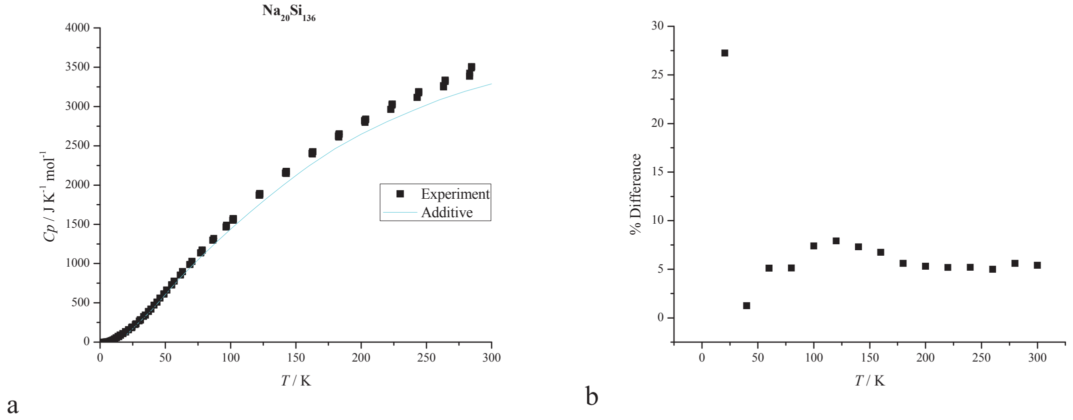

<u>Figure 3.28</u> – (a) Experimental heat capacity data for $Na_{20}Si_{136}$ plotted alongside its additive model (C_p ($Na_{20}Si_{136}$) = 20 [C_p (Na)] + 136 [C_p (Si)]) representation. (b) demonstrates agreement between experiment and the additivity model as % difference, relative to experimental heat capacity values.

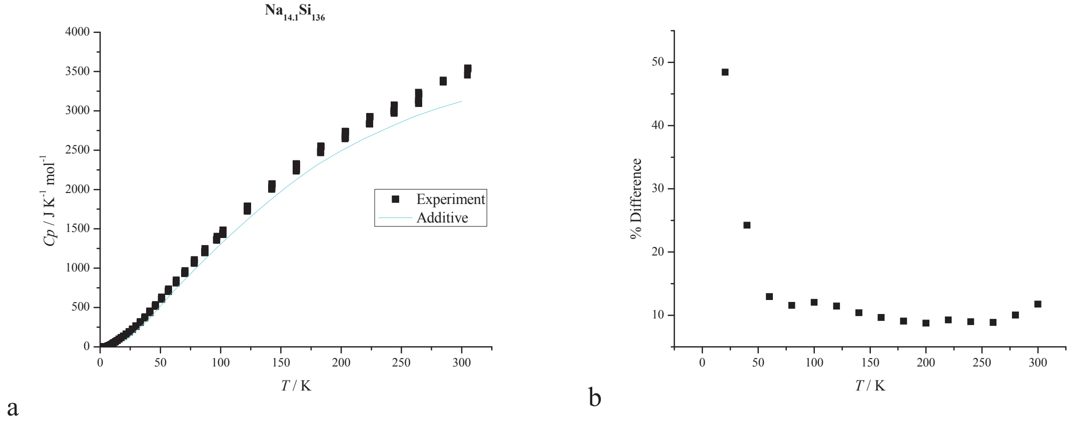

Figure 3.29 – (a) Experimental heat capacity data for $Na_{14.1}Si_{136}$ plotted alongside its additive model ($C_p(Na_{14.1}Si_{136}) = 14.1\ [C_p(Na)] + 136\ [C_p(Si)]$) representation. (b) demonstrates agreement between experiment and the additivity model as % difference, relative to experimental heat capacity values.

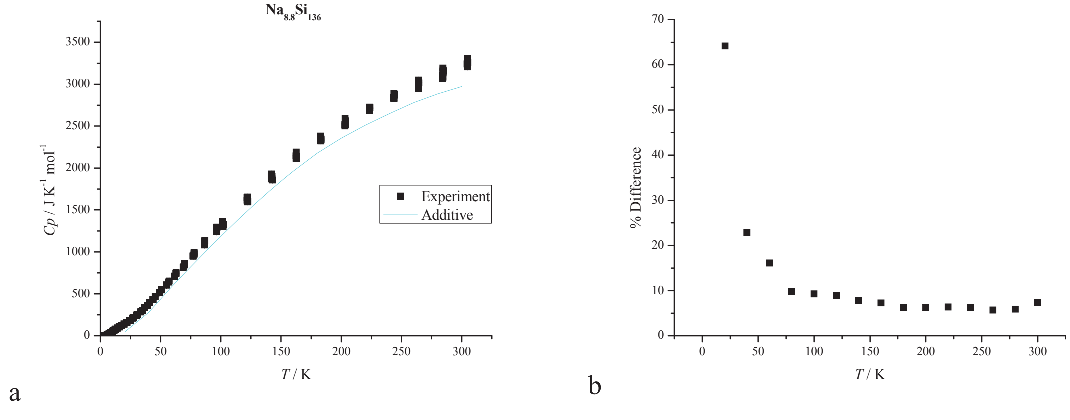

Figure 3.30 – (a) Experimental heat capacity data for $Na_{8.8}Si_{136}$ plotted alongside its additive model ($C_p(Na_{8.8}Si_{136}) = 8.8\ [C_p(Na)] + 136\ [C_p(Si)]$) representation. (b) demonstrates agreement between experiment and the additivity model as % difference, relative to experimental heat capacity values.

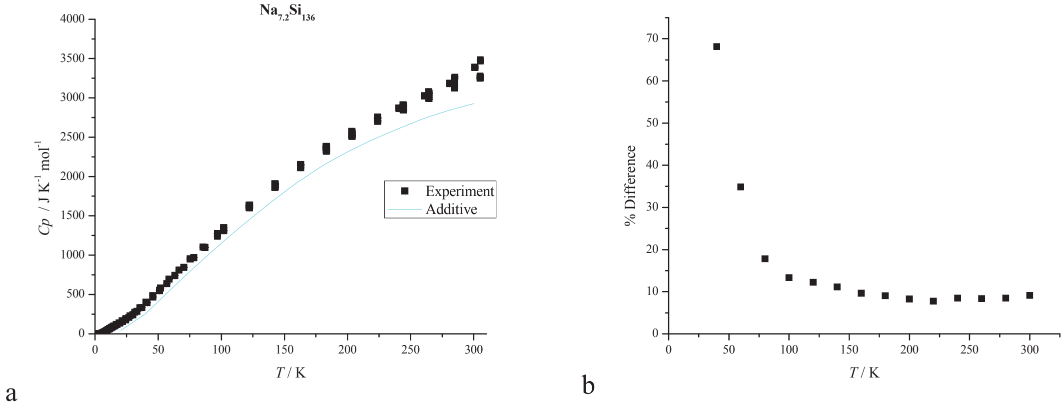

Figure 3.31 – (a) Experimental heat capacity data for $Na_{7.2}Si_{136}$ plotted alongside its additive model ($C_p\,(Na_{7.2}Si_{136}) = 7.2\,[C_p\,(Na)] + 136\,[C_p\,(Si)]$) representation. (b) demonstrates agreement between experiment and the additivity model as % difference, relative to experimental heat capacity values.

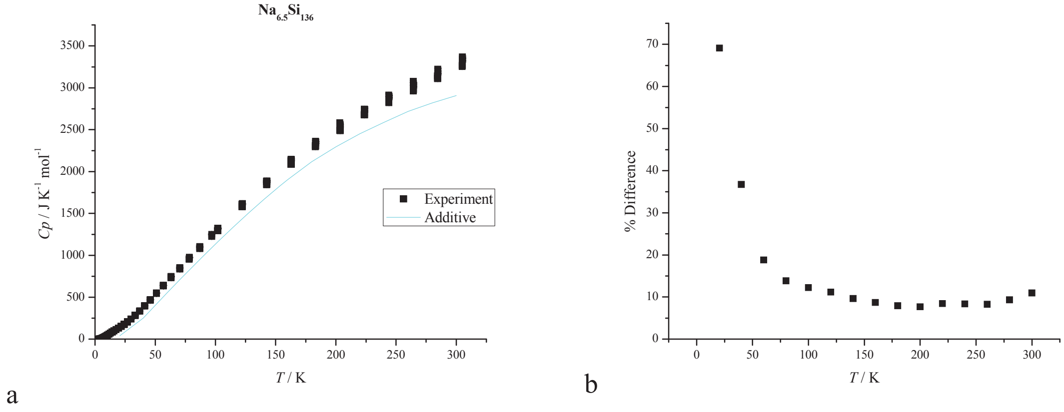

Figure 3.32 – (a) Experimental heat capacity data for $Na_{6.5}Si_{136}$ plotted alongside its additive model ($C_p\,(Na_{6.5}Si_{136}) = 6.5\,[C_p\,(Na)] + 136\,[C_p\,(Si)]$) representation. (b) demonstrates agreement between experiment and the additivity model as % difference, relative to experimental heat capacity values.

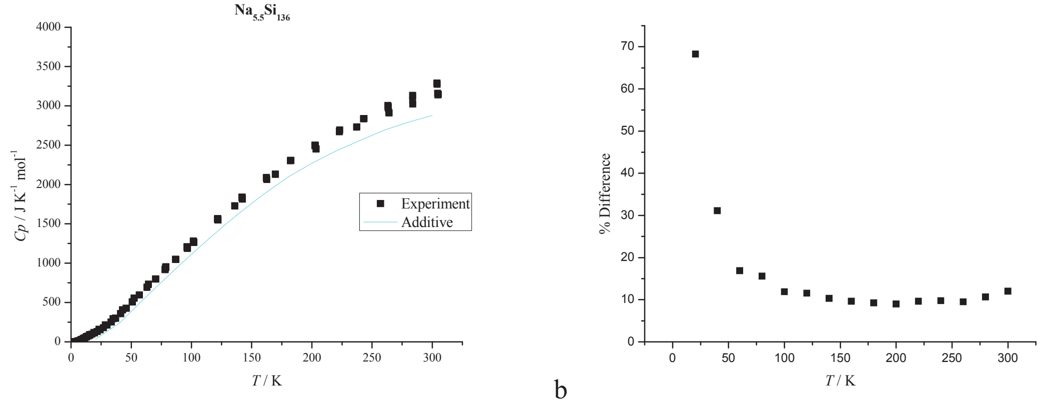

a

b

Figure 3.33 – (a) Experimental heat capacity data for $Na_{5.5}Si_{136}$ plotted alongside its additive model (C_p ($Na_{5.5}Si_{136}$) = 5.5 [C_p (Na)] + 136 [C_p (Si)]) representation. (b) demonstrates agreement between experiment and the additivity model as % difference, relative to experimental heat capacity values.

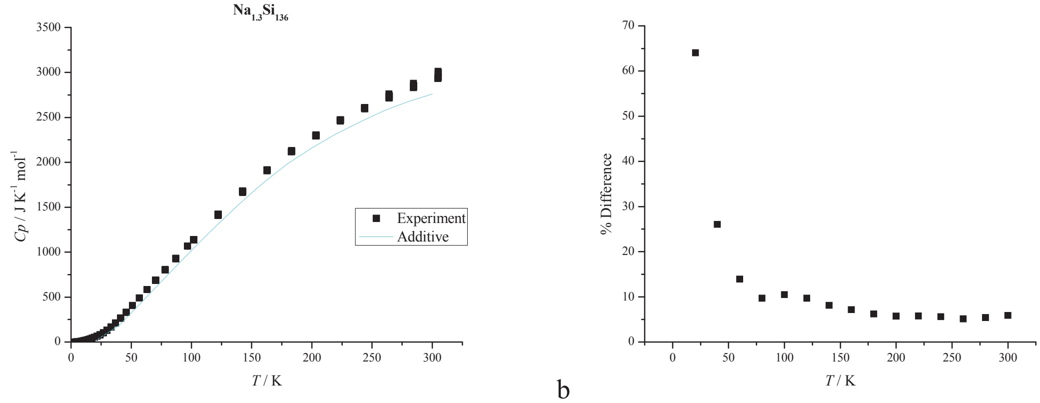

a

b

Figure 3.34 – (a) Experimental heat capacity data for $Na_{1.3}Si_{136}$ plotted alongside its additive model (C_p ($Na_{1.3}Si_{136}$) = 1.3 [C_p (Na)] + 136 [C_p (Si)]) representation. (b) demonstrates agreement between experiment and the additivity model as % difference, relative to experimental heat capacity values.

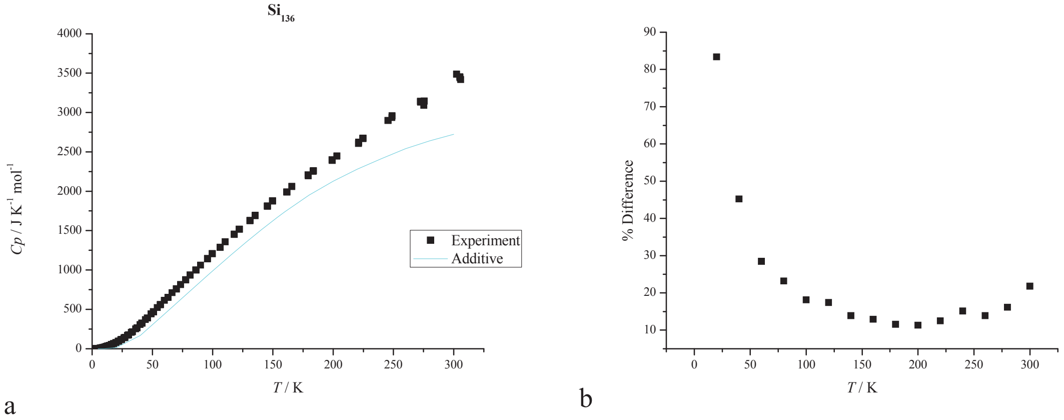

Figure 3.35 – (a) Experimental heat capacity data for Si_{136} plotted alongside its additive model ($C_p\,(Si_{136}) = 136\,[C_p\,(Si)]$) representation. (b) demonstrates agreement between experiment and the additivity model as % difference, relative to experimental heat capacity values.

From Figure 3.26 through Figure 3.35 it is apparent that for all but $x = 24$, experimental values exceeded those of the additive model. This was true across the entire temperature range. This underestimation of the additive model decreases with increasing Na content, so that at higher Na loadings there is good agreement between the model and experiment. $Na_{24}Si_{136}$ is quite accurately described by the additive model. Figure 3.36 demonstrates this trend as a plot of the % difference between experiment and the additive model averaged across all temperatures.

The trend presented in Figure 3.36 shows that as the Si framework becomes more fully occupied by Na, the heat capacities of Na_xSi_{136} samples tends towards the heat capacity of their elemental constituents. However, $x = 1.3$ is an outlier in Figure 3.36. It shows significantly closer agreement to the additivity model than either $x = 0$ or $x = 5.5$. This finding can be related to earlier discussion regarding lattice stiffening, where a

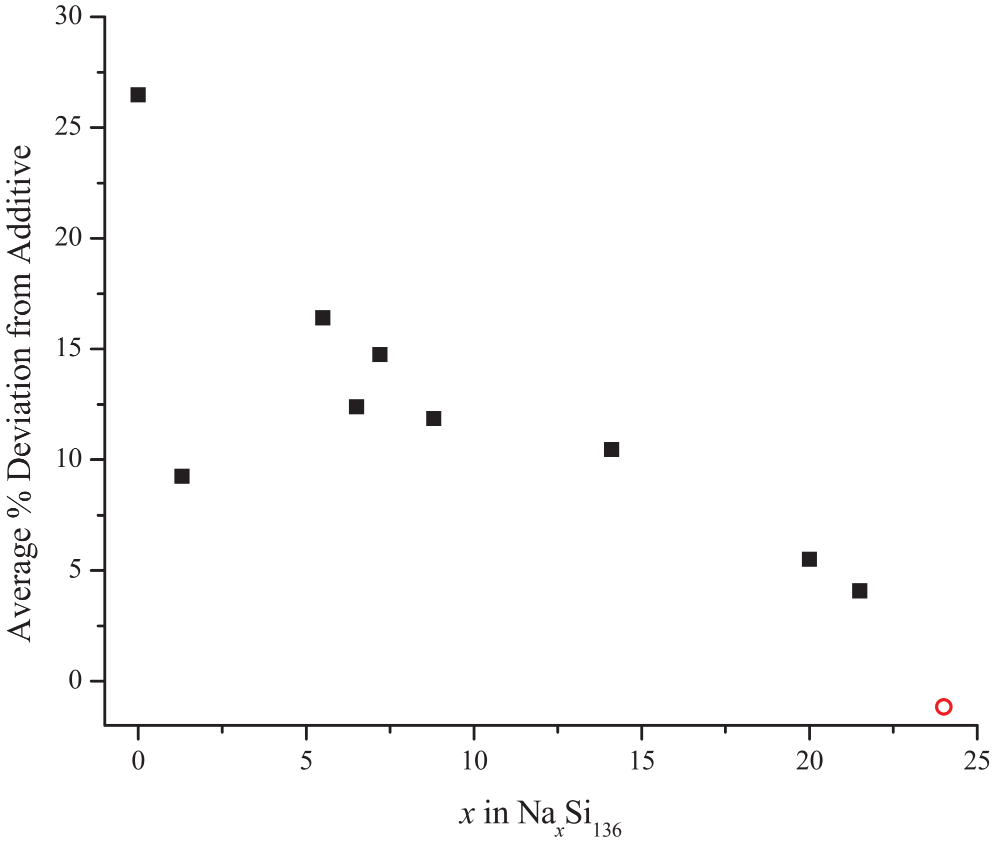

Figure 3.36 – Average deviation from the constituent additivity model (C_p (Na_xSi_{136}) = x [C_p (Na)] + 136 [C_p (Si)]) decreases with increasing Na content for the Na_xSi_{136} series of samples. This figure includes literature data for $x = 24$ (○).[118]

significant increase in the θ_D^{eff} was calculated with the initial addition of Na to the lattice. A stiffer lattice is reflective of both greater strain on the framework and stronger Na-Si attractive interactions.

Closer agreement between experimental heat capacities and those of the additivity model indicates greater similarity between Na_xSi_{136} samples and their elemental constituents. At higher Na contents, the Na guests are more restricted, a situation more akin to that of the close-packed, body-centred cubic structure[137] of the elemental material than the expanded Si cage structure. In addition, elemental Si has a Debye temperature of ~ 650 K,[136] whereas $Na_{24}Si_{136}$ has been shown to have a Debye temperature of 593 K.[118] The increasing effective Debye temperature with increasing Na content (Figure 3.25) shows that the Na_xSi_{136} samples become more similar to elemental Si, the majority constituent, with increasing Na content. Heat capacities of Na_xSi_{136} are better described by the additivity model with increasing Na content because lattice dynamics of the Na_xSi_{136} samples become more like those of the elemental constituents with increasing Na content.

Outside of the anomalous $x = 1.3$ point, Figure 3.36 shows that experimental heat capacity data consistently tended towards the additive model with increasing Na content. This is indicative of higher frequency vibrational modes (lattice stiffening) with increasing Na content, as indicated by Figure 3.24 and Figure 3.25. As the lattice stiffens with increasing Na content, its dynamics start to more resemble those of the close packed elemental constituents.

3.3.3.2.4 Na Contributions

Since relative cage occupations were known for the Na_xSi_{136} series of samples, it has been possible to demonstrate how the inclusion of Na in the two different environments (Si_{20} and Si_{28}) affect heat capacity differently. Again, this was possible because heat capacity is a nearly additive property. The different effects were estimated by taking the difference in heat capacity data between two compositions that differed in the amount of only one type of Na guest (*i.e.* the difference in heat capacity between two compositions where $x < 8$ and the difference in heat capacity between two compositions where $x > 8$). By subtracting the $x = 14.1$ heat capacity data from the $x = 21.5$ data and dividing the result by the difference in Na content ($\Delta x = 7.4$) it was possible to perceive how heat capacity changed due to the incorporation of Na into the Si_{20} cages, on a per Na basis. The same was done using the $x = 1.3$ and 5.5 data to isolate the changes due to inclusion of Na within the Si_{28} cages. Figure 3.37 shows the results of this analysis alongside heat capacity data for elemental Na, for comparison.

Figure 3.37 shows that the heat capacity of the system increases more from the addition of Na to the Si_{28} cages than can be accounted for by the elemental Na heat capacity curve while the opposite is true when Na is added to the Si_{20} cages. The difference between the contributions of Na in Si_{20} cages and Na in Si_{28} cages to heat

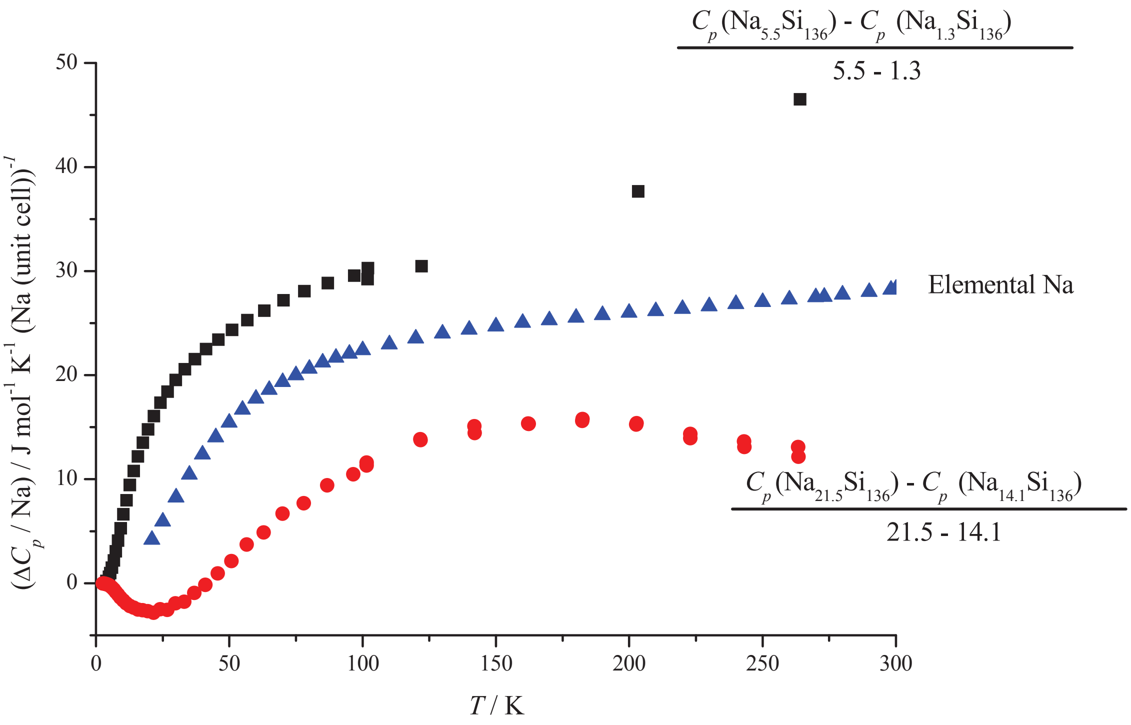

Figure 3.37 – Experimental difference plots illustrating how the addition of Na to each of the two different Si cage environments affects overall heat capacity. These data are presented on a per Na unit bases. Heat capacity data for elemental Na have been reproduced from Ref. 138.

capacity is almost a factor of two at 175 K and becomes more significant at higher temperatures. Materials with higher Debye temperatures, those with stiffer lattices, have lower heat capacities at a given temperature than materials with lower Debye temperatures.[24] This then shows that the Na atoms in Si_{20} cages are more restricted in the lattice and also act to stiffen it, while the Na in Si_{28} cages act to soften it.

When compared to the elemental heat capacity of sodium, Na in Si_{20} is lower throughout the entire temperature range, suggesting greater atomic restriction than in elemental Na. Conversely, Na in Si_{28} demonstrates greater heat capacity across the entire temperature range, showing greater ease of atomic motion and weaker interactions with surrounding atoms when compared to elemental Na. The lowered contributions of Na in Si_{20} to heat capacity of Na_xSi_{136} compared to elemental Na and the increased contributions of Na in Si_{28} compared to elemental Na help to explain the trend in agreement between experimental heat capacity and the additive model. At low loadings, $x < 8$, when Na is present only in the Si_{28} cages, Na contributes more to the heat capacity of the Na_xSi_{136} material than would elemental Na and the additive model more significantly underestimates the heat capacity. This increase is counteracted by the addition of Na to Si_{20} which decreases heat capacity relative to elemental Na.

Since heat capacity due to Na in Si_{20} cages is lower than that of elemental Na by an amount approximately equal to that by which the heat capacity due to Na in Si_{28} cages exceeds it, one might expect the values of the additive heat capacity model to approach the experimental values when Si_{20} and Si_{28} cage occupations are equal ($x = 16$). However, from Figure 3.35 it can be seen that the heat capacity of the Si_{136} framework also exceeds the predictions of the additive model, reflecting that Si_{136} is a looser structure than the diamond-structure of Si. This explains why the additive model underestimates the heat capacities of Na_xSi_{136} samples for all but the highest Na loading, $Na_{24}Si_{136}$.

3.3.3.2.5 Composite Model

A more detailed understanding of how the lattice dynamics change with Na content was obtained by considering a somewhat more complex heat capacity model. This model included terms to account for electronic contributions, lattice contributions and a term to account for the effects of thermal expansion. Electronic contributions have already been discussed in section 3.3.3.1. Thermal expansion effects were accounted for via a C_p-C_v term, defined as[24]

$$C_p - C_v = \frac{TV\alpha^2}{\beta_T} \tag{3.10}$$

where C_p and C_v are heat capacity at constant pressure and heat capacity at constant volume, respectively, V is molar volume, α is the coefficient of thermal expansion and β_T is the coefficient of isothermal compressibility. Since α and β_T data were not available for the Na filled type II Si clathrate samples, β_T was assumed to be same as that of Si_{136}[139] and α was calculated from Na_xSi_{136} lattice parameters assuming a similar temperature dependence to that of the empty clathrate.[36] Calculated $C_p - C_v$ values were less than 0.2 % of total heat capacities at high temperatures, where differences between C_p and C_v are most significant. All C_p-C_v values were, thus, well below measurement uncertainty and C_p can be taken as equal to C_v within uncertainty.

An accurate description of the lattice contribution to the heat capacities of the Na_xSi_{136} series of samples required many terms. In a real solid there are $3N$ vibrational modes where N is the number of atoms per unit cell. These are comprised of 3 acoustic modes and $3N - 3$ optic modes. Since phonon density of states data were not available for this system, heat capacities curves for the Na_xSi_{136} samples were approximated using the Einstein[37] and Debye[38] models for heat capacity. Initially, simple models were used (*e.g.* using one Debye term to describe the Si framework and one Einstein term for each of the two Na sites), but they failed to accurately reproduce the experimental heat capacity data. The simplest model that fit the heat capacity data for the Na_xSi_{136} samples required the use of: one Einstein term for Na in the Si_{28} cages, denoted C_{ENal}; one Einstein term for Na in the Si_{20} cages, C_{ENas}; two Si Einstein terms, C_{ESi1} and C_{ESi2}, with degeneracies of 3×16 and 3 × 20 respectively; and one Si Debye term, C_{DSi}, with degeneracy of 3 × 100. The Si modes give a total of 3 × 136 modes for the 136 Si atoms, to describe the Si framework contribution. The $3N$ vibrational degrees of freedom for each of the Na_xSi_{136} samples (3 × 136 for the Si framework + $3x$ for Na content) were distributed between these five terms and summed to describe the lattice contributions to heat capacities. The vibrational degrees of freedom of Si were mostly dominated by the Debye term. Thus the lattice contributions to heat capacities of the Na_xSi_{136} samples were described as,

$$C_v^{lattice} = 3 \times 100 \times C_{DSi} + 3 \times 16 \times C_{ESi1} + 3 \times 20 \times C_{ESi2} + 3 \times y \times C_{ENal} + 3 \times z \times C_{ENas}, \quad (3.11)$$

where $y + z = x$, as per the filling scheme from the Rietveld analyses[115] and supported by XAS studies.[54] Table 3.7 presents the values of y and z for each composition of the Na_xSi_{136} sample series.

The expression for lattice heat capacity from Equation (3.11) was combined with terms for electronic contributions and C_p-C_v to give a description of the total heat capacity of the Na_xSi_{136} samples:

$$C_p^{total} = \gamma T + C_v^{lattice}(T) + (C_P - C_V)(T). \tag{3.12}$$

The values of θ_{DSi}, θ_{ESi1}, θ_{ESi2}, θ_{ENas} and θ_{ENal}, the Debye and Einstein temperatures for the corresponding C_{DSi}, C_{ESi1}, C_{ESi2}, C_{ENal}, and C_{ENas} terms in Equation (3.11) were then optimized to best fit the experimental heat capacity data for Na_xSi_{136} samples. Figure 3.38 illustrates the optimized terms for each composition of the Na_xSi_{136} series of samples.

Table 3.7 – Na occupations of the Si_{28}, y, and Si_{20}, z, cages of Na_xSi_{136} samples with varying total Na content, x.

x	y	z
21.5	8	13.5
20	8	12
14.1	8	6.1
8.8	8	0.8
7.2	7.2	0
6.5	6.5	0
5.5	5.5	0
1.3	1.3	0
0	0	0

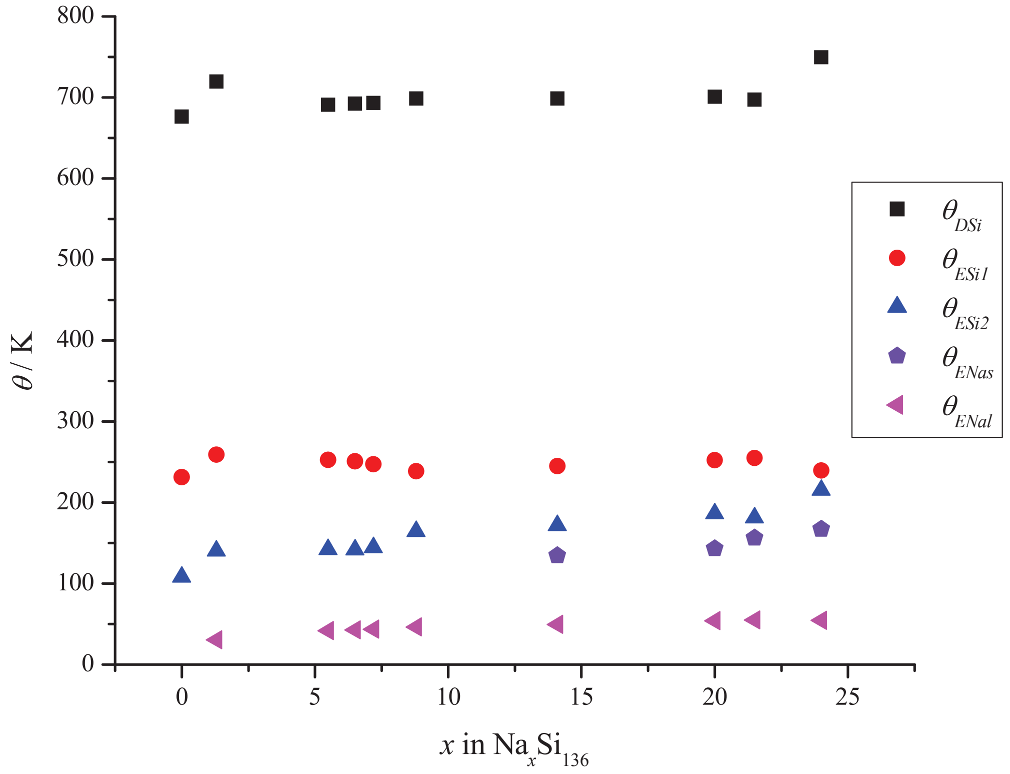

Figure 3.38 – Changes in the Debye and Einstein temperatures with varying Na content as determined from fitting experimental heat capacity data of the Na_xSi_{136} series of samples to the model presented in Equation (3.12) as a function of x and T. θ_{DSi}

Figure 3.38 shows that the Debye temperature, $\theta_{DSi,}$ for the Si lattice, at ~ 700 K, is high compared to the other terms and approximately independent of Na content in this series of Na filled Si clathrates. The Einstein temperature associated with the 20 Si Einstein modes, θ_{ESi1}, also appears to be independent of Na content. However, the Einstein temperature of the other 16 Si Einstein modes, θ_{ESi2}, is dependent on Na loading and shifts to higher energies with increasing Na content. Figure 2.13 shows that the lattice constant increases as x increases. The present results show stiffening of the Si framework with increasing lattice parameter and increasing Na content. This is consistent with trends in (overall) effective Debye temperature, Figure 3.25.

While PXRD studies have indicated an increase in lattice parameter with increasing Na content,[115] the Debye-Waller factors determined by XAS[54] for the $x = 14.1$ and $x = 21.5$ samples have indicated less dynamic disorder for Na in Si_{28} cages with increasing Na content. These trends show that despite increasing unit cell size with increasing x, Na motions within the Si_{28} cages become lower in amplitude with increasing Na content. This is also consistent with Na being less off-centre of the Si_{28} cages with increasing Na content.[116,119] Figure 3.38 indicates a slight, but steady, trend of increasing θ_{ENaI} with increasing Na content. This means that decreased vibrational amplitude is accompanied by increased vibrational frequency, as shown from the above analysis as well as by inelastic neutron scatting for Na_3Si_{136} and $Na_{23}Si_{136}$.[140] These changes in rattler dynamics are also supported by observed changes in C_p/T^3 peak position and magnitude, Figure 3.23 and Figure 3.24.

Figure 3.38 shows the Na motions in Si_{20} cages were of energies higher than those of the Na in Si_{28} cages. The higher energy motions of the Na in Si_{20} cages are consistent with stronger interactions between Na and the Si_{20} compared to the interactions between Na and Si_{28} cages. Neutron studies have led to the same conclusion,[140] as have XAS derived Debye-Waller factors.[54]

With the exception of $x = 0$ and $x = 24$, a subtle increase in heat capacity was observed with increasing Na content (Figure 3.19). Increases in heat capacity due to increases in the content of Na in Si_{28} cages are muted since the mobility of the Na atoms in Si_{28} cages is reduced with increasing Na content. This is shown through the reduced amplitude of the C_p/T^{-3} peak, Figure 3.23. In addition, vibrations of Na within the Si_{28} cages becomes higher in energy with increasing Na content as shown by the increase in the Einstein temperature, θ_{ENaI}, Figure 3.38, and temperature of the C_p/T^{-3} peak, Figure

3.24. This means that, at a given temperature, Na atoms in Si_{28} cages contribute less per Na atom to heat capacity with increasing Na content.

Vibrational modes associated with Na in Si_{20} cages are of higher energy than those of the Na in Si_{28} due to repulsive interaction and the slight increase in θ_{ENas} with increasing x shown in Figure 3.38 suggests that repulsion is increased at higher Na loadings. While increased attraction between Na and the Si_{28} cages and increased repulsion between Na and the Si_{20} cages decreases dynamic disorder with increasing Na content, these changes also result in a stiffening of the Si lattice as evidenced by the increase in θ_{ESi2} as seen in Figure 3.38. The increases in θ_{ENal} and θ_{ESi2} with increasing Na content are also reflected in increased θ_D^{eff} values, Figure 3.25.

3.3.4 Further *κ* Discussion

A material's speed of sound can be related to its Debye temperature through[24]

$$\theta_D = \frac{\nu h}{2\pi k}\left(\frac{6\pi^2 N}{V}\right)^{1/3}, \tag{3.13}$$

where v is the speed of sound, N is the number of atoms in the unit cell and V is the volume of the unit cell. Since the Debye temperatures determined here, Figure 3.25, are *effective* values, Equation (3.13) returns *effective* speeds of sound which serve well for internal comparison. The speeds of sound, Figure 3.39, calculated using θ_D^{eff} through Equation (3.13), closely follow θ_D^{eff}. There is an increase in v for $x = 1.3$ compared to the empty clathrate, a slight decrease in the intermediate Na content samples ($x = 1.3$ to

7.2) and another region of increase in the higher content samples, $x = 7.2$ to 21.5. Increased speed of sound with Na content is reflective of the lattice stiffening indicated by increasing θ_{ENa1} and θ_{ESi2} values, Figure 3.38.

Given that thermal conductivity is dependent on speed of sound through Equation (1.23),[24] the changing speed of sound can account for some of the change in κ with changing Na content. Differences in speeds of sound with changing Na content are not as pronounced as the observed differences in thermal conductivity, Figure 3.15. Therefore, lattice dynamical changes resulting in differences in speed of sound can only account for

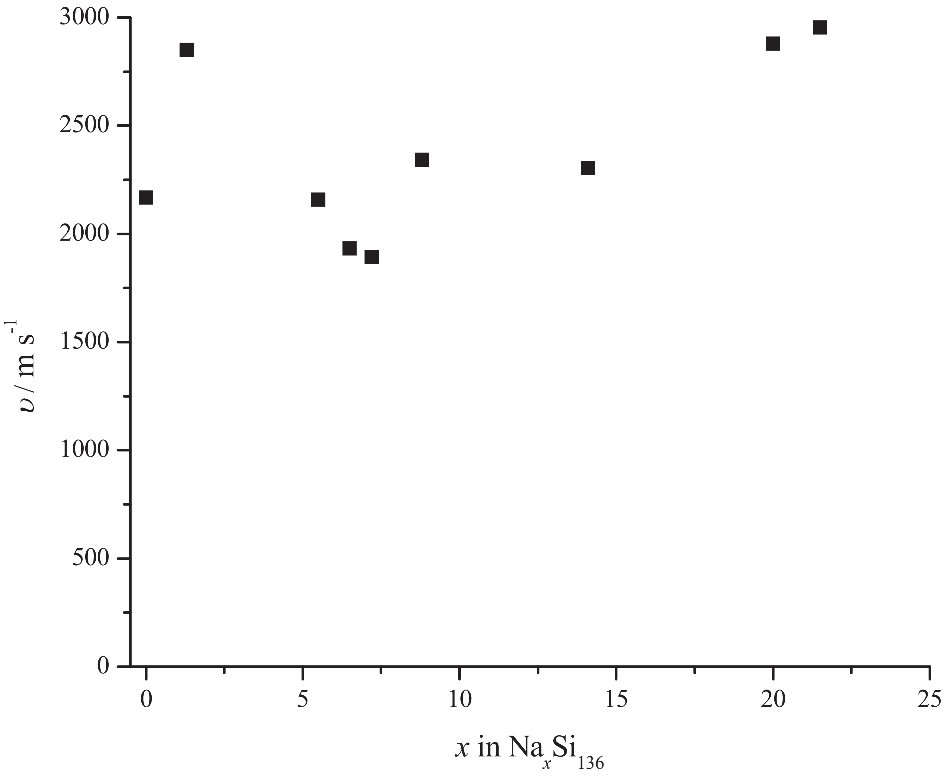

Figure 3.39 – Speed of sound, derived from θ_D^{eff} through Equation (3.13), for Na_xSi_{136} samples. Values are plotted with changing x. These data closely follow those of the effective Debye temperatures seen in Figure 3.25.

some of the increased thermal conductivity with increased Na content seen in Figure 3.15.

By assuming that all heat conduction is phononic and combining the speed of sound results presented in Figure 3.39 with measured thermal conductivity and heat capacity data, it is possible to estimate the effective phonon mean free path in the Na_xSi_{136} samples (Equation (1.23)). Figure 3.40 shows how effective phonon mean free path changes with Na content at 200 K.

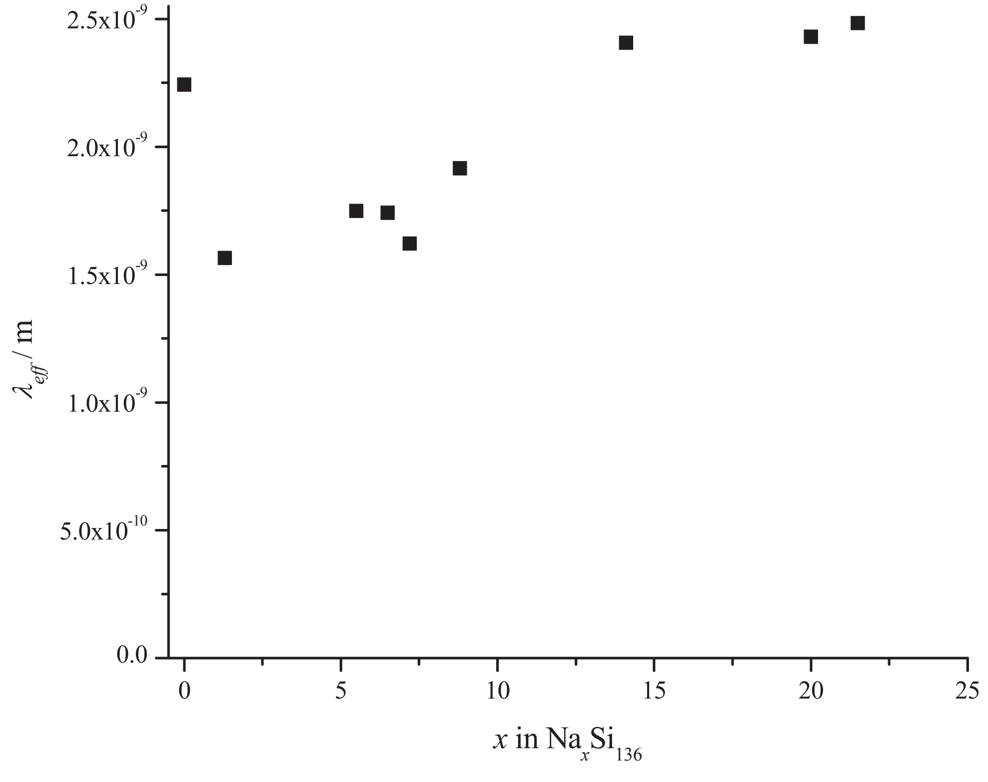

Figure 3.40 – Effective phonon mean free path as calculated from experimental κ and C_p data and calculated v data (Figure 3.39) via Equation (3.13). Results are presented as a function of Na content for data for $T = 200$ K.

Figure 3.40 shows that effective phonon mean free path is most noticeably reduced from that of Si_{136} with the initial inclusion of Na, $x = 1.3$. At low loadings, $x = 1.3$ to 7.2, the effective phonon mean free path is on the order of one unit cell length and is not sensitive to Na content. Given the reasonable length scale of these values and that heat capacity (and therefore thermal conductivity) has been shown to be completely phononic for Na_xSi_{136} samples were $x < 8$ (Table 3.4) these data are a good approximation of the phonon mean free path of Na_xSi_{136} samples for $x < 8$. Further addition of Na, $x \geq 8.8$, results in an increase in the effective phonon mean free path of Na_xSi_{136} samples. Since the $x = 1.3$, 5.5, 6.5 and 7.2 values do not show strong Na content dependence it is unlikely that the increases seen for $x \geq 8.8$ are due to increased interaction between Na and the Si_{28} cages or lattice effects. Rather, it is expected that this increase in apparent phonon mean free path is a result of increased electronic thermal conductivity for $x \geq 8.8$, as discussed further below.

It has been shown that interactions with guest molecules is the dominant phonon-scattering process in THF clathrate hydrates.[21] If, by reasonable analogy, one assumes the Na atoms to be the dominant phonon scattering centres in Na_xSi_{136} and takes the average distance between Na atoms in the unit cell as the phonon mean free path, it is possible to compare the thermal conductivity calculated from Equation (1.23) to the experimental data. Equation (1.23) is an oversimplification, since it ignores dispersion[141] (*i.e.*, it treats the frequency of all phonons as independent of position in the Brilliouin zone), however, it can be "corrected" by a factor, β (= $\kappa_{\text{experiment}} / \kappa_{\text{calculated}}$). This correction factor can then be applied to higher Na content samples to estimate the lattice (and, by difference, the electronic) contribution to thermal conductivity in these materials at high x. Table 3.8 presents data obtained from this β procedure analysis for thermal conductivity at 200 K. The data presented in Table 3.8 indicate that phonon contributions to thermal conductivity are more significant if only the Si_{28} Na act as phonon scattering centres. The observed stiffening of the lattice that occurs with the addition of Na to Si_{20} suggests that Na in Si_{20} cages do less to inhibit phonon propagation. The first case gives an upper limit for lattice contributions to thermal conductivity. Minimum lattice contributions were estimated by assuming that both large and small Na act as phonon scattering centres. It is likely that the true lattice contributions lie between these extremes, with the remainder of the thermal conductivity being attributed to electrons. Figure 3.41 presents the estimated range of lattice contributions with varying Na content alongside experimental thermal conductivity data at 200 K.

Table 3.8 – Results from β procedure analysis. Results are presented under two different assumptions 1) that both Si_{20} and Si_{28} Na act as scattering centres for heat carrying phonons ("All Na") and 2) that only Si_{28} Na act as phonon scattering centres ("Si_{28} Na"). x represents the Na content in $\mathrm{Na}_x\mathrm{Si}_{136}$, bulk κ is the measured thermal conductivity at 200 K, β is the correction factor determined from comparing measured values to calculated values. v is the speed of sound, calculated from θ_D^{eff} values, $C_{p,vol}$ is the heat capacity per cubic meter determined from measured molar values and PXRD derived unit cell parameters, λ is the mean free path assuming Na guests as the dominant scattering centres, and κ_{ph} are the calculated phononic contributions to thermal conductivity.

x	Bulk κ / W m^{-1} K^{-1}	β (Avg = 2.06)	v / m s^{-1}	$C_{p,\,vol}$ / J K^{-1} m^{-3}	λ / m All Na	κ_{ph} (All Na) / W m^{-1} K^{-1}	λ / m Si_{28} Na	κ_{ph} (Si_{28}) / W m^{-1} K^{-1}
1.3	1.8	1.16	2850	1.21E+06	1.35E-09			
5.5	1.63	2.10	2158	1.30E+06	8.33E-10	1.60	8.33E-10	
6.5	1.51	2.21	1933	1.35E+06	7.88E-10	1.41	7.88E-10	
7.2	1.36	2.13	1894	1.33E+06	7.61E-10	1.32	7.61E-10	
8.8	2.00	2.69	2342	1.34E+06	7.12E-10	1.53	7.35E-10	1.58
14.1	2.59		2304	1.40E+06	6.09E-10	1.35	7.35E-10	1.63
20	3.43		2879	1.47E+06	5.42E-10	1.58	7.35E-10	2.14
21.5	3.66		2953	1.50E+06	5.29E-10	1.61	7.35E-10	2.23

From the data presented in Figure 3.41 it can be seen that there is a decrease in experimentally determined thermal conductivity upon addition of Na from $x = 0$ to $x = 1.3$. This is attributed to the low energy rattler modes of the Na atom in Si_{28} cages. Accompanying the incorporation of this small amount of Na is an expansion of the lattice compared to that of Si_{136}.[115] As a result of this small amount of Na, the lattice stiffens, as indicated by the higher θ_D^{eff}, Table 3.6, value and increased speed of sound, Figure 3.39, promoting increased thermal conductivity. The reduced phonon mean free path that

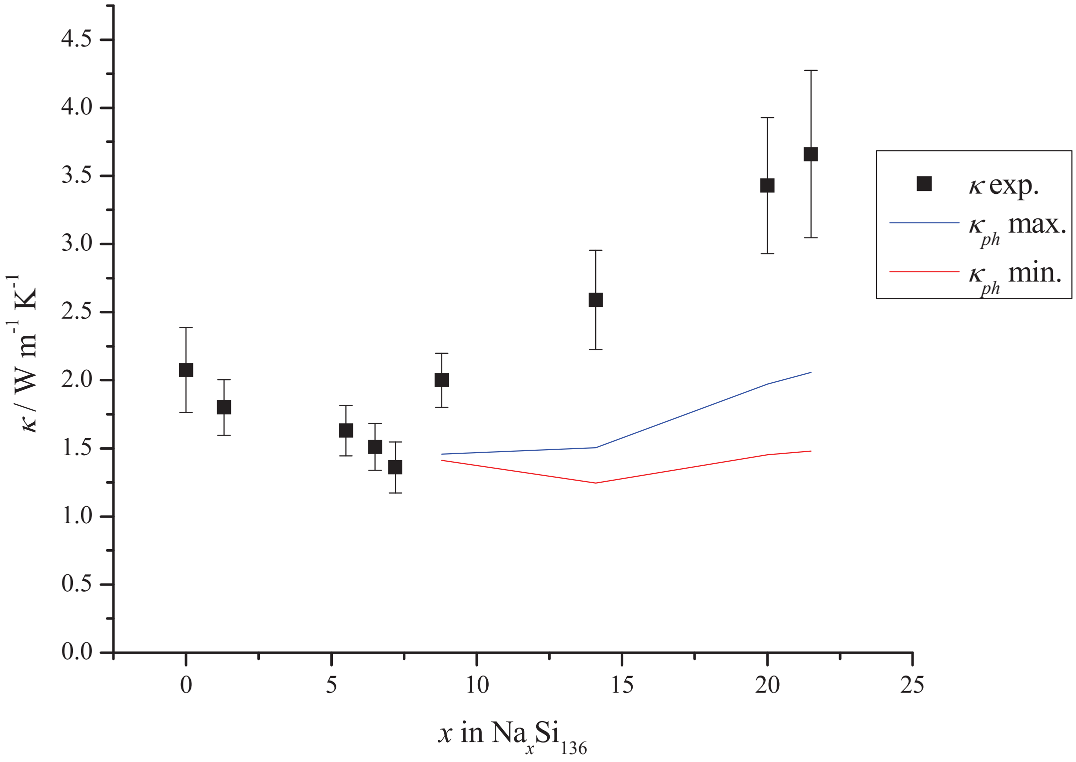

Figure 3.41 – Thermal conductivities of Na_xSi_{136} samples at 200 K as a function of x. Error bars indicate the 5 % uncertainty associated with measurements[91] and in porosity and 15 % for Si_{136} since its data point was extracted from a published plot.[73] Assuming Na in Si_{28} cages to be the dominant phonon scattering centres gives a maximum lattice contribution (—) while assuming Na atoms in both cages to be phonon scattering centres gives a minimum (—) for samples where $x \geq 8.8$.

occurs with minimal Na incorporation, however, acts to hinder thermal transport more than the stiffened lattice does to help it. The net result is that the most significant reduction in κ relative to Si_{136} is seen at the lowest Na loading investigated, $x = 1.3$.

Upon further addition of Na to the Si lattice, beyond $x = 1.3$, thermal conductivity is further reduced, although to a lesser extent than on the initial introduction of Na into the Si_{136} lattice. There is a slight contraction of the lattice with the further addition of Na and the Si framework becomes somewhat less stiff, as manifest in the reduced speed of sound compared to that of the $x = 1.3$ sample, Figure 3.39. The Na in Si_{28} of the $x = 5.5$, 6.5 and 7.2 samples show slightly reduced rattler mobility. Lattice stiffening and reduced rattler mobility, however, are offset by increased number of rattling atoms. The net result is a decrease in thermal conductivity compared to the $x = 1.3$ sample.

For $x \geq 8.8$, electronic contributions must be considered. From Figure 3.41 it can be seen that the electronic contributions (the difference between the experimental data and the calculated lattice contributions) increase as x increases beyond 8.8. This follows with the increase in charge carrier density that occurs with increased Na loading.[54] The minimum lattice contribution model suggests that lattice contributions are approximately independent of x beyond $x = 8.8$. From the maximum lattice contribution model, there is an increase in the phononic contribution to κ with increasing x in approximate proportion to calculated speed of sound values, Figure 3.39. Speed of sound increase is attributed to lattice stiffening. The overall result of these trends is that changes in thermal conductivity are quickly dominated by electronic contributions at Na contents greater than $x = 8.8$, although the increase is likely, in part, also due to increasing phononic contributions.

Figure 3.42 shows how the electronic and phononic contributions to thermal conductivity change in Na_xSi_{136} with changing Na content compare to experimental data.

From Figure 3.42 it can be seen that lattice thermal conductivity decreases with increasing x in the range of $x = 0$ to $x = 7.2$. At x values greater than 7.2 ($x = 8.8$ and greater) the lattice thermal conductivity flattens off or increases slightly. Electronic thermal conductivity becomes apparent in measured values starting at x values as low as

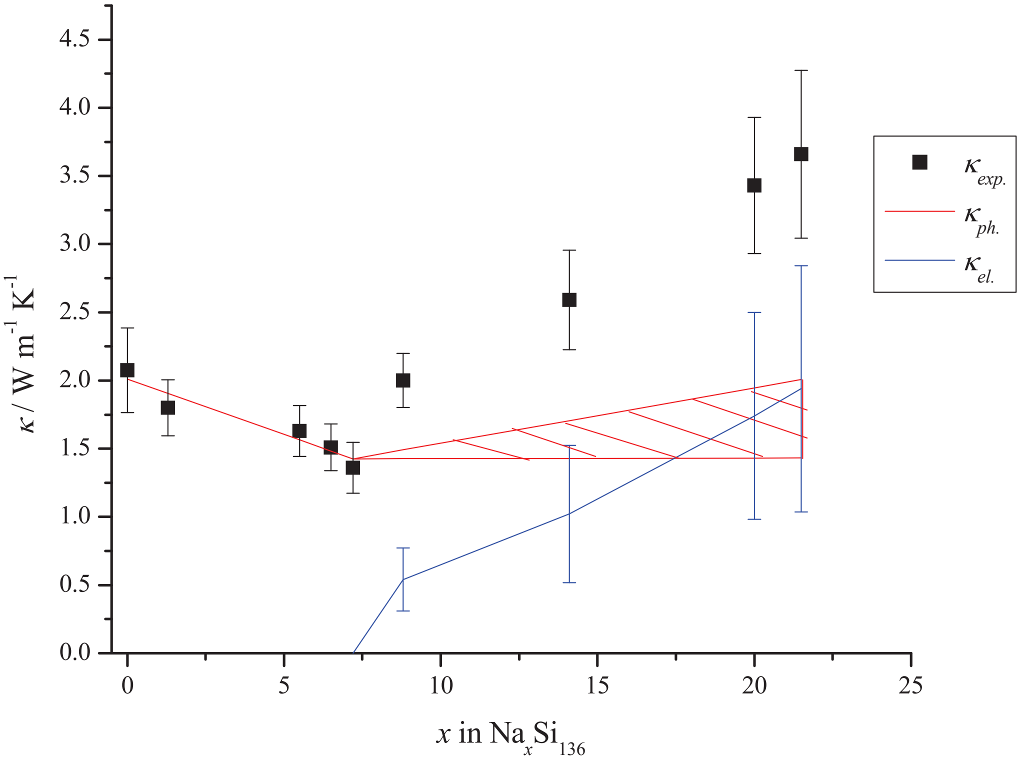

Figure 3.42 – Thermal conductivities of Na_xSi_{136} samples at 200 K as a function of x. Error bars indicate the 5 % uncertainty associated with measurements[91] and in porosity and 15 % for Si_{136} since its data point was extracted from a published plot.[73] The calculated phononic (—) and electronic (—) contributions to thermal conductivity are also presented. Electronic contributions were taken as the difference between experiment and average calculated phononic contributions. Error bars for electronic contributions arise from the range of possible phononic contributions as determined assuming Na in Si_{28} cages to be the dominant scattering centres (maximum phononic contributions) and all Na in both cages to be the dominant scattering centres (minimum phononic contributions), combined with uncertainty from the experimental points.

8.8 and contributes substantially to overall thermal conductivity at high x values: electronic contributions account for nearly 50 % of thermal conduction of the $x = 21.5$ sample at 200 K. In general, the lattice thermal conductivity is reduced by the presence of Na in Si_{28} cages and not reduced further, or possibly increased, by Na in Si_{20} cages. Electronic thermal conductivity increases as Na occupies the Si_{20} cages. Overall, this leads to decreased thermal conductivity due to the inclusion of Na in Si_{28} cages and increased thermal conductivity due to the inclusion of Na in the Si_{20} cages.

3.3.5 Wiedemann-Franz Law

The Wiedmann-Franz law states the empirical observation that for metals the ratio of electrical conductivity to thermal conductivity is proportional to temperature. More formally, this can be written as[24]

$$L = \frac{\kappa}{\sigma T} = 2.45 \times 10^{-8}\ \mathrm{W\,\Omega\,K^{-2}}, \tag{3.14}$$

where L is the Lorenz number. Experimentally derived effective Lorenz numbers ($L_{eff} = \kappa/\sigma T$, which is only equal to 2.45×10^{-8} for metals) for the Na_xSi_{136} series of samples have been determined from the present thermal conductivity data and literature values[118,125,126] (assuming a constant trend in σ magnitude with changing Na content based on the data for the non-cold-pressed samples shown in Figure 3.12). Table 3.9 presents the effective Lorenz numbers for the Na_xSi_{136} samples.

Table 3.9 – Effective Lorenz numbers for Na_xSi_{136} samples at 300 K as derived from the present thermal conductivity data and literature values for electrical conductivities.[118,125,126]

x	L_{eff} / W Ω K^{-2}
21.5	1.45E-07
20	6.93E-07
14.1	1.05E-04
8.8	1.98E-03
7.2	4.00E-03
6.5	5.67E-03
5.5	8.56E-03
1.3	3.22E-02
0	1.00E-01

From Table 3.9 it can be seen that effective Lorenz numbers tend from high values (indicative of semiconductors) in the low Na content samples to very low values, approaching the Lorenz number of metals, in high Na content samples. This indicates that thermal and electrical transport in Na_xSi_{136} samples moves from semiconducting to semi-metallic character with increasing Na content. This is consistent with the above finding, Figure 3.42, of increased electronic thermal conductivity with increasing Na content and makes sense in terms of increasing electron transfer to the Si framework with increasing Na content.

3.4 *ZT*

Because of the different processing dependencies of the constituent physical properties and the available processing being limited to cold-pressing, it was not possible to determine *ZT* values for a Na_xSi_{136} sample from one single experiment or sample. Given that thermoelectric energy conversion relies on all three properties simultaneously,

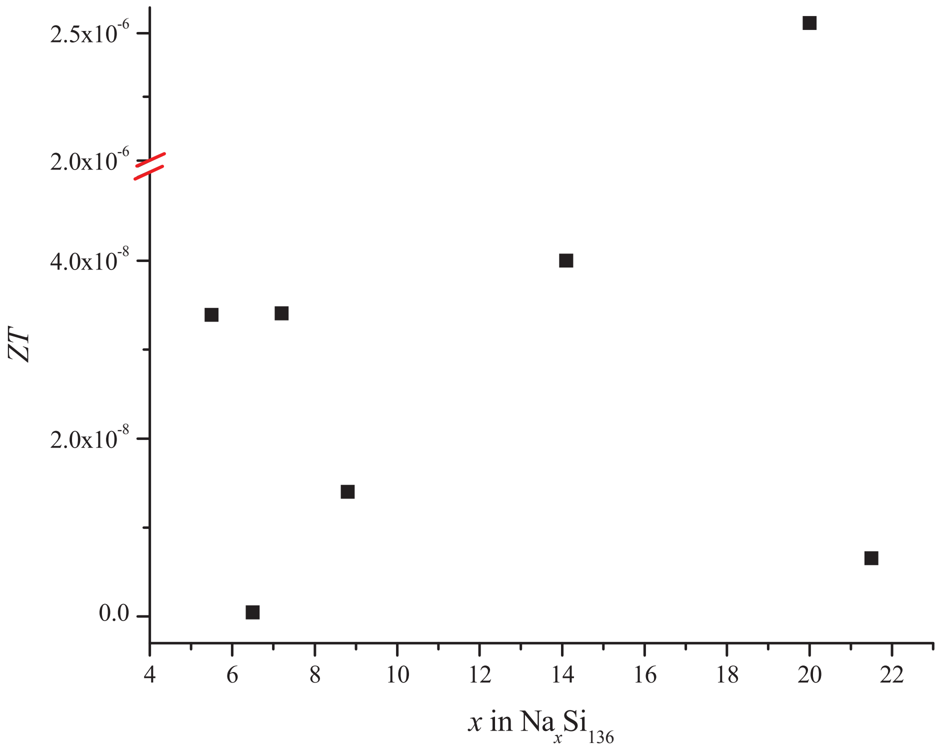

Figure 3.43 – Composite ZT values at 300 K for the Na_xSi_{136} samples studied.

values of ZT composed of S, σ and κ values from different experiments are not fully representative of a material's ability to interconvert thermal and electrical energies. Such values are, however, instructive when considering effects of changes in the contributing properties. Therefore, composite ZT values for the Na_xSi_{136} series of samples are presented in Figure 3.43.

When the S, σ and κ data are combined to describe thermoelectric performance, the resulting ZT values show that Na_xSi_{136} materials are far from efficient energy converters. Their ZT values are several orders of magnitude lower than those of the materials that are currently used in devices (as discussed in section 1.7). The values are low mostly due to the low electrical conductivity values observed for the cold-pressed samples. Figure 3.43 shows a significantly larger *ZT* value for the hot-pressed sample than any other Na_xSi_{136} sample. The highest values presented in Figure 3.43 are six to eight orders of magnitude lower than *ZT* values of current thermoelectric materials. Even well processed Na_xSi_{136} materials with high electrical conductivities would show *ZT* values significantly lower than 1. Thus, these materials serve to illustrate how the inclusion of loosely bound atoms can affect transport properties, although they are not themselves suitable for thermoelectric applications (even with better processing).

3.5 Transport Conclusions

When Na atoms are added to the Si_{136} framework, they first occupy the large Si_{28} cages within which they are able to vibrate significantly. These rattling vibrations are of sufficiently low energy to be in the range of the heat carrying, acoustic, phonons and as such can interact with them, reducing the phonon mean free path and resulting in reduced thermal conductivity. As more Na is added, there is a reduction in the vibrational freedom of Na within the Si_{28} cages, limiting their interaction with acoustic phonons. The diminished mobility of Na within the Si_{28} cages is counterbalanced by the increased amount of Na and the overall result is further reduction of thermal conductivity with increasing Na content down to a minimum when $x \sim 8$.

Further incorporation of Na beyond $x = 8$ goes into the small, Si_{20}, cages, the lattice expands and stiffens, and electronic contributions begin to be significant. At a minimum, there is no net effect on the lattice contributions to thermal conductivity due to increased Na content in Si_{20} cages. At most, Na atoms in Si_{20} cages cause an increase in lattice thermal conductivity. Most significantly, it has been found that increased inclusion of Na within the Si_{136} framework does not continue to decrease thermal conductivity to a minimum when the structure is full. Rather, at loadings above the point where the Si_{28} cages are full, additional Na acts to increase thermal conductivity. This is largely credited to electronic contributions, but phononic effects are not necessarily negligible.

It is interesting that S and σ have such different sensitivities to the apparent pathways across a sample given that both are electronic transport properties. The relative sensitivity of σ to the presence of oxide compared to the insensitivity of S is reflective of fundamental differences in the transport of electrons. Seebeck voltages arise from the diffusion of electrons, an entropy mediated process, whereas electrical conduction is governed by the Coulombic interactions of imposed potential differences. Oxide layers act to shield conduction electrons from the imposed electric potential but do little to interfere with their thermal excitation or diffusion mobilities.

Cold-pressed samples could consistently produce reliable results for only one variable, either S or κ, in a single experiment. The hot-pressed sample did not suffer from this restriction. It was thick enough to provide good separation between heater and heat sink for S measurements, and had sufficient internal contact to allow heat flow for κ measurements. Given that the densities of cold-pressed samples were comparable to or greater than that of the hot-pressed sample, it would be instructive to compare electrical conductivity measurements on samples that have been cold-pressed in an inert atmosphere to those of hot-pressed samples of similar compositions. This would help to determine if difficulties in obtaining electrical conductivity data on cold-pressed samples were due to grain oxidation or otherwise poor inter-granular contact. Whatever the effects of processing on the magnitudes of the physical properties are, it is clear that the resistance to mechanical strain that comes with well consolidated samples is a decided experimental benefit.

A well consolidated (SPS or single crystal) four-probe TTO measurement compatible sample, free of oxide prior to consolidation would be optimal (if wishful thinking) for obtaining simultaneous S, σ and κ data. However, a geometrically well defined sample with large lead separation ($l > 1$ mm) and a cross-section close to those of the cold-pressed pellets ($d = 4.8$ mm) is a more viable processing option which, at worst, would require a second experiment for electrical conductivity measurements. Future studies on powder semiconductor materials ought to emphasize good consolidation and appropriate sample geometries to ensure best results.

Chapter 4: Ge and Sn Clathrates

It has been shown that in addition to Si, clathrates with Ge[65,72] and Sn[142,143] frameworks are also stable. By studying group 14 analogues to the Na_xSi_{136} materials previously discussed it is hoped that a more general understanding of the structure-property relationships of clathrates can be obtained. This chapter presents results from the production and characterization of such materials.

4.1 Synthesis

The Na_xSi_{136} clathrate samples discussed in the previous chapters were prepared using high temperature methods.[113,114] Indeed, clathrates are most commonly produced from high temperature treatments of elemental starting materials or precursor compounds.[144] An alternative "softer" chemical route to the guest free type II germanium clathrate Ge_{136} was reported in 2006.[85] That procedure was employed at Dalhousie University for the present study.

4.1.1 Ge_{136}

The new, softer method of type II Ge clathrate production entailed the oxidation of alkali metal germanides (*e.g.* Ge_9^{4-} anions) under milder conditions (compared to thermal decomposition) by ionic liquids and led to the high-yield synthesis of an unoccupied type II clathrate form of germanium (Ge_{136}): no guest removal from the produced clathrate structure was required. The synthesis has been rationalized as an assembly polymerization-oxidation of Ge anions from a Zintl ion starting material. It has been proposed that the soft oxidation follows the Hofmann elimination mechanism.[145] Equation 4.1 describes this proposed route to Ge_{136}:

$$4[CH_3(CH_2)_{11}N(CH_3)_3]^+ + 4Ge_x^{4-} \rightarrow xGe^0 + 4CH_3(CH_2)_9CH{=}CH_2 + 4N(CH_3)_3 + 2H_2. \quad (4.1)$$

4.1.1.1 NaGe Precursor Preparation

As with Si_{136} production, the published synthesis[85] of Ge_{136} called for the production of a sodium-containing precursor compound, namely $NaGe_{2.25}$. This material was produced by melting high purity elemental starting materials (99.999 % pure Ge powder and ACS reagent grade Na from Sigma-Aldrich) at 1375 K within a sealed Ta container for an hour, followed by a two day annealing period at 1075 K. The resulting ionic polycrystalline material was air and moisture sensitive.

While this procedure, in theory, is relatively straightforward there were some challenges. Since neither a suitable Ta nor Nb container was available for the high temperature synthesis, reaction in stainless steel was attempted first. The initial attempt confirmed suspicions that the stainless steel would not withstand the reaction conditions. Specifically, it is likely that the Na vapour put significant strain on the stainless steel container and that high temperature Ge reacted with the C in the stainless steel. After the initial failure of the stainless steel reaction vessel another preparation attempt was made, however, the temperature was reduced to slightly above the melting point of Na (Na mp ~ 370 K, actual temperature used = 400 K). This resulted in no reaction.

A series of experiments to test the viable temperature range of stainless steel revealed that the container could withstand temperatures of up to 1075 K. After reaction at 1075 K the stainless steel tubing was severely discoloured and had expanded at the crimped ends due to the high vapour pressure of Na. Above this temperature the tubing was not able to withstand the pressure of the Na vapour or attack from the Ge. A mixture of starting materials remained in the reaction vessel after sustained heating at 1075 K for 48 hours: no reaction was observed. The presence of metallic ingots (Na metal) amidst a grey powder (Ge starting material) confirmed that the desired reaction, indeed, required temperatures greater than 1075 K. Most likely, the presence of liquid Ge is required for Zintl ion formation. Therefore, a reaction temperature of > 1210 K was used.

Ta tubing with a wall thickness of 0.51 mm and an outside diameter of 0.64 mm was procured from A. T. Wall Company and used as the reaction vessel for the production of the $NaGe_{2.25}$ Zintl ion. The starting materials were sealed in the tubing under argon using an arc furnace. Because of the geometry of the arc furnace and holder, the tubing lengths were restricted to 5 cm or less. A 5 cm length of tubing provides adequate volume for ~ 1 g of starting materials. To further isolate the reaction system from the atmosphere the Ta tubing, containing the starting materials, was sealed in a quartz-glass ampoule under argon.

The first attempt led to reaction with and subsequent failure of the Ta tubing. This was attributed to either O_2 presence due to brief exposure of the unsealed tubing (containing starting materials) to the atmosphere prior to the high temperature treatment, or reaction with a contaminant or oxide layer on the tubing surface. Brief exposure to the ambient atmosphere was unavoidable when transferring starting products in the Ta tubing into the arc furnace. Starting materials were placed in the Ta tubing (with one end already sealed) under Ar atmosphere (heavy in comparison to atmospheric constituents) and exposure was for less than five seconds. The possible presence of a contaminant in the Ta tubing was, therefore, believed to be the more likely cause of failure.

To reduce chances of reaction with contaminants or oxygen, the Ta tubing was cleaned with concentrated HCl and care was taken to minimize exposure of the unsealed tubing to the atmosphere to all practical extents. In addition, to reduce strain on the reaction vessel due to the high vapour pressure of Na at these temperatures, starting materials were kept to ~ 0.6 g. While the reaction proceeded to completion, the resulting PXRD patterns of the products best corresponded to published NaGe patterns,[146] albeit with significant apparent impurities. Since it had also been found that, using the equivalent procedure for the production of Ge_{136}, a NaGe precursor could be used more effectively,[147] a 1:1 Na:Ge reaction was attempted and the resulting products gave a much cleaner, NaGe pattern that was in better agreement with literature structures. All further syntheses used a 1:1 Na:Ge ratio of starting materials (0.14 g Na, 0.46 g Ge). Figure 4.1 shows a comparison of the experimental PXRD pattern to a pattern calculated[148] from published structural data.[146]

The products from some high temperature treatments displayed a peak at 27° in addition to those observed in Figure 4.1. The characteristic polycrystalline Ge peak is located at 27° and the anomalous peak was, therefore, attributed to unreacted Ge.[149] It

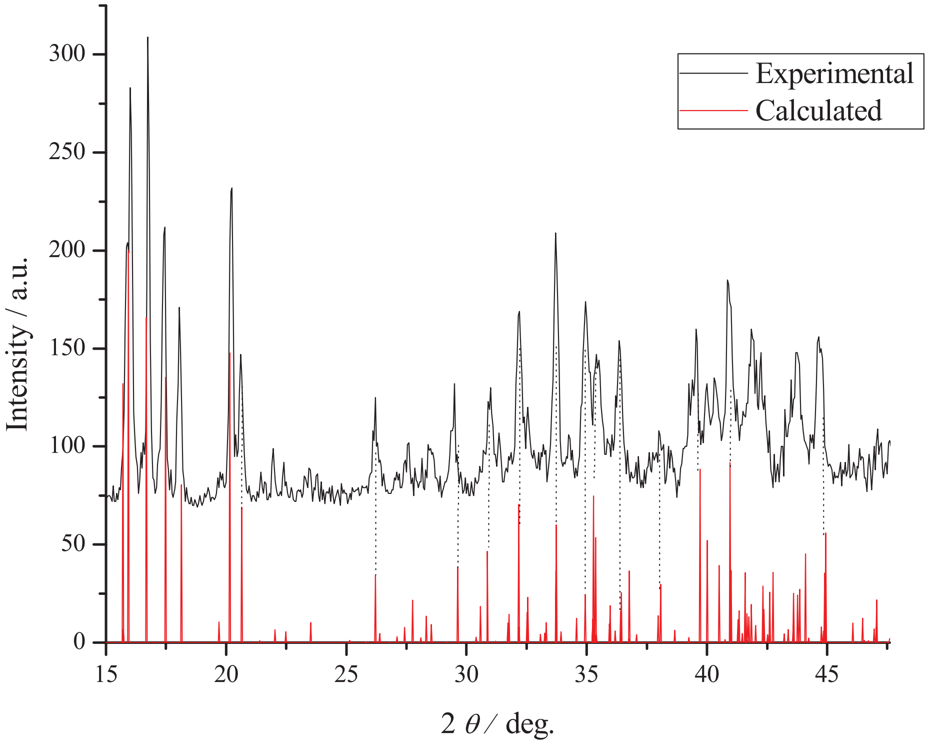

Figure 4.1 – Experimental PXRD data from Zintl ion preparation compared with a calculated[148] pattern (red) for NaGe. Major peaks are in consistent agreement with both published calculated patterns[150] and that calculated here.[148] Only minor impurity peaks are present.

was also found that a pattern calculated[148] using *a*, *b* and *c* parameters of 12.25 Å, 6.65 Å and 11.27 Å respectively rather than the 12.33 Å, 6.7 Å and 11.42 Å from literature,[146] produced better agreement with experimental data. The published P21/c space group and *β* angle of 119.9º resulted in the best agreement with the experimental pattern. Some of the lower magnitude, higher angle, experimental peaks are slightly shifted compared to the calculated[148] pattern. This might indicate a slight difference in some lattice parameters compared to the published structure. However, overall agreement between experimental, calculated[148] and published patterns is good, indicating that the

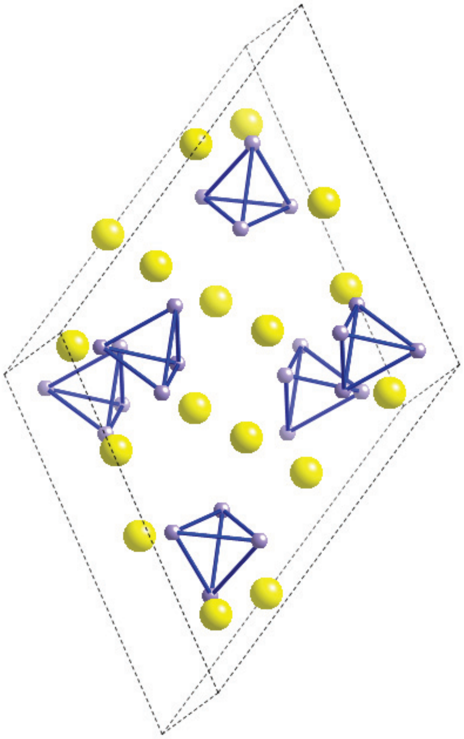

Figure 4.2 – Physical arrangement of the Ge tetrahedral (grey spheres connected with blue lines) and Na counter ions (yellow spheres) in the NaGe Zintl phase precursor compound.[146]

NaGe Zintl phase was produced. Physically, this structure is comprised of Ge^{4-} tetrahedra that are neutralized by 4 Na counter ions. Figure 4.2 shows how the Ge and Na components are arranged in space.[146]

4.1.1.2 Type II Ge Clathrate Production

The ionic reaction medium (for the oxidation of the NaGe precursor) was prepared by mixing 1:1 stoichiometric amounts of purified dodecyltrimethylammonium chloride (≥ 99 % pure, Sigma-Aldrich) and high-purity aluminium chloride (anhydrous, sublimed ≥ 98 % pure, from Sigma-Aldrich) in an Ar filled glove box. Mixing of the two components was done at ~ 325 K since the ionic liquid melts at 315 K. The ionic liquid was then placed into the quartz-glass reaction vessel already containing the NaGe precursor compound (0.1 g of NaGe in ~ 1.5 g ionic liquid). Finally, the mixture was heated to 575 K, the threshold for decomposition of the ionic liquid,[147] and held at that temperature for 24 hours under an Ar atmosphere. Following the high temperature treatment, the reaction mixture had changed from a golden yellow to dark brown. This indicated that the ionic liquid had degraded over the course of the reaction. Once cooled to room temperature, concentrated HCl, acetone and ethanol washes were used to separate the product from the product mixture. The product was then rinsed with distilled water and allowed to dry.

Products were isolated in yields of 40 to 60 % for each of the three successful synthetic attempts. It is expected that yields could be improved by increasing the amount of starting materials and using a larger, wider mouth, reaction vessel. A larger opening would facilitate transfer of the ionic liquid reaction medium to the vessel as well as removal of final products from the reaction vessel. This, in turn, would reduce the losses due to handling.

In addition to the ionic liquid and clathrate compounds, there was a brilliantly blue coloured, low viscosity liquid present atop the ionic liquid mixture following one reaction. This was decanted under an inert atmosphere and stored in an airtight container. The liquid turned from bright blue to brown over the course of several days, before its composition could be analysed.

PXRD patterns of the Ge clathrate products obtained were compared to both calculated[148] and published[85,147] patterns for Ge_{136}. Experimental patterns were found to

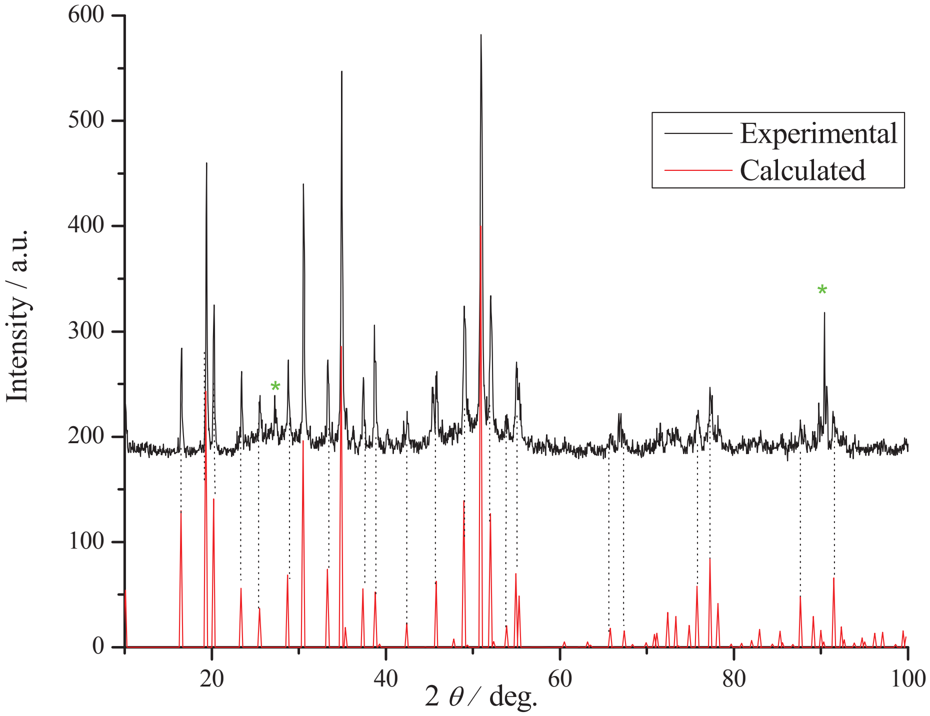

Figure 4. 3 – PXRD pattern for the soft oxidation products alongside a calculated[148] pattern (red) for Ge_{136}. The two * marked peaks are not present in the simulated pattern. The lower angle * peak (~ 27°) is attributed to polycrystalline Ge and the high angle * peak (~ 92°) has not been identified.

be in good agreement with both calculated[148] and literature patterns. Figure 4.3 shows the PXRD pattern for the products compared to a calculated[148] pattern.

The experimental pattern shows good agreement in peak position and intensity with both the published[85] pattern for Ge_{136} and the pattern calculated[148] for the present study. The peak at 27°, marked with an asterisk, was due to the presence of polycrystalline Ge. The high angle peak, ~ 92° was not found in published XRD pattern and has been attributed to an unidentified impurity.

4.1.1.3 Importance of Reaction Time

Although ionic liquids have often been lauded as low vapour pressure solvents,[151] significant pressure arose during these procedures. When the ionic liquid components were mixed, a visible off-gassing ensued. Because of difficulty in manipulating the viscous liquid, mixing of the components for the original synthesis attempt was performed in the quartz-glass reaction ampoule. The components mixed, with some effort, at elevated temperature (using a heat gun). When the NaGe/ionic liquid mixture was heated to 575 K for the oxidative step, the ampoule failed. While transferring the pre-mixed ionic liquid was cumbersome compared to placing unmixed powders into the ampoule, it led to reaction pressures that the quartz-glass ampoule could withstand. It is, therefore, *essential* that the ionic liquid components be mixed prior to sealing the reaction ampoule. Transfer of the reaction components would be facilitated by a larger mouth, reusable, preferably metal, reaction vessel.

If the reaction mixture was removed from the furnace after 15 hours (rather than 24 hours) an amorphous Ge product, rather than the desired type II clathrate, was formed. Figure 4.4 shows a PXRD pattern for a NaGe oxidation attempt that was stopped after 15 hours of heating. The pattern shows two broad amorphous peaks: one in the vicinity of the major polycrystalline Ge peak (~ 27°) and one near the primary clathrate peak (~ 51°). In addition, there is a peak near 32° (31.78°) indicating the presence of Na oxide. This produced an amorphous Ge sample, for which transport measurements (S, κ and σ) were also measured.

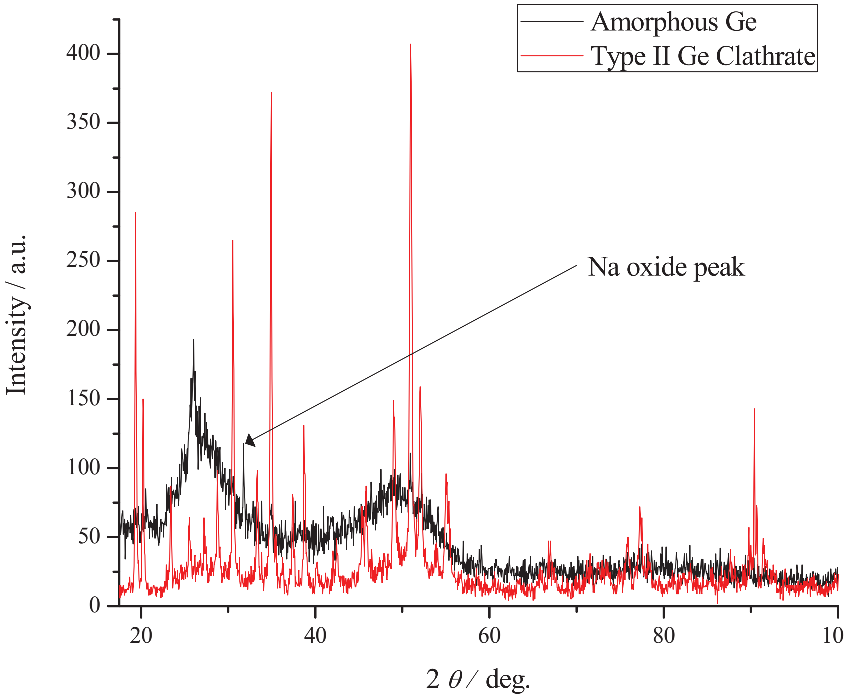

Figure 4.4 – PXRD patterns for both the product resulting from a 15 hour reaction time (primarily amorphous Ge) as well as that obtained from a 24 hour reaction time (confirmed Ge_{136}) (red). The peak ~ 32° indicates the presence of sodium oxide. The broad peaks, centred at ~ 27° and ~ 51°, are indicative of an amorphous majority phase.

4.1.1.4 Na Content

The relative intensities of the strongest diffraction peaks for Na_xSi_{136} materials have been shown to be sensitive to Na content and location: they can be used to determine relative cage occupations and overall Na content.[66,116] X-ray diffraction patterns simulated for Na_xGe_{136} materials indicate that the ratio of the peaks located at 34.9° and 30.4° (attributed to the 135 and 115 planes) respectively range from 1.5 in the empty Ge clathrate, Ge_{136}, to 1.13 when the Ge_{28} cages are fully occupied, Na_8Ge_{136}. Full occupation of the Ge_{20} cages (with no Na in the Ge_{28} cages) results in a ratio of 1.4.

Other peak ratios show similar, but less pronounced, Na content dependencies. Since the presence of Na in the two different environments has been calculated to have subtle and opposite effects on PXRD peak intensities and since samples of varying Na content are not available for comparison, PXRD is not currently a practical technique for quantitative determination of Na content in type II Ge clathrates. PXRD can, however, be used to qualitatively indicate the presence of Na within the Ge_{136} framework.

The materials produced in the three successful synthetic attempts of the present study showed (135):(115) peak intensity ratios of 1.25 to 1.4. Given that these are both smaller than 1.5, the ratio shown in patterns calculated[148] for the empty Ge_{136} structure, this suggested that Na was present within the Ge_{136} framework. Since PXRD was not a practical means of Na content determination, alternative methods were used to assess the Na content of the type II Ge clathrate.

Following consolidation and physical property measurement, energy dispersive (EDS) and wave dispersive (WDS) spectroscopies were employed to determine the Na content of the sample. The sample examined was a cold-press consolidated mixture of the three successful syntheses. First, EDS was used to determine the elemental identities of the sample's major compositional components. EDS analysis indicated the presence of Si, O and Ag contamination within the sample. Figure 4.5 highlights the regions of Si and Ag contamination.

None of the contaminant elements were present in large quantities and the origins of all contaminants are known. Silver was detected as a result of the incomplete removal of the conductive epoxy used to mount the sample for TTO measurements and is restricted to low lying regions of the sample. The O signal was the result of surface

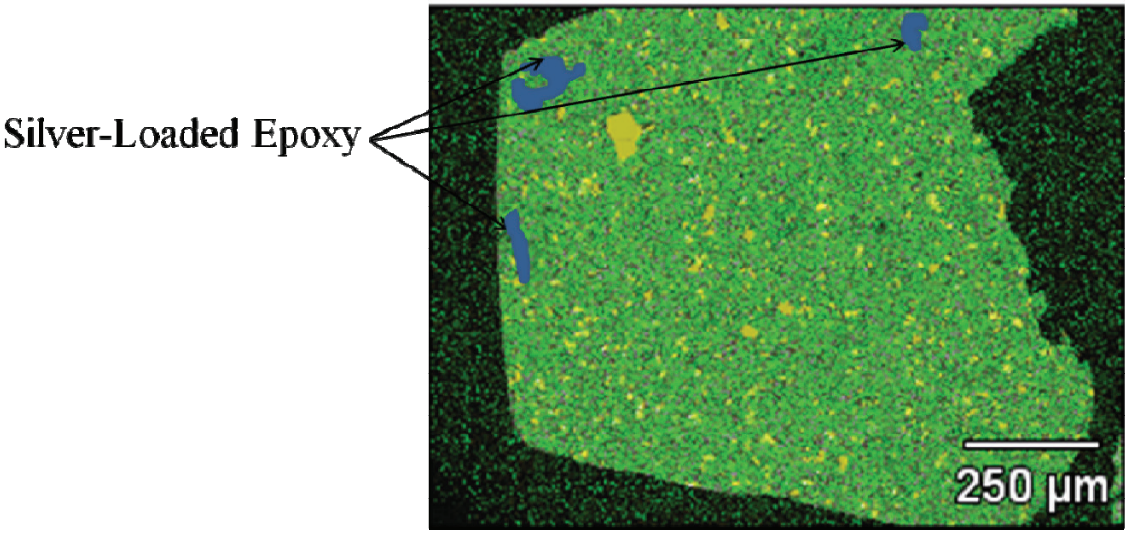

Figure 4.5 – EDS derived compositional map of a Ge clathrate sample. The blue areas are traces of the silver-loaded epoxy, used to secure the sample to TTO leads, incompletely removed. Outside of the Ag contamination areas, green indicates Ge. The yellow areas are Si resulting from contamination from laboratory equipment.

oxidation upon exposure to the atmosphere. Si is present in distinct regions, as imbedded shards of cold-pressed pellets throughout the sample, carried over from Na_xSi_{136} sample preparation. This contamination resulted from the use of mortar and pestle that were not completely free of Na_xSi_{136}. It was found that it was quite difficult to entirely remove the silicon clathrate from the corundum grinding tools. An HF wash was found to be necessary to completely clean the surfaces of the grinding tools. The low level Si contamination, estimated to be on the order of a few percent, is not expected to greatly impact the physical properties of the Ge clathrate sample.[85]

Figure 4.6 shows that Na and O were homogeneously distributed throughout the sample. From Figure 4.6 (a) it can be seen that the silicon clathrate impurity in the Ge

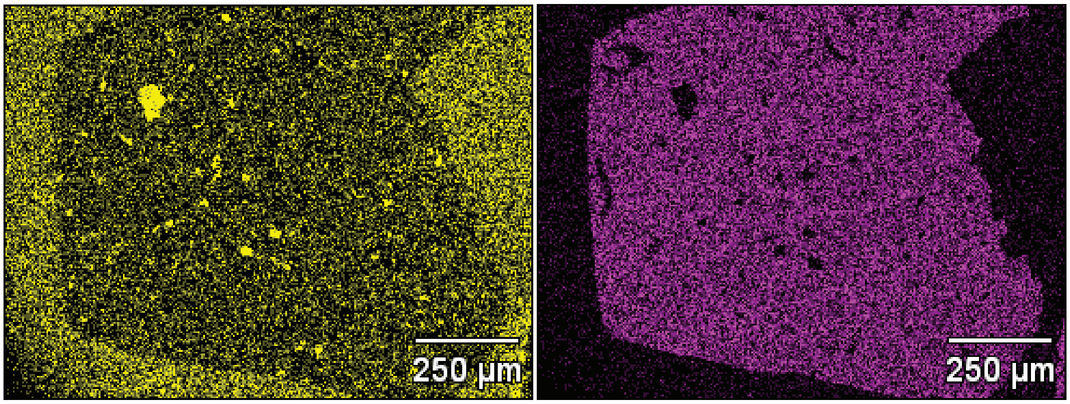

Figure 4.6 – Qualitative EDS results from the Ge clathrate sample. (a) shows the O signal (yellow) and (b) the Na signal (purple).

clathrate sample shows a stronger O signal and weaker Na signal than the Ge sample. This indicates that the Si clathrate samples were more significantly oxidized compared to the Ge clathrate produced.

Table 4.1 – Microprobe, WDS, data obtained from Na and Ge analysis of the type II Ge clathrate produced for the present study. Oxygen comprises the remainder of the sample composition (~ 15 %). Quantitative data were obtained from a polished, carbon coated sample using an exciting accelerating voltage of 15 keV and a beam diameter of 20 μm.

Spot number	Na Atomic %	Ge Atomic %
1	6.95	79.9
2	4.06	83.3
3	4.53	86.1
4	6.18	81.7
5	5.26	85.8
6	5.09	83.3
7	5.71	84.7
8	6.81	81.1
9	4.81	77.2
10	5.18	79.6
Average	5.46	82.3
Standard Deviation	0.95	2.9

Following the qualitative EDS compositional study, WDS was employed as a means to quantify the Na content of the Ge clathrate sample. Spot size and locations for analysis were chosen in order to avoid regions of silver epoxy and silicon contamination. Table 4.1 presents results from the WDS analysis.

From data presented in Table 4.1 it can be seen that an empty clathrate was not obtained. Indeed, these data indicate an average x value of 9 for this sample. In addition to a larger Na content than expected, these results suggest that the sample was not completely homogeneous. While the Ge fraction is consistent (82 ± 3), Na shows significant variation (5.5 ± 0.9). The inhomogeneity was in part due to the sample being a mixture of three synthetic batches (it was necessary to combine the products from more than one synthesis in order to produce a pellet of sufficient size for physical property measurements). There is a possibility that the elevated Na content was the result of unreacted Na and/or Na oxide. However, since concentrated HCl washes were employed when isolating the compound, before it had been exposed to the ambient atmosphere, incorporation of Na into the Ge framework is more likely.

Guloy[85] found a 0.8 % Na content by mass in their Ge_{136} sample, via inductively coupled plasma optical emission spectroscopy. In the same study, using electron energy loss spectroscopy, a very weak Na signal was obtained from a minor, amorphous Ge, impurity phase. Consequently, Na content was concluded to reside in the amorphous Ge phase. Assuming that the amorphous Ge phase comprised 10 % of the sample or less, a 0.8 mass % of Na represents approximately 1/3 of the impurity phase by mole, or more. This would be expected to be detected as a significant signal and suggests that the Na content has not been entirely accounted for. Since it was not possible to separate the Ge clathrate from impurity phases and PXRD studies showed that there was Na in the Ge clathrate structure produced here, Na content for the present study has been assumed to be incorporated into the clathrate framework. Therefore, the Ge material produced will be referred to as Na_9Ge_{136} in further discussions.

4.1.2 Sn Clathrate

The same procedure that produced Na_9Ge_{136} was applied to tin since there are a number of examples of Sn clathrates known in the literature.[142,143] In addition, the clathrand is expected to be stable[152] and filled type II examples are expected to have improved rattling qualities compared to type II clathrates of lower mass, group 14 elements.[153,154]

4.1.2.1 NaSn Precursor

The Sn Zintl ion precursor, NaSn, was produced by subjecting ~ 1 g (0.16 g Na with 0.84 g Sn) of a 1:1 stoichiometreic Na: Sn (99.8 % pure tin shot from Sigma-Aldrich) mixture to 1075 K for 30 minutes, followed by a two hour annealing period at 775 K. This was done in stainless steel, since the temperatures used were below the 1075 K threshold discussed above. The diffraction pattern shown in Figure 4.7 indicates that the desired compound was produced.

The NaSn PXRD pattern presented in Figure 4.7 also indicates the presence of elemental tin. More complete conversion of the starting materials to the Zintl ion might

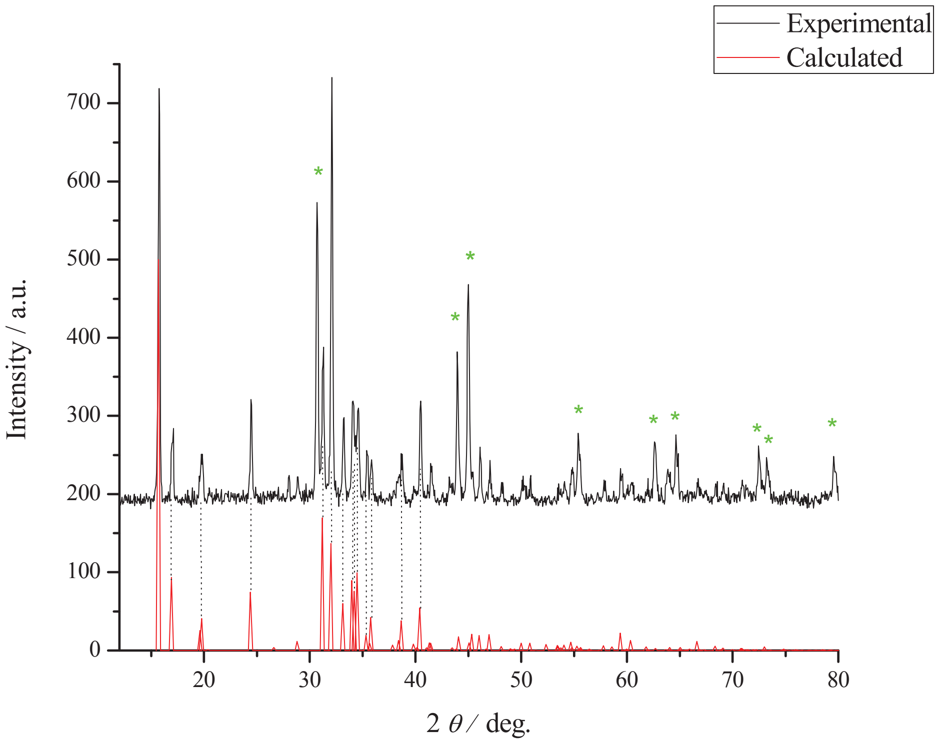

Figure 4.7 – PXRD pattern of the NaSn Zintl ion along with a calculated[148] pattern (red). Peaks marked with asterisks correspond to elemental Sn.

be achieved with longer heating periods and/ or higher temperature annealing. Further study is required in order to optimize NaSn production. While a purer NaSn precursor material would have been optimal, the product obtained allowed for an attempt at Sn_{136} production via soft oxidation by ionic liquid.

4.1.2.2 Soft Oxidation of NaSn

Although the NaSn Zintl ion is stable to 851 K,[155] it was assumed that, as with the Ge and Si cases, the clathrand form of Sn would have a lower melting temperature than its standard allotrope (tin melts at 505 K). The oxidation step was performed at 485 K, just below the melting temperature of Sn so as not to "soften" reaction conditions too much. This attempt was not successful: once washed, the x-ray pattern showed only tetragonal, elemental Sn. Despite this initial lack of success, there is still work to be done before this approach should be wholly abandoned.

It is likely that the oxidation was carried out at too high a temperature for Sn clathrate formation. Ge_{136} has been reported as stable to 690 K[85] compared to 1210 K for diamond structured Ge. Na containing type II Si clathrates are stable to ~ 600 K[102] and Si_{136} is stable to 1475 K[156,157] compared to 1683 K for diamond structured Si. It would, therefore, be worthwhile to attempt the oxidation step at a comparable fraction, ~ 40-60 %, of the melting point of tin's standard allotrope, *i.e.* near the melting point of the ionic liquid reaction medium.

4.2 Physical Properties

All of the thermoelectrically relevant physical properties, S, σ and κ were measured on two Ge clathrate samples and an amorphous Ge sample. There was significant variation between the two different Ge clathrate samples. The first experiments were performed on a larger sample of unknown Na content. Following these measurements, the sample was re-ground, had the confirmed Ge clathrate products of another synthetic run added to it and the sum was re-pressed for measurement. The re-processed sample is that for which compositional data are presented above. Differences in the physical properties of the two Ge clathrate samples are attributed to differences in Na content. Since compositional details of the earlier sample are not known it has not been possible to delineate trends in physical properties with changing Na content.

However, the preliminary data of the present study are strongly reminiscent of those obtained for the type II silicon clathrate series and provide direction for further study into the type II Ge clathrate system.

4.2.1 Seebeck Coefficient, *S*

4.2.1.1 Results

Seebeck voltages were measured for the Na_9Ge_{136} sample. Figure 4.8 presents these data as well as those for $Na_{8.8}Si_{136}$, the most comparable Na_xSi_{136} sample available.

The data in Figure 4.8 show the same trend with temperature seen in the Si clathrate series of samples: negative *S* values go linearly to zero with decreasing temperature. From Figure 4.8 it can also be seen that the Na_9Ge_{136} clathrate produced larger Seebeck voltages than did the Si analogue. Seebeck coefficient data were not obtained for the first Na_xGe_{136} sample, nor did the amorphous Ge sample produce Seebeck coefficient data.

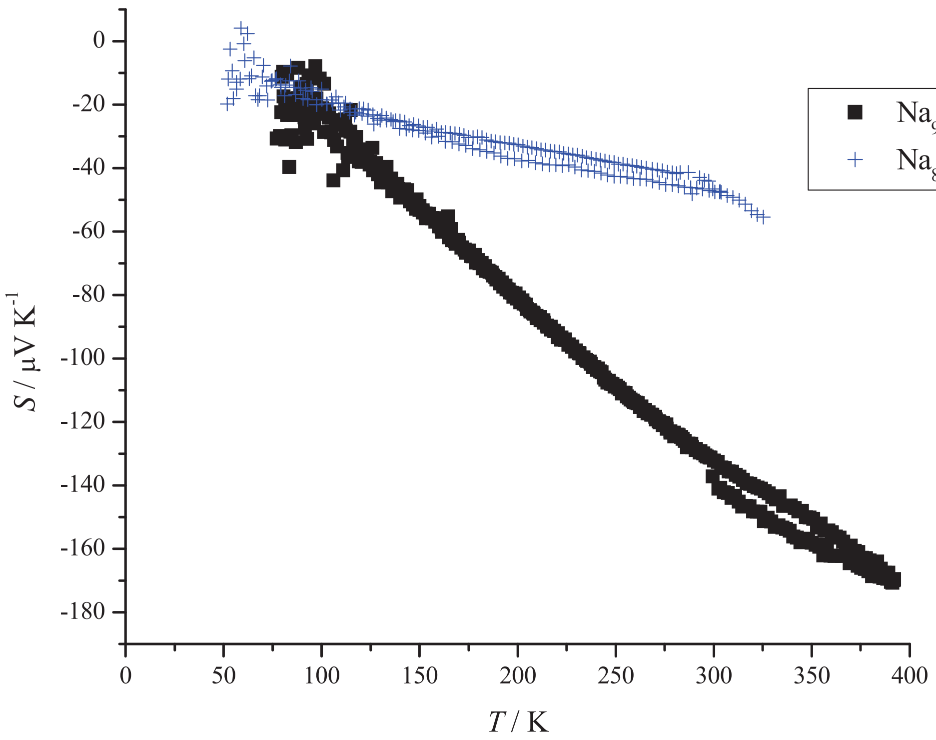

Figure 4.8 – Seebeck coefficient data for the Na_9Ge_{136}. Data for the Na_xSi_{136} analogue ($x = 8.8$) are also presented for comparison.

4.2.1.2 Literature Comparison

While no data exist in the literature for partially Na filled type II Ge clathrates, Seebeck coefficients are reported for filled type II Si and Ge clathrates. $Cs_8Na_{16}Ge_{136}$ has shown a Seebeck coefficient of -6 µV/K at 300 K[158] while $Cs_8Na_{16}Si_{136}$ has shown a value of -27 µV/K at 300 K.[159] These magnitudes are significantly lower than those presented in Figure 4.8, indicating greater charge transfer between the Cs and Na rattler atoms and the Si and Ge frameworks, according to the trend set forth in Figure 1.7.

In addition, the trend in magnitude with framework constituent is reversed in the present data. Figure 4.8 shows an increase in Seebeck coefficient magnitude upon going from a Si_{136} framework to Ge_{136}. Na_9Ge_{136} shows a room temperature Seebeck value of ~ 140 μV/K at 300 K. This is approximately 1.5 times that of the highest room temperature value observed in any of the Na_xSi_{136} series of samples, Figure 3.8.

4.2.1.3 Discussion

Since Na_xSi_{136} experiments showed that thicker pellets were more likely to produce S data, it is surprising that the later Na_9Ge_{136} experiment, performed on a 0.40 mm thick pellet, produced S data while the earlier experiment for Na_xGe_{136}, performed on a 0.76 mm thick pellet, did not. Na_xSi_{136} experiments also showed that Seebeck coefficient magnitudes were dependent on Na content, increasing with decreasing content and then becoming unmeasureable. Given that the Ge sample of greater thickness did not produce S data and the Na content dependence seen in the Na_xSi_{136} samples, the lack of data from the earlier experiment performed on the Na_xGe_{136} sample is tentatively attributed to low Na content. Similarly, with no Na content, the lack of S data for the amorphous Ge sample is attributed to a lack of mobile electron density.

Since $|S|$ decreases with increasing charge carrier concentration, Figure 1.7, the higher magnitude S data obtained from the Na_9Ge_{136} sample compared to the Na_xSi_{136} samples indicate that there is less charge transfer between Na and the Ge framework than between Na and the Si framework in these type II clathrates. This is in contrast to what is observed in the filled, $Cs_8Na_{16}Ge_{136}$[158] and $Cs_8Na_{16}Si_{136}$[159] systems in which the Si analogue exhibits larger Seebeck coefficient. Low temperature XAS studies would be helpful in clarifying the origins of the differences between the systems.

4.2.2 Electrical Conductivity

4.2.2.1 Results

In contrast to the Si samples, electrical conductivity data were obtained for all Ge samples studied. All samples displayed some measureable electrical conductivity while the low Na content Si samples, $x = 1.3$ and 5.5 showed no measureable electrical conduction. Figure 4.9 presents the electrical conductivity data for all Ge products as.

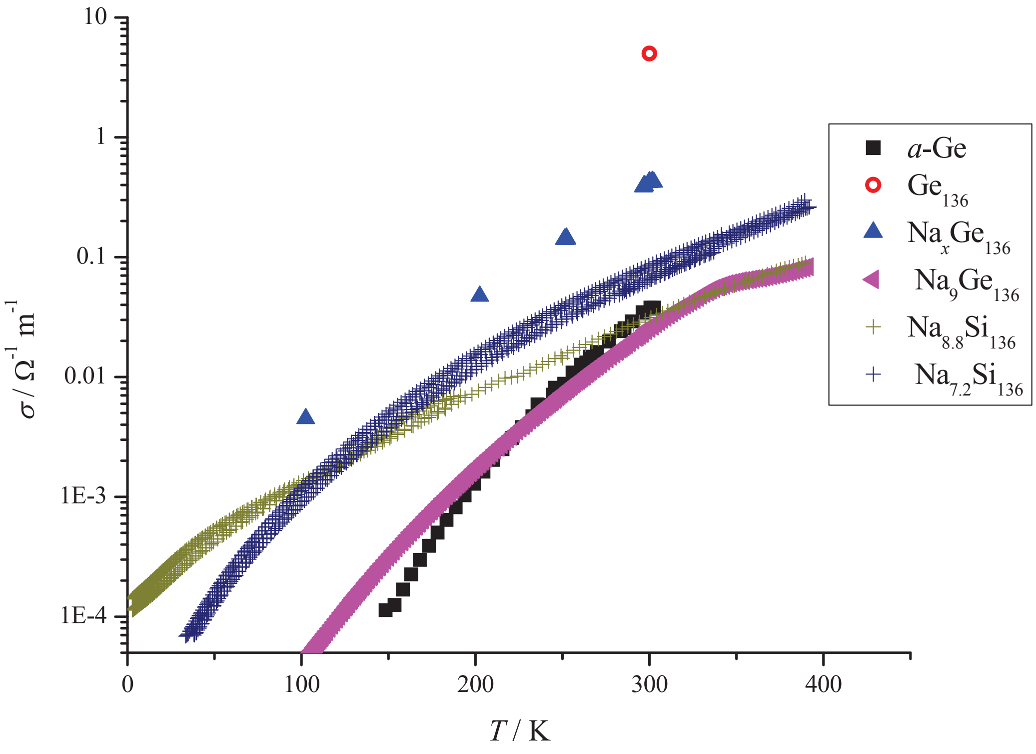

Figure 4.9 – Electrical conductivity data for products resulting from Ge clathrate syntheses, including partially Na filled type II Ge clathrates and amorphous Ge. The Ge_{136} data point is taken from literature[85] and data from the present study for the Na_xSi_{136} samples of similar Na content ($x = 8.8$ and 7.2) are presented for purposes of comparison.

well as data for $Na_{7.2}Si_{136}$ and $Na_{8.8}Si_{136}$, the two Si clathrates measured for the present study that were closest in Na content to Na_9Ge_{136}

The data in Figure 4.9 show electrical conductivity magnitudes similar to those seen in the similar Na_xSi_{136} samples. These data also show semiconducting trends for all samples (increasing conductivity with increasing temperature). DC measurements confirmed the AC transport values for Na_9Ge_{136}. The low values shown in Figure 4.9 are therefore attributed to the sample and not measurement technique.

4.2.2.2 Literature Comparison

$Cs_8Na_{16}Ge_{136}$[158] and $Cs_8Na_{16}Si_{136}$[159] have shown electrical conductivities with metallic temperature dependencies and room-temperature values of $5 \times 10^5\ \Omega^{-1}\ m^{-1}$ and $1.5 \times 10^5\ \Omega^{-1}\ m^{-1}$, respectively. Both the filled Si structure and the filled Ge structure demonstrate significantly higher electrical conductivities compared to the partially Na filled structures measured for the present study. From these literature data one might expect to observe an increase in electrical conductivity going from the Si to Ge type II structure. However, electrical conductivity measurements on cold-pressed type II Na containing clathrates have not been shown to be of adequate sensitivity to detect differences on this scale.

Electrical conductivity measured on a cold-pressed sample of the reported Ge_{136} showed a room-temperature electrical conductivity of ~ $5\ \Omega^{-1}\ m^{-1}$.[85] This is more than an order of magnitude higher than data shown in Figure 4.9. The higher literature values are attributed to performing consolidation under inert atmosphere. The present data were recorded from a sample that had been exposed to the ambient atmosphere before cold-pressing and was therefore somewhat oxidized.

4.2.2.3 Discussion

The higher electrical conductivity exhibited by the Na_xGe_{136} sample, compared to Na_9Ge_{136}, could be a result of intrinsic effects or less oxidation. Since cold-pressed Na_xSi_{136} samples were found to be relatively insensitive to Na content and quite sensitive to oxidation, it is likely that increased oxidation is responsible for the change in electrical conductivity. The Na_9Si_{136} sample was pressed and re-ground several times while attempting to produce a coherent pellet. This additional processing likely resulted in further oxidation of the sample.

The present data indicate that the type II Ge clathrates have electrical conductivities comparable to the Na_xSi_{136} series of samples with similar Na loadings. In addition, it is apparent that the electrical conductivities of cold-pressed Na_xGe_{136} samples, like those of the Na_xSi_{136} samples, are more sensitive to oxidation than Na content. Preparing samples for σ measurements in inert atmosphere would improve results.

4.2.3 Heat capacity

4.2.3.1 Results

The heat capacity of Na_9Ge_{136} was measured from 2.5 K to 300 K. Figure 4.10 presents the results of those measurements.

The experimental data shown in Figure 4.10 were taken from two different Na_9Ge_{136} samples of differing masses, 6.46 mg and 9.69 mg. Sample coupling values for all measurement reported in Figure 4.10 were greater than 96 %. Sample heat capacities accounted for 30 to 70 % of the total heat capacity (sample and grease) in the 9.69 mg sample and 20 to 60 % in the 6.46 mg sample. Below 160 K, the 6.46 mg sample contributed 30% or more to the total heat capacity. Reduced heat capacity contributions from the 6.46 mg sample at higher temperatures ($T > 160$ K) account for the increased

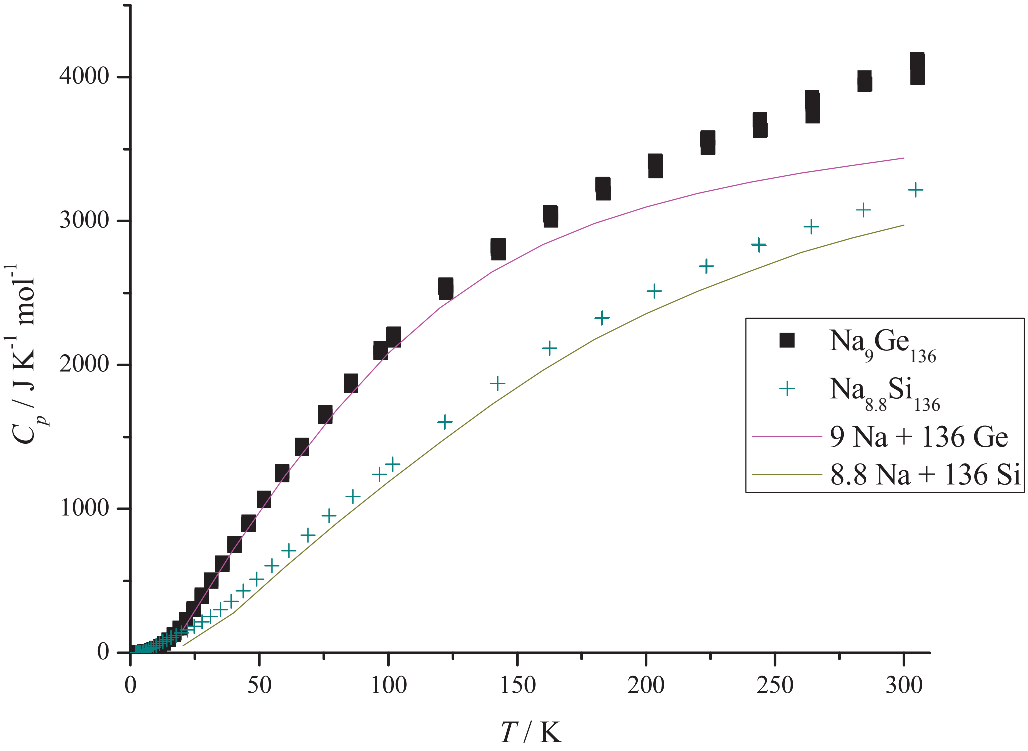

Figure 4.10 – Experimental heat capacity data for Na_9Ge_{136} and the Na_xSi_{136} sample with the most similar Na content, $x = 8.8$. Data derived from the constituent additivity model are also included for both materials.

uncertainty at higher temperatures. Values at 300 K, the high temperature limit of the experiment where uncertainty is greatest, show standard deviations about the average value of 3 % or less.

4.2.3.2 Literature Comparison

Heat capacity data for type II Ge clathrate systems are not available in the literature.

4.2.3.3 Discussion

Like the Na_xSi_{136} samples, the Na_9Ge_{136} samples showed smooth, phase transition free, heat capacity curves. Not unexpectedly, since Ge has a higher heat capacity than Si,[160] the Ge clathrate has a higher heat capacity than the Si analogue. Also similar to the Na_xSi_{136} samples, the heat capacity of the Ge clathrate exceeds the heat capacity of its constituent additivity model. Figure 4.11 illustrates how experimental data differ from the additivity model with varying temperature.

From Figure 4.11 it can be seen that below 150 K the additivity model predicts the heat capacity of Na_9Ge_{136} within ~ 5 %, but the difference increases with increasing temperature. In this way, the Ge clathrate is similar to the unoccupied Si clathrate, Figure 3.35 (b), which shows increased deviation from the additive model with increasing temperature. However, the more consistent deviation from the additivity model at lower temperatures, below 150 K, is more reminiscent of the Na containing Si clathrates,

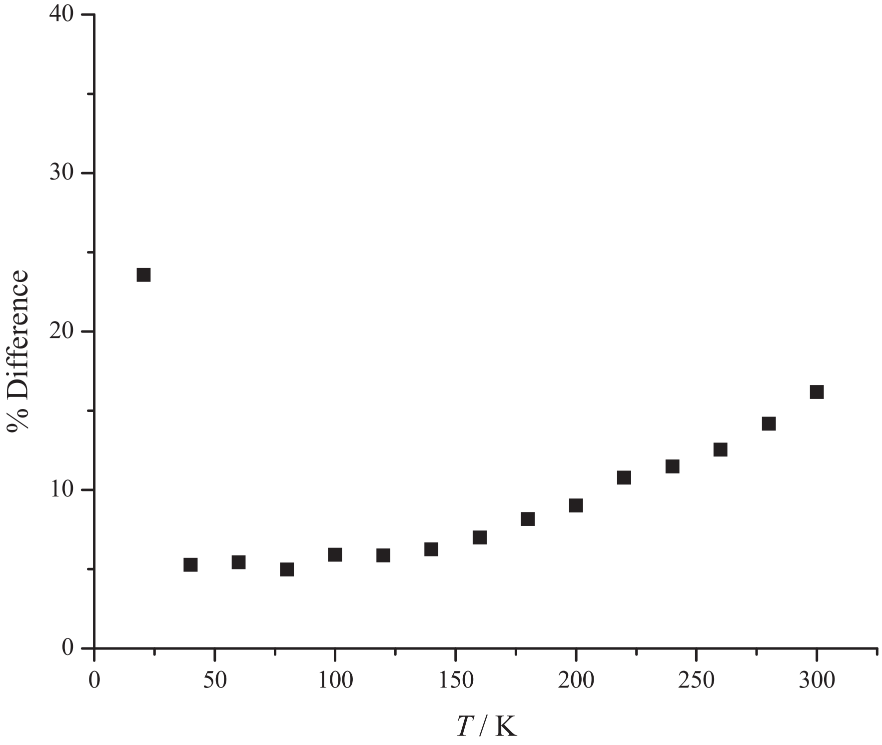

Figure 4.11 – Difference between experimental heat capacity of Na_9Ge_{136} and the additivity mode. Difference is plotted as % relative to the experimental data.

Figures 3.27 to 3.34. Deviation from the additivity model indicates that the Na_9Ge_{136} structure is less stiff compared to its elemental constituent structures.

4.2.3.3.1 Low Temperature Heat Capacity

As with the Na_xSi_{136} series of samples, by dividing low temperature heat capacity values by T^3 and plotting the resulting values against T^2, it was possible to demonstrate heat capacity contributions from low frequency modes. Figure 4.12 presents data from Na_9Ge_{136} compared with $Na_{8.8}Si_{136}$ in this context.

Figure 4.12 shows a different low temperature profile for Na_9Ge_{136} compared to that of $Na_{8.8}Si_{136}$. Values for Na_9Ge_{136} increase with decreasing temperatures. The increase becomes more apparent with decreasing temperature and a significant slope is seen at the lowest temperatures. This shape is reminiscent of the 75 K^2 to 400 K^2 portion of the $Na_{8.8}Si_{136}$ curve. The increase seen in the Na_9Ge_{136} curve continues down to temperatures below the lower limit of the experiments presented in Figure 4.12. As such,

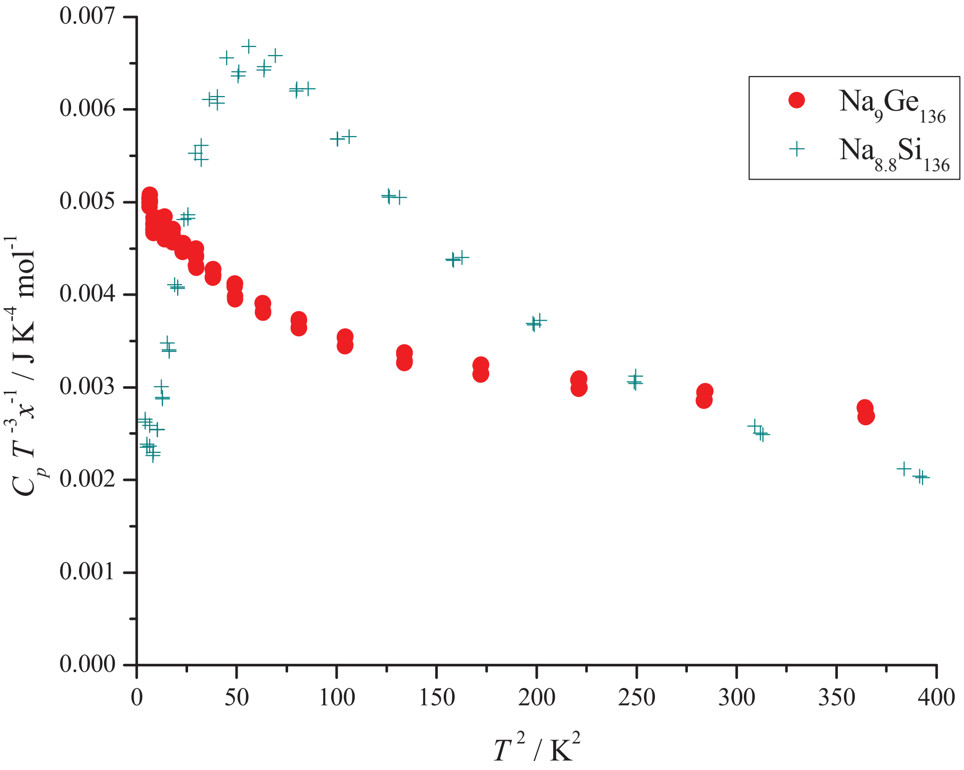

Figure 4.12 – Low temperature $C_p\,T^{-3}\,x^{-1}$ versus T^2 data demonstrating the presence of low energy vibrational modes associated with Na guest atoms. These data present rattler contributions to sample heat capacities on per Na content bases for both Na_9Ge_{136} and $Na_{8.8}Si_{136}$.

unlike in the $Na_{8.8}Si_{136}$ curve, Figure 3.23, no complete peak is observed and lower temperature experiments are required to confirm or refute the presence of a low temperature peak in the type II Ge clathrate.

In addition, since the sample is likely quite inhomogeneous the low temperature feature may be due to the presence of several peaks of varying magnitudes and positions. Nevertheless, it is apparent from Figure 4.12 that there are low temperature vibrations causing the heat capacity to deviate from the expected low temperature behaviour. This is especially true at the low temperature limit where the increase is most dramatic. More homogeneous samples and lower temperature heat capacity measurements are required for a more complete description of these modes.

Assuming the increase in heat capacity at the low temperature limit of the data is associated with a peak, Figure 4.12 indicates a significant shift towards lower energy modes compared to the $Na_{8.8}Si_{136}$. This would be in keeping with the larger unit cell of the Ge_{136} framework since the extra room, compared to the Na_xSi_{136} structures, would allow more freedom for Na motion. This hypothesis is strengthened by examining the differences in unit cell size. The Ge clathrate described by Guloy,[85] had a unit cell parameter of 15.21 Å and the Si clathrates with $x \leq 8.8$ have unit cell parameters of approximately 14.65 Å.[115] If the Si_{20}, Si_{28}, Ge_{20} and Ge_{28} cages are approximated as spheres and assumed to have volumes proportional to the number of atoms they are comprised of, the increase in lattice parameter corresponds to increases in cage volumes from 115 $Å^3$ and 162 $Å^3$ for Si_{20} and Si_{28}, respectively, to 129 $Å^3$ and 181 $Å^3$ for Ge_{20} and Ge_{28}. This means that overall there is more room for the Na to rattle inside the cages of the Ge structure than in the Si structure and Na in Ge_{20} cages is more likely to have associated low energy vibrations than in the Si_{20} cages. However, the Ge_{20} cage is still smaller than the Si_{28} cage, the only structure for which rattling modes have been confirmed. It, therefore, cannot be said that Na in Ge_{20} does have associated rattler modes, but it is likely that inclusion of Na within Ge_{20} more subtly affects the lattice dynamics of type II Ge clathrates than those of the type II Si clathrates. In addition to more homogeneous samples, samples of varying Na content are required to confirm this hypothesis.

4.2.3.3.2 Electronic Heat Capacity

In addition to examining the possibility of Na rattling in the Ge clathrate, as for the Na_xSi_{136} sample series, low temperature heat capacity over T versus T^2 has been plotted in order to evaluate electronic contributions to heat capacity. Figure 4.13 presents the result of this data treatment.

Fitting the data presented in Figure 4.13 to Equation (3.4) gives the values for the electronic contribution to heat capacity as the y-intercept and a slope from which the phononic contribution can be estimated. These values are presented in Table 4.2.

The values presented in Table 4.2 are consistent with one another. Both have the same slope and return the same value for the Sommerfeld constant. These values indicate greater electronic contributions to heat capacity than were indicated for the Si clathrate samples of $x < 21.5$, Table 3.4. This is significant since $Na_{8.8}Si_{136}$ showed only small electronic contributions. Calculating the electronic density of states at the Fermi level, $D(E_F)$ from γ using Equation 4.5 gives a value of 36 eV^{-1}. This is slightly lower than the value calculated for $Na_{21.5}Si_{136}$ (42 eV^{-1}) and approximately half that of the fully occupied

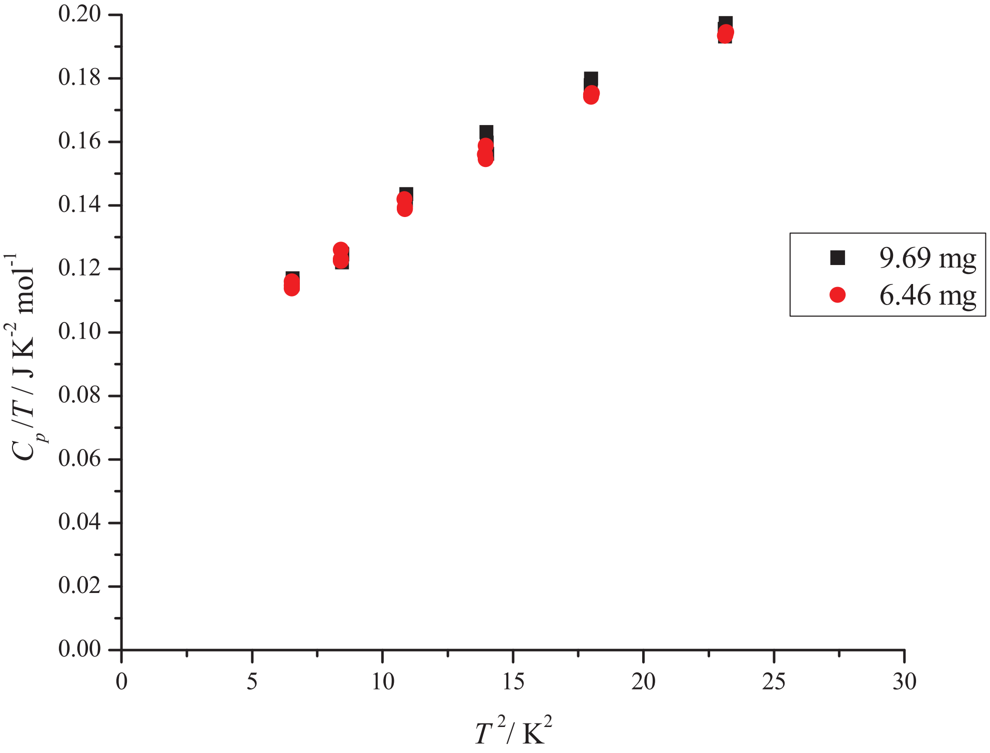

Figure 4.13 – Low temperature heat capacity data used to determine the electronic contributions to the heat capacity of Na_9Gei_{136} sample. Heat capacities have been divided by temperature and plotted against T^2.

Table 4.2 – Electronic contribution to heat capacity of Na_9Ge_{136} as determined from a linear fit of C_p/ T versus T^2 at very low temperatures. Results are presented for measurements made on two different samples of the same composition, Na_9Ge_{136}, and are in very good agreement.

Mass / mg	Slope / J K^{-4} mol^{-1}	γ / J K^{-2} mol^{-1}
9.69	0.0049 ± 0.0002	0.086 ± 0.003
6.46	0.0048 ± 0.0001	0.086 ± 0.002

single crystalline $Na_{24}Si_{136}$ sample ($D(E_F) = 68$ eV^{-1}). Given that Ge is a heavier element with significantly more electrons, it is not surprising that electronic contributions to heat capacity are more significant at lower Na loadings compared to the type II Si clathrates.

Through Equation 3.7, θ_D^{eff} can be determined from the slopes presented in Table 4.2. This corresponds to an effective Debye temperature of 386 K for Na_9Ge_{136}. This is 70 K larger than the highest value for the Na_xSi_{136}, Table 3.6. The large effective Debye temperature for the Ge clathrate is not consistent with Na_9Ge_{136} showing higher heat capacity values than $Na_{8.8}Si_{136}$ at all temperatures. In addition, elemental Si and Ge have Debye temperatures of 645 K and 374 K, respectively.[133] The clathrate forms of these elements appear to show a reversal of this trend, and an θ_D^{eff} of the expanded Ge, clathrate, phase greater than the Debye temperature of diamond phase Ge. The difference likely is related to the use of low-temperature data to assess θ_D^{eff} for Na_9Ge_{136} for which the low-temperature data show a significant anomaly, Figure 4.12.

Furthermore, through Equation 3.13 the speed of sound was determined to be 3.8×10^3 m s^{-1} for Na_9Ge_{136}. These θ_D^{eff} and v values suggest that Ge clathrates have stiffer lattices than Si clathrates of comparable compositions. The higher heat capacity of Na_9Ge_{136} compared to $Na_{8.8}Si_{136}$ shown in Figure 4.10, however, suggests that the Ge clathrate should have a lower effective Debye temperature (given that it shows higher heat capacities for the Ge clathrates throughout the temperature range) and correspondingly lower speed of sound. Indeed elemental, diamond structured, Si and Ge have heat capacities of 20 J K^{-1} mol^{-1} and 23.4 J K^{-1} mol^{-1} at room-temperature, respectively[160] and speeds of sound of 5900 m sec^{-1} and 3600 m sec^{-1} respectively (calculated from literature values for Debye temperature and crystallographic data through Equation (3.13)).[161,149] Given the low-temperature anomaly seen in the Na_9Ge_{136} heat capacity data, more detailed low-temperature studies are required to properly evaluate the dynamics of type II Ge clathrates.

4.2.4 Thermal Conductivity, *κ*

4.2.4.1 Results

Figure 4.14 presents porosity corrected thermal conductivity data for the products obtained from several Ge clathrate synthesis attempts.

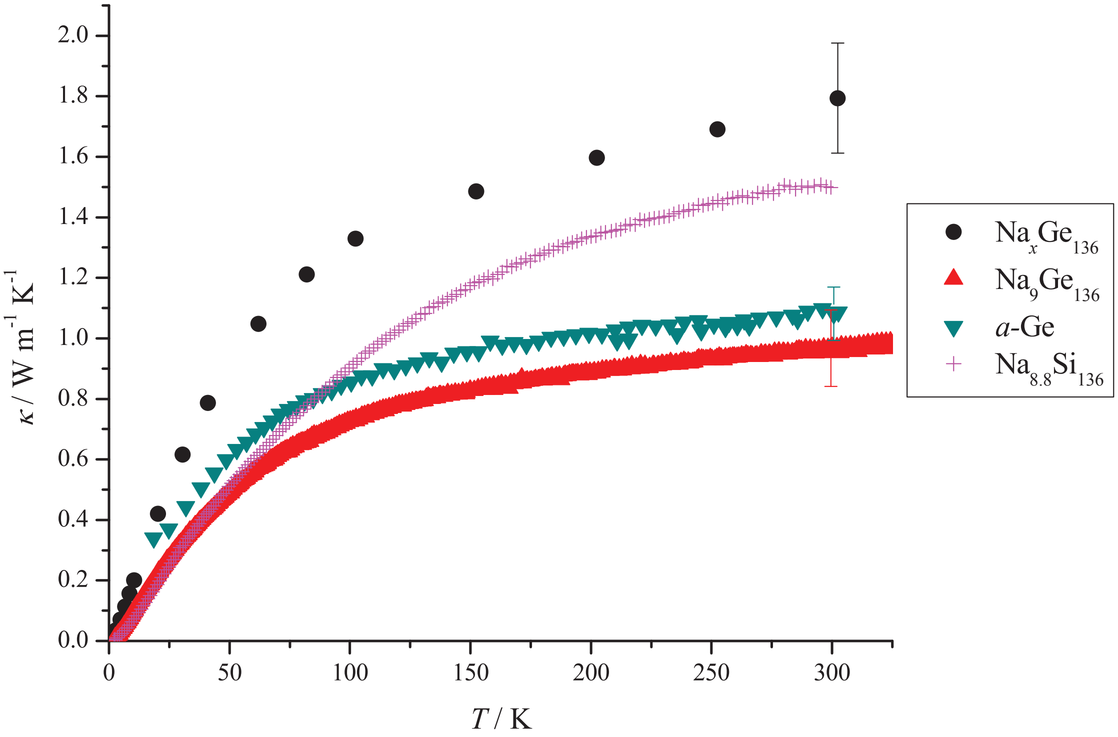

Figure 4.14 – Porosity corrected thermal conductivity data for products resulting from Ge clathrate syntheses. These products include two partially Na filled Ge clathrates, one of unknown Na content (Na_xGe_{136}) and one of known content (Na_9Ge_{136}), and also amorphous Ge. Error bars are included for values at 300 K and indicate error in porosity propagated through the typical 5 % uncertainty associated with measurements on glassy materials using a PPMS.[91] Data for the Na_xSi_{136} analogue ($x = 8.8$) are also presented for purposes of comparison.

Density calculations for the Ge clathrates assumed a lattice parameter equal to that published by Guloy[85] and an x value of 9. Given how little the lattice parameter was seen to change with increasing Na content in the Si series, that the type II Ge clathrate framework has a larger unit cell parameter than the type II Si clathrate, and how much more massive the Ge framework is compared to the Na content, these approximations introduce negligible error on the calculated bulk thermal conductivity values. Published density data from XRD studies of amorphous Ge films were used for *a*-Ge porosity corrections. The density value was 5.35 g cm^{-3} for amorphous Ge,[162] which is very close to that of diamond structured Ge, 5.3234 g cm^{-3}.[163] Table 4.3 presents data used to correct thermal conductivity values for porosity.

Table 4.3 – Pellet geometry, bulk density, ρ_{bulk}, effective density, ρ_{eff}, and fractional porosity ϕ data used to correct thermal conductivity data for porosity. Values are included for each Ge sample presented in Figure 4.14.

Sample	Thickness / cm ± 0.002 cm	Cross-section / cm	ρ_{bulk} / g cm^{-1}	ρ_{eff} / g cm^{-1}	ϕ
Na_xGe_{136}	0.076	0.181 ± 0.002	3.19 ± 0.003	4.76 ± 0.09	0.33 ± 0.04
a-Ge	0.112	0.181 ± 0.002	3.39 ± 0.003	5.35 ± 0.09	0.36 ± 0.03
Na_9Ge_{136}	0.040	0.181 ± 0.002	3.84 ± 0.003	4.76 ± 0.09	0.19 ± 0.07

4.2.4.2 Literature Comparison

As with *S* and *σ*, no thermal conductivity data were available from the literature for partially Na filled type II Ge clathrates. Filled examples were, therefore, looked to for trend comparisons. $Cs_8Na_{16}Ge_{136}$ shows a room-temperature thermal conductivity of 4.5 W m^{-1} K^{-1},[158] while the Si analogue, $Cs_8Na_{16}Si_{136}$, shows a value of 9 W m^{-1} K^{-1} at room-temperature.[159] In addition, single crystal diamond structured Si exhibits a room temperature value of 149 W K^{-1} m^{-1} and diamond structured Ge has a value of 60.2 W K^{-1} m^{-1}.[163] Both of these examples show thermal conductivities of Ge structures that are about half those of the equivalent Si structures. From Figure 4.14 it can be seen that Na_9Ge_{136} has approximately half the thermal conductivity of $Na_{8.8}Si_{136}$. It would be interesting to see if the trend continues to higher Na loadings, where electronic contributions are more significant.

4.2.4.3 Discussion

Figure 4.14 shows glasslike thermal conductivity data for the type II Ge clathrates produced for the present study. Values for Na_9Ge_{136} are very similar to those for the amorphous Ge sample studied: there is significant overlap of the error bars of those two samples at 300 K. In keeping with elemental trends, Na_9Ge_{136} shows thermal conductivities of approximately half those of the Si clathrates with the closest Na content.

The Ge clathrate of unknown Na content, shows higher values for thermal conductivity, compared to Na_9Ge_{136}. Since data for both the Na_xGe_{136} and Na_9Ge_{136} samples have been considered reliable based on the four criteria discussed in section

2.1.2.3, the differences are believed to be due to different compositions. According to trends observed in the Si system, this could indicate either higher or lower Na content for Na_xGe_{136}compared with Na_9Ge_{136}. Since the sample of unknown Na content did not produce Seebeck coefficient data, however, it is believed that the Na_xGe_{136} sample is of lower Na content than the Na_9Ge_{136} sample.

The origin of the low thermal conductivity of Na_9Ge_{136} compared with $Na_{8.8}Si_{136}$ is still unclear. The higher heat capacity of the Ge clathrate implies a lower speed of sound, which might be the major factor. However, further studies are necessary in order to determine the role of Na in heat conduction in type II Ge clathrates.

4.3 Conclusions

Ionic liquids have been successfully used in the production of type II Ge clathrate materials. NaGe is a better intermediate than Na_4Ge_9 since it can be produced more reliably than NaGe and at lower temperature. In addition, it has been shown to more readily produce the Ge clathrate.[147] This is not surprising given that Ge_{136} framework is composed of polyhedra comprised of tetrahedrally bonded Ge atoms and NaGe is composed of anionic Ge tetrahedra with neutralizing Na ions, whereas Na_4Ge_9 is composed of similarly neutralized Ge anionic nonahedra.

While the oxidation product of the NaGe precursor displayed type II clathrate structure (from PXRD), the product formed showed appreciable Na content. Due to the small amounts of product produced in each synthesis attempt it was necessary to combine products from more than one batch for physical property measurements. As a result, elemental analysis showed significant inhomogeneity. Future studies should strive for larger quantities of product from each synthetic attempt and evaluate Na content for each product. In doing so, physical property measurements can be more thoroughly explored in terms of lattice dynamics and dependence on Na content. In addition, it may also make possible the identification of synthetic variables that can be used to control Na content. Increased knowledge of the synthetic technique would make it more amenable to extension to other framework elements.

Although the samples studied were mixtures of Na containing Ge clathrates, the preliminary physical property data presented above can be used to draw some significant conclusions. The Ge clathrate samples examined for the present study have been shown to be more amenable than the Si clathrates to physical property measurements using the PPMS. All three relevant transport properties, S, σ and κ were obtained from a single experiment performed on a thinner pellet (0.4 mm) than would produce S data in the Na_xSi_{136} samples. As with the Na_xSi_{136} samples, S data indicate electrons to be the majority charge carriers in Na filled type II Ge clathrates. Seebeck coefficients were found to be higher than any of those measured in the Na_xSi_{136} series of samples with a room-temperature S value of -130 μV/K.

The heat capacity of Na_9Ge_{136} was found to be higher than the Si clathrate of the most similar composition, $Na_{8.8}Si_{136}$. Indeed, the heat capacity of Na_9Ge_{136} was found to be larger than any of the type II Si clathrates examined for the present study. In addition, electronic contributions to heat capacity, and thus thermal conductivity, were found to be nearly on par with the $Na_{21.5}Si_{136}$ sample (the sample showing the highest electronic contribution to heat capacity in the present study). Despite the high heat capacity and electronic contributions of Na_9Ge_{136}, the type II Ge clathrates investigated for the present study showed a room-temperature thermal conductivity of comparable magnitudes to the low Na content ($x \leq 8.8$) Na_xSi_{136} samples. In fact the, presumably, higher Na content sample, Na_9Ge_{136} has been shown to have a room-temperature thermal conductivity of 1 W m^{-1} K^{-1}, significantly lower than the minimum of 1.5 W m^{-1} K^{-1}observed for the $x = 7.2$ sample of the Na_xSi_{136} series.

While these data for Ge clathrates are preliminary, they are representative of Na filled type II Ge clathrates and show improved thermoelectric characteristics over the equivalent Si clathrate structures. The room-temperature data presented here, in combination with published electrical conductivity data,[85] indicate a room-temperature ZT value of 2.8×10^{-5} for Na_9Ge_{136}. Although this value is derived using the higher magnitude literature value for electrical conductivity, it is expected to be an underestimation of the true ZT value. The intrinsic electrical conductivity of Na_9Ge_{136} is expected to be larger than that of Ge_{136} due to the trend of increasing electrical conductivity with increasing Na content seen in the Na_xSi_{136} series of samples. Therefore, further exploration into the production and characterization of Na filled type II Ge clathrates should be encouraged. However, as with the type II Si clathrates better consolidated, less oxidized samples are needed for more accurate descriptions of electrical conductivity. In addition, syntheses should be designed so as to produce quantities of Ge clathrate on the order of 100 mg or more in order to facilitate physical property measurements (and enable repeat measurements). And finally, more thorough structural and physical property characterizations will lead to a better understanding of the dynamics that govern the physical properties of type II Ge clathrates and why they differ from those of the Na_xSi_{136} samples.

Chapter 5: Conclusion

The present study examined structural and physical properties of Na filled Si and Ge type II clathrates within the context of thermoelectric energy conversion. This work has led to a better understanding of how Na guest content and framework composition affect thermoelectrically relevant physical properties, S, σ and κ.

XAS studies on Na filled type II Si clathrates of the general formula Na_xSi_{136} (where $0 \leq x \leq 21.5$) indicated that Na displacement off-centre of the Si_{28} cages and dynamic disorder decreased with increasing Na content. These studies also showed that charge transfer from Na to Si_{28} cages is Na content dependent (varying from 0.72 e^- at low loadings to 0.8 e^- at high loadings) and slightly greater than charge transfer from Na to Si_{20} cages (0.7 e^-).

Seebeck coefficients were found to increase with decreasing Na content in Na_xSi_{136} samples and became unmeasureable at the lowest Na contents ($x < 5.5$). In addition, it was found that Seebeck coefficients are relatively insensitive to sample oxidation and consolidation methods.

Electrical conductivities of Na_xSi_{136} indicate poorly conducting semiconductors that appeared to be more sensitive to oxidation and consolidation technique than Na content. Electrical conductivities increased somewhat with increasing Na content. However, better consolidation methods, such as spark plasma sintering, are needed in order to quantify this trend.

Thermal conductivities of the Na_xSi_{136} samples studied were found to have glass-like temperature dependencies. Thermal conductivity was found to decrease with increasing Na occupation of Si_{28} cages and to increase with increasing occupation of the

Si_{20} cages. Heat capacity measurement and modeling indicated that the decreases in thermal conductivity associated with Na in Si_{28} cages are due to rattling modes while the increases associated with Na in the Si_{20} cages are due to lattice stiffening and electronic contributions.

Cold-pressed Na_xSi_{136} samples showed a maximum room-temperature ZT of 4×10^{-8} while the hot-pressed $Na_{20}Si_{136}$ samples, having significantly greater electrical conductivity, showed a ZT of 2.5×10^{-6}. Better consolidation processes (such as SPS) are expected to increase ZT values and facilitate simultaneous measurement of multiple physical properties. Although ZT values are too low for Na_xSi_{136} clathrates to be applicable as thermoelectrics, the knowledge gained by these studies provides significant insight into the relationship between structure and properties.

While the present study has increased understanding of transport properties and lattice dynamics of type II Si clathrates, heat capacity measurements at $T < 2.5$ K would further increase that understanding. In particular, the heat capacities of the $Na_{1.3}Si_{136}$ and Si_{136} samples showed anomalous low temperature behaviour. Heat capacity measurements at very low temperatures would help determine the origins of these anomalies.

Na filled type II Ge clathrates were produced in this study using an ionic liquid reaction medium. Physical property measurements of thermoelectrically relevant physical properties, S, σ and κ were performed on the type II Ge clathrate samples produced here. Results are preliminary since the samples examined were somewhat inhomogeneous mixtures of several synthetic products. However, it has been possible to draw several conclusions regarding the thermoelectric properties of type II Ge clathrates.

Na_9Ge_{136} showed higher magnitude S values than any of the Na_xSi_{136} samples, with a room-temperature value of - 140 μV/K compared to the highest Na_xSi_{136} clathrate value of - 80 μV/K at room-temperature, seen in $Na_{1.3}Si_{136}$. Electrical conductivities of the Ge clathrate samples were of comparable magnitudes and temperature dependencies to those of the Na_xSi_{136} samples. This shows that type II clathrate structures are more sensitive to oxidation and consolidation methods than they are to framework composition. The Ge clathrate samples were found to have lower thermal conductivities compared to the Na_xSi_{136} samples with Na_9Ge_{136} showing a room temperature value of ~ 1 W m^{-1} m^{-1} K^{-1}, about half that of the $Na_{8.8}Si_{136}$.

The Na_9Ge_{136} samples, despite being cold-pressed were amenable to simultaneous measurements of multiple physical properties and, compared to Na_xSi_{136} samples, showed a significantly higher ZT value at room-temperatures, 2.8×10^{-5}. Better synthesis and processing techniques, as well as lower temperature heat capacity data ($T < 2.5$ K) are needed in order to determine the origin of the better thermoelectric properties of Na_9Ge_{136}.

Future work should focus on more thorough structural characterization of Na containing Ge clathrates, increasing understanding of synthetic methods and very low temperature ($T < 2.5$ K) heat capacity studies. A more detailed understanding of the Na filled type II Ge clathrate structure is necessary for interpretation of physical property measurements. It has been seen that Na in the Si_{28} cages affects physical properties differently than Na in Si_{20} cages. A thorough understanding of physical property data for Na filled type II Ge clathrates, therefore, requires knowledge of how occupation of the Ge_{28} and Ge_{20} cages changes with Na content. While the presence of Na within the type II Ge clathrates structure was unexpected, it suggests that it is possible to achieve Ge structures of varying Na content. A better understanding of how the synthesis variables (heating time, heating temperature, ratio of ionic liquid to precursor, etc.) affect the composition of the final product could make accessible a Na_xGe_{136} series, comparable to the Na_xSi_{136} series examined in the present work. In addition, better understanding of the synthetic method could allow for expansion of the method to other group 14 elements (*e.g.* Sn and Pb).

While the Ge clathrates have been shown to be more amenable to the simultaneous measurement of physical properties (S, σ and κ were all measured successfully in a single experiment), it would be beneficial for studies of both the Si and Ge clathrates to have better consolidation processes. Physical property measurements obtained from cold-pressed samples for the present study were hindered by sample oxidation and fragility. Specifically, denser, more robust pellets would be less likely to fail during physical property measurement and, more significantly, would lead to electrical conductivity measurements more indicative of intrinsic values. Single crystal or SPS samples would be preferred for future studies.

Although the materials studies for the present work did not produce ZT values as large as those of currently used thermoelectric materials, they have provided insight to improved thermoelectric efficiency through the phonon glass electron crystal approach to thermoelectric materials design. The present study suggests that caged structures for thermoelectric applications should have large cages and frameworks made of heavy elements in order to most efficiently interconvert thermal and electrical energy.

References

[1] J. Yang and T. Caillat, *MRS Bulletin,* **31**, 224 (2006).

[2] http://www2.jpl.nasa.gov/basics/bsf11-3.php and http://saturn.jpl.nasa.gov/mission/introduction/, (accessed June 7, 2011).

[3] G. S. Nolas, J. Sharp and H. J. Goldsmith, *Thermoelectrics Basic Principles and New Materials Developments*, (Springer-Verlag, New York, 2001).

[4] L. Solymar and D. Walsh, *Electrical Properties of Materials, sixth edition*, (Oxford Science Publications, New York 1998).

[5] T. M. Tritt and M. A. Subramanian, *MRS Bulletin*, **31**, 188 (2006).

[6] G. A. Slack and D. M. Rowe, *CRC Handbook on Thermoelectrics*, (CRC Press, Boca Raton, FL, 1995).

[7] A. F. Ioffe, *Semiconductor Thermoelements and Thermoelectric Cooling*, (Infosearch, London, 1957).

[8] K. Kurosaki, H. Uneda, H. Nuta and S. Yamanaka, *Journal of Alloys and Compounds*, **376**, 43 (2004).

[9] F. J. DiSalvo, *Science*, **285**, 703 (1999).

[10] G. D. Mahan and J. O. Sofo, *Proceedings of the National Academy of Sciences of the United States of America*, **93**, 7436 (1996).

[11] G. S. Nolas, J. Poon and M. Kanatzidis, *MRS Bulletin*, **31**, 199 (2006).

[12] G. F. Snyder and E. S. Toberer, *Nature Materials*, **7**, 105 (2008).

[13] M. G. Kanatzidis, *Chemistry of Materials*, **22**, 648 (2010).

[14] J.- S. Rhyee, K. Ahn, K. H. Lee, H. S. Ji and J.- H. Shim, *Advanced Materials*, **19**, 2191 (2011).

[15] S. H. Yang, T. J. Zhu, C. Yu, J. J. Shen, Z. Z. Yin and X. B. Zhao, *Journal of Electronic Materials*, **40**, 1244 (2011).

[16] B. Poudel, Q. Hao, Y. Ma, Y. Lan, A. Minnich, B. Yu, X. Yan, D. Wang, A. Muto, D. Vashaee,, X. Chen, J. Liu, M.S. Dresselhaus, G. Chen and Z. Ren, *Science*, **320**, 634 (2008).

[17] M. Zhou, J.- F. Li, H. Wang, T. Kita, L. Li and Z. Chen, *Journal of Electronic Materials*, **40**, 862 (2011).
[18] R. Venkatasubramanian, E. Siivola, T. Colpitts and B. O'Quinn, *Nature*, **413**, 597 (2001).

[19] T. M. Tritt, *Annual Review of Materials Research*, **41**, 433 (2011).

[20] A. Shakouri, *Annual Review of Materials Research*, **41**, 399 (2011).

[21] J. S.Tse and M. A. White, *Journal of Physical Chemistry*, **92**, 5006 (1988).

[22] G. S. Nolas, G. A. Slack and S. B. Schujman, *Semiconductors and Semimetals*, **69**, 255 (2001).

[23] C. Uher, *Semiconductors and Semimetals*, **69**, 136 (2001).

[24] M. A.White, *Physical Properties of Materials*, (CRC Press, Boca Raton, FL, 2012).

[25] R. S. Berry, S. A. Rice and J. Ross, *Physical Chemistry*, (Oxford University Press, New York, 2000).

[26] C. Kittel, *Introduction to Solid State Physics, Sixth Edition* (John Wiley & Sons, Inc., 1986).

[27] F. Brochin, B. Lenoir, X. Devaux and H. Scherrer, *18th International Conference on Thermoelectrics*, 390 (1999).

[28] A. Yamamoto and T. Ohta, *15th International Conference on Thermoelectrics*, 464 (1996).

[29] M. Hamabe, H. Takahashi, S. Yamaguchi, T. Komine, T. Eura, H. Okumura, Y. Okamoto and J. Morimoto, *Japanese Journal of Applied Physics,* **42**, 6779 (2003).

[30] S. -M. Lee, D. G. Cahill and R. Venkatasubramanian, *Applied Physics Letters,* **70**, 2957 (1997).

[31] Y. Muro, T. Sasakawa, T. Suemitsu, T. Takabatake, R. Tamura and S. Takeuchi, *Japanese Journal of Applied Physics*, **41**, 3787 (2002).

[32] E. Macia, *Physical Review B*, **70**, 100201 (2004).

[33] Y. Adjallah, C. Blackwell and J. Kakalios, *Materials Research Society Symposium Proceedings* (*Amorphous and Polycrystalline Thin-Film Silicon Science and Technology*), 1245 (2010).

[34] H. Takiguchi, Z. Yoshikawa, H. Miyazaki, Y. Okamoto and J. Morimoto, *Journal of Electronic Materials*, **39**, 1627 (2010).

[35] G. P. Srivastava, *MRS Bulletin*, **26,** 445 (2001).

[36] X. Tang, J. Dong, P. Hutchins, O. Shebanova, J. Gryko, P. Barnes, J. K. Cockcroft, M. Vickers and P. F. McMillan, *Physical Review B*, **74**, 014109 (2006).

[37] A. Einstein, *Annalen der Physik*, **22**, 180 (1907).

[38] P. Debye, *Annalen der Physik*, **39**, 789 (1912).

[39] A. K. Cheetham and P. Day, *Solid-State Chemistry Techniques* (Clarendon Press, Oxford, 1987).

[40] J. Androulaki, P. Migiakis and J. Giapintzakis, *Applied Physics Letters*, **84,** 1099 (2004).

[41] H. Ibach and H. Lüth, *Solid-State Physics An Introduction to Principles of Materials Science*, *Fourth Edition* (Springer, New York, 2009).

[42] J. S. Kasper, P. Hagenmuller, M. Pouchard and C. Cros, *Science*, **150**, 1713 (1965).

[43] G. S. Nolas, X. Lin, J. Martin, M. Beekman and H. Wang, *Journal of Electronic Materials*, **38**, 1052 (2009).

[44] H. Kawaji, H.-O. Horie, S. Yamanaka and M. Ishikawa, *Physical Review Letters*, **74**, 1427 (1995).

[45] S. Yamanaka, E. Enishi, H. Fukuoka and M. Yasukawa, *Inorganic Chemistry*, **39**, 56 (2000).

[46] K. Moriguchi, S. Munetoh and A. Shintani, *Physical Review B*, **62**, 7138 (2000).

[47] C. Mogens, J. Simon and B. B. Eversen, *Dalton Transactions*, **39**, 178 (2010).

[48] Y. Liu, L. Wu, L. Li, S. Du, J. D. Corbett and L. Chen, *Angewandte Chemie International Edition*, **48**, 5305 (2009).

[49] D. Neiner, N. L. Okamoto, C. L. Condron, Q. M. Ramasse, P. Yu, N. D. Browning and S. M. Kauzlarich, *Journal of the American Chemical Society*, **129**, 13857 (2007).

[50] S. B. Schujman, G. S. Nolas, R. A. Young, C. Lind, A. P. Wilkinson, G. A. Slack, R. Patschke, M. G. Kanatzidis, M. Ulutagay and S.-J. Hwu, *Journal of Applied Physics*, **87**, 1529 (2000).

[51] N. J. English and J. S. Tse, *Physical Review Letters*, **103**, 015901 (2009).

[52] K. Ichikawa, K. Nakata and M. M. Ibrahim, *Chemistry Letters*, **7**, 796 (2000).

[53] C. Cros, M. Pouchard and P. Hagenmuller, *Journal of Solid State Chemistry*, **2**, 570 (1970).

[54] A. D. Ritchie, M. A. MacDonald, P. Zhang, M. A. White, M. Beekman, J. Gryko and G. S. Nolas, *Physical Review B*, **82**, 155207 (2010).

[55] P. Simon, Z. Tang, W. Carrillo-Cabrera, K. Chiong, B. Bohme, M. Baitinger, H. Lichte, Y. Grin and A. M. Guloy, *Journal of the American Chemical Society* , **133**, 7596 (2011).

[56] A.M. Guloy, Z. Tang, R. Ramlau, B. Boehme, M. Baitinger and Y. Grin, *European Journal of Inorganic Chemistry*, **2009**, 2455 (2009).

[57] D. T. Morelli, G. P. Meisner, B. Chen, S. Hu and C. Uher, *Physical Review B*, **56**, 7376 (1997).

[58] G.S. Nolas, T. J. R. Weakley, J. L. Cohn and R. Sharma, *Physical Review B*, **61**, 3845 (2000).

[59] P. Rogl and D. M. Rowe, *Thermoelectrics Handbook: Macro to Nano*, (CRC Press, Boca Raton, FL, 2006).

[60] J. Kim, N. Okamoto, K. Kishida, K Tanaka and H. Inui, *Acta Materialia*, **54**, 2057 (2006).

[61] S. Bobev and S. C. Sevov, *Journal of the American Chemical Society*, **123**, 3389 (2001).

[62] J. L. Cohn, G. S. Nolas, V. Fessatidis, T. H. Metcalf and G. A. Slack, *Physical Review Letters*, **82**, 779 (1999).

[63] D. Huo, T. Sakata, T. Sasakawa, M. A. Avila, M. Tsubota, F. Iga, H. Fukuoka, S. Yamanaka, S. Aoyagi and T. Takabatake, *Physical Review B,* **71**, 075113 (2005).

[64] G. S. Nolas, T. J. R. Weakley and J. L. Cohn, *Chemistry of Materials*, **11**, 2470 (1999).

[65] S. Bobev and C. Sevov, *Journal of Solid State Chemistry*, **153**, 92 (2000).

[66] G. Ramachandran, J. Dong, J. Diefenbacher, J. Gryko, R. Marzke, O. Sankey and P. McMillan, *Journal of Solid State Chemistry*, **145**, 716 (1999).

[67] J. S. Tse, K. Uehara, R. Rousseau, A. Ker, C. I. Ratcliffe, M. A. White and G. MacKay, *Physical Review Letters*, **85**, 114 (2000); *ibid.* **86**, 4980 (2001).

[68] G. S. Nolas, J.-M. Ward, J. Gryko, L. Qiu, and M.A. White, *Physical Review B*, **64**, 153201 (2001).

[69] L. Qiu, M. A. White, Z. Li, J. S. Tse, C. I. Ratcliffe, C. A. Tulk, J. Dong and O. F. Sankey, *Physical Review B*, **64**, 024303 (2001).

[70] See, for example, L. Qiu, I. P. Swainson, G. S. Nolas and M. A. White, *Physical Review B*, **70**, 035208 (2004).

[71] A. Ammar, C. Cros, M. Pouchard, N. Jaussaud, J. M. Bassat, G. Villeneuve, M. Duttine, M. Menetrier and E. Reny, *Solid State Sciences*, **6**, 393 (2004).

[72] J. Gryko, R. F. Marzke, G. A. Lamberton, Jr., T. M. Tritt, M. Beekman and G. S. Nolas, *Physical Review B*, **71**, 115208 (2005).

[73] G. S. Nolas, M. Beekman, J. Gryko, G. A. Lamberton, Jr., T. M. Tritt and P. F. McMillan, *Applied Physics Letters*, **82,** 910 (2003).

[74] M. Zakrzewski and M. A. White, *Physical Review B*, **45**, 2809 (1992).

[75] M. Beekman and G.S. Nolas, *Journal of Materials Chemistry*, **18**, 842 (2008).

[76] E. Reny, P. Gravereau, C. Cros and M. Pouchard, *Journal of Materials Chemistry*, **8**, 2839 (1998).

[77] S. B. Roy, K. E. Sim and A. D. Caplin, *Philosophical Magazine B*, **65**, 1445 (1992).

[78] J. C. Conesa, C. Tablero and P. Wahnon, *Journal of Chemical Physics*, **120**, 6142 (2004).

[79] É. Reny, M. Ménétrier, C. Cros, M. Pouchard and J. Sénégas, C. R. *Comptes Rendus de l'Academie des Sciences, Serie IIc*, **1**, 129 (1998).

[80] J. He**,** D. D. Klug, K. Uehara, K. F. Preston, C. I. Ratcliffe and J. S. Tse, *Journal of Physical Chemistry B*, **105**, 3475 (2001).

[81] F. Tournus, B. Masenelli, P. Mélinon, D. Connétable, X. Blase, A. M. Flank, P. Lagarde, C. Cros and M. Pouchard*, Physical Review B*, **69**, 035208 (2004).

[82] H. Libotte, J. –P. Gaspard, A. San Migueal and P. Melinon, *Europhysics Letters*, **64**, 757 (2003).

[83] B. C. Sales, B. C. Chakoumakos and D. Mandrus, *Journal of Solid State Chem.*, **146**, 528 (1999).

[84] G. S. Nolas, D. G. Vanderveer, A. P. Wilkinson and J. L. Cohn, *Journal of Applied Physics*, **91**, 8970 (2002).

[85] A. M. Guloy, R. Ramlau, Z. Tang, W. Schnelle, M. Baitinger and Y. Grin, *Nature*, **443**, 320 (2006).

[86] J. Dong, O. F. Sankey and C. W. Myles, *Physical Review Letters*, **86**, 2361 (2001).

[87] J. B. Marion, *Physics and the Physical Universe*, 3rd Edition, (John Wiley Sons, Toronto, 1980).

[88] Quantum Design, *Physical Property Measurement System Resistivity Option User's Manual* (Quantum Design, San Diego, 1999).

[89] N.R. Dilley, R.C. Black, L. Montes, A. Wilson and M.B. Simmonds, *Materials Research Society Symposium Proceedings*, **691**, 85 (2002).

[90] http://www.qdusa.com/sitedocs/productBrochures/tto_rev7-06.pdf, (accessed October 14, 2011).

[91] C. Bryan, *Honours Thesis*, (Dalhousie University, Halifax, 2011).

[92] O. Maldonado, *Cryogenics*, **32**, 908 (1992).

[93] M. J. Assael, K. Gialou, K. Kakosimos and I. Metaxa, *International Journal of Thermophysics*, **25**, 397 (2004).

[94] C. Kennedy, *PhD Thesis*, (Dalhousie University, Halifax, 2005).

[95] J.S. Hwang, K.J. Lin and C. Tien, *Review of Scientific Instruments*, **68**, 94 (1997).

[96] C. A. Kennedy, M. Stancescu, R.A. Marriott and M.A. White, *Cryogenics*, **47**, 107(2007).

[97] C. A. Swenson, *Review of Scientific Instruments*, **70**, 2728 (1999).

[98] J. Glusker, M. Lewis and M. Rossi, *Crystal Structure Analysis for Chemists and Biologists*, (VCH publisher, New York, 1994).

[99] R. C. Reynolds, Jr., *Modern Powder Diffraction*, (The Mineralogical Society of America, Washington, 1989).

[100] C. Giacovazzo, H. Monaco, D. Viterbo, F. Scordari, G. Gilli, G. Zanotti and M. Catti, *Fundamentals of Crystallograph*, (International Union of Crystallography Oxford University Press, Oxford, 1992).

[101] V.K. Pecharsky and P.Y. Zavalij, *Fundamentals of Powder Diffraction and Structural Characterization of Materials*, (Springer, New York, 2005).

[102] M. K. Beekman, *PhD Thesis*, (University of South Florida, Tampa, 2009).

[103] A. C. Larson and R. B. Von Dreele, *General Structure Analysis System (GSAS)*, Los Alamos National Laboratory Report LAUR 86-748, (2004).

[104] B. H. Toby, *Applied Crystallography*, **34**, 210 (2001).

[105] R. Stumm von Bordwehr, *Annales de Physique (Paris, France)*, **14**, 377 (1989).

[106] G. Bunker, *Introduction to XAFS*, (Cambridge University Press, Cambridge, 2010).

[107] D. Bog, E. Bunu, L. Fratila, M. Vasile, L. Georgescu, M. Kiraly, D. Cornuejols, J. –F. Manzoni-Etxepare, G. Admans, J. Mc Carthy and K. Fletcher, *Exploring matter with synchrotron light*, (iMediasoft, 2002).

[108] D.Koningsberger and R. Prins , *X-ray Absorption, Principles, Applications, Techniques of EXAFS, SEXAFS and XANES*, (Wiley-Interscience Publications, Toronto,1988).

[109] A. L. Ankudinov, B. Ravel, J. J. Rehr and S. D. Conradson, *Physical Review B*, **58**, 7565 (1998).

[110] L. D. Menard, H. P. Xu, S. P. Gao R. D. Twesten, A. S. Harper, Y. Song, G. L. Wang, A. D. Douglas, J. C. Yang, A. I. Frenkel, R. W. Murray and R. G. Nuzzo, *Journal of Physical Chemistry B*, **110**, 14564 (2006).

[111] J. Goldstein, D. Newbury, D. Joy, C. Lyman, P. Echlin, E. Lifshin, L. Sawyer and J. Michael, *Scanning Electron Microscopy and X-Ray Microanalysis*, (Springer Sience + Business Media, Inc., New York, 2003).

[112] http://www.earthsciences.dal.ca/research/facility/probelab/, (accessed February 2, 2011).

[113] J Gryko, *U.S. Patent No. 6,423,286.*

[114] J. Gryko, P. F. McMillan, R. F. Marzke, G. K. Ramachandran, D. Patton, S. K. Deb and O. F. Sankey, *Physical Review B*, **62**, R7707 (2000).

[115] M. Beekman, *Private Communication* (2008).

[116] M. Beekman, E. N. Nenghabi, K. Biswas, C. W. Myles, M. Baitinger, Y. Grin and G. S. Nolas, *Inorganic Chemistry* **49**, 5338 (2010).

[117] B. K. Teo, *EXAFS: basic principles and data analysis*, (Springer-Verlag, New York, 1986).

[118] M. Beekman, W. Schnelle, H. Borrmann, M. Baitinger, Yu. Grin and G. S. Nolas, *Physical Review Letters*, **104**, 018301 (2010).

[119] M. Beekman, C. P. Sebastian, Y. Gri and G. S. Nolas, *Journal of Electronic Materials*, **38**, 1136 (2009).

[120] F. Brunet, P. Mélinon, A. SanMiguel, P. Kéghélian, A. Perez, A. M. Flank, E. Reny, C. Cros and M. Pouchard, *Physical Review B,* **61**, 16550 (2000).

[121] B. Waestberg, A. Rosen and D. E. Ellis, *Zeitschrift fuer Physik D*, **13**, 153 (1989).

[122] M. Volmer, C. Sternemann, J. S. Tse, T. Buslaps, N. Hiraoka, C. L. Bull, J. Gryko, P. F. McMillan, M. Paulus and M. Tolan, *Physical Review B.*, **76**, 233104 (2007).

[123] P. Zhang, S. J. Naftel and T. K. Sham, *Journal of Applied Physics*, **90**, 2755 (2001).

[124] N.F. Mott, *Journal of Solid State Chemistry*, **6**, 348 (1973).

[125] M. Beekman, S. C. Peter, Y. Grin and G. S. Nolas, *Journal of Electronic Materials*, **38**, 1136 (2009).

[126] M. Beekman and G. S. Nolas, *Physica B*, **383**, 111 (2006).

[127] P.G. Klemens, *High Temperaturess – High Pressures*, **23**, 241 (1991).

[128] S. Stefanoski, J. Martin and G. S. Nolas, *Journal of Physics*, **22**, 485404 (2010).

[129] G. S. Nolas, *Private Communication* (2006).

[130] T. M. Tritt, *Private Communication* (2006).

[131] M. Beekman, *Private* Communication (2011).

[132] T. H. K. Barron and J. A. Morrison, *Canadian Journal of Physics*, **35**, 799 (1957).

[133] C. Kittel, *Introduction to Solid State Physics, Eighth Edition* (John Wiley & Sons, Inc., 2005).

[134] L. Qiu and M. A. White, *Journal of Chemical Education*, **78**, 1076 (2001).

[135] M. A. White, L. Qiu and G. S. Nolas, *Thermal Conductivity, 27(Thermal Expansion 15)*, 72 (2005).

[136] H. –M Kagaya, T. Soma and M. R. Brozel, *EMIS Datareviews Series*, **20**, 151 (1999).

[137] C. S. Barrett, *Acta Crystallographica*, **9**, 671 (1956).

[138] D. L. Martin, *Proceedings of the Royal Society of London. Series A, Mathematical and Physical Sciences*, **256**, 433 (1960).

[139] G. K. Ramachandran, P. F. McMillan, S. K. Deb, M. Somayazulu, G. Gryko, J. Dong and O. F. Sankey, *Journal of Physics: Condensed Matter*, **12**, 4013 (2000).

[140] M. Beekman, R. P. Hermann, A. Mochel, F. Juranyi and G. S. Nolas, *Journal of Physics*, **22**, 355401 (2010).

[141] G. Chen, *International Journal of Thermal Sciences*, **39**, 471 (2000).

[142] G. S. Nolas, J. L. Cohn, J. S. Dyck, C. Uher and J. Yang, *Physica Review B.*, **65**, 165201 (2002).

[143] L. Mollnitz, N. P. Blake and H. Metiu, *Journal of Chemical Physics*, **117**, 1302 (2002).

[144] M. Christensen, S. Johnsen and B. B. Iversen, *Dalton Transactions*, **39**, 178 (2010).

[145] E. Grovenstein, Jr. and R. W. Stevenson, *Journal of the American Chemical Society*, **81**, 4850 (1959).

[146] V. J. Witte and H. G. Schnering, *Zeitschrift fur Anorganische und Allgemeine Chemie*, **327**, 260 (1964).

[147] M. Qian, *Optimizing the Synthesis of a Novel Guest-Free Germanium Clathrate, Ge_{136}*, University of Houston (2006).

[148] CrystalMaker Software, *CrystalDiffract for Windows v. 1.4.1* (2011).

[149] Match! Phase Identification from Powder Diffraction, Version 1.2, Crystal Impact (2004), T. Swanson, National Bureau of Standards (U.S.), Circ. 539 **I**, 18 (1951).

[150] Match! Phase Identification from Powder Diffraction, Version 1.2, Crystal Impact (2004), Calculated from NIST using POWD-12++ 327, 260 (1964).

[151] Z. Ma, J. Yu and S. Dai, *Advanced Materials*, **22**, 261 (2010).

[152] C. W. Myles, J. Dong and O. F. Sankey *Physical Review B.*, **64**, 165202 (2001).

[153] C. W. Myles, J. Dong, O. F. Sankey, C. A. Kendziora and G. S. Nolas, *Physical Review B.*,**65**, 235208 (2002).

[154] C. W. Myles, J. Dong and O. F. Sankey, *Physica Status Solidi B: Basic Research*, **239**, 26 (2003).

[155] R. Winter, O. Leichtweis, C. Biermann, M.-L. Saboungi, R. L. McGreevy and W. S. Howells, *Journal. Non-Crystalline Solids*, **205**, 66 (1996).

[156] M. Wilson and P. F. McMillan, *Physical Review Letters*, **90**, 135703 (2003).

[157] P. F. McMillan, *Nature Materials*, **1**, 19 (2002).

[158] M. Beekman, J. A. Kaduk, J. Gryko, W. Wong-Ng, A. Shapiro and G. S. Nolas, *Journal of Alloys and Compounds*, **470**, 365 (2009).

[159] M. Beekman, G. S. Nolas, J. Gryko, G. A. Lamberton, T. M. Tritt and C. A. Kenziora, *Electrochemical Society Proceedings*, **2003-27**, 271 (2004).

[160] P. Flubacher, A. J. Leadbetter and J. A. Morrison, *Philosophical Magazine*, **4**, 273 (1959).

[161] Match! Phase Identification from Powder Diffraction, Version 1.2, Crystal Impact (2004), National Bureau of Standards (U.S.), Monograph 25, **13**, 35 (1976).

[162] T. B. Light, *Physical Review Letters*,**22**, 999 (1969)

[163] R. C. Weast and M. J Astle, *CRC Handbook of Chemistry and Physics 61st Edition*, (CRC Press, Boca Raton, FL, 1980).